Dynamics of Passively Coupled Continuous-Wave and Mode-Locked Lasers

by

Sudarshan Sivaramakrishnan

A dissertation submitted in partial fulfillment
of the requirements for the degree of
Doctor of Philosophy
(Electrical Engineering)
in The University of Michigan
2017

Doctoral Committee:

Professor Herbert G. Winful, Chair
Professor Almantas Galvanauskas
Professor Peter D. Miller
Professor Kim A. Winick

Sudarshan Sivaramakrishnan

sivas@umich.edu

ORCID iD: 0000-0002-6224-2094

DEDICATION

To my parents and to my younger brother

ACKNOWLEDGMENTS

My PhD journey has been deeply enriching and enlightening, as well as the most challenging endeavor that I have ever undertaken. As such, I am grateful to all involved for the motivation, support, and engagement that made graduate life as fulfilling and fun of an experience as it was.

First and foremost, I would like to thank my research advisor, Professor Herbert Winful, for his dedication, patience, and enthusiasm to help me successfully complete my PhD. It has been a privilege to work with and learn from him across a diverse array of fascinating topics, and I am indebted to him for aiding my growth as a researcher and as an individual. From my first meeting with him (an advising appointment when I was an undergraduate freshman declaring my major in Electrical Engineering) to joining his research group in the summer before graduate school to the present, he has been a persistent source of wisdom, encouragement, and equanimity. His thoughtful guidance has enabled me to explore new scientific problems and steer my own path through the research process, while time and again his friendly smiles and ever-positive outlook replenished my belief in the value of my work whenever I lost my way. Last but not least, Prof. Winful is one of the nicest and most genuine people I have ever known.

Next, I appreciate the valuable help, feedback, and guidance from my dissertation committee. Professor Almantas Galvanauskas provided key practical insights and asked thought-provoking questions in our collaboration on the beam combining project; I also enjoyed taking his optics courses as an undergraduate and in graduate school. Professor Peter Miller helped me to develop

a good conceptual understanding of the mathematical theory through his clear and concise explanations. Professor Kim Winick was generously accommodative to serve on my committee as a late substitution and to share his discerning perspective throughout the thesis review process.

I would also like to acknowledge all of the faculty supervisors during my tenure as a Graduate Student Instructor (GSI), and in particular Professors Alexander Ganago, Anthony Grbic, Andrew Yagle, Somin Lee, Leung Tsang, and Kim Winick. The GSI experience across several subjects (circuits, signals and systems, and electromagnetics I/II) helped develop my teaching and communication skills, hands-on and laboratory skills, and the ability to think about engineering from a practical, applied, intuition-based perspective. It has well-complemented my primary research work in regard to overall academic and professional growth.

Special thanks go to Professor Alexander Ganago for his mentorship in teaching and for giving me a unique opportunity to translate my GSI work (and musical interests) into engineering education research and lab/curriculum development. Prof. Ganago's friendliness, enthusiasm, creative ideas, and genuine interest in teaching and education inspired me to approach my GSI duties and other aspects of graduate school in a similar light.

In addition, I appreciate the timely assistance, helpful information, and flexible coordination of the EECS department, especially staff members Karen Liska, José Rubio, Anne Rhoades, Punam Vyas, and Beth Stalnaker, as well as Rob Giles from lab support. Also, the Engineering Career Resource Center was a valuable resource for me as I considered my post-graduation options.

I have been fortunate to interact with and learn from many people throughout my long tenure as a student at the Michigan. However, these acknowledgments would be remiss without specific mention of my colleague and friend Dr. Wei-Zung (Wayne) Chang, who was a collaborator on the beam combining project. I am very grateful for his mentorship, insightful discussions, and interest in my research area during the first several years of my PhD. Also to mention is Professor Gabor Orosz for his help with numerical bifurcation analysis and DDE-BIFTOOL.

Outside of academics, Michigan's superb culture and community of student organizations gave me the chance to actively take part and have leadership roles in the Hindu Students Council, GradTONES A Cappella, Maize Mirchi A Cappella, the ECE Graduate Student Council, and the Michigan Synthetic Biology Team, all of which I thoroughly enjoyed. I also had a lot of fun as a regular member of the ECE intramural soccer, football, and frisbee teams over the many seasons. My involvement in all of these extracurricular activities was a crucial and formative element of my college experience. It provided me the necessary, unique, and wholesome outlets for self-development, community engagement, and leadership experience, and it equipped me with a broad, well-rounded skillset and perspective. In a similar light, I also want to communicate my gratitude to all of my friends through the years for their positive impact and diverse perspectives and to all of my former teachers, supervisors, mentors, and schools for helping me acquire the knowledge, experience, and confidence to pursue my education and career to date. Likewise, I thank my extended family for the greetings, regular inquiries, and caring nature (even from afar).

Finally, I wish to convey my utmost appreciation to my immediate family - my parents and my younger brother - for the unbounded support, belief, and love. I am nothing without them.

TABLE OF CONTENTS

LIST OF TABLES

LIST OF FIGURES

LIST OF APPENDICES

ABSTRACT

This thesis focuses on theoretical and numerical investigation of the dynamics of coupled lasers and laser arrays, specifically through the avenue of two different systems of interest: 1) passive coherent beam combining of continuous-wave fiber laser arrays, and 2) passive coupling of mode-locked semiconductor lasers.

The coherent beam combining work contributes to understanding the phasing dynamics in externally-coupled fiber laser arrays (specifically here, a spatially-filtered, ring-oscillator combining geometry) by use of a multi-longitudinal-mode, dynamical model to study the system. The results show that the passive phasing and locking processes operate on a much faster timescale than that of the power and gain transients, and the system is able to recover its phase-locked state within just a few cavity roundtrips after a strong perturbation from steady-state; the results agree with previous experiments. The simulations also demonstrate that the non-resonant Kerr nonlinearity is detrimental to the system's combining efficiency and ability to coherently lock in phase, as determined by qualitative examination and quantitative assessment of the far-field output and its on-axis intensity. A physical explanation of the role of the nonlinearity and a comparison to 50:50 directionally-coupled arrays, both presented within the context of coincident mode theory, is provided to accompany the numerical results.

The mode-locked semiconductor lasers work examines the dynamics of two evanescently coupled, ring-cavity semiconductor lasers (with saturable absorbers) by use of a delay

differential equation model (that is extended to incorporate the action of a directional coupler) and with the aid of numerical simulations and bifurcation analyses methods. The findings in this thesis include the following catalog of the variety of complex, interesting, and important phenomena in this system and their dependence on coupling, unsaturated gain, and linewidth enhancement factors: 1) symmetry-breaking effects that lead to strong modulations of and delayed synchronization between the two lasers' pulse trains; 2) the evolution of the coupled lasers from an initial unsynchronized state to nearly-perfect, in-phase synchronization; 3) a subharmonic mode-locked regime in which the two lasers pulsate in anti-synchrony (i.e. anti-phase) and, in the case of lasers with identical roundtrip times, at one half the solitary laser's fundamental mode-locked repetition rate; 4) fractional harmonic mode-locking regimes with repetition rates corresponding to three-halves and five-halves the fundamental mode-locking frequency of the solitary lasers; 5) a destabilization of mode-locking and continuous-wave operation; and 6) multistability between the different dynamical regimes and behaviors. These behaviors can be observed even in the presence of noise.

CHAPTER 1

Introduction

Coupled lasers, and more generally coupled oscillators, present a vast and rich domain of complex and fascinating dynamical phenomena that is of theoretical and practical interest and importance. To name just a few areas of work regarding coupled lasers, there is research in scaling of output power/brightness, coherent locking and phase synchronization, optical computing and/or communications, chaos, and multistable behavior. Research work in the broader scope of coupled nonlinear oscillators and dynamical systems is prevalent in numerous other fields, including but certainly not limited to astronomy, biology, chemical systems, ecology, electronic and electrical systems, geology, mathematics, mechanical systems, music, nuclear physics, oceanography, quantum physics, seismology, and vehicular traffic.

1.1 Research objectives

This thesis and the associated research work focuses on theoretical and numerical investigation of the dynamics of two different systems of interest:

1) Passive coherent beam combining of continuous-wave fiber laser arrays
2) Passive coupling of mode-locked semiconductor lasers

For the first topic, the objective is to address several aspects of the passive phasing dynamics and to contribute to a more complete understanding of the underlying physical mechanisms that

influence the dynamical evolution and growth toward coherence (or lack thereof) of continuous-wave fiber laser arrays coupled in a spatially-filtered unidirectional ring architecture:

1) The behavior of the coherent phase locking processes within the fiber laser array, including its relation to…
    a) the evolution of the array output (i.e. power and far-field intensity distribution)
    b) the lasing medium's population dynamics
2) The robustness of phase-locking, specifically with regard to the coupled system's response to external perturbations applied after reaching steady-state
3) The influence of fiber nonlinearities – specifically here the non-resonant Kerr nonlinearity – on passive phasing and array combining efficiency
4) The effect of optical path differences encountered in the coupling optics (which occur external to the individual fibers)
5) A comparison to other coupling geometries

For the second topic, the objective is to explore the dynamical regimes and interesting phenomena (of theoretical interest and/or for direct, practical application) that occur when two semiconductor lasers – each with saturable gain and saturable absorption – are passively coupled to each other (e.g. evanescently or via a dedicated directional coupler). Due to the parameter space and already-present complexity of the system, despite a design that in principle is seemingly simple, the scope of this exploration and investigation at present is narrowed to focus on the following aspects in the context of two identical lasers:

1) Occurrences of coupling-induced symmetry-breaking
2) The presence (or absence) and dynamical structure of synchronization of the two lasers

3) The organization of and multistability between various regimes of operation (e.g. continuous-wave, mode-locked, burst-mode, quasi-periodic, chaotic) – synchronized, delayed-synchronized, or unsynchronized – with respect to the coupling strength, pump power, linewidth enhancement factors, initial state / initialization, and noise
4) A comparison of the dynamics for weak coupling vs. 50:50 coupling vs. strong coupling (including the special case of complete cross-coupling)
5) The role of linewidth enhancement factors and the influence of noise on all of the above

1.2 Outline of the thesis

CHAPTER 2 presents the context and the research work regarding passive coherent beam combining of continuous-wave fiber laser arrays. The chapter begins with an overview of fiber lasers as sources for laser light, introduces the main concepts and methods of beam combining, and establishes a motivation for the thesis work in this field. Then comes a brief review of the various types of passive coherent beam combining systems (internally vs. externally coupled fiber arrays) and a discussion of the relevant scientific literature in modeling approaches used for theoretical and numerical investigation, including the dynamic, multi-longitudinal-mode model of fiber lasers that is adapted to the specific research work of this thesis. The methods section that follows explains the physical model for the spatially-filtered ring geometry coupling architecture, the mathematical model based on the Nonlinear Schrödinger Equation for the electric field and rate equations for the laser gain, the numerical methods used for simulation of the system, and the important simplifying assumptions. The remaining sections present and discuss the main results and conclusions of this research work, with the bulk of the emphasis on the nature of the passive phasing dynamics and the role that the Kerr nonlinearity plays in this

system and its combining efficiency. These two aspects are addressed from several perspectives, including 1) the temporal evolution of power, gain, and phasing between the fibers in the array, 2) the temporal evolution of the extracted output's far-field pattern, 3) the output frequency and phase spectra and the regions of coherently-locked, self-selected composite cavity modes, and 4) a combining efficiency metric derived by comparing the scaling of the far-field on-axis intensity in the presence vs. in the absence of coupling.

CHAPTER 3 presents the context and the research work regarding passively coupled, mode-locked semiconductor lasers. The chapter begins with an overview of semiconductor lasers as sources for laser light, introduces the research interest and applications associated with coupled semiconductor lasers, and establishes a motivation for the thesis work in this field. Then comes a review of the scientific literature regarding passively coupled, continuous-wave semiconductor lasers, as well as a discussion on the more recent studies of mode-locked semiconductor lasers. These sections present the main methodologies (for modeling and analysis), types of physical phenomena, and varieties of coupled systems that have been previously explored and observed within the field, from which this thesis work draws guidance, context, and techniques to adapt to the research study. Also included are brief conceptual summaries of passive mode-locking via saturable absorbers and of linear stability and bifurcation analyses (specifically as they relate to delay differential equations). The methods section that follows explains the physical model for two evanescently/directionally coupled, unidirectional-ring-cavity semiconductor lasers, along with both the partial differential equation and delay differential equation mathematical models, the numerical methods used for simulation and bifurcation analysis, and the relevant simplifying assumptions. The remaining sections present and discuss the main results and conclusions

obtained from the research work, cataloging the rich variety of phenomena observed in this coupled system, including coupling-induced symmetry-breaking of identical lasers, perfect synchronization, delayed-synchronization, destabilization of regular mode-locked pulse trains, emergence of a subharmonic mode-locked regime for fully cross-coupled lasers, burst-mode operation at high gain, and the robustness of these behaviors in the presence of noise and linewidth enhancement factors. Special attention is accorded to the subharmonic mode-locking phenomenon. The dynamical structure of the coupled lasers is explored from several vantage points: 1) numerical simulation results of the temporal power, complex-valued amplitudes, axial mode spectra, and gain/loss dynamics; 2) one-parameter bifurcation diagrams generated from iterations of simulations with up- and down-sweeps of the relevant parameters to examine the multistable regimes; and 3) two-parameter numerical "continuation" of the equilibria and bifurcations to identify stable and unstable branches of steady states and relative periodic orbits.

CHAPTER 4 summarizes the work of the thesis, highlights the main contributions with respect to the research objectives, and offers several suggestions for future directions.

The APPENDICES provide 1) the detailed derivations for the mathematical models developed or extended as part of this thesis work, and 2) information about the numerical codes (written in MATLAB) used for the simulations and bifurcation analysis.

CHAPTER 2

Passive coherent beam combining of fiber laser arrays

2.1 Introduction

Rare-earth-ion-doped optical fibers present an attractive option for the generation of laser output in visible and infrared wavelength ranges [1, 2]. Optical fiber amplifiers consist of a host medium (typically silica or some other glass) along with rare-earth dopants (such as Ytterbium and Erbium) to establish the energy transition levels (in a three- or four-level structure) that are utilized in conjunction with optical pumping (to establish the population inversion) for optical gain via stimulated emission [1]. With the addition of feedback to the fiber amplifier, and for sufficient pump levels, lasing can commence. These "fiber lasers" allow for several desirable characteristics: built-in waveguiding, compact-yet-long gain regions, wide gain bandwidth, efficient pump conversion, high beam quality, effective heat dissipation, efficient pump conversion, to name a few [1, 3, 4, 5]. Although many advances have been made to increase output intensity of a single fiber laser, various physical limitations continue to pose challenges for further power and brightness scaling, including Stimulated Raman Scattering, Stimulated Brillouin Scattering, self-phase modulation, self-focusing, mode instabilities, and ultimately material damage [1, 3, 5, 6].

Accordingly, to circumvent many of these obstacles, there is concurrent research in methods to combine the outputs of multiple fiber amplifiers, both for continuous-wave (CW) as well as

pulsed (e.g. mode-locked, Q-switched) modes of operation. Some common combining methods include spectral / wavelength beam combining, coherent beam combining, incoherent beam combining, and polarization beam combining [3, 7, 8]. Figure 2.1 provides simplified illustrations to help visualize the conceptual basis for each of these methods; of course, the actual systems used in practice contain more complexity, as well as variety in implementation. Coherent beam combining (CBC) techniques can typically be categorized into active-control methods and passive (self-organization) methods; the primary challenge is to ensure in-phase-locking (constructive interference) among all elements of the fiber array and minimizing relative phase deviations / variations [7, 9, 10]. This is unlike incoherent beam combining, which implements no phase control and simply "stacks" the beams incoherently on top of each other.

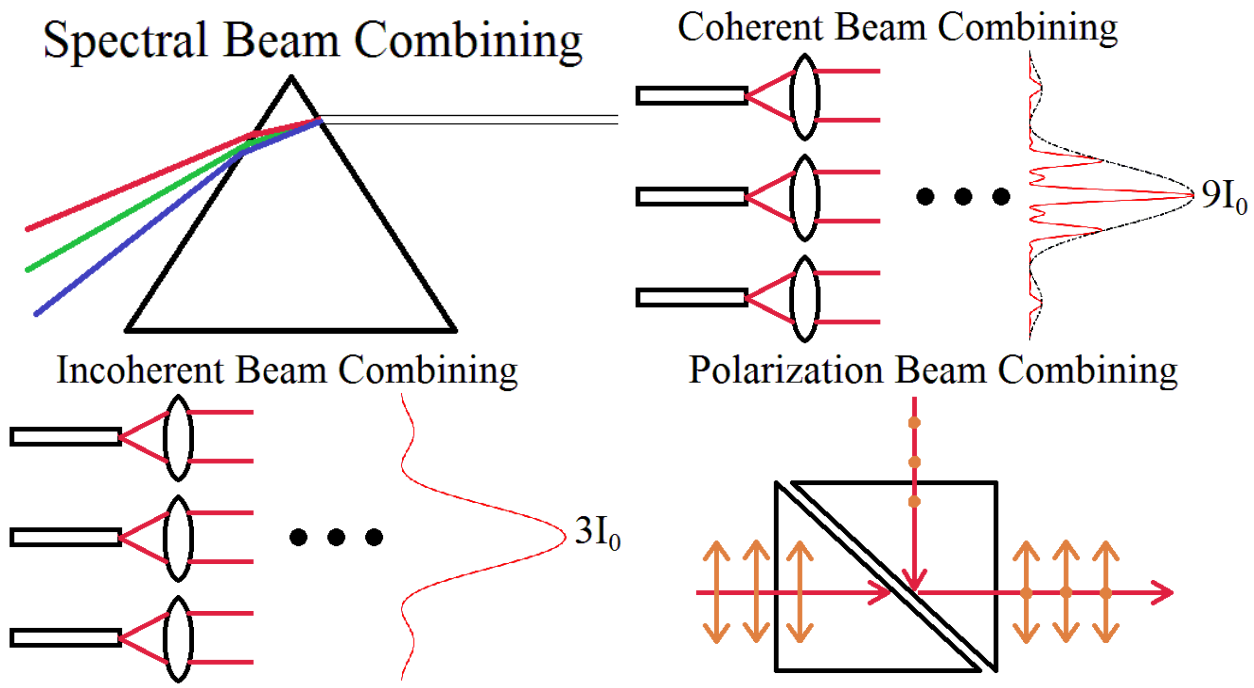

Figure 2.1: Simplified illustrations that depict the concept behind several types of beam combining methods. For CBC, perfect phase-locking leads the peak brightness to scale as N^2, where N is the array size.

Passive CBC is one approach that is of great research interest, especially in terms of identifying and assessing its prospects for robustness, scalability, and combining efficiency. A number of

coupling architectures have been proposed and further studied in the scientific community, but much of the current literature in theoretical/numerical analyses of these systems are based on either steady-state or dynamic but single-longitudinal-mode models. Although these approaches provide valuable insight into the practicality and underlying physics of the proposed fiber laser array coupling geometries, a dynamic multi-longitudinal-mode model can be used to obtain a more complete picture, since the evolution of the system and the stability of steady-state solutions are dictated by the dynamics. An understanding of the dynamics can lead to a more comprehensive demonstration of coherent phasing or lack thereof for the fiber laser array. This can be used to better compare different beam combining approaches, understand their limitations, seek methods to overcome them, and guide design considerations. In addition, it can assist the scientific community to better understand and reach a consensus regarding the role of fiber nonlinearities (e.g. Kerr effect, thermal effects, and the Kramers-Kronig relations) in the passive phasing process and their ability to help improve (or hinder) combining efficiency [3].

Hence, there is a motivation for the research work to model the phase locking dynamics and examine the role of fiber nonlinearity in the context of passive coherent beam combining of fiber laser arrays. The work covered in this chapter, particularly in SECTION 2.3, SECTION 2.4, and SECTION 2.5, has been published in [11].

2.2 Background and literature review

2.2.1 Various passive coherent beam combining architectures

Several types of coherent beam combining architectures have been studied in the literature theoretically and/or experimentally. Internally-coupled methods include fiber lasers coupled

pair-wise via 50:50 directional couplers in a “tree arrangement” [12, 13] and multicore fiber lasers in which the cores are internally, evanescently coupled [14]. Externally-coupled fiber laser arrays present another avenue of exploration; examples of common approaches discussed in the scientific literature are the utilization of a self-Fourier cavity [15, 16, 17], Talbot cavity [18, 19], diffractive optical element [20, 21], or a spatially-filtering ring geometry [10, 22, 23, 24, 25, 26]. Other externally-coupled geometries have been introduced by specific research groups. An experimental study of passive phasing of 25 lasers utilized a system that facilitated investigation of many different configurations of “connectivities” (between the individual array elements) by way of independently orienting four coupling mirrors [27].

Finally, several authors have examined the role of the resonant Kramers-Kronig (KK) nonlinearity in the phasing process. In [28, 29], an experimental test-bed, consisting of two fiber lasers coherently coupled by an external Dammann grating, was constructed in order to isolate the role of the KK nonlinearity in the passive phasing process and show that it can correct for applied phase errors. The mechanism was described as a redistribution of power between the two fibers that leads to gain changes and correspondingly KK-nonlinearity-induced phase shifts. In addition, recent papers by a different research group introduced a setup in a ring geometry with a phase-contrast filter to map phase-deviations in the array output to amplitude redistributions in the injected feedback, which in conjunction with the KK nonlinearity, provides an additional degree of freedom to assist passive phase locking [30, 31, 32]. In these papers, the authors reported initial experimental results of this new technique that look promising, although their mathematical modeling approach was limited to single-longitudinal-mode-based

simulations (repeated for each mode individually in order to observe for which one optimal output behavior was achieved).

2.2.2 Theoretical/numerical studies of passive coherent beam combining

Much of the relevant literature in modeling and theoretical/numerical studies of passive CBC, particularly for externally-coupled fiber laser arrays, has been limited to steady-state and perturbative analysis or dynamic but single-longitudinal-mode approaches. The initial models to focus on the dynamics utilized an iterative map approach, required a fixed phase difference as an input, and did not yield spectral information, as they were based on single-longitudinal-mode analysis [33, 34]. A more recent model addressed a Q-switching instability found from a linear stability analysis and presented only a few preliminary results from the numerical solution of the propagation equations [10, 22]. On the other hand, a dynamic, multi-longitudinal-mode model [35] for the fiber laser can facilitate further study of the passive phasing dynamics and emergence of the cavity modes self-selected by the array to suffer minimal roundtrip loss. For the case of fiber laser arrays coupled internally via directional couplers, such a model was developed and extensively utilized to investigate and explain the natural selection of longitudinal modes to achieve phase-locking, the prospects and challenges of array scalability, and the effect of the Kerr nonlinearity on combining efficiency [36, 37, 38].

For the externally-coupled geometries, there are some limitations in the scopes of several theoretical/numerical works that make claims regarding the role of fiber nonlinearities: 1) there is ambiguity in distinguishing the contributions from the Kerr nonlinearity vs. the KK nonlinearity, 2) the models do not account for the full dynamical evolution, and/or 3) the models

do not consider the interaction between different longitudinal modes [17, 30, 39, 40, 41, 42]. For this reason, the adaptation of the dynamic, multi-longitudinal-mode model for externally-coupled fiber laser arrays would assist in understanding the passive phasing dynamics and the influence of nonlinearities present in the fibers for a different class of beam combining architectures. Furthermore, it would aid in an understanding of the theoretical, physical, practical aspects that govern various passive beam combining systems, perhaps ideally in the endeavor to design new and improved methods. Note that for the present thesis work, the role of the Kerr nonlinearity is isolated; the future direction would be to incorporate the KK nonlinearity as well (the studies in [22, 39, 42] account for the KK nonlinear phase contribution, thus suggesting ideas for how to include the KK effect in the mathematical model used in this thesis).

2.3 Methods

2.3.1 Physical model

Figure 2.2 illustrates an array of fiber amplifiers arranged in a spatially-filtered, unidirectional, ring geometry architecture. The individual amplifiers are coupled externally by means of a lens that focuses the output into a single-transverse-mode fiber, which then feeds back the radiation to the individual amplifiers through a 1:N coupler. A beam splitter provides the output coupling as shown, thus allows for extraction a fraction of the circulating radiation. The entire system forms a composite cavity that functions as a laser, given sufficient (i.e. threshold) pump power of the individual fiber amplifiers. The output of the system is assumed to be measured and/or utilized in the far-field regime, and thus the output power spatial distribution is also tiled, according to the Fourier Transform of the near-field radiation (at the exit plane of the fiber amplifier array). This thesis work studies a 1-D fiber laser array, but it can also provide insight into the 2-D case.

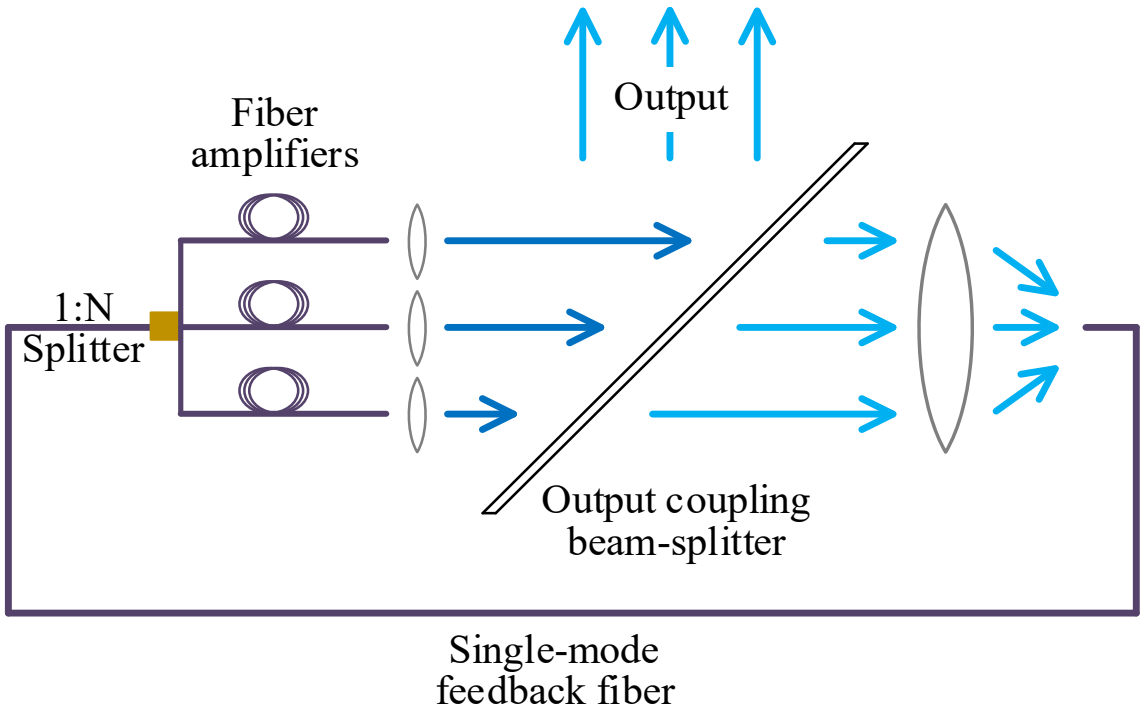

Figure 2.2: Diagram of a tiled-array of fiber amplifiers in a unidirectional ring composite cavity, passively coupled/combined via the spatially-filtered ring-geometry architecture. Unidirectional operation is assumed, in the case of this figure, to be in the clockwise direction.

Spatial filtering refers to the fact that only the on-axis intensity at the entrance of the feedback fiber (i.e. radiation focused into the angular acceptance range of the feedback fiber, dictated by its numerical aperture) is fed back. Due to the Fourier transform effect of the coupling lens, this on-axis intensity is maximized when the individual fibers are coherently phase-locked. The presence and axial mode spectrum of this phase-locked state of operation is strongly affected by the degree of variation / mismatch in fiber lengths and any additional path lengths in the coupling optics. As an aside, the transverse position of the feedback fiber, relative to the coupling lens, can spatially steer the central lobe of the output; this is referred to as "pointing agility" in [23].

There is an important issue that could limit the practicality and versatility of this coupling architecture, particularly as the array size increases. Care is required in dealing with optical path

length differences external to the fiber, i.e. within the coupling optics. This is because the system as presented is designed to self-select axial modes / frequencies that achieve good phasing in entrance plane of the feedback fiber, whereas the output (extracted beam quality) is determined by the phasing at the near-field plane at the exit of the fiber array. If external path length differences are present and the coupling lens does not correct for them, then the axial modes that are suitable for good (i.e. perfectly constructive) phasing at the feedback entrance plane may not be appropriate to achieve perfect constructive phasing at the array (near-field) exit plane; the potential consequence is poor beam quality in the (extracted) output far-field plane.

Nevertheless, the system serves as a useful model in which to study the passive phasing dynamics of externally coupled fiber laser arrays. Several researchers have investigated and/or demonstrated this specific beam combining geometry, both theoretically [10, 22] and experimentally [23, 24, 26]. In addition, researchers have studied other varieties of externally coupled architectures (see SECTION 2.2.1), and it is a worthwhile endeavor to understand, compare, and contrast the physical mechanisms at play across the different systems. SECTION 2.7 provides a brief comparison between the spatially-filtered ring geometry and the system with fibers coupled internally via 50:50 directional couplers.

This issue regarding optical path length differences and their effect in the context of the phasing dynamics is further discussed later, in SECTION 2.6. However, the rest of this chapter neglects the optical path length differences; it assumes that they are either absent or properly corrected for by the coupling optics.

2.3.2 Mathematical model

The system is mathematically described by use of a dynamic model that automatically accounts for multiple longitudinal modes by employing partial differential equations for the space-time evolution of the cavity fields [35, 36, 37]. Specifically, the model uses the Nonlinear Schrödinger Equation (NLSE) to describe the nonlinear wave propagation through each individual fiber amplifier (see [43]). The model also relies on rate equations governing gain dynamics and population inversion for each fiber. Appropriate choices of boundary conditions are required to model various coupling mechanisms. In the simulations, the system begins from noise and is allowed to evolve toward steady-state operation over the course of many roundtrips. From [36, 37], the model equations are given below. Table 2.1 provides descriptions of the variables and parameters in the equations.

$$\frac{\partial E_j}{\partial z} = \frac{1}{2}\left(g_j - \alpha\right)E_j - \beta_1 \frac{\partial E_j}{\partial t} + \frac{1}{2}(b - i\beta_2)\frac{\partial^2 E_j}{(\partial t)^2} + i\gamma\left|E_j\right|^2 E_j \tag{2.1}$$

$$\tau \frac{\partial g_j}{\partial t} = g_{0j} - g_j - \frac{\left|E_j\right|^2}{P_{SAT}} g_j \tag{2.2}$$

Table 2.1: List of variables and parameters used in the model (NLSE and rate equations) of passively coupled fiber lasers; see Equations (2.1) and (2.2).

Variable / Parameter	Description
z	Longitudinal position along each fiber ($z = 0$ is the position adjacent to the 1:N splitter)
t	Time ($t = 0$ is the moment of "turn-on" of the system)
Subscripts j	Used to indicate the jth element of the array
$E_j(z,t)$	Slowly-varying electric field envelope in each fiber (normalized such that $\|E\|^2$ yields optical power)
$g(z,t)$	Gain in each fiber
α	Fiber propagation loss

β_1	Reciprocal of group velocity
b	Accounts for frequency-dependent losses and limitations of the bandwidth of the spectrum of longitudinal modes that evolve from the system
β_2	Group velocity dispersion (GVD)
γ	Coefficient of the non-resonant Kerr nonlinearity ($\gamma = 2\pi n_2/\lambda A_{eff}$, where n_2 is the nonlinear refractive index and A_{eff} the effective mode area of the fiber [43])
τ	Population relaxation time
g_0	Small-signal (unsaturated) gain
P_{SAT}	Saturation power

2.3.3 Simplifying assumptions

In order to facilitate numerical simulations, the model makes a few simplifying assumptions. First, it only considers single polarization, single-transverse-mode, forward-propagating waves in the fibers [36]. Second, as earlier mentioned, optical path length differences and other aberrations in the coupling optics (including the 1:N splitter) are neglected; hence, the only source of path length differences and non-idealities in imaging arise from possible mismatches between the fiber amplifiers' lengths (which are assumed here to not vary in time, e.g. due to thermal effects). Furthermore, the delay time and phase accumulation due to propagation through the external coupling and feedback sections are ignored, as it is expected that these aspects are not significantly relevant to the intrinsic passive phasing process within the fiber array that is of interest in this study. Next, the term b for frequency-dependent losses in Equation (2.1) imposes a band-pass filter on the spectrum of the modes that evolve from the system. Practical systems generally incorporate some bandwidth limiting elements in the cavity. Higher order dispersion and other nonlinear effects (e.g. the resonant nonlinearity associated

with the Kramers-Kronig phase shift) are neglected, although it should be feasible to extend this model accordingly.

Finally, with regard to the spatial distribution of the fiber output ports, these tiled apertures are assumed to have a high fill factor (e.g. for these simulations a 5:1 ratio of fiber output width to spacing between adjacent fiber outputs) and the near-field a "top-hat" transverse profile (instead of the typical Gaussian profile used to approximated the fundamental spatial mode). These assumptions are made for computational convenience in the simulations; indeed, in practice one could achieve a high fill factor effectively by inserting a microlens array, similar to that shown in Figure 2.2, at the near-field plane of the fiber outputs [44].

2.3.4 Numerical methods

Numerical solution of the equations presented in SECTION 2.3.2 facilitates simulation of the spatiotemporal evolution of the system, starting from low-amplitude noise and dynamically evolving toward steady-state operation. Each cavity roundtrip is simulated via a beam propagation method that utilizes the Symmetric Split-Step Fourier Method for the NLSE in Equation (2.1) and the Euler method for the gain dynamics in Equation (2.2), as detailed in [43] and [37], respectively. Here, waves are propagated through each fiber by accounting for the linear portion of the NLSE in frequency domain and the nonlinear portion in time domain. At the beginning of the first cavity roundtrip, the field $E_j(0, t)$ for each fiber is initialized as low-amplitude noise (numerically, an array of random complex numbers) defined within a computational time window T, while g_j is initialized as zero. Numerical boundary conditions (detailed below) account for the coupling / feedback mechanism, once the wave in each

individual element reaches the end of the fiber length, in order to set up the simulation of the subsequent cavity roundtrip. The process of propagation, coupling, and feedback is repeated over numerous roundtrips to yield the dynamic evolution of the system to steady-state.

In the spatially-filtered ring-geometry, as shown in Figure 2.2, the individual amplifiers are coupled externally by means of a lens that focuses the output into a single-mode fiber, which then feeds back the radiation through a 1:N coupler. This process is implemented in the boundary condition for the mathematical model in a manner similar to the description in [23]. Numerically, external coupling is accomplished as follows. The near-field output of the fiber array is taken as a spatial distribution of rectangular slits corresponding to each individual fiber output, and so at each spatial point is a time-varying field amplitude in the near-field. The Fourier Transform along the near-field spatial dimension is used to compute the far-field pattern, which is equivalent to the effect of the coupling lens. The spatial filtering imposed by the single-mode feedback fiber is accomplished numerically by extracting the *on-axis* time-varying field from the "far-field array", which is then fed back to the 1:N splitter to begin the simulation of the subsequent roundtrip.

2.3.5 Parameter values for the numerical simulations

For this numerical simulation and investigation of the ring-geometry coupling mechanism, the fibers considered here are Ytterbium-doped. Table 2.2 summarizes the important parameter values used for all simulations. The following elaborates on a few of these parameter values. The coefficient of the Kerr nonlinearity is nominally $\gamma = 0.003\ \mathrm{W^{-1}m^{-1}}$ (corresponding to the nonlinear index $n_2 = 3.2 \times 10^{-20}\ \mathrm{m^2/W}$) [22, 38]. In pursuit of studying the effect of

nonlinearity on the system, the value is varied over a large range in the numerical simulations. In experiment, the Kerr nonlinearity itself is generally a fixed material parameter, and the Kerr phase shift, which is proportional to $\gamma|E_j|^2$ as seen in Equation (2.1), increases as the system operates at higher powers. In an alternative approach, as used in this thesis work, the role of the Kerr phase effect and its influence on the underlying physics of the passive phasing processes can be explored in the simulations by varying the nonlinear coefficient itself, in order to draw qualitative comparisons and intuition. The chosen computational time window spans roughly two roundtrips for each individual fiber. Given the limitations of the numerical data array sizes, this choice allows for sufficient temporal and spectral resolution as well as adequate spectral bandwidth.

In addition, the population relaxation time is several orders of magnitude greater than the roundtrip time. Lastly, the chosen value for the loss dispersion b results in a Gaussian-shaped band-pass filter around the center frequency (i.e. the point of zero detuning from the optical carrier frequency) with FWHM $\sim$230 GHz. This bandwidth is indeed small compared to the gain bandwidth, but it is chosen for computational convenience so as to ensure that the spectral power is contained well within the boundaries of the computational frequency window (in order to avoid the numerical issues associated with the periodicity inherent in the usage of the discrete/fast Fourier Transform). Nevertheless, the underlying physics and the qualitative trends from this thesis work are expected to hold. Simulations with increased filter bandwidth and an increased computational frequency window verify that this expectation is well-founded.

Table 2.2: Simulation parameters for a ytterbium-doped fiber laser array coupled in the ring geometry.

Parameter	Symbol	Value(s)	Reference
Refractive index of the fibers	n	1.5	[36]
Optical carrier / center wavelength	λ	1080 nm	[22]
Output coupler reflectivity	r_{OC}	0.1	Chosen
Fiber lengths (with random variations)	ℓ	A three fiber array with lengths [10 m, 9.9 m, 10.013 m] (unless otherwise noted)	[22]
Computational time window	T	110 ns	Calculated
Computational frequency window	B	298 GHz	Calculated
Unsaturated gain	g_0	$0.2\ \mathrm{m}^{-1}$ or $2.67\ \mathrm{m}^{-1}$ (unless otherwise noted)	[38]
Fiber propagation loss	α	$1.84 \times 10^{-3}\ \mathrm{m}^{-1}$	[38]
Frequency-dependent loss parameter	b	$0.13 \times 10^{-24}\ \mathrm{s}^2/\mathrm{m}$	[36]
Group velocity dispersion	β_2	$0.024 \times 10^{-24}\ \mathrm{s}^2/\mathrm{m}$	[38]
Non-resonant Kerr nonlinearity coefficient	γ (n_2)	varied	Chosen
Saturation power	P_{SAT}	30 mW	Calculated
Population relaxation time	τ	1 ms	[36]

2.4 Passive phasing dynamics

The solution of the full set of dynamic equations makes it possible to observe the evolution of the total power, the gain dynamics, and the onset of phase-locking in real time. This is done via simulations of the dynamical evolution of the coupled system toward steady-state (ideally, phase-locked) from an incoherent phase state. Here, the incoherent state represents either the initial state of the system at "turn-on" or the state of a system in the immediate aftermath of perturbations. Assessment of the degree of phase-locking considers the dynamics of the

temporal and spectral phase profiles, the far-field intensity pattern, and a coherence/order parameter. The results agree with published state-state and experimental analyses.

2.4.1 Dynamical evolution from turn-on

The results clearly show that phase locking occurs before the first peak of relaxation oscillations and that once that occurs, the amplifiers act as one in concert. The simulations also show the self-selection of common axial modes as the system evolves from noise to the phase locked state. Figure 2.3 presents two sets of dynamic evolution results, one for uncoupled lasers and the other for lasers coupled by means of the single mode fiber. Highly damped relaxation oscillations are seen in the near-field output power and the gain after the system is turned on. Note that all of the fibers have equal near-field output power, due to the fact that the 1:N splitter equally distributes the radiation to all of the fibers every roundtrip (the phase of the radiation, however, can vary across fibers in the array, depending on the degree of phase-locking achieved).

More interestingly, in the bottom row (Figure 2.3c, f) the phase differences between uncoupled lasers evolve randomly over the entire range of $\pm 2\pi$, whilst the phase differences for coupled lasers undergo a sharp transition to a state of reduced fluctuations at about the time the gain parameter crosses the threshold value. This transition occurs before the first relaxation oscillation peak is attained. The phase differences do not quite settle down to zero due to the presence of the Kerr nonlinearity, which results in self-phase modulation. Note that the phase differences are calculated as follows: the blue trace is the phase of the complex field amplitude (evaluated at the near-field, exit plane of the array) for the 9.9 m fiber relative to that of the 10 m fiber, the green trace is the phase for the 10.013 m fiber relative to that of the 10 m fiber, and

the red trace is that of the 10 m fiber (relative to itself, which is why in the phase difference subplots the red trace is always equal to zero).

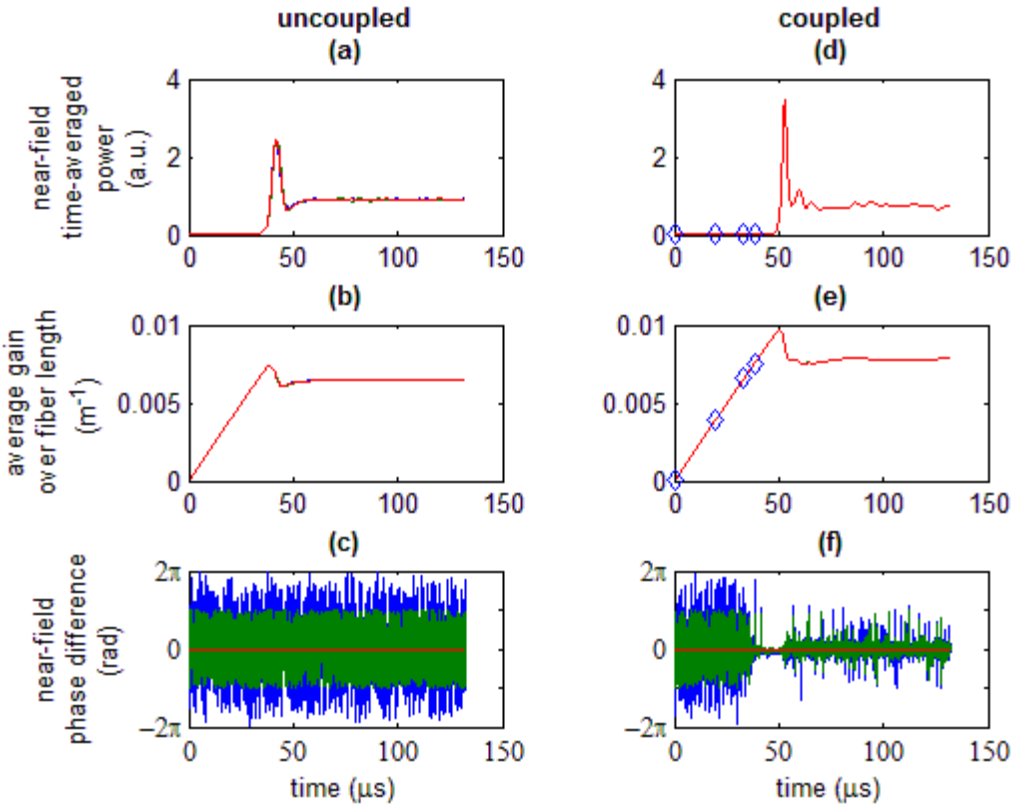

Figure 2.3: Temporal evolution of near-field power, gain, and near-field phase difference for 3 fibers. Subplots (a-c) show the results for uncoupled fibers, whereas subplots (d-f) are for fibers coupled in the ring-geometry architecture. The blue, diamond-shaped markers in (d, e) correspond to the time-stamps of the snapshots of the far-field in Figure 2.4. Phase differences in (c, f) are calculated relative to the phase of the 10 m fiber. The nonlinearity is $\gamma = 0.003$ W^{-1}m^{-1}, the unsaturated gain is $g_0 = 0.2$ m^{-1}, and the other parameter values are given in Table 2.2.

The transition to a more coherent state can also be seen in the far field evolution. Figure 2.4 shows snapshots of the far field profile taken at the instants marked on the power evolution curve in Figure 2.3d. For simplicity, a top-hat profile is assigned to the near-field distribution of each amplifier. The far field is initially the broad sinc^2 profile associated with randomly phased, incoherent sources. It rapidly and smoothly narrows as the gain approaches threshold and attains the final locked profile before the first relaxation oscillation peak occurs. This confirms the fact,

also seen in the directionally coupled beam combining geometry [37], that phase locking occurs prior to the onset of relaxation oscillations and that the array acts as one laser by the time threshold is reached.

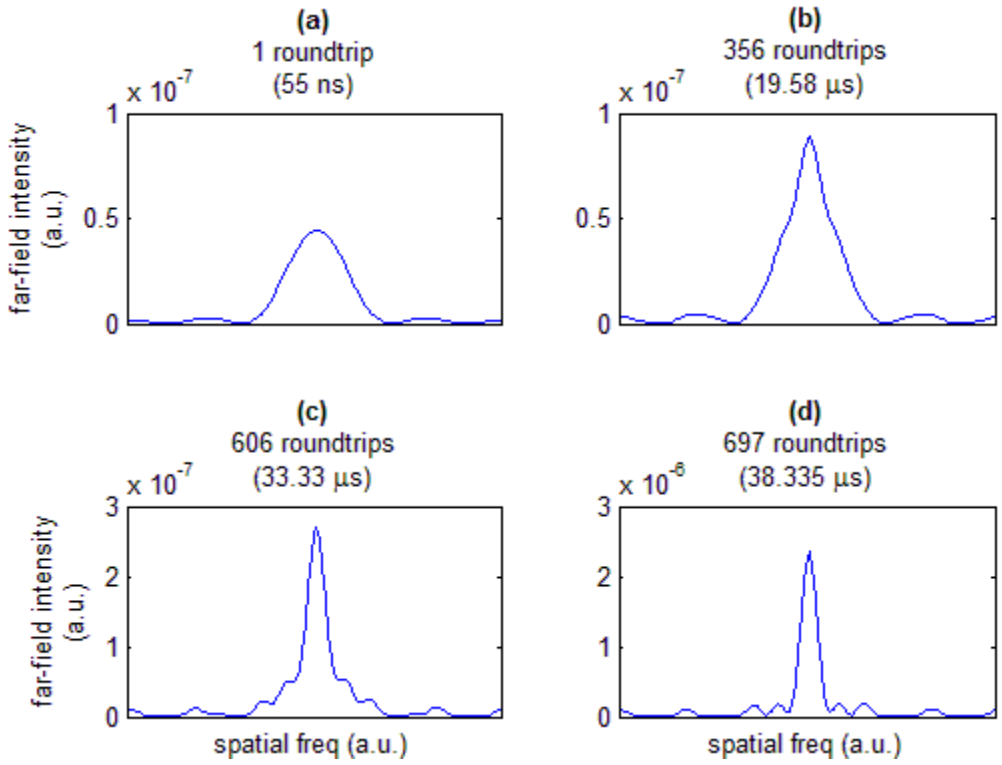

Figure 2.4: Temporal evolution of the far-field output intensity pattern for 3 coupled fibers. Subplots (a-d) represent "snapshots" of the far-field taken at the instants marked in Figure 2.3d, e. The nonlinearity is $\gamma = 0.003$ $W^{-1}m^{-1}$, the unsaturated gain is $g_0 = 0.2$ m^{-1}, and the other parameter values are given in Table 2.2. Note: the vertical scales / axes are not the same for all plots.

The simulation results shown in Figure 2.3 and Figure 2.4 are for a low value of the small-signal gain: $g_0 = 0.2\ \mathrm{m}^{-1}$. For higher values of gain, phase locking and the transition to steady state operation occur much faster. Figure 2.5 shows the near-field power, gain, and relative phase dynamics for $g_0 = 2.67\ \mathrm{m}^{-1}$, considering two values for the nonlinearity coefficient: (i) $\gamma = 0$, and (ii) $\gamma = 0.003\ \mathrm{W}^{-1}\mathrm{m}^{-1}$.

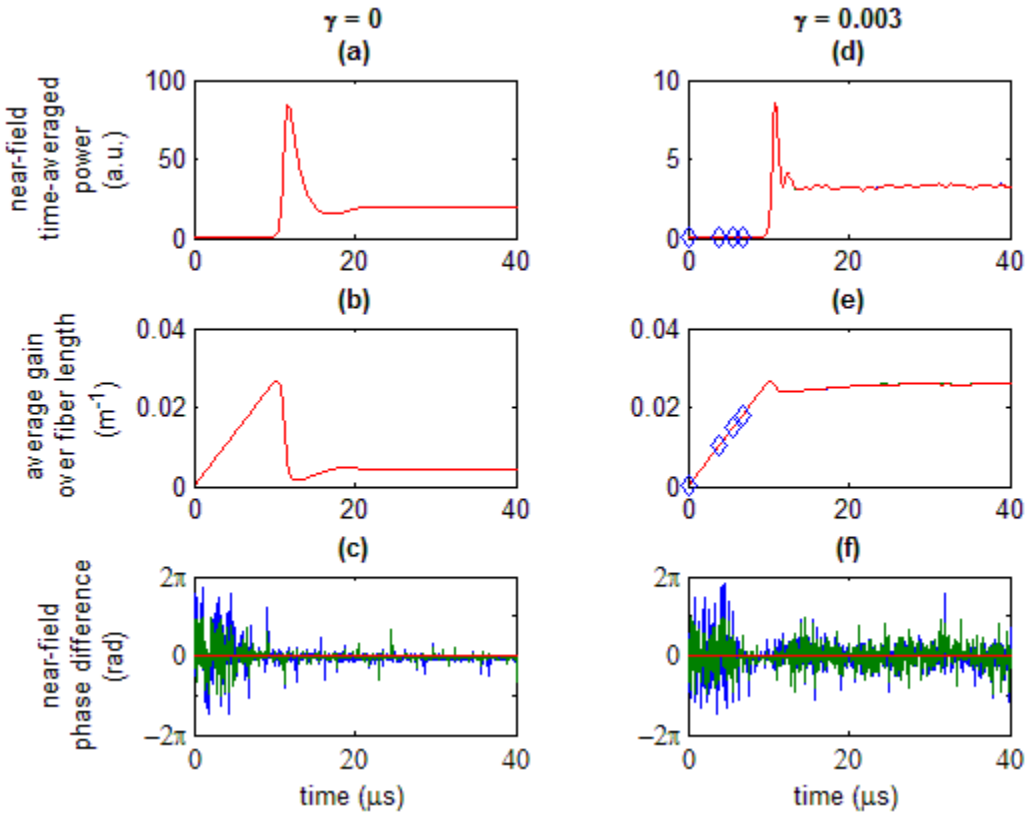

Figure 2.5: Temporal evolution of near-field power, gain, and near-field phase difference for 3 coupled fibers. Subplots (a-c) are for zero nonlinearity, and subplots (d-f) are for $\gamma = 0.003$ $W^{-1}m^{-1}$. The blue, diamond-shaped markers in (d, e) correspond to the time-stamps of the snapshots of the far-field in Figure 2.6. Phase differences in (c, f) are calculated relative to the phase of the 10 m fiber. The unsaturated gain is $g_0 = 2.67$ m^{-1}, and the other parameter values are given in Table 2.2.

The phase plots in Figure 2.5 show that phase locking occurs within 7 μs of turn-on, compared to 40 μs for the low-gain case (Figure 2.3f). It is also clear that the Kerr nonlinearity is responsible for the phase and intensity fluctuations that occur after threshold is reached and that there is enough intensity in the fibers to cause self-phase modulation (see SECTION 2.5 for more details). The more rapid transition to phase locking at higher gain is also confirmed in the sequence of far-field plots shown in Figure 2.6.

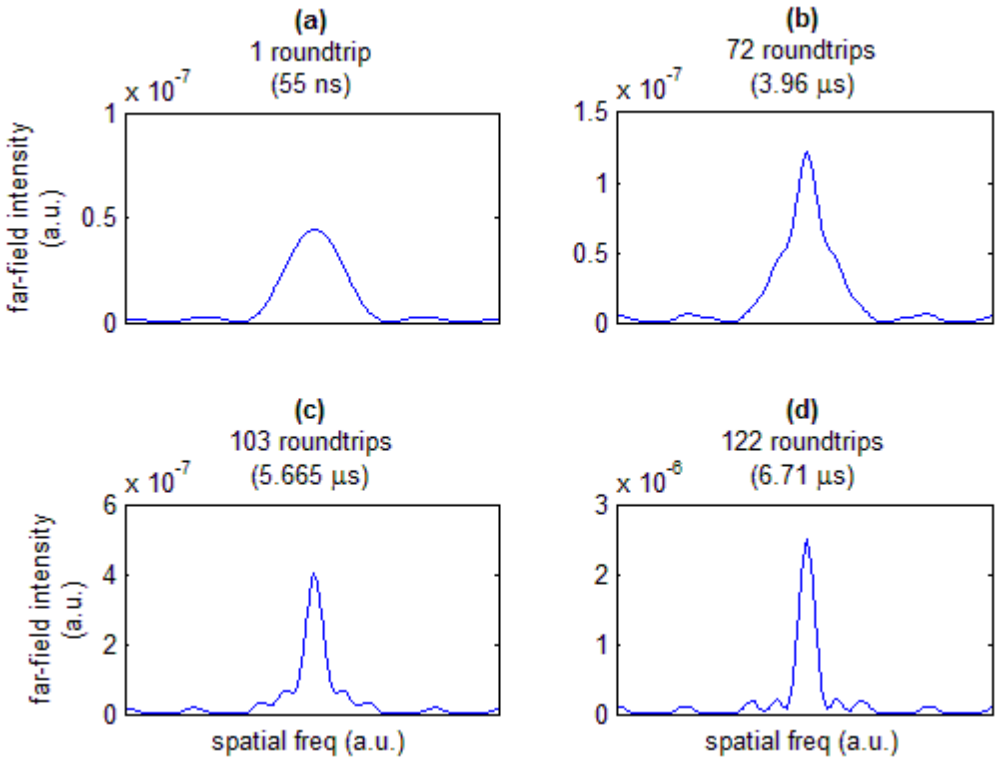

Figure 2.6: Temporal evolution of the far-field output intensity pattern for 3 coupled fibers. Subplots (a-d) represent "snapshots" of the far-field taken at the instants marked in Figure 2.5d, e. The nonlinearity is $\gamma = 0.003$ W^{-1}m^{-1}, the unsaturated gain is $g_0 = 2.67$ m^{-1}, and the other parameter values are given in Table 2.2. Note: the vertical scales are not the same for all plots.

The process that leads the system from an unlocked initial state to the final phase-locked (or at least partially phase-locked) state can be observed by examining the phase differences between array elements as a function of frequency. Figure 2.7 shows the phase differences between the first and second lasers (blue lines) and between the first and third lasers (green lines) in the array, plotted versus frequency for $g_0 = 2.67\ \mathrm{m}^{-1}$. Two snapshots are shown – one at turn-on and the other at the first peak of relaxation oscillations. The system begins from noise (Figure 2.7a), and the self-selected array modes emerge by the time the relaxation oscillations begin (Figure 2.7b).

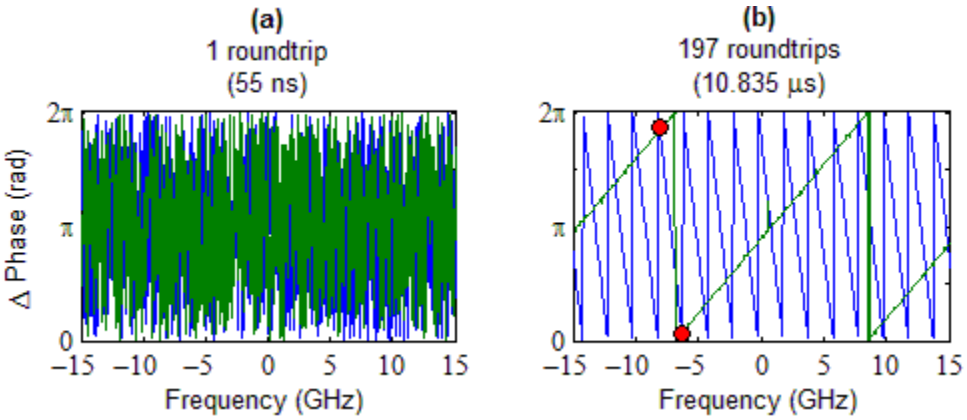

Figure 2.7: Snapshots of the phase difference vs. frequency detuning (from the optical carrier) profile for 3 coupled fibers. The plot in (a) is taken at the beginning of the simulation (i.e. at "turn-on"), while the plot in (b) is taken at the time at which the first peak in power occurs (as seen in Figure 2.5d). The phases of the 9.9 m fiber (blue trace) and the 10.013 m fiber (green trace) are computed relative to the phase of the 10 m fiber. The nonlinearity is $\gamma = 0.003\ W^{-1}m^{-1}$, the unsaturated gain is $g_0 = 2.67\ m^{-1}$, and the other parameter values are given in Table 2.2. The red dots in (b) are positioned at the same two frequencies as marked in Figure 2.8c.

Ideally, these selected modes are common resonant modes for all fiber elements, in which case the corresponding field amplitudes are locked in-phase across the array. If no such perfectly "coincident" modes exist within the bandwidth of available modes, then the system proceeds to select the modes that suffer the least loss per round trip, in a manner similar to that shown in [37]. Due to the non-zero width of the spectral peaks in the frequency combs, partial overlap of non-coincident modes is possible. Here, "least-loss" refers to the situation where the array operates with a high degree of coherent locking (i.e. a fixed-phase relationship over time) and a state close to in-phase locking (i.e. phase differences between fiber outputs are near 0 modulo 2π). The two red dots in Figure 2.7b indicate the frequencies at which both the blue and green traces intersect near 0 or 2π; they correspond to two of the array modes, as confirmed by comparison to the location of the markers in Figure 2.8c.

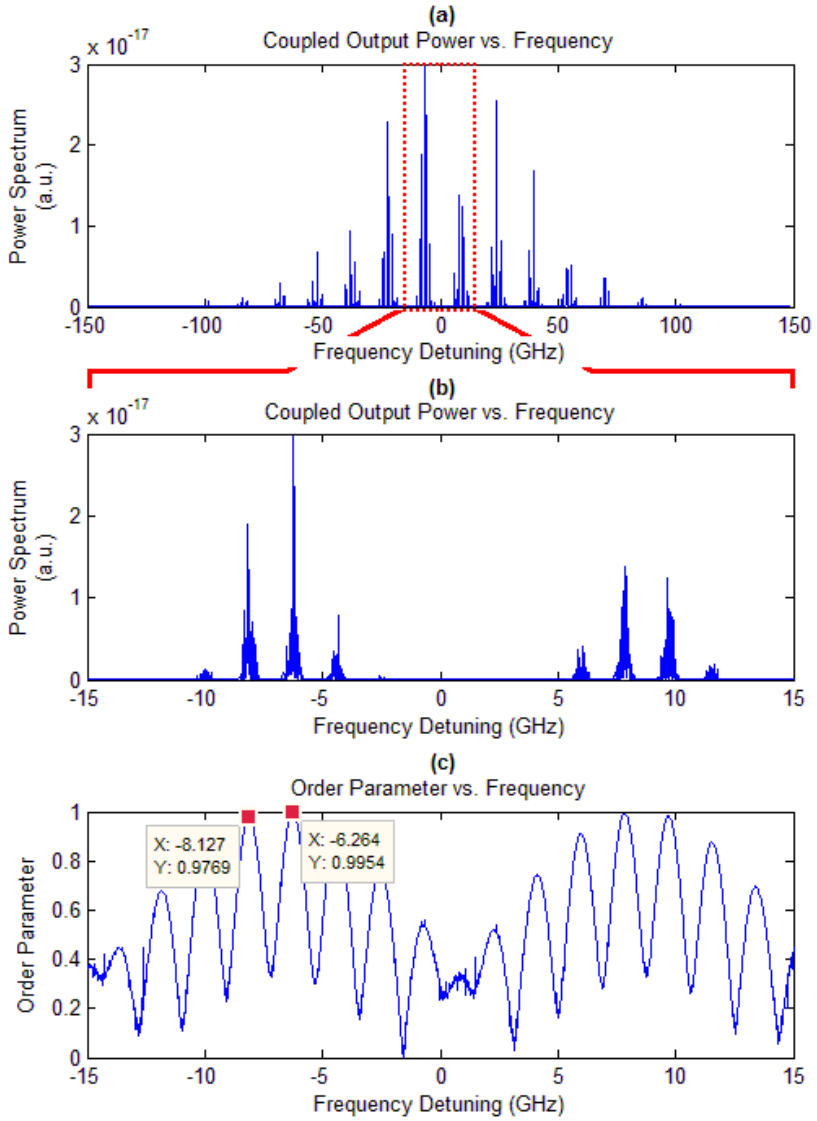

Figure 2.8: Plots of the steady-state (near-field) power (a, b) and order parameter (c) vs. frequency detuning (from the optical carrier) for 3 coupled fibers. The nonlinearity is $\gamma = 0.003$ $W^{-1}m^{-1}$, the unsaturated gain is $g_0 = 2.67$ m^{-1}, and the other parameter values are given in Table 2.2. The data is taken after 2200 cavity roundtrips.

Figure 2.8 illustrates the dependence of the output power and the "order parameter" (or coherence parameter) on the detuning from the operating wavelength of 1080 nm, as generated by the simulation results. The definition is adopted from [22]: the order parameter is equal to $|\sum_{n=1}^{N} E_n| / \sum_{n=1}^{N} |E_n|$, where E_n is the near-field amplitude at the output of the nth fiber in the array of N fibers. The order parameter aims to characterize the degree of phasing in the array; if

all fibers are coherently in phase at a specific frequency, then $|\sum_{n=1}^{N} E_n| = \sum_{n=1}^{N} |E_n|$, and thus the order parameter equals unity. Accordingly, the order parameter's spectral "lobes" (Figure 2.8c) align with the axial modes self-selected by the system (Figure 2.8b).

The results in Figure 2.8c agree with the previously published steady-state results (specifically, Fig. 2a in [22]), with regard to the order parameter structure and the spacing between the lobes. From Figure 2.8c, note that the frequency spacing between the centers of two adjacent lobes is $\Delta f \approx 1.86$ GHz, which is equivalent to a wavelength spacing of $\Delta\lambda = (\lambda^2/c) \cdot \Delta f \approx 7.2$ pm, in agreement with [22]. Again, recall that these simulations assume that there are no external path delays due to the coupling optics. Inclusion of such delays does not affect the array dynamics, but it does result in a small shift of the order parameter spectrum from the power spectrum [4]. SECTION 2.6 elaborates on the external path delays.

2.4.2 Recovery after perturbation

With the array operating in the steady state, phase-locked condition, it is of interest to see how quickly phase-locking is restored after a perturbation. This would provide insight into the robustness of the phasing processes (especially since SECTION 2.4.1 already demonstrates that the phasing dynamics occur faster than the relaxation oscillations). This perturbation event is simulated by starting from steady state and applying a phase varying from -3.5π to 5π radians to each laser and then observing the phase spectrum and far-field profiles after the perturbation. The results are shown in Figure 2.9 and Figure 2.10. When the lasers operate above threshold, the simulations show that the in-phase locked state is recovered within two round trips of the

perturbation, in agreement with experimental results of [25], as well as theoretical results for directionally-coupled arrays [37].

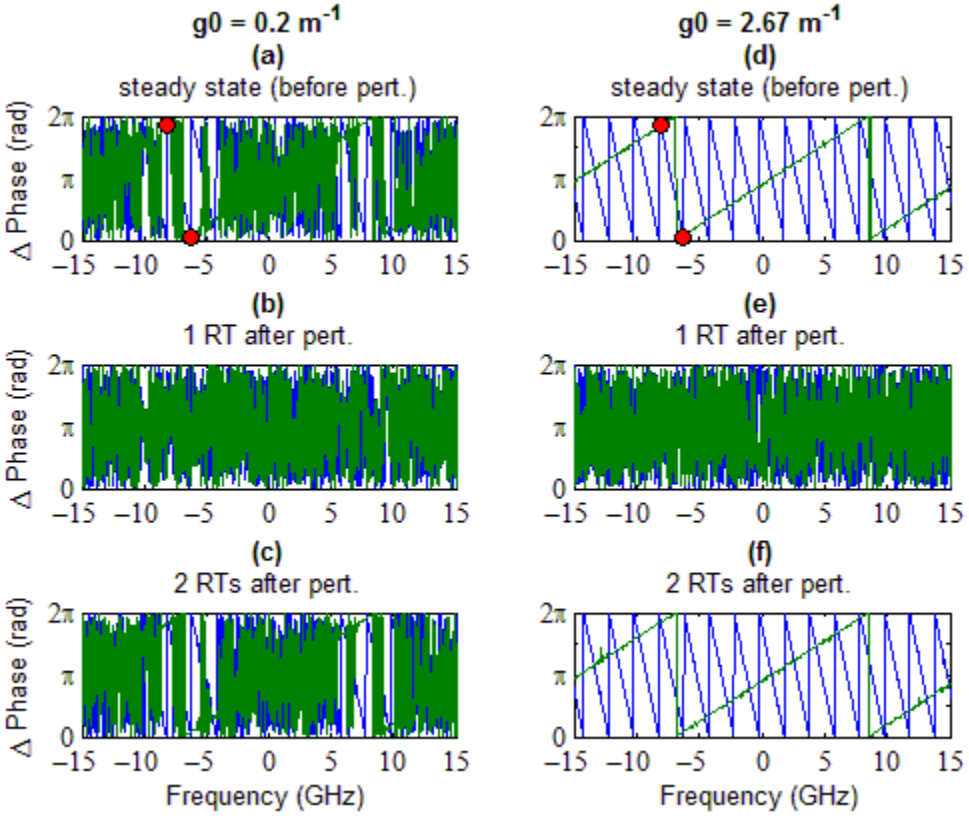

Figure 2.9: Temporal evolution of the phase difference vs. frequency detuning profile after application of a phase perturbation for 3 coupled fibers. Two sets of data are provided; each set uses a different value for the unsaturated gain, all above threshold: (a-c) $g_0 = 0.2$ m^{-1}, and (d-f) $g_0 = 2.67$ m^{-1}. The phases of the 9.9 m fiber (blue trace) and the 10.013 m fiber (green trace) are computed relative to that of the 10 m fiber. The nonlinearity coefficient is $\gamma = 0.003$ W^{-1}m^{-1}, and the other parameter values are given in Table 2.2. The red dots in (a, d) are positioned at the same two frequencies as marked in Figure 2.8c.

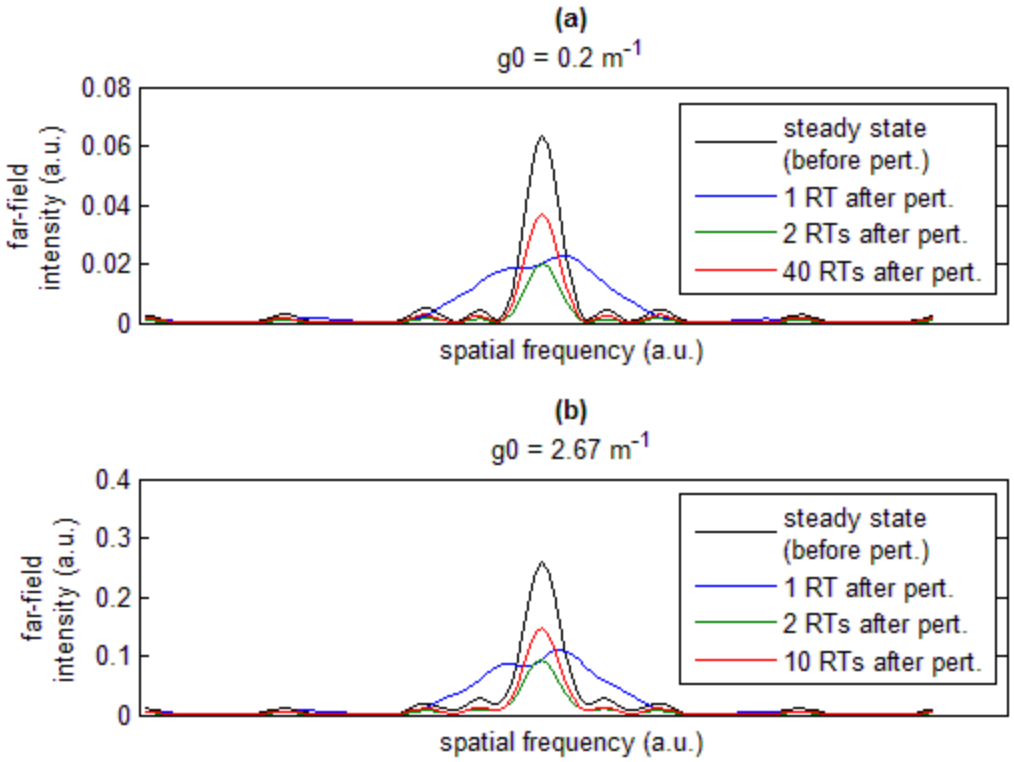

Figure 2.10: Temporal evolution of the far-field output intensity pattern after application of a phase perturbation for 3 coupled fibers. Each subplot uses a different value for the unsaturated gain, all above threshold: (a) $g_0 = 0.2$ m^{-1}, and (b) $g_0 = 2.67$ m^{-1}. The nonlinearity is $\gamma = 0.003$ W^{-1}m^{-1}, and the other parameter values are given in Table 2.2. Note that the vertical scales / axes of (a) and (b) are different, since the plots are for different pump powers.

Of course, although the phase-locked state is recovered very rapidly, the temporal power takes longer. A series of relaxation oscillations recommence as the temporal power recovers from the perturbation over numerous roundtrips to the steady-state level, as shown in Figure 2.10 (compare the black vs. red traces), Figure 2.11 and Figure 2.12. Again, there is an evident difference in time scales for the phase-locking mechanism vs. the power and population dynamics, and the results illustrate how steady-state operation is more quickly reached for higher small-signal gain / pump power.

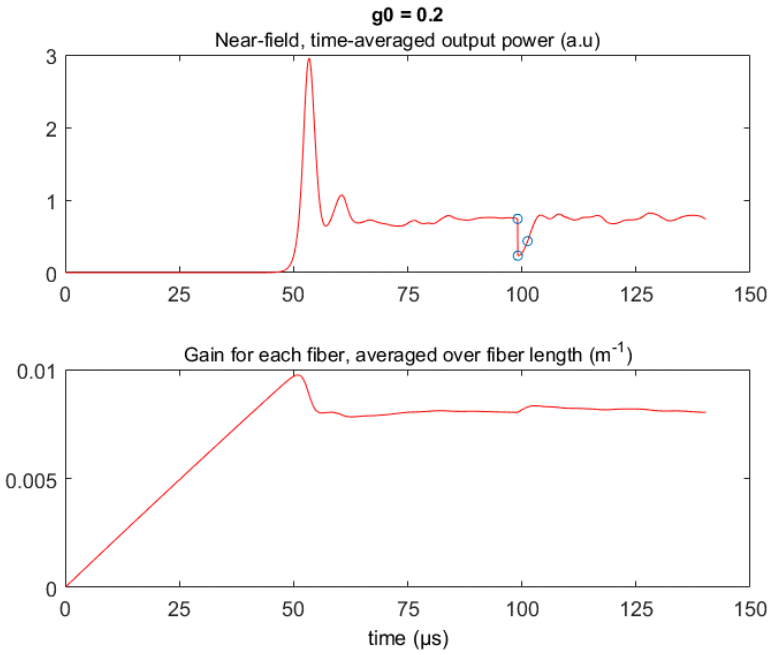

Figure 2.11: Temporal evolution of near-field power and gain for 3 coupled fibers. The perturbation occurs just before t = 100 μs. The blue, circular markers, in chronological order, indicate the following moments: steady-state before the perturbation, 1 roundtrip after the perturbation, and 40 roundtrips after the perturbation. These correspond to the black, blue, and red traces of Figure 2.10a.

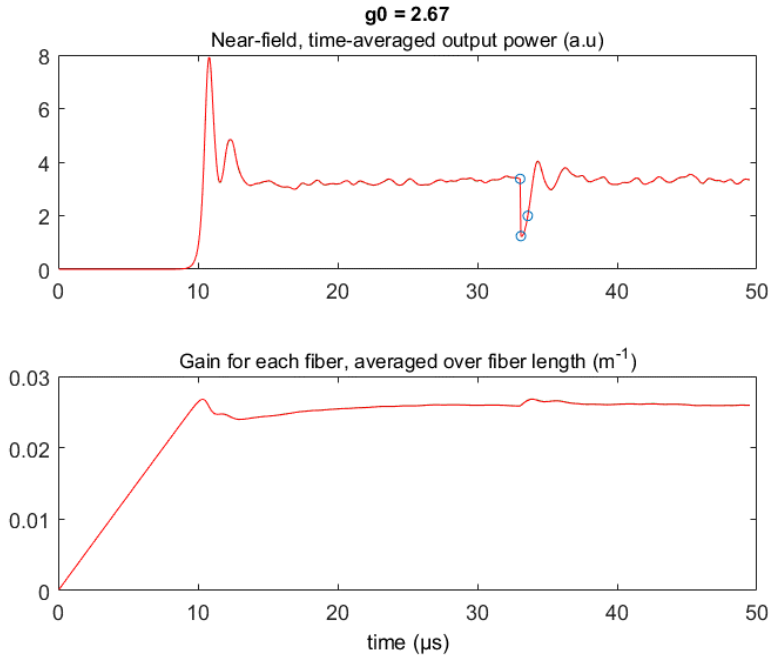

Figure 2.12: Temporal evolution of near-field power and gain for 3 coupled fibers. The perturbation occurs just around t = 33 μs. The blue, circular markers, in chronological order, indicate the following moments: steady-state before the perturbation, 1 roundtrip after the perturbation, and 10 roundtrips after the perturbation. These correspond to the black, blue, and red traces of Figure 2.10b.

2.5 Effect of the non-resonant Kerr nonlinearity

As mentioned in SECTION 2.3.5, the coefficient γ in the NLSE (non-resonant Kerr nonlinearity) can be varied in order to see the effect that nonlinearity has on the passive phasing mechanism in the ring-geometry approach. This effect can be viewed from the perspective of the output power and relative phase spectra, the far-field output intensity profiles, and a combining efficiency metric. Again, the following work looks at solely at the non-resonant Kerr nonlinearity, separately from other phase/index nonlinearities (e.g. due to the Kramers-Kronig relations).

2.5.1 Excitation of more modes via Kerr-induced spectral broadening

First, the nonlinear coefficient γ is set to zero, and simulations facilitate examination of the spectrum and relative phases in steady state. In the absence of nonlinearity, for the chosen fiber lengths used in Figure 2.13, the array operates at only one mode/frequency (Figure 2.13a, c); the corresponding phase profile is shown in Figure 2.13b, d. The existence of only one array mode is predicted by the Vernier effect, which requires that the common array mode spacing of the multiple cavities of different length be the least common multiple of the individual cavity resonances. As shown in [36], the spacing between these common frequencies is related to the greatest common divisor (gcd) of the length differences: $\Delta f = (c/n)/\gcd(\{\Delta L\})$. For the array used in Figure 2.13 (with lengths of 10 m, 9.9 m, and 10.013 m), the length differences are 0.1 m and 0.113 m (relative to the 9.9 m fiber). The gcd of length differences is 0.001 m, which leads to a mode spacing of 200 GHz via the Vernier Effect formula. However, only one mode is observed, near the center of the frequency window (in the absence of nonlinearity); the common array mode spacing is too large for any more than one mode to sit well within the 230 GHz filter bandwidth (set by the loss dispersion) without suffering excessive loss.

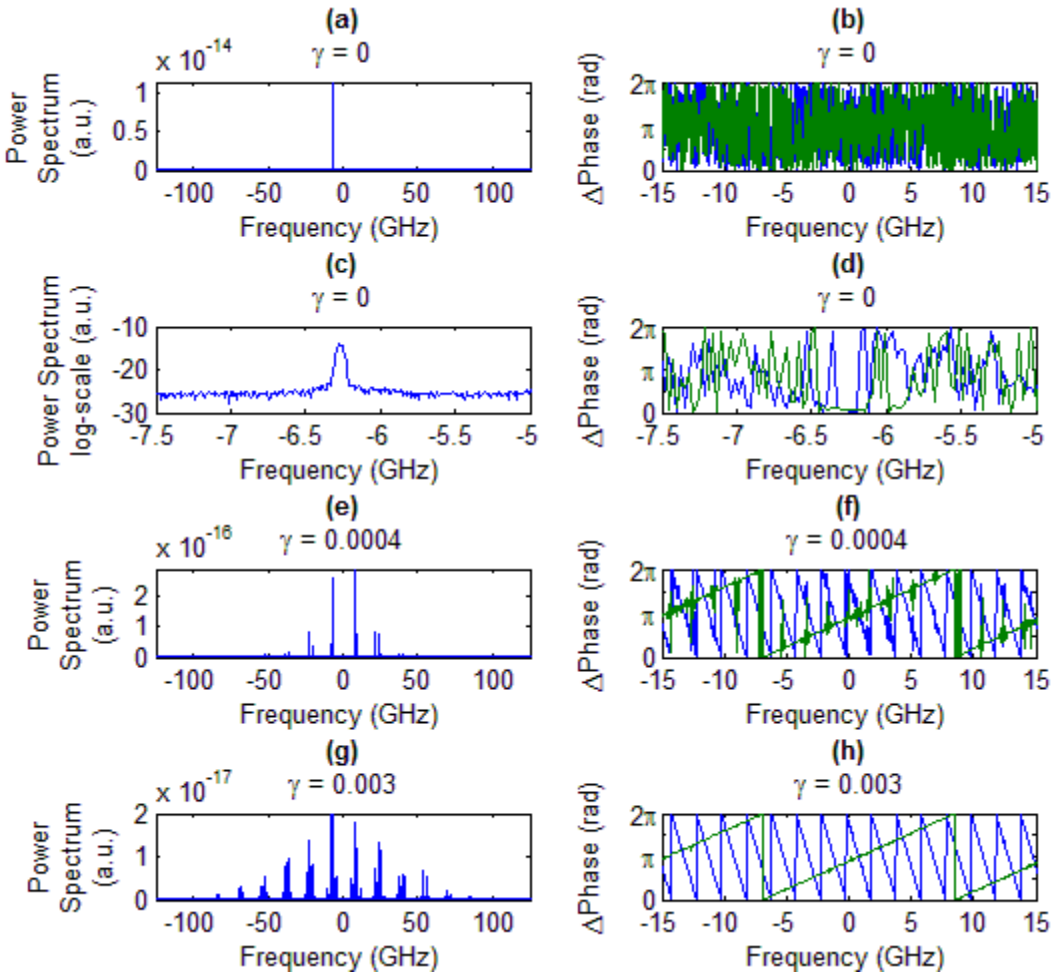

Figure 2.13: Plots of the steady-state (near-field) power spectrum (a, c, e, g) and phase difference (b, d, f, h) vs. frequency detuning as nonlinearity γ is varied for 3 coupled fibers. The values of γ listed in the subplot labels are in units of $W^{-1}m^{-1}$. The plots in (c, d) are zoomed-in versions of the plots in (a, b), respectively. The phases of the 9.9 m fiber (blue trace) and the 10.013 m fiber (green trace) are computed relative to that of the 10 m fiber. The unsaturated gain is $g_0 = 2.67\ m^{-1}$, and the other parameter values are given in Table 2.2. All plots are taken after 2200 roundtrips.

Introduction of a small amount of nonlinearity ($\gamma = 0.0004\ W^{-1}m^{-1}$) results in the excitation of several more axial modes. These modes are a result of the Kerr-induced spectral broadening and four-wave mixing that make it possible to achieve approximate mode coincidences. The relative phase between the array elements, however, is not zero modulo 2π at these frequencies. Increasing the nonlinear coefficient further leads to even greater spectral broadening and the excitation of more array modes, as shown in Figure 2.13.

2.5.2 Degradation of in-phase coherent locking and combining efficiency

Next, the system is evaluated in terms of a practical metric for quantifying beam combining efficiency η, as per Equation (2.3) for an N-element array, in a manner similar to the approaches used in [44] and for the Strehl Ratio. For a perfectly phased-locked array, the on-axis peak in the far-field output intensity pattern scales with array size as N^2, and the interference fringe pattern "underneath" the single fiber output aperture diffraction lobes is of unity visibility. On the other hand, in the complete absence of coherence across the fiber laser array, the on-axis peak scales as N, there is no observable interference fringes. Partial phase-locking of the array yields a scenario intermediate to these two extremes. Accordingly, η is computed by numerically simulating two cases for the same parameter set describing a fiber laser array: one with coupling "on" and the other with coupling off (each fiber operates with independent feedback). The on-axis intensity is extracted for each case, and Equation (2.3) is applied.

$$\eta = \frac{I_{\substack{\text{on-axis} \\ \text{coupled}}}}{I_{\substack{\text{on-axis} \\ \text{perfectly} \\ \text{coupled}}}} = \frac{I_{\substack{\text{on-axis} \\ \text{coupled}}}}{N \cdot I_{\substack{\text{on-axis} \\ \text{uncoupled}}}} \tag{2.3}$$

Figure 2.14 shows the output far-field profiles of the 3-fiber array as the nonlinearity is varied, while Table 2.3 lists the computed values for the combining efficiency. The results indicate that the non-resonant Kerr nonlinearity introduced in the system is detrimental to coherent, in-phase combination of fibers in the ring-geometry coupling scheme from Figure 2.2, leading to lower on-axis output intensity in the far-field as well as decreased efficiency of combination, as quantified by η in Equation (2.3).

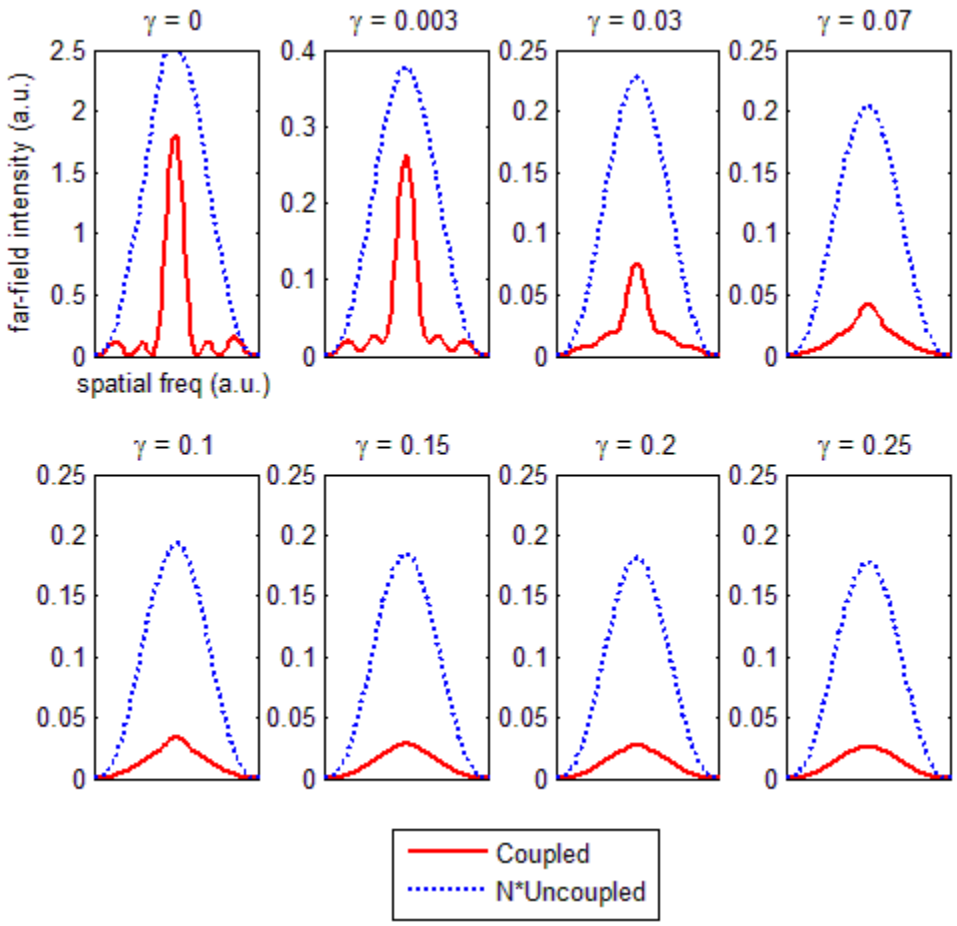

Figure 2.14: Far-field output intensity patterns (at steady-state) as non-resonant Kerr nonlinearity γ is varied for 3 fibers (N = 3) coupled in the ring-geometry architecture. The plots display only the portion of the far field that lies within the central diffraction lobe, so that fine details can be more easily discerned. In any case, power outside the central diffraction lobe is typically not very useful in the tiled array structure. The listed values of γ are in units of $W^{-1}m^{-1}$. The unsaturated gain value is $g_0 = 2.67\ m^{-1}$, and the other parameter values are given in Table 2.2. All plots are taken after 2200 cavity roundtrips. Note: the vertical scales are not the same for all plots.

Table 2.3: Steady-state, far-field intensity, and combining efficiency η as nonlinearity is varied, for a 3-fiber array (lengths 10 m, 9.9 m, and 10.013 m) coupled in the ring geometry.

Nonlinearity γ ($W^{-1}m^{-1}$)	**Far-field, on-axis intensity with coupling (a.u.)**	**Far-field, on-axis intensity without coupling (a.u.)**	**Combining efficiency η (%)**
0.000	1.8020	0.8486	70.79
0.003	0.2621	0.1261	69.29
0.030	0.0758	0.0759	33.31
0.070	0.0433	0.0681	21.17

0.100	0.0349	0.0645	18.01
0.150	0.0289	0.0616	15.63
0.200	0.0273	0.0605	15.02
0.250	0.0264	0.0593	14.83

Figure 2.14 illustrates the far-field profile's dependence on the Kerr nonlinearity coefficient. The red trace (solid) shows the far-field when coupling is turned on. The blue trace (dashed) shows the far-field for the uncoupled system (with same nonlinearity as the coupled system), multiplied by the number of elements – in this case there are 3 fibers. From the latter, the on-axis intensity corresponding to perfect coherent combination is extrapolated, as in the denominator in the right-hand-side of Equation (2.3). For $\gamma = 0$, the steady state far field profile shows the narrowed central peak and the interference nulls associated with in-phase locking of three elements. As nonlinearity increases, the graphs clearly indicate leakage of power from the main (on-axis) lobe to interference side lobes. In addition, the overall amplitude of the far-field profile decreases. The presence of large side lobes in the far-field indicates deficiencies in the coherent, in-phase locking, due to phase fluctuations and mismatches. Meanwhile, the decrease in the overall far-field amplitude implies that there is increased loss in the cavity for the dominant modes that emerge from the system (specifically, losses that arise from the lack of perfect co-phasing and the frequency-dependent loss factor).

2.5.3 Physical interpretation in the context of coincident mode theory

Coincident mode theory helps to establish a physical picture that can be used to explain the above results (see [17, 36, 37, 45]). Each individual fiber element has its own frequency comb, comprised of the modes that satisfy the specific fiber's roundtrip phase constraint. Hence, this

frequency comb is length-dependent. In the passive combining method used here, the coincident modes – those that satisfy the roundtrip phase constraints of all of the fibers – are the ones that emerge from the system. These coincident modes arise at the overlap of the frequency combs of all of the fiber elements. Figure 2.15 provides a simple illustration of this concept.

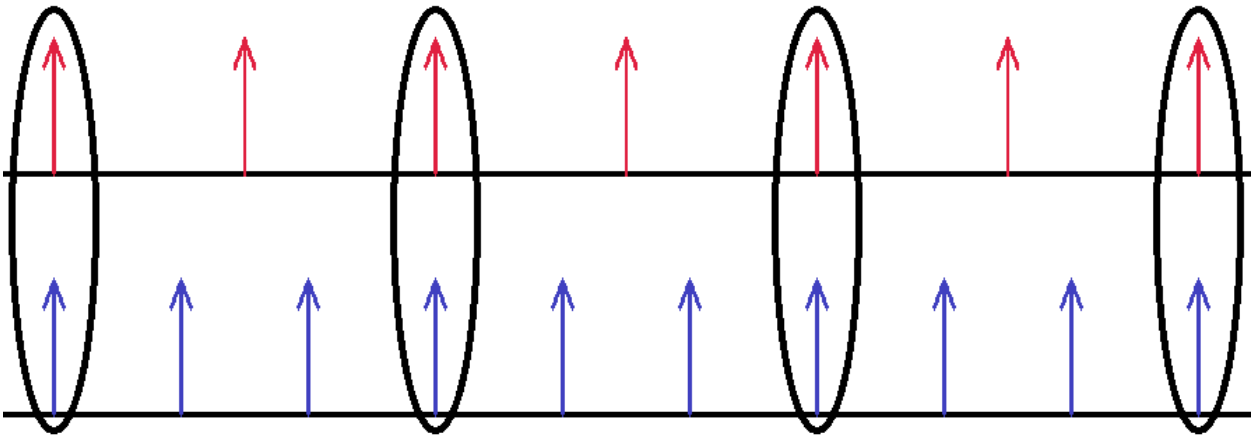

Figure 2.15: Illustration of coincident modes arising from the overlap between the frequency combs of the individual array elements. In this diagram, the horizontal axis is frequency, and the arrows/peaks denote the locations of the resonant longitudinal mode frequencies for each fiber.

In many cases, especially as the number of elements is increased, the likelihood of achieving coincident modes, within the bandwidth of available modes, is greatly reduced. This leads to a reduced chance of coherent locking of the system. As the system self-adjusts to coherently lock the elements, the modes that emerge are those that best satisfy the roundtrip phase constraints of all of the fibers. When there is no "exact" coincident mode in the spectral bandwidth, partial overlap of peaks from different frequency combs yield the modes that emerge. In this process, the system is expected to self-select modes that incur the least loss in the system as a whole [37]. Here, loss in the system can arise due to phasing mismatches and the loss dispersion (i.e. the spectral band-pass filter). Nevertheless, coherent, in-phase locking is more difficult when there are no perfectly coincident modes.

Nonlinearity can increase the likelihood of finding coincident modes [17]. It is known that the Kerr nonlinearity leads to spectral broadening, which in the coincident mode model yields broadened peaks in the frequency combs. This in turn increases the chance of overlap across multiple frequency combs. Consequently, nonlinearity broadens the range of frequencies over which the overlap occurs. Moreover, in the context of four-wave mixing, nonlinearity provides a mechanism for communication between modes in different frequency combs. The nonlinear effect redistributes energy from modes in one frequency comb to modes of another, thus influencing the coupling mechanism. It seems that nonlinearity also plays a role in large arrays with random length variations, where it becomes very difficult to find spectral regions in which there is at least partial overlap of all of the individual fibers' frequency combs.

However, in the same manner, the four-wave mixing and phase fluctuations that arise from the Kerr nonlinearity lead to greater loss in the system and decreased in-phase, coherent locking among the fiber elements. While the nonlinearity increases overlap of spectral peaks, it also results in the transfer of energy from coincident or partially coincident modes to modes that suffer high loss in the cavity (via phase mismatches and the loss dispersion); this effectively reduces the power coupled out of the cavity. The nonlinear phase accumulation also contributes to increased phase fluctuations in the output, and this effect manifests itself in decreased efficiency of coherent locking and increased power leakage to the interference side lobes in the far-field region of the tiled output and the back focal plane of the feedback lens. Elevated side lobes in the far-field translate to loss in the combining scheme, since the combined output power of the fiber array is designed to be extracted from the central (on-axis) channel.

Lastly, note that in the simulation results presented, the uncoupled system's far-field output also decreases as nonlinearity increases; this is attributed to the loss dispersion coefficient b in Equation (2.1). The bandwidth limitation is required for computational feasibility in the simulations. Nevertheless, the overall trend of decreasing efficiency with increasing nonlinearity is still expected to hold in the absence of the narrow loss dispersion filter. In addition, real/physical systems all include some bandwidth limiting elements; hence, such systems are expected to behave in a similar manner when nonlinearity is increased.

2.6 Effect of external path length differences due to the coupling optics

As mentioned earlier in SECTION 2.3.1, external path length differences due to the coupling optics can degrade the extracted output beam quality. The coupling mechanism is set up in a manner such that the phasing quality at entrance to feedback entrance plane determines the axial modes that are self-selected to emerge from the system. Meanwhile, the phasing at the near-field plane at the exit of the fiber array determines the output (extracted) beam quality. In the absence of external path length differences, the phasing is the same at the two planes. However, if external path lengths are present, then the axial modes/frequencies that are suitable for good (i.e. perfectly constructive) phasing at the feedback entrance plane may not be appropriate to achieve perfect constructive phasing at the array (near-field) exit plane, thus potentially resulting in poor beam quality in the (extracted) output far-field plane. The coupling system as modeled cannot correct through the self-organization processes for this issue. Figure 2.16 and Figure 2.17 demonstrate the effect of external path length differences, for two different values of nonlinearity. The axial modes selected on the merits of phasing in the feedback entrance plane result in stark phase mismatches in the outputs of the fibers in the array (near-field) exit plane.

An increase in Kerr nonlinearity results in larger near-field phase fluctuations, and as expected it is unable to correct for the issue of phase mismatches due to the external path length differences.

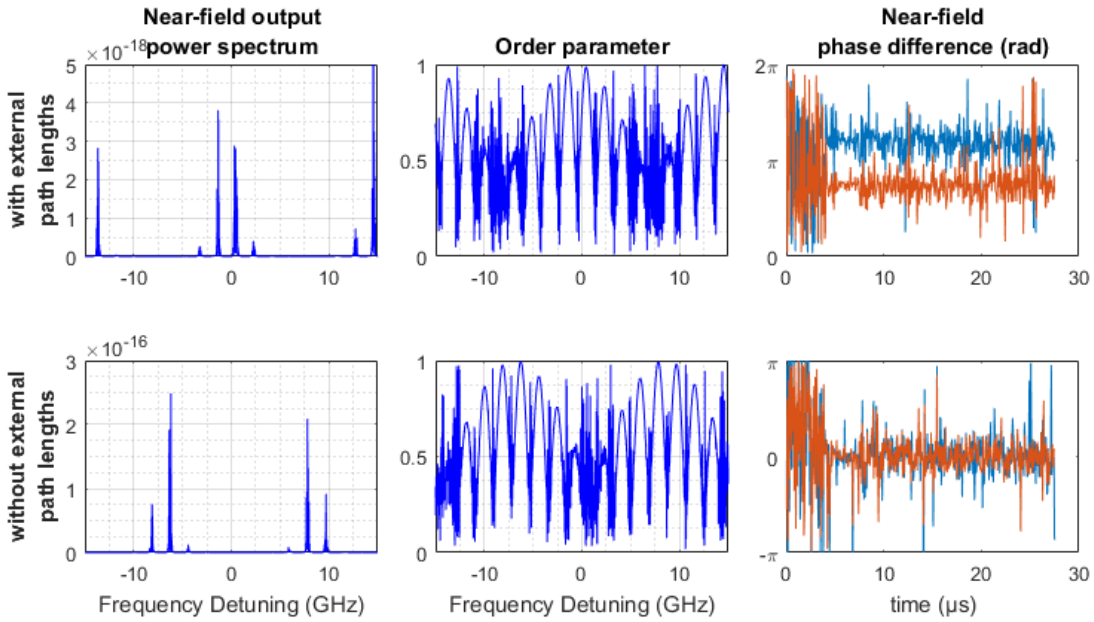

Figure 2.16: Demonstration of the effect of external path lengths. For the top row, the external path lengths are 0 m, 0.005 m, 0.00233 m [22]; for the bottom row, they are all set to zero. The near-field phase differences are calculated relative to the phase for the 10 m fiber. The nonlinearity is $\gamma = 0.0004$ $W^{-1}m^{-1}$, the unsaturated gain is $g_0 = 2.67$ m^{-1}, and Table 2.2 lists the other parameter values.

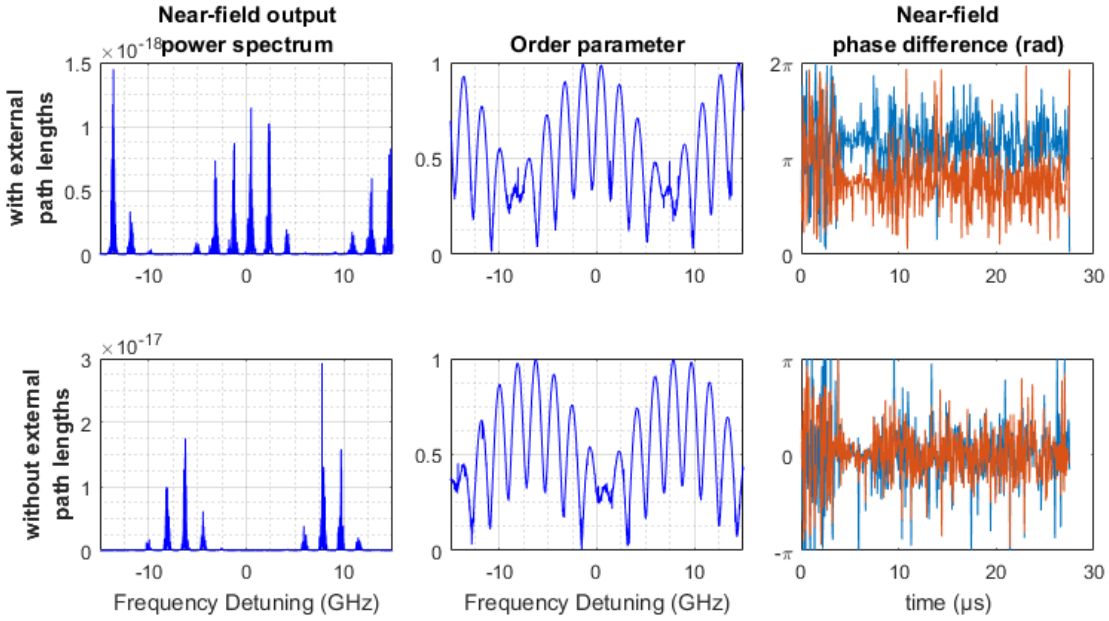

Figure 2.17: Same as Figure 2.16, except that the nonlinearity coefficient is increased to $\gamma = 0.003$ $W^{-1}m^{-1}$.

2.7 Comparison with 50:50 directionally-coupled arrays

Previous dynamic, multi-mode studies have investigated, numerically and experimentally, the passive phasing mechanism in the 50:50 directional coupler approach, as well as the role of the Kerr nonlinearity [36, 37, 38]. Regarding the passive phasing mechanism, their results indicate that the system self-adjusts and self-selects modes with least loss. As for the role of nonlinearity, these studies seem to indicate that nonlinearity does not significantly contribute to the ability of the system to coherently lock all of the fiber elements and that nonlinearity can even be detrimental to the phase-locking. Again, coincident mode theory is used establish the physical picture, in which the coincident modes that satisfy the roundtrip phase constraints of all of the fibers and experience the minimal loss are the ones that survive the system's self-selection process and emerge. In the 50:50 directional coupler system, additional constraints on the phases of the outputs from each fiber element arise in part from the matrix describing the couplers [36]:

$$\begin{bmatrix} E_{out,1} \\ \\ E_{out,2} \end{bmatrix} = \frac{1}{\sqrt{2}} \begin{bmatrix} 1 & -i \\ \\ -i & 1 \end{bmatrix} \begin{bmatrix} E_{in,1} \\ \\ E_{in,2} \end{bmatrix} \tag{2.4}$$

The 50:50 couplers used here send $E_{out,2}$ to an angle-cleaved facet that effectively serves as a loss port, and they retain $E_{out,1}$ as the output. In order for the inputs $E_{in,1}$ and $E_{in,2}$ to combine most efficiently, they must ideally have a phase difference of $\pi/2$ with respect to each other, so that all of the power is sent to the output port and none of the power is sent to the loss port. This phase constraint is imposed by every coupler upon its two inputs, and thus the system as a whole, in its efforts to self-select modes that experience minimal loss, strives to satisfy these constraints in addition to the overall roundtrip phase constraints. Kerr nonlinearity introduced to the system leads to spectral broadening and increased likelihood of overlap of the frequency combs of the individual fiber elements. However, it also introduces nonlinear phase accumulation in each

fiber element, which must be included in the total roundtrip phase calculation and made to satisfy the respective phase constraints, including those imposed by the 50:50 couplers. The additional requirement of satisfying the phase constraints of the couplers makes it difficult for the nonlinear effect to improve coherent locking. In fact, very high values of the nonlinearity coefficient can lead to large fluctuations in the phase and increased loss to the cavity, which become detrimental to the phase-locking mechanism. Similar to the case of the ring-geometry architecture, nonlinearity can cause the transfer of energy from low-loss modes to high-loss modes that do not sufficiently satisfy the imposed phase constraints, leading to reduced power and lower efficiency.

2.8 Conclusion

In conclusion, this chapter has investigated the dynamics of passive coherent beam combining of fiber laser arrays using the spatially-filtered ring geometry coupling scheme. It has also examined the role of the non-resonant Kerr nonlinearity in the coherent phase-locking process. The results from the simulations regarding phase-locking dynamics are consistent with previous steady-state results as well as experimental results: (i) phase-locking occurs quickly and smoothly after the system is turned on, operating on a time scale shorter than that of the gain dynamics and relaxation oscillations, and (ii) once in steady-state operation, the system recovers from phase perturbations very quickly, within just a few round trips in the composite cavity. In addition, numerical simulations indicate that the presence of the Kerr nonlinearity hinders the system's ability to coherently lock the fiber lasers in phase, limiting the system from achieving efficient combining in this ring-geometry architecture. Here, the combining efficiency is quantified by a metric that examines the far-field output intensity pattern of the tiled array.

CHAPTER 3

Coupled mode-locked semiconductor lasers

3.1 Introduction

Semiconductor lasers also serve as a popular source for laser light. Given the diverse set of semiconductor materials that can be used as the gain medium, they collectively enable access to a wide range of the wavelengths, including parts of the ultraviolet, visible, and infrared ranges [46, 47]. They offer several benefits that incentivize their widespread use and versatility: they are compact, relatively inexpensive, can be electrically pumped with good efficiency [2, 46, 48]. In addition, manufacturing processes can allow them to be readily integrated on chip or a monolithic platform, which is often a very desirable quality. A brief review of semiconductor laser physics is provided in the following paragraph.

Semiconductor materials are well known for their band structure, which form when a large collection of atoms (each with its own set of atomic orbital energy levels) come within close proximity of each other (e.g. in a crystal lattice) [2]. The resultant groups of densely packed (but distinct) molecular orbitals form an approximate continuum, leading to so-called "bands" of energy levels [2]. The two important bands are the valence and conduction bands, where the latter is at the higher energy and generally unoccupied by the electrons unless they are excited to that state; the energy "bandgap" separates the two levels [48]. The basic example of a semiconductor optical amplifier is a p-n junction, which is formed by adjacent p-type and n-type

semiconductors that have holes and electrons, respectively, as the main charge carriers [2, 48]. When a forward-biased current is applied across the p-n junction, then the two types of charge carriers are pushed to cross the junction to the other side; along the way, they can interact with each other through a recombination process to produce photon emission [2, 46]. This "injection current" can be used to create a population inversion of carriers (electrons in the conduction band, holes in the valence band) in this active region between the p-type and n-type materials, which can then enable stimulated emission and thus optical gain [2, 48]. In practice, the p-n junction is accompanied by a (single or double) heterostructure design that essentially provides better confinement of the charge carriers (thus enhancing recombination processes to improve gain) as well as waveguiding of the generated light [2, 46, 48]. The addition of a feedback mechanism facilitates the construction of a semiconductor laser.

The versatility of semiconductor lasers has spurred high interest in the specific study of coupled semiconductor lasers and arrays for diverse applications and theory. First, it is already well-known that coupled continuous-wave (CW) semiconductor lasers are a source for a richly complex breadth of phenomena that have theoretical and practical importance, such as phase-locking and synchronization, symmetry-breaking and leader-laggard dynamics, chaos (including synchronized chaos), and multistable behaviors (see SECTION 3.2.1 for a detailed literature review). In fact, even after decades of research by numerous groups, there is continued interest and activity to better understand the varieties of systems and behaviors that exist. Second, semiconductor lasers with saturable absorbers are themselves able to produce complex behavior, both in isolation as well as when coupled to passive/external feedback cavities, particularly in the

domain of mode-locking and pulse generation (see SECTION 3.2.4 for a review of the relevant scientific literature).

It is therefore natural to anticipate an even greater degree of complexity when two or more mode-locked semiconductor lasers are mutually coupled. At present, however, there is scarcely any prior work, for both the evanescently coupled and face-to-face/delay coupled cases. Both cases can be expected to yield new, intriguing physical phenomena and novel dynamical behavior, which, given the versatility and inexpensiveness of semiconductor lasers, can be utilized for practical applications (e.g. communications, computing, clocking, frequency combs) and exploit the speed and bandwidth capacity of all-optical constructs. In addition, coupled, mode-locked lasers can serve as a readily accessible platform/test-bed for theoretical and experimental studies of coupled nonlinear oscillators and dynamical systems, in a similar manner as the CW counterpart has been. As an example of a promising practical application, a study of two ring-cavity semiconductor lasers, actively mode-locked via electro-optic modulators and passively coupled via 50:50 directional couplers, reported the construction of an all-optical flip-flop [49]. Granted, this study did not involve passive mode-locking (via saturable absorbers) and was limited in exploration of the coupling dynamics and other possible phenomena.

Hence, there is a motivation for the research work to model and investigate the dynamics and synchronization properties of passively coupled mode-locked semiconductor lasers. The work covered in this chapter, particularly in SECTION 3.3, SECTION 3.4, and SECTION 3.6, will be included in several manuscripts currently under preparation.

3.2 Background and literature review

3.2.1 Coupled continuous-wave semiconductor lasers

Passively coupled CW semiconductor lasers and the dynamics of their "compound laser modes" or "supermodes" have been studied in great detail in the scientific literature. Many different coupling setups have been explored analytically, numerically, and experimentally. Two important categories are delay-coupled lasers and evanescently coupled lasers [47]. The following review highlights a sample of important studies and diversity of interesting nonlinear dynamical phenomena that occur; exposure to these works has assisted in developing a direction, applying mathematical techniques, and identifying/interpreting the results for this thesis work.

One of the early systems that set the framework for much of the studies of delay-coupled lasers is that of a single semiconductor laser with external, delayed feedback – in a sense, this is a self-coupled system [47]. In the case of weak or moderate external feedback, the Lang-Kobayashi (L-K) model was developed to investigate the delay-coupling-induced frequency shift (due to competition between the active and external feedback cavities' modes), relaxation oscillation enhancement and instabilities, multistability, and hysteresis [50]. The L-K model has two equations: the first is a delay differential equation for the electric field (where the delayed term accounts for the feedback delay time), and the second is a rate equation for the population inversion. Numerous subsequent papers have extensively used linear stability and bifurcation analyses methods (analytical and numerical) to further study the L-K equations, with interests such as the dynamics and stability of the external cavity mode solutions, routes to "coherence collapse" and chaos (e.g. via a process that undampens the relaxation oscillations), and a closer look at "mode-hopping" and multistability. A small subset of such works are found in [51, 52,

53, 54, 55], and a review of a larger collection of works is given in [47]. A limitation of the L-K model is the single-longitudinal-mode framework, but there have been extensions to multimode versions, e.g. by writing L-K equations for each lasing mode in consideration and coupling the sets of equations for each mode to those of the other modes via cross-saturation terms [56].

The L-K equations serve as an important foundation and basis for models of many of the various systems of delay-coupled semiconductor lasers, such as unidirectionally and mutually-injected coupled lasers. The modeling approaches for coupled lasers is to assign a set of L-K equations to each laser and apply coupled-mode theory, specifically by including the electric field of one laser as an additional source term in the delay differential equation of the electric field amplitude of the other laser. Unidirectionally coupled lasers are set up with asymmetry in the manner that coupling is one-way: a fraction of the drive laser's output is injected or coupled into the response laser, with the delay arising from the time of propagation between the lasers [47]. The coupled system then can exhibit several behaviors, such as frequency-locking and synchronization, delayed synchronization, absence of synchronization, or synchronized chaos induced in the response laser by a chaotic drive laser [47].

On the other hand, for two mutually-injected lasers, the two lasers are placed face-to-face with each other, such that a portion of each laser's output is injected into one of the facets of the other laser. As such, the delay time arises from propagation of light from one laser to the other, and vice versa. The symmetry in this setup provides avenues for interesting synchronization and/or symmetry-breaking phenomena to naturally occur and be observed. Mutually-injected semiconductor lasers have been studied in the context of "compound laser modes" (CLMs) and

the framework they provided for organizing the dynamics [47]. CLMs are simple, CW solutions to the coupled L-K equations, for which the two lasers are frequency-locked, maintain constant amplitudes, and possibly have a time-independent phase difference [57]. Several papers have explored different facets of the dynamics of CLMs, including their stability regions and bifurcation pictures, because the CLMs' structure can provide information about the frequency-locking and synchronization behavior [57, 58, 59]. These papers also considered small frequency detuning between the solitary modes of the two lasers (thus introducing an asymmetry to consider) and the associated impact on the trajectories and stability of the CLMs in the presence of coupling [57, 58, 59]. Recent papers have further explored detuning effects [60, 61].

In another set of numerical and experimental studies, for otherwise perfectly identical lasers (including zero frequency detuning), the coupled system was found to spontaneously break symmetry and assume robust leader-laggard delayed synchronization between the two lasers , even when both lasers operated in chaotic regimes (i.e. delay-synchronized chaos was also observed) [62, 63]. Here, the numerical simulations showed that zero-lag synchronization occurred for the two lasers if they were given the same initial conditions and the noise sources were absent, whereas the addition of a spontaneous emission noise term to the model equations caused the zero-lag scenario to lose stability and the leader-laggard delayed synchronization scenario to prevail [62, 63]. Alternatively to numerical bifurcation analysis, a recent paper suggested a complementary group-theory-based approach in order to examine and classify symmetry-breaking bifurcations of coupled identical lasers and extend to larger symmetric coupled laser arrays [64].

Asymmetry has also been further explored in mutually-injected semiconductor lasers. In fact, one of the earlier studies – numerical and experimental – considered weakly mutually-coupled lasers with non-identical coupling strengths and gains [65]. The authors observed localized synchronization (strong oscillations in one laser, weak oscillations in the other) and entrainment of one laser to weakly oscillate at the relaxation oscillation frequency of the other laser [65]. Furthermore, they addressed the dependence of this behavior on the asymmetry in laser pumping and (and thus solitary relaxation oscillation frequencies) and in coupling strength [65].

One additional study considered the limiting case for which the delay approaches zero (but the electric field phase rotation due to propagation is retained as a parameter) and thus the face-to-face coupling is instantaneous [47, 66]. The authors showed how the dynamics and stability of synchrony and anti-synchrony between two identical lasers (without any frequency detuning between them) depend on the coupling strength and especially the phase of the instantaneous mutual injection [66]. The paper also addresses phase-locked CW operation, self-pulsations, and chaos when symmetry is broken through frequency detuning [66].

The second category, evanescently coupled lasers, lends itself to slightly different modeling approaches and behaviors. A key difference is that, typically, there is negligible delay time in the process of coupling the field of each laser to the other – coupling can be treated as instantaneous. The relevant theoretical studies employed models predominantly of the ordinary or partial differential equation variety, as opposed to delay differential equations [67, 68, 69]. Some of the significant findings and observations included, among others, 1) the dynamic instability and strong chaotic pulsing for individual lasers in a phase-locked array whose total

array output relaxed toward quasi-steady-state [67], 2) the ability of the lasers in the array to phase-lock and its dependence on various parameters [68, 70], and 3) synchronized chaos [69].

3.2.2 Conceptual review of passive mode-locking with a saturable absorber

The essential idea behind mode-locking is the phase-locking of many longitudinal modes / frequencies in a manner that yields a periodic train of pulses. To illustrate the basic concept, Figure 3.1 depicts the difference between the scenario of randomly-phased, uncorrelated sinusoids and the scenario of phase-locked sinusoids. In the case of a laser, the set of modes that can be phase-locked in order to generate the pulse train are limited by two main factors. First, the modes must satisfy the roundtrip phase constraint of the cold cavity (i.e. these frequencies are equidistantly spaced by the cavity's free-spectral range, $1/T$, where T is the roundtrip delay time). Second, the modes must observe sufficient net gain in order to lase. The width of each pulse in the train is inversely proportional to the bandwidth of the mode spectrum available.

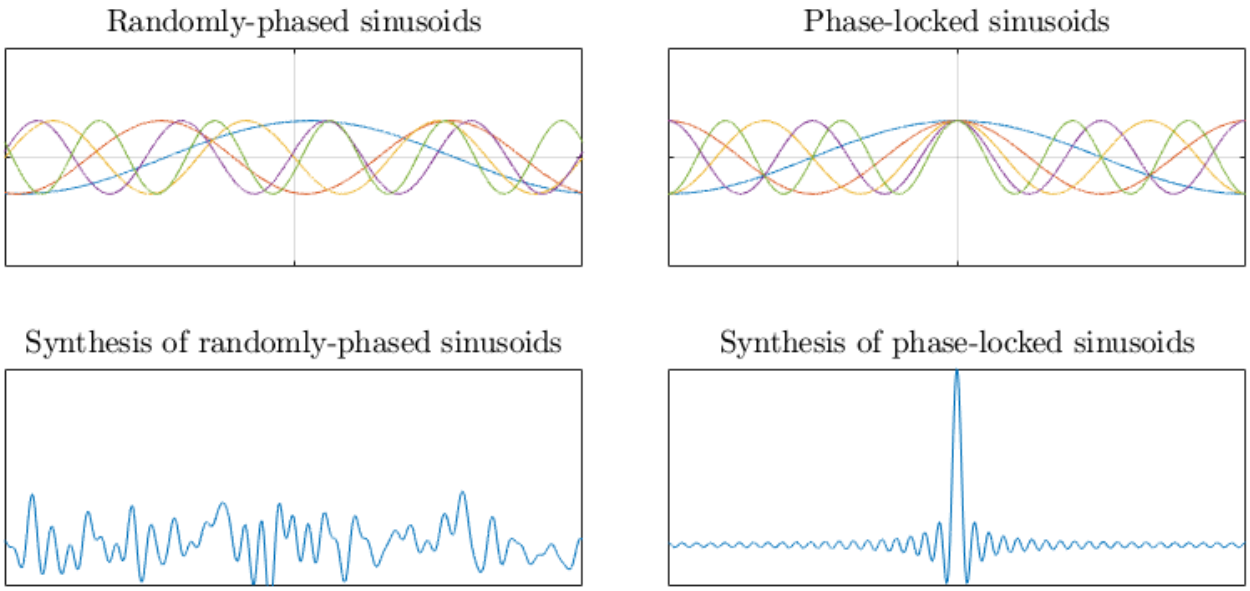

Figure 3.1: Illustration of the basic concept of mode-locking. In the left column, the sinusoids are randomly-phased, while in the right column all of the sinusoids phase-locked. Note that for the sake of clarity, the top row shows only the first 5 harmonics, whereas the bottom row shows the synthesis of up to 40 harmonics. The horizontal axis is time, while the vertical axis is amplitude/power.

There are several popular techniques that are used in order to achieve mode-locking in a laser, and a good review of many techniques and the history of their development can be found in [71]. This section, however, will review only mode-locking using a saturable absorber. The saturation of the absorption coefficient leads to an intensity-dependent transmission profile: when the optical intensity passing through it is sufficiently high, the absorption saturates and thus attenuation is thus low; when the optical intensity is low (e.g. after the pulse passes through), the absorption recovers and the attenuation becomes high again [2]. Therefore, the saturable absorber can be used to shorten the pulse circulating in the laser cavity as the pulse passes through it, and the saturable absorber can meanwhile suppress/attenuate noise and other weaker fluctuations before and after the pulse. In the context of semiconductor laser, the absorber section can be implemented similarly as the gain section, except with the application of a reverse bias: when the circulating pulse passes through the absorber, many charge carriers (electron-hole pairs) are created and the material's absorption decreases; as the pulse leaves, the reverse bias quickly sweeps the charge carriers out of the active section in order to recover the high-attenuation state of the absorber [72, 73]. Note that this reverse bias can be used to adjust the absorber's recovery time: larger reverse bias levels can lead to faster absorber recovery and, consequently, further shortening of the pulses [72].

The recovery time of the saturable absorber is an important parameter in the mode-locking process, as is the depth/strength of the absorber saturation. For a fast saturable absorber, the recovery time is shorter than the width of the circulating pulse, and so the absorber responds and recovers nearly instantaneously with respect to the time scale of the pulse [74]. The saturation needs to be strong enough in order to open a window of net gain [71, 75]. The left column of

Figure 3.2 shows an example of pulse formation in the presence of fast saturable absorption, as described in [71]. Note that, in this figure, the gain is assumed to have a very slow relaxation time and to be only negligibly saturated by the passage of a single pulse, in which case the gain is saturated primarily by the average circulating power and can be considered more or less constant on the time scale of a single pulse (this is reasonable, for example, in the case of solid-state lasers with small gain cross-sections) [74, 75]. On the other hand, mode-locking is also possible with a slow saturable absorber, one with a recovery time that is much longer than the pulsewidth but shorter than the cavity roundtrip time, as exemplified in the right column of Figure 3.2 and described in [71, 76]. In this figure, note the interplay between absorber saturation and gain saturation in order to open and close the net gain window around the pulse (here, the gain is saturated appreciably by the pulse and is clearly time-varying on the time scale of the pulse and the cavity roundtrip time) [71]. As the pulse arrives, the absorber saturates first, deeply/strongly enough to open a window of net gain, which is then closed through a combination of gain saturation and absorption recovery as the pulse departs [71]. The absorption recovers then faster than does the gain, such that, after the pulse passes through and generally between subsequent pulses, there is higher loss than gain and consequently near-zero intensity [71, 76]. There is also another, slightly different scenario for mode-locking with a slow absorber that can occur, as shown in Figure 3.3. Here, the general idea still holds regarding the formation of the net gain window to sustain pulsed operation, but an interesting observation is that stable mode-locking can occur even if the opening of this window slightly precedes the leading edge of the pulse [72, 77]. In addition, it has been observed and reported that stable mode-locking can also be achieved even if the closing of the net gain window occurs slightly after the pulse's trailing edge [78, 79].

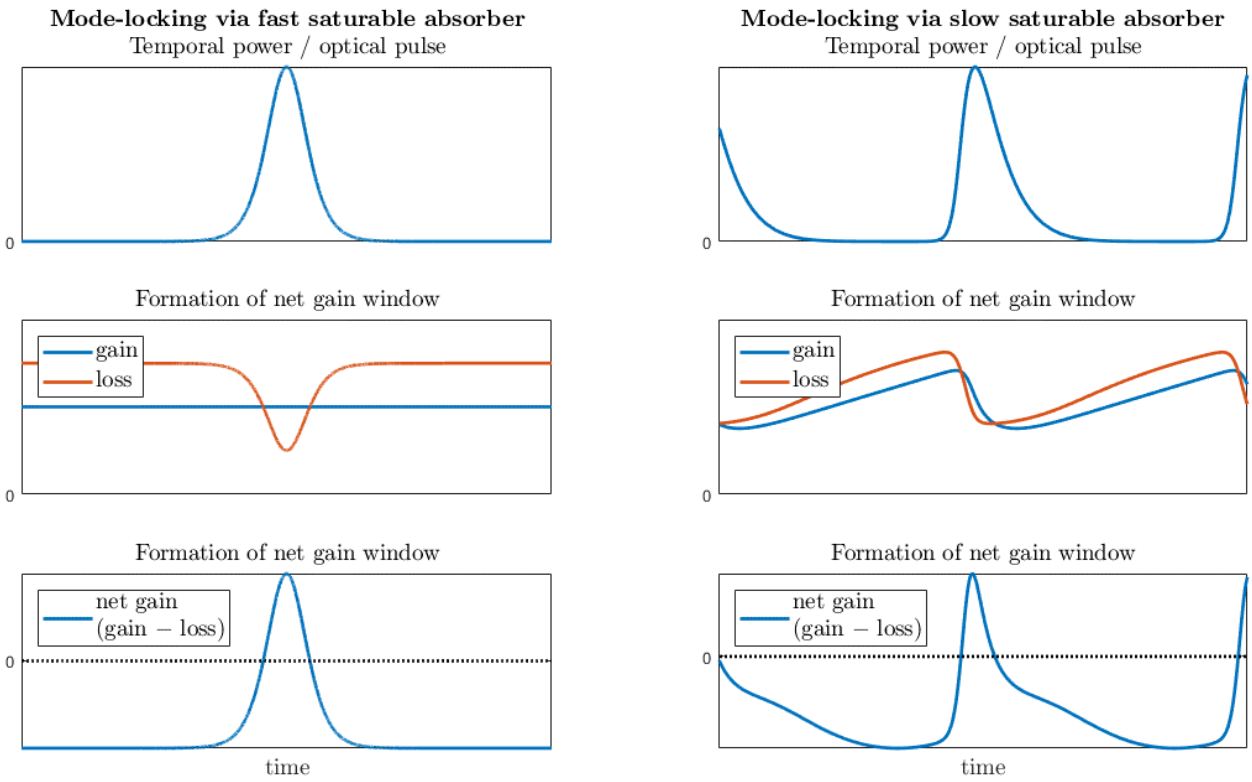

Figure 3.2: Example of the dynamics of passive mode-locking via saturable absorber, distinguishing between the usages of fast vs. slow absorbers. It is seen that the fast absorber saturates with a profile that tracks the pulse's instantaneous and peak power, whereas the slow absorber saturates depending on the pulse energy (in a sense, the saturation profile tracks the integral of the pulse power) [75]. Note that the horizontal and vertical scales in the subplots are in arbitrary units, because the purpose of this figure is simply to provide a qualitative illustration.

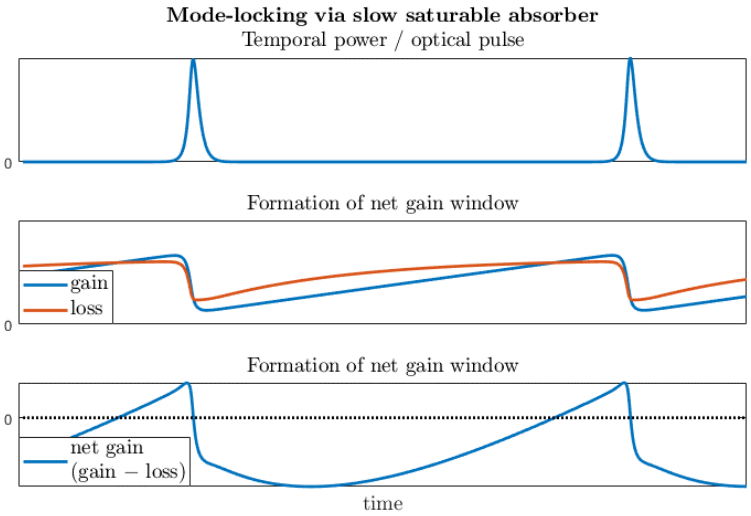

Figure 3.3: Example of mode-locking with slow saturable absorber in which the opening net gain window slightly precedes the leading edge of the pulse.

3.2.3 Conceptual review of linear stability analysis and bifurcation theory

A brief recap of the linear stability analysis and relevant bifurcation theory of DDEs is provided here. Namely, the Hopf bifurcation is described here, as it is used in this thesis work to understand and describe the mode-locked regimes for the single laser and the coupled system. Of course, there are many other types of bifurcations, local and global, often seen in dynamical systems. An excellent introduction to bifurcation theory and its applications can be found in [80] (although the material in this book is covered in the context of ordinary differential equations, the conceptual framework is qualitatively similar to that of delay differential equations), and a brief review of linear stability analysis of DDEs as well as a list of references that treat the theory in greater rigor are both provided in [81]. The following recap of linear stability analysis and bifurcation theory refers to the material explained and presented in [80, 81].

Without a loss of generality, consider a system of DDE with a single delay (T) given by $\frac{d}{dt}x(\tau) = f\big(x(\tau),\ x(\tau - T)\big)$, where the state variable is $x(\tau) \equiv [x_1(\tau) \quad x_2(\tau) \quad \cdots]^{\intercal}$. Suppose x° is an equilibrium/steady-state of the system, i.e. $f(x^\circ,\ x^\circ) = 0$. The local stability of this equilibrium can be found as follows. First, the DDE is linearized around x° via the Jacobian; the DDE that results from linearization is called the "variational equation" and has the form $\frac{d}{d\tau}x(\tau) \approx f(x^\circ,\ x^\circ) + \frac{\partial f(x^\circ,x^\circ)}{\partial x(\tau)}(x(\tau) - x^\circ) + \frac{\partial f(x^\circ,x^\circ)}{\partial x(\tau - T)}(x(\tau - T) - x^\circ)$. Note here the use of the shorthand: $\frac{\partial f}{\partial x(\tau)}$ and $\frac{\partial f}{\partial x(\tau - T)}$ are actually the Jacobian matrices evaluated at the equilibrium; the elements are given as $J_{ij}(\tau) = \partial f_i(x^\circ,\ x^\circ)/\partial x_j(\tau)$ and $J_{ij}(\tau - T) = \partial f_i(x^\circ,\ x^\circ)/\partial x_j(\tau - T)$, respectively. Next, a small perturbation from the equilibrium $x(\tau) = x^\circ + x_p e^{\lambda\tau}$, where x_p is a constant vector and λ is a constant scalar, is inserted into the variational equation in order to

derive the characteristic equation: $\det\left(-\lambda I + \frac{\partial f(x^\circ,x^\circ)}{\partial x(\tau)} + e^{-\lambda T}\frac{\partial f(x^\circ,x^\circ)}{\partial x(\tau-T)}\right) = 0$, where I is the identity matrix.

The roots of the characteristic equation (generally complex-valued) are the eigenvalues, and this "eigenvalue spectrum" provides information about the local stability of the equilibrium x° for the DDE: if all of the eigenvalues are in the open left-half plane, then the equilibrium is stable, and if there are any eigenvalues in the open right-half plane, then the equilibrium is unstable. This is clear from examination of the perturbation: $x(\tau) = x^\circ + x_p e^{\lambda\tau}$, and so if $\mathrm{Re}\{\lambda\} < 0$, then $x(\tau)$ eventually "returns" to x°, whereas is $\mathrm{Re}\{\lambda\} > 0$, then it does not. Moreover, the right-most eigenvalue in the complex plane is the one that determines the stability. Typically, as one of the parameters of the differential equation is gradually and smoothly varied, the equilibria of the system may smoothly change in value too, but the system remains qualitatively similar in its structure/topology. Bifurcations occur when the system encounters a qualitative/topological change in its dynamical behavior as a result of a smooth variation of one of the parameters. Examples are the creation and/or annihilation of one or more equilibria and/or limit cycles, the exchange of stability between equilibria, etc. Bifurcations can be identified when the right-most eigenvalue crosses the imaginary axis of the complex plane.

Now, in the case of ordinary differential equations, only the first two terms are present inside the determinant for the characteristic equation. As a result, the characteristic equation is a polynomial, which has a finite number of roots. However, for DDEs, the situation is more complicated, due to the factor of $e^{-\lambda T}$ in the third term inside the determinant. The characteristic equation here is transcendental, and consequently it generally has an infinite number of

roots/eigenvalues. Fortunately, it can be shown for a causal system (positive values of the delay T) that there are only a finite number of eigenvalues in any right-half plane $\mathrm{Re}\{\lambda\} > \mathrm{const} \in \mathbb{R}$. This facilitates numerical computation (see SECTION 3.3.4 and APPENDIX B.3).

Hopf bifurcations occur when a complex-conjugate pair of stability-determining eigenvalues cross the imaginary axis. Recalling the form of the small perturbation $x(\tau) = x^\circ + x_p e^{\lambda\tau}$ from the equilibrium x°, a pair of purely imaginary eigenvalues (that are complex-conjugates) for the term $x_p e^{\lambda\tau}$ corresponds to oscillatory behavior around the equilibrium x°, and this oscillation is also known as a periodic orbit or a limit cycle. Thus, the Hopf bifurcation signifies the creation or annihilation of a limit cycle from the equilibrium point. As an example in the context of mode-locked semiconductor lasers, a CW state can be considered an equilibrium point of a differential equation of the slowly-varying envelope of the complex field (i.e. the slowly-varying envelope is a constant) while a mode-locked pulse train (i.e. the slowly-varying envelope itself is a periodic function) is seen to emerge as a limit cycle that bifurcates from the CW solution. The point along the imaginary axis at which the eigenvalues cross for a Hopf bifurcation is the frequency of the limit cycle that is created. Therefore, in the mode-locked lasers example given, the imaginary part of the eigenvalue at the Hopf bifurcation would yield the repetition rate of the mode-locked pulse train. There are two varieties of Hopf bifurcations, depending on the nature of the limit cycle that emerges from it. The first is called supercritical, in which a stable equilibrium becomes unstable in favor of the generation of a stable limit cycle. The second is subcritical, in which an unstable equilibrium becomes stable, and an unstable limit cycle emerges at the bifurcation point.

3.2.4 Passively mode-locked semiconductor lasers

The work of Haus with the "master equation" approach was a key development in the theory of passive mode-locking via a saturable absorber (both fast and slow) [71, 74, 76]. However, the drawbacks of this model arise for semiconductor lasers due to the model's assumptions of small gain and loss per roundtrip [77, 82]. This led to the development of a more general model that made fewer assumptions, aside from the stipulation of a unidirectional ring cavity, and was formulated as a delay differential equation (DDE) system [77, 82]. This model has been used in many subsequent works on passively mode-locked semiconductor lasers. It is general enough to account for the dynamical phenomena, it facilitates easy and efficient numerical simulation, and it allows for rigorous bifurcation analysis and some analytical insight (in contrast to spatio-temporal, traveling-wave models, which although very general, are computationally expensive to solve numerically and are limited in yielding physical insight from analytical methods) [72].

To date, however, the relevant recent literature following the introduction of this DDE model has been predominantly focused on the following setups (for an excellent and very detailed review of the first two items and a thorough study of the third item in this list, one can refer to [73]):

1) A single laser within a ring cavity restricted to unidirectional operation [77, 82, 83, 84], where the studies identified through simulations and bifurcation analysis different dynamical regimes of operation (e.g. CW, mode-locked, harmonic mode-locked, Q-switched mode-locked), assessed the effect of the linewidth enhancement factors, and examined the multistability at the transitions between the different operating regimes
2) A single laser within a linear cavity that permits counter-propagating waves [85]; although this study did not specifically use the DDE modeling approach, it did provide a

comparison between the dynamics of the linear cavity vs. the unidirectional ring cavity, which indicates the DDE model can yield insight for linear cavities too

3) A single active cavity coupled to one passive cavity [86, 87] or two passive cavities [88, 89]; the authors in [86] report results on harmonic mode-locking at a repetition rate determined by the passive cavity length and optical bistability, while the authors for each of the other three papers use the passive cavities in order tune the pulse repetition rates and to reduce/stabilize pulse timing jitter
4) Extensions of the DDE model specifically for mode-locked quantum-dot lasers [90, 91]

At present, prior work on the dynamics of two coupled, mode-locked semiconductor lasers is scarce. The case of two mode-locked semiconductor lasers coupled in a face-to-face configuration has been mentioned [89] but accorded limited attention. Given the wealth of dynamic phenomena and synchronization behaviors observed for passively coupled CW semiconductor lasers, it is important to examine the mode-locked case. Using the DDE model earlier introduced for a single mode-locked, ring-cavity laser, this thesis sets out to explore the coupled-laser case in the context of evanescent coupling.

3.3 Methods

3.3.1 Physical model

Figure 3.4 illustrates the setup of the two coupled laser cavities, each with separate saturable gain and saturable absorption sections (note: these are slow saturable absorbers), as well as a lumped-element spectral filtering element; “passive sections” are present in between. Both cavities are assumed to operate in a unidirectional manner (as labeled in Figure 3.4), and the two are

evanescently coupled by means of a directional coupler within the passive sections that precede the output coupler. Coupling is assumed to be lossless and well-phase-matched; the latter assumption is reasonable when the field amplitude envelope is slowly-varying compared to the optical frequency, e.g. in this case picosecond-scale pulses enveloping femtosecond-scale optical carrier oscillations. This model for the coupled system is an extension of the single, mode-locked semiconductor laser cavity in [77, 82, 83, 84]. Both lasers are considered identical, except for the possibility of asymmetry in pumping (i.e. gain injection currents), cavity roundtrip time, and/or the initial state before "turning on" the coupling. Further details of the simplifying assumptions are provided in SECTION 3.3.3.

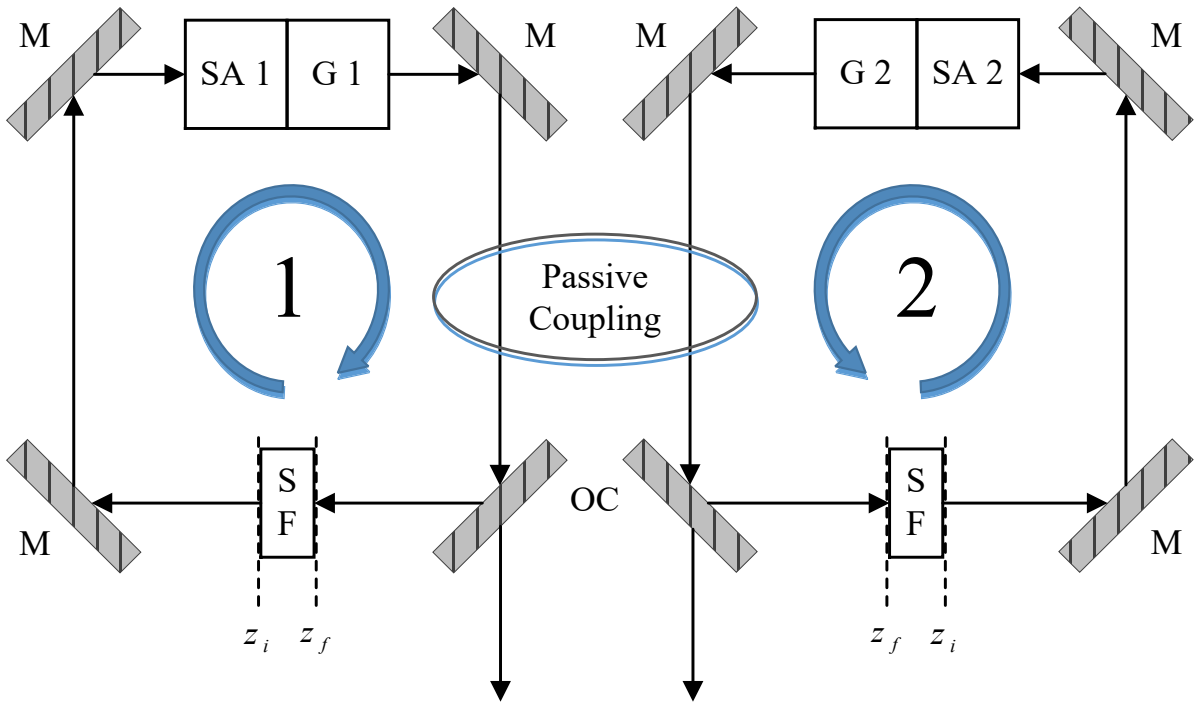

Figure 3.4: Diagram of two passively coupled, mode-locked, unidirectional ring-cavity semiconductor lasers. The labels denote saturable absorbers (SA), gain sections (G), lumped element spectral filtering (SF), mirrors with 100% reflectivity (M), and output couplers (OC). The spaces between the lumped elements are "passive sections" in the cavities. In each cavity, the labels z_i and z_f denote the beginning and end, respectively, of a roundtrip.

As an aside, the location chosen here at which mutual coupling occurs (i.e. immediately before the output coupler) simplifies the derivations involved when transforming the partial differential equation model into the delay differential equation model. This thesis work at present does not consider alternative locations for coupling, such as after the spectral filter or within the gain and/or saturable absorber sections. Indeed, it would be interesting to examine these scenarios in the future, especially for passive coupling immediately after the spectral filter (which could serve as a step towards extending the model to systems of three or more adjacently coupled lasers).

3.3.2 Mathematical model and parameter values for numerical simulations

The two coupled lasers are mathematically described as per Equations (3.1) – (3.6). Here, a set of traveling wave (partial differential) equations – similar to that utilized in [77] – accounts for the evolution of the slowly-varying, complex-valued envelope of the electric field through each absorber, gain, and passive section. For the gain and absorber sections, accompanying rate equations model the respective carrier densities. For the passively coupled region, standard coupled mode theory is utilized [2, 69, 70, 92, 93]. Table 3.1 describes each and every variable and parameter used in the equations.

For the absorber/gain sections,

$$\frac{\partial E_{1,2}(t,z)}{\partial z}+\frac{1}{v}\frac{\partial E_{1,2}(t,z)}{\partial t}=\frac{g_r\Gamma_r}{2}(1-i\alpha_r)\left(N_{(1,2),r}(t,z)-N_r^{tr}\right)E_{1,2}(t,z) \qquad (3.1)$$

$$\frac{\partial N_{(1,2),r}(t,z)}{\partial t}=J_{(1,2),r}-\gamma_r N_{(1,2),r}(t,z)-vg_r\Gamma_r\left(N_{(1,2),r}(t,z)-N_r^{tr}\right)\left|E_{1,2}(t,z)\right|^2 \qquad (3.2)$$

For the passive sections with and without coupling, respectively,

$$\frac{\partial E_{1,2}(t,z)}{\partial z}+\frac{1}{v}\frac{\partial E_{1,2}(t,z)}{\partial t}=0 \tag{3.3}$$

$$\frac{\partial E_{1,2}(t,z)}{\partial z}+\frac{1}{v}\frac{\partial E_{1,2}(t,z)}{\partial t}=+i\mathrm{K}_{12,21}E_{2,1}(t,z) \tag{3.4}$$

To account for the ring cavities' periodic boundary conditions,

$$E_{1,2}\big(t,z+L_{1,2}\big)=E_{1,2}(t,z) \tag{3.5}$$

To describe the spectral filtering with frequency response function $\hat{f}(w)$ – where ^ denotes the Fourier Transform, and Figure 3.4 indicates the positions z_i and z_f – for each laser cavity,

$$\hat{E}_{1,2}(w,z_i)=\hat{E}_{1,2}\big(w,z_i+L_{1,2}\big)=\hat{f}(w)\hat{E}_{1,2}\big(w,z_f\big) \tag{3.6}$$

Table 3.1: List of variables and parameters in the partial differential equation model of two coupled mode-locked semiconductor lasers; see Equations (3.1) – (3.6).

Variable / Parameter	Description
t	Temporal coordinate
z	Spatial coordinate (with respect to the position in each cavity, along its longitudinal direction)
Subscripts 1 and 2	Referring to lasers 1 and 2, respectively
Subscripts $r = g$ and q	Referring to the gain and absorber sections
$E_{1,2}(t,z)$	Electric field (slowly-varying envelope)
$L_{1,2}$	Cavity roundtrip lengths
$N_{(1,2),(g,q)}(t,z)$	Carrier densities in the gain and absorber sections
$N_{g,q}^{tr}$	Carrier densities at transparency threshold
v	Light group velocity
$\alpha_{g,q}$	Linewidth enhancement factors
$g_{g,q}$	Differential gains
$\Gamma_{g,q}$	Transverse modal fill factors

$\mathrm{K}_{12,21}$	Coupling coefficients, referring to coupling from laser cavity $2 \rightarrow 1$ or $1 \rightarrow 2$, respectively
$\gamma_{g,q}$	Carrier density relaxation rates
$J_{(1,2),(g,q)}$	Injection currents (note that $J_{(1,2),q} = 0$)

After non-dimensionalizing the above equations (including a coordinate change to a retarded time frame that moves along with the circulating wave/pulse), evaluating the transformation of each field amplitude from the beginning of its roundtrip through all of the cavity sections to the end of the same roundtrip, and then applying the spectral filters (treated as Lorentzian in lineshape) and boundary conditions, the model equations yield a system of six delay differential equations (DDE) that serve as the basis for the numerical simulation and bifurcation analysis results of this chapter. The DDE system is given below in Equations (3.7) – (3.16), while the full details of its derivation are relegated to APPENDIX A.1. The action of the directional coupler is captured by the coupling matrix in Equation (3.17). Table 3.2 describes the variables and parameters in the model, along with the parameter values used in the numerical simulations.

The amplitude equations are given below:

$$\frac{\partial A_1(\tau)}{\partial \tau} = -\gamma A_1(\tau) + \gamma e^{-i\varphi_1}\left(R_{11}(\tau - T_1)A_1(\tau - T_1) + R_{12}(\tau - T_1)A_2(\tau - T_1)\right) \quad (3.7)$$

$$\frac{\partial A_2(\tau)}{\partial \tau} = -\gamma A_2(\tau) + \gamma e^{-i\varphi_2}\left(R_{21}(\tau - T_2)A_1(\tau - T_2) + R_{22}(\tau - T_2)A_2(\tau - T_2)\right) \quad (3.8)$$

Here, the terms R_{ij} that describe the coupling are given below:

$$R_{11}(\tau) \equiv \cos(\mathrm{K}'\ell)\sqrt{\kappa}e^{(1-i\alpha_g)G_1(\tau)/2-(1-i\alpha_q)Q_1(\tau)/2} \quad (3.9)$$

$$R_{12}(\tau) \equiv \frac{i}{\mathrm{K}''}\sin(\mathrm{K}'\ell)\sqrt{\kappa}e^{(1-i\alpha_g)G_2(\tau)/2-(1-i\alpha_q)Q_2(\tau)/2} \quad (3.10)$$

$$R_{21}(\tau) \equiv i\mathrm{K}''\sin(\mathrm{K}'\ell)\sqrt{\kappa}e^{(1-i\alpha_g)G_1(\tau)/2-(1-i\alpha_q)Q_1(\tau)/2} \quad (3.11)$$

$$R_{22}(\tau) \equiv \cos(\mathrm{K}'\ell)\,\sqrt{\kappa}e^{(1-i\alpha_g)G_2(\tau)/2-(1-i\alpha_q)Q_2(\tau)/2} \tag{3.12}$$

The gain equations are given below:

$$\frac{\partial G_1(\tau)}{\partial \tau} = g_{01} - \Gamma G_1(\tau) - e^{-Q_1(\tau)}\left(e^{G_1(\tau)} - 1\right)|A_1(\tau)|^2 \tag{3.13}$$

$$\frac{\partial G_2(\tau)}{\partial \tau} = g_{02} - \Gamma G_2(\tau) - e^{-Q_2(\tau)}\left(e^{G_2(\tau)} - 1\right)|A_2(\tau)|^2 \tag{3.14}$$

The absorber equations are given below:

$$\frac{\partial Q_1(\tau)}{\partial \tau} = q_0 - Q_1(\tau) - s\left(1 - e^{-Q_1(\tau)}\right)|A_1(\tau)|^2 \tag{3.15}$$

$$\frac{\partial Q_2(\tau)}{\partial \tau} = q_0 - Q_2(\tau) - s\left(1 - e^{-Q_2(\tau)}\right)|A_2(\tau)|^2 \tag{3.16}$$

The coupling matrix below describes the transfer of radiation from each laser cavity to the other, where $\mathrm{K}'\ell$ is the coupling parameter (physically, $\mathrm{K}'\ell = 0$ indicates uncoupled lasers, $\mathrm{K}'\ell = \pi/4$ indicates 50:50 coupling, and $\mathrm{K}'\ell = \pi/2$ indicates complete cross-coupling):

$$\begin{bmatrix} A_1(\tau) \\ A_2(\tau) \end{bmatrix}_{\text{after coupling}} = \begin{bmatrix} \cos(\mathrm{K}'\ell) & i\sin(\mathrm{K}'\ell) \\ i\sin(\mathrm{K}'\ell) & \cos(\mathrm{K}'\ell) \end{bmatrix} \cdot \begin{bmatrix} A_1(\tau) \\ A_2(\tau) \end{bmatrix}_{\text{before coupling}} \tag{3.17}$$

Table 3.2: List of variables and parameters – with values used for simulations – in the delay differential equation model of two coupled mode-locked semiconductor lasers; see Equations (3.7) – (3.16).

Variable / Parameter	**Description**	**Value(s)**	**Reference**
τ	Temporal coordinate $\tau = \gamma_q(t - z/v)$	n/a	
γ_q $(1/\gamma_q)$	Saturable absorber carrier density relaxation time (note that this term is not explicitly present in the DDE model; instead, a typical, example value is provided here simply to give a sense for the physical time scale and to accordingly aid interpretation of the numerical simulation results; $t = \tau \cdot 1/\gamma_q$ for $z = 0$)	100 GHz (10 ps)	[82, 83]

Subscripts 1 and 2	Referring to lasers 1 and 2, respectively	n/a	
$A_{1,2}(\tau)$	Amplitude at the beginning of the roundtrip (complex-valued, normalized)	n/a	
$G_{1,2}(\tau)$	Saturable gain (real-valued, normalized)	n/a	
$Q_{1,2}(\tau)$	Saturable absorption (real-valued, normalized)	n/a	
$T_{1,2}$	Cold-cavity roundtrip times (normalized), i.e. $T_{1,2} = \gamma_q L_{1,2}/v$ (for nearly all of the simulation results, the two lasers have identical lengths / roundtrip times, i.e. $T_1 = T_2 = T$)	Unless otherwise specified, two different values are used: 1.875 (in SECTION 3.4 and SECTION 3.5) and 2 (in SECTION 3.6)	[77]
γ	Spectral filtering bandwidth/FWHM (normalized)	33.3	[77]
κ	Accounts for the total, linear, roundtrip loss/attenuation (in intensity) for each cold cavity	0.1	[77]
$\alpha_{g,q}$	Linewidth enhancement factors for the gain and absorber sections, respectively (the two lasers are assumed to have identical linewidth enhancement factors, i.e. $\alpha_{g1} = \alpha_{g2} = \alpha_g$ and $\alpha_{q1} = \alpha_{q2} = \alpha_q$)	0 (if left unspecified), otherwise two other sets of values are used: $\alpha_g = 3$ and $\alpha_q = 1$ or $\alpha_g = \alpha_q = 3$	
$\varphi_{1,2}$	$\varphi_{1,2} = \Omega T_{1,2}$, where Ω is the detuning between the filter's center and the nearest cold cavity axial mode/frequency	0	
$g_{0(1,2)}$	Unsaturated gain parameter for each laser (in all of the simulation results for this thesis work, the two lasers are identically pumped, i.e. $g_{01} = g_{02} = g_0$)	Varied from 0 to 9	
Γ	Ratio between gain/absorber relaxation rates	1.33×10^{-2}	[77]
q_0	Unsaturated absorption parameter (assumed to be the same for both lasers)	4 (unless otherwise specified)	
s	Ratio between gain/absorber sections' saturation intensities, i.e. $s = (g_q\Gamma_q)/(g_g\Gamma_g)$	25	[77]
$\mathrm{K}'\ell$	Coupling parameter $\mathrm{K}'\ell = \sqrt{\mathrm{K}'_{12}\mathrm{K}'_{21}} \cdot \ell$, where ℓ is the normalized length (i.e. multiplied by γ_q/v) of the passive section of the two cavities within which coupling occurs	Varied in the range 0 to 2π, but mainly from 0 to $\pi/2$	
K''	$\mathrm{K}'' = \sqrt{\mathrm{K}'_{21}/\mathrm{K}'_{12}}$, assumed to equal to unity (generally, $\mathrm{K}_{12} = \mathrm{K}^*_{21}$ due to symmetry in the coupling setup)	1	[93]

$\begin{bmatrix} A_{10}, & G_{10}, & Q_{10}, \\ A_{20}, & G_{20}, & Q_{20} \end{bmatrix}$	Initial "history"/state for the numerical integration (the DDE system is accompanied by a set of "initializations" for the variables, in this case as constant-valued, continuous functions defined from $\tau = -\max\{T_1, T_2\}$ to $\tau = 0$; these initial histories are analogous to initial conditions for an ODE system)	Unless otherwise specified, three main initialization sets are used in the simulations: $\begin{bmatrix} 0.6, & 2.5, & 0.1, \\ 0.6, & 2.5, & 0.1 \end{bmatrix}$ (referred to here as "in-phase history"), $\begin{bmatrix} 0.6, & 2.5, & 0.1, \\ i\,0.6, & 2.5, & 0.1 \end{bmatrix}$ (referred to here as "90° out-of-phase history"), and $\begin{bmatrix} 0, & 0, & 0, \\ 0, & 0, & 0 \end{bmatrix}$ (referred to here as "zero-state history" and used for the simulations with noise)	

This DDE system can be numerically integrated in order to investigate the temporal profiles and dynamics of the two coupled lasers. However, it needs to be further manipulated in order to facilitate stability and bifurcation analyses via numerical continuation methods. Specifically, the S^1 group symmetry corresponding to rotation of the complex-valued field amplitudes $A_{1,2}$ must be removed from the equations, so as to yield isolated equilibria of the system. Otherwise, the characteristic equation from the linearization would persistently contain a zero eigenvalue from the S^1 equivariance of the DDE system. This observation can be intuitively explained as a result of the fact that the set of equilibria for which the amplitudes differ only by rotation around the complex plane all simultaneously have the same stability; essentially, the DDE system sees no difference between these equilibria. The presence of the zero eigenvalue could then obfuscate the numerical determination of the stability and bifurcation scenarios, since the bifurcations themselves are identified by a change in stability (i.e. when an eigenvalue crosses zero as a parameter is varied) [94]. Specifically, if a zero eigenvalue is always present, then the stability is always left undetermined, and so this zero eigenvalue that results from the S^1 symmetry must be

removed by removing the symmetry. This type of issue is commonly encountered in the literature [57, 94, 95, 96, 97, 98, 99], including the studies that utilize the Lang-Kobayashi equations for continuous-wave lasers (see some of the aforementioned references) and the DDE model for mode-locked lasers [77]. As described in the references, the standard approach that is used to proceed is to insert into the DDEs the ansatz $A_{1,2}(\tau) = A_{r(1,2)}(\tau)e^{iA_{\phi(1,2)}(\tau)}$, where $A_{r(1,2)}(\tau)$ and $A_{\phi(1,2)}(\tau)$ are all real-valued quantities, and then separate the respective derivative terms in order to obtain a system of eight DDEs.

The starting point for linear stability and bifurcation analysis is to consider rotating-wave (CW) solutions of the system equations (note that non-CW solutions, e.g. mode-locked pulses, can be treated as time-dependent modulations of real-valued amplitudes $A_{r(1,2)}(\tau)$, and these can bifurcate from the "constant-amplitude" CW solutions, e.g. as periodic orbits). To do this, one sets $A_{\phi 1}(\tau) = \gamma\omega\tau$ and $A_{\phi 2}(\tau) = \gamma\omega\tau + \sigma$, where $\gamma\omega$ represents the (normalized) frequency of the rotation around the complex plane, and σ is a constant, time-independent phase difference. Furthermore, ω and σ are treated as "free" parameters, i.e. not as variables. The resultant system consists of six DDEs (two for $A_{r(1,2)}(\tau)$, two for $G_{1,2}(\tau)$, and two for $Q_{1,2}(\tau)$) and two algebraic, "constraint" equations (because $dA_{\phi(1,2)}/d\tau = \gamma\omega$). The rotational symmetry having been removed, this modified system now has isolated equilibria that are ready for numerical continuation and bifurcation analysis. The equations and derivations are provided in APPENDIX A.2. For the sake of clarity in the following sections, the phrase "the rotating-wave DDE model" is used to refer to this resultant system, whereas "the DDE model" is used to refer to the system earlier described by Equations (3.7) – (3.16).

3.3.3 Simplifying assumptions

Several model simplifications have been assumed in order to contain the model's complexity for the purpose of the present investigation. First, the traveling wave equations operate within the slowly-varying-envelope approximation for the electric field, which is reasonable for the time scale examined: picosecond-scale mode-locked pulses. Furthermore, the traveling wave equation model, as presented in Equations (3.3) and (3.4), does not account for multiple transverse spatial modes and field polarization (rather, it only focuses on the behavior in the axial spatial direction) [100, 101, 102], assumes no carrier diffusion [100] (instead, the carrier densities are assumed to be uniform and thus the rate equations take their average [101]), and neglects group velocity dispersion and the Kerr nonlinearity [84]. The carrier densities are modeled with a relatively simple set of rate equations in a phenomenological manner [72, 101]. Although it is feasible (albeit more complicated) to incorporate greater modeling complexity and precision to account for other aspects of the carrier dynamics (i.e. those corresponding to specific constructs, e.g. quantum-well vs. quantum-dot vs. bulk semiconductor media) in order to better compare numerical results with experiments, the simplicity of the model used here can still lend insights into the qualitative trends and underlying physics, and thus the simple carrier rate equations can be considered sufficient for the initial study in this thesis work.

Second, in order to incorporate the conventional coupled-mode theory into the traveling wave model, the coupling process is assumed to be lossless and well-phase-matched (again, valid under the slowly-varying-envelope approximation and the identicality of the two cavities' material parameters and waveguide structures). Third, a few assumptions are made in the subsequent derivation of the DDE equation model [82]: each laser is treated as unidirectional

cavity in order to avoid spatial effects (e.g. spatial hole-burning, self-interference), the spectral filter is given a Lorentzian lineshape that accounts for all frequency-dependent effects (e.g. gain bandwidth, mirror dispersion) into one lumped element, and all cold-cavity propagation losses are accounted for in a lumped manner at the boundary condition (i.e. along with the spectral filter). Finally, for all of the results in this chapter, each laser's spectral filter is assumed to be centered exactly on one of its cold-cavity resonant modes (i.e. $\Omega = 0 \rightarrow \varphi = \Omega T_{1,2} = 0$). This assumption is made for the sake of simplicity in the efforts to isolate and identify the effects on the dynamics that arise purely due to the coupling mechanisms.

3.3.4 Numerical methods

The study of this system calls for both time simulation and bifurcation analysis in order to explore the dynamical picture. The MATLAB function `dde23()` (see [103, 104] and APPENDIX B.2) is used for numerical integration of the DDE model and limited bifurcation analysis. DDE-BIFTOOL (see [105, 81] and APPENDIX B.3) is used for more extensive bifurcation analysis of the rotating-wave DDE model and numerical continuation of its equilibria, limit cycles, and bifurcations in the parameter space. The former tool provides versatility in terms of fewer constraints and simplifying assumptions on the model equations (e.g. avoidance of explicitly fixing the frequency ω and phase difference σ as parameters, which is a limitation of the rotating-wave DDE model), whereas the latter tool facilitates observation and computation of both stable and unstable equilibria and orbits (also often enabling exploration of a larger parameter space). The two approaches complement one another.

3.4 Coupling dynamics of two identical lasers

This study of the coupled system begins by considering the situation in which both laser cavities are fully identical. In terms of the parameters of the model equations, this means that the gain parameters $g_{01} = g_{02} = g_0$ and the roundtrip times $T_1 = T_2 = T$. An important consideration in the solution of any delay differential equation system is the initial history of the state variables. Much of the theoretical literature regarding coupled lasers modeled by delay differential equations lacks clear mention of the role of the initial history. This information is important, and its choice can influence the solution of the delay differential equations, along with the understanding of the dynamical picture, especially where regions of multistability exist. The effect of the initial history needs to be considered in exhaustive detail in a future study to acquire a comprehensive understanding of the coupled, mode-locked laser system. For now, the simulations in this section primarily use two sets of initializations. The first, referred to here as the "in-phase" history, uses the initialization $\begin{bmatrix} A_{10}, & G_{10}, & Q_{10}, \\ A_{20}, & G_{20}, & Q_{20} \end{bmatrix} = \begin{bmatrix} 0.6, & 2.5, & 0.1, \\ 0.6, & 2.5, & 0.1 \end{bmatrix}$, which represents two lasers that are in-phase and equal in amplitude (and equal in carrier densities) immediately prior to the "activation" of coupling. The second, referred to here as "90° out-of-phase" history, uses the initialization $\begin{bmatrix} A_{10}, & G_{10}, & Q_{10}, \\ A_{20}, & G_{20}, & Q_{20} \end{bmatrix} = \begin{bmatrix} 0.6, & 2.5, & 0.1, \\ i\,0.6, & 2.5, & 0.1 \end{bmatrix}$, which represents two lasers whose amplitudes are equal but have a phase difference of 90° prior to coupling. Alternatively, as done in SECTION 3.6, the inclusion of a stochastic source term can enable simulation of the system from an initialized state of low-amplitude, random noise to assist in better understanding the preferred (a)synchronized states and the robustness of the phenomena with regard to noise perturbations. Also, for the initial investigation and in order to isolate the dynamics that arise due to the coupling processes, the linewidth enhancement factors for the gain

and absorber sections of both laser cavities are set to zero (i.e. $\alpha_{g,q} = 0$), unless otherwise specified. Later, in SECTION 3.5, it is of interest to generalize the results to the more realistic scenarios of non-zero and possibly unequal α factors (i.e. $\alpha_g \neq 0 \neq \alpha_q$).

In this section of the thesis, the synchronization dynamics of the coupled lasers are the focus. However, first the frequency comb perspective is presented. Next, the ability of the lasers to synchronize is examined from the lasers' output temporal profiles across a range of parameter values. Specifically, it is seen that there is the possibly of a symmetry-breaking effect leading to delay-synchronized or anti-synchronous modulations of the pulse amplitudes; this is in spite of the fact that the two lasers are completely identical, and it occurs even when they are initialized identically with the in-phase history. Alternatively, it is also seen that the two lasers can evolve into perfect, in-phase synchronization, even when initialized non-identically (e.g. out of phase or with other differences in initial amplitudes). Finally, this section concludes with a close look at a special case of the anti-synchronous behavior of the lasers, a "subharmonic mode-locked" regime, which arises for fully cross-coupled lasers.

3.4.1 Coupling-induced frequency shift/detuning

As shown in Figure 3.5, the frequency spectrum for the single (or uncoupled) laser can exhibit one of several types of profiles, depending on the pump and unsaturated absorption parameters, including the following:

- A single dominant mode for continuous wave (CW) operation
- A "comb" of frequencies for mode-locked regimes of operation (spaced by the pulse repetition rate, which is an integer multiple of the reciprocal of the cavity roundtrip time)

- "Packets" of spectral peaks for Q-switched mode-locked operation (within each packet the peaks are spaced by the Q-switching frequency, while the spacing between the strong comb lines of adjacent packets is the reciprocal of the cavity roundtrip time)

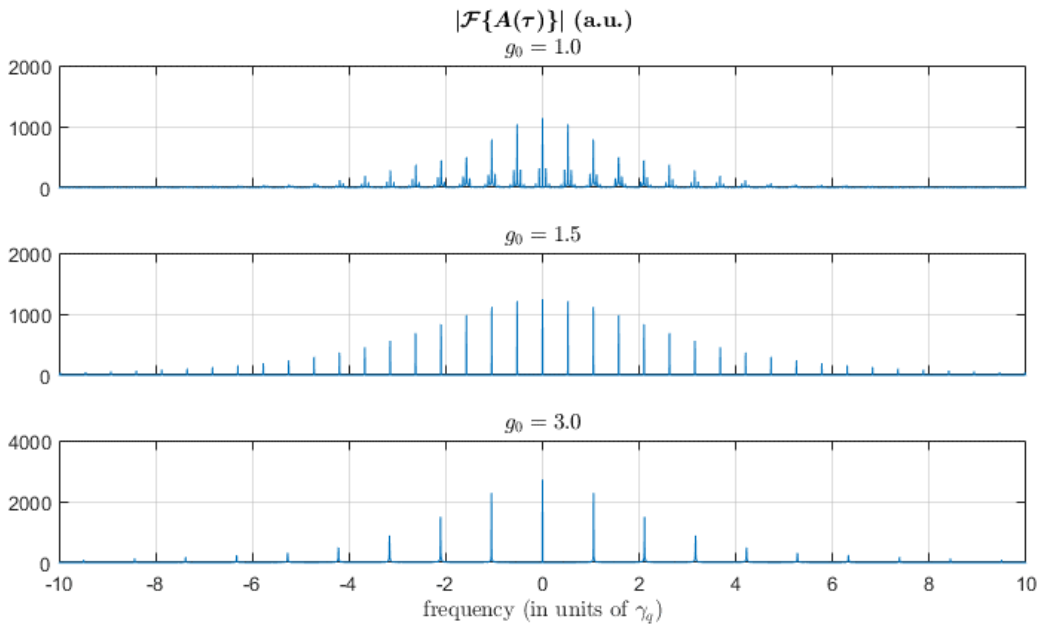

Figure 3.5: Frequency spectrum for a single (or uncoupled) laser for three different values of unsaturated gain, corresponding to Q-switched mode-locked, fundamental mode-locked, and 2nd harmonic mode-locked regimes. Table 3.2 lists the parameter values, and the initial history used for the numerical simulations is $[A, G, Q] = [0.6, 2.5, 0.1]$.

For the single laser, there are mechanisms that can cause the spectrum to shift horizontally and/or become asymmetric. The DDE model accounts for two such mechanisms. The first is the presence of amplitude-phase coupling (see Figure 3.6), via the linewidth enhancement α-factors for the gain and/or absorber sections, which causes a self-phase modulation due to the carrier densities' influence on the refractive index [85, 106]. The second is a result of the detuning Ω between the spectral filter peak and the nearest cold-cavity mode (results not shown here). Here, the laser may be forced to select frequencies that deviate slightly from the cold-cavity resonances, which satisfy the roundtrip phase constraint, in order to optimize for the attenuation due to the spectral filter.

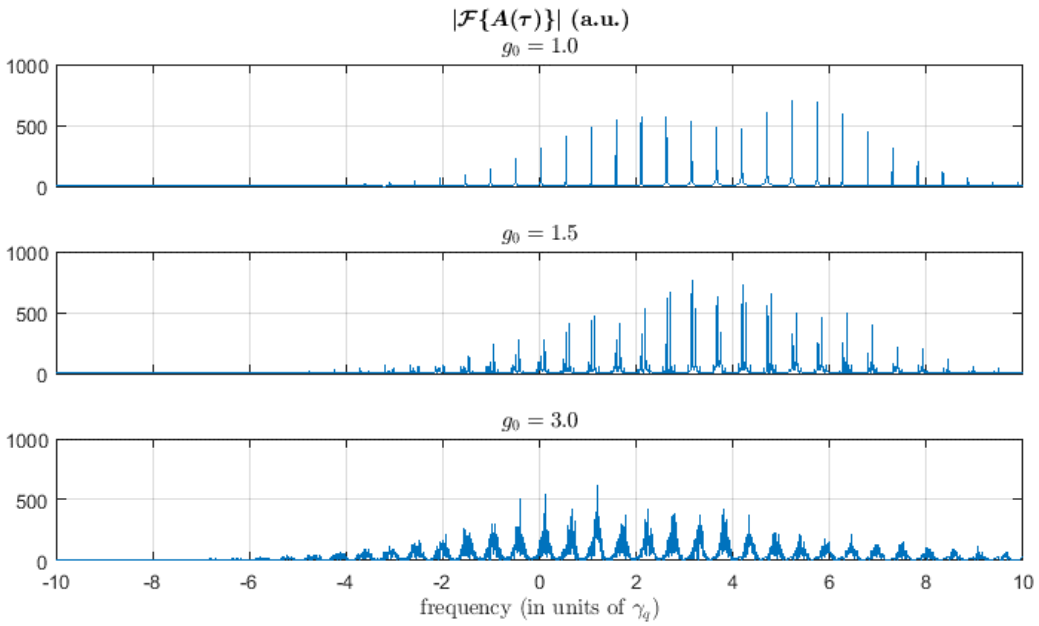

Figure 3.6: Same as Figure 3.5, except that linewidth enhancement factors are non-zero: $\alpha_G = 3$ and $\alpha_Q = 1$. The spectrum is shifted to the right, and the amplitude-phase coupling broadens and degrades the quality of the spectral peaks, increasingly with the pump level.

Figure 3.7, Figure 3.8, Figure 3.9, and Figure 3.10 show the spectra for two coupled, identical lasers for various coupling and unsaturated gain parameter values. In the absence of the two aforementioned frequency-pulling mechanisms (i.e. with $\alpha_{g,q} = 0$ and $\Omega = 0$) and even though the two lasers are identical in every respect, coupling induces a frequency shift relative to the solitary laser modes. This frequency shift increases (decreases) as the coupling parameter is increased from 0 to π (from π to 2π). The shift is small compared to the cavity's free spectral range (i.e. the reciprocal of the roundtrip cavity time, or the fundamental mode-locked frequency comb spacing), but it is on a similar scale as the Q-switching frequency, a result whose relevance resurfaces in the subsequent sections. In fact, the maximum shift, obtained when $K'\ell = \pi$, is one half of the cavity's free spectral range. Physically, the frequency shifts can be explained as a result of the extra roundtrip phase accumulation that each laser acquires from the coupling processes. This extra phase causes the solitary lasing modes to suffer higher loss, due to the

disruption of their 0 modulo 2π total roundtrip phase conditions. Consequently, the two coupled lasers each detune from their solitary modes to frequencies that meet a more optimal balance in minimizing the losses from both the roundtrip phase accumulation and the spectral filter.

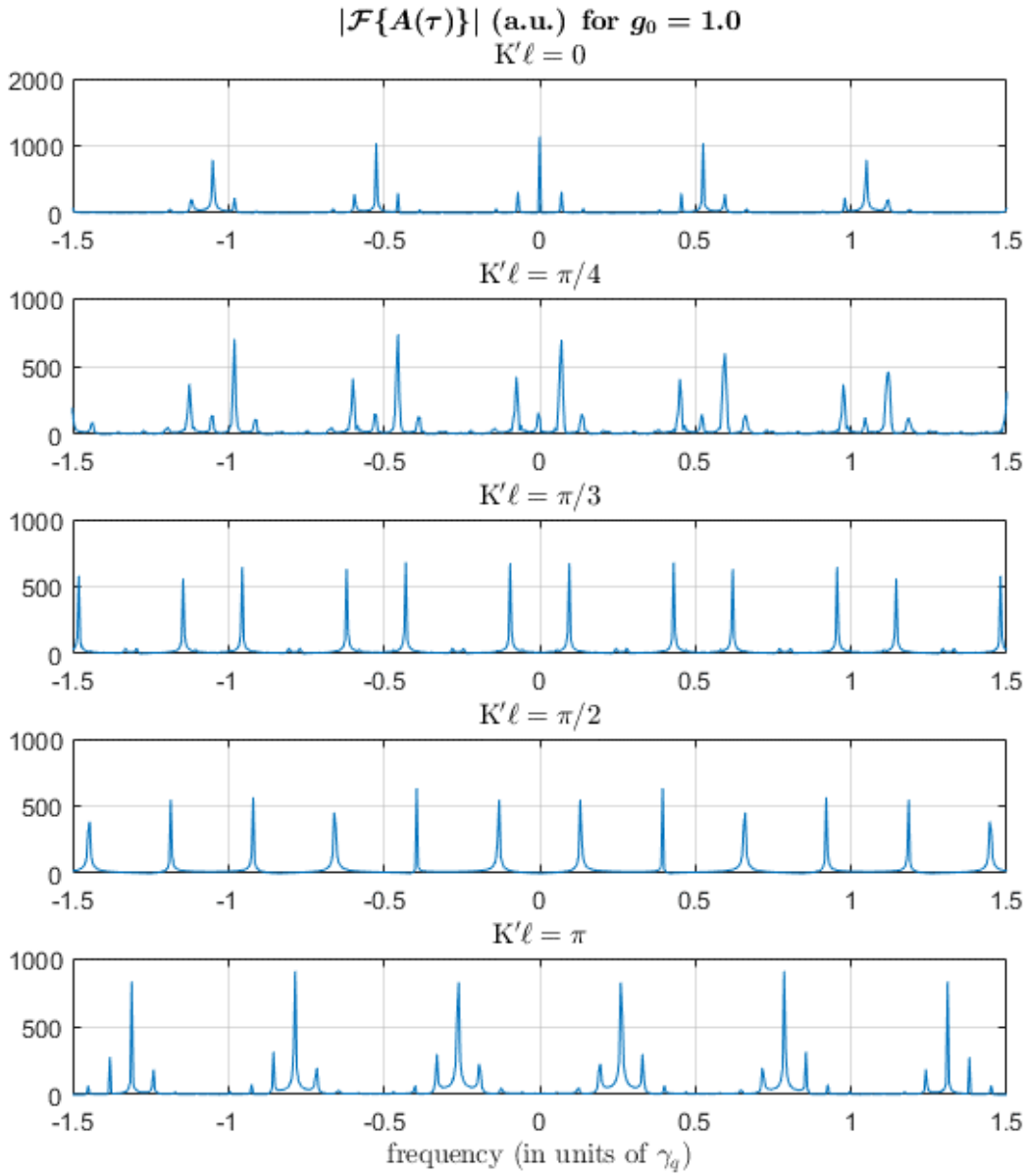

Figure 3.7: Frequency spectrum (in arbitrary units) for two coupled lasers at low pump levels for several values of the coupling parameter. The frequency detuning increases as coupling increases, and the magnitude of this shift is comparable to the Q-switching frequency (the fine spacing, between the spectral side-bands), while it is less than half of the cold-cavity free spectral range (the coarse spacing, $1/T = 1/1.875 \approx 0.53$, between the strong comb lines). For $K'\ell = \pi/2$, the two scales become degenerate; this corresponds to the subharmonic mode-locked regime (refer to SECTION 3.4.3). Table 3.2 lists the other parameter values, and here the in-phase initial history is used.

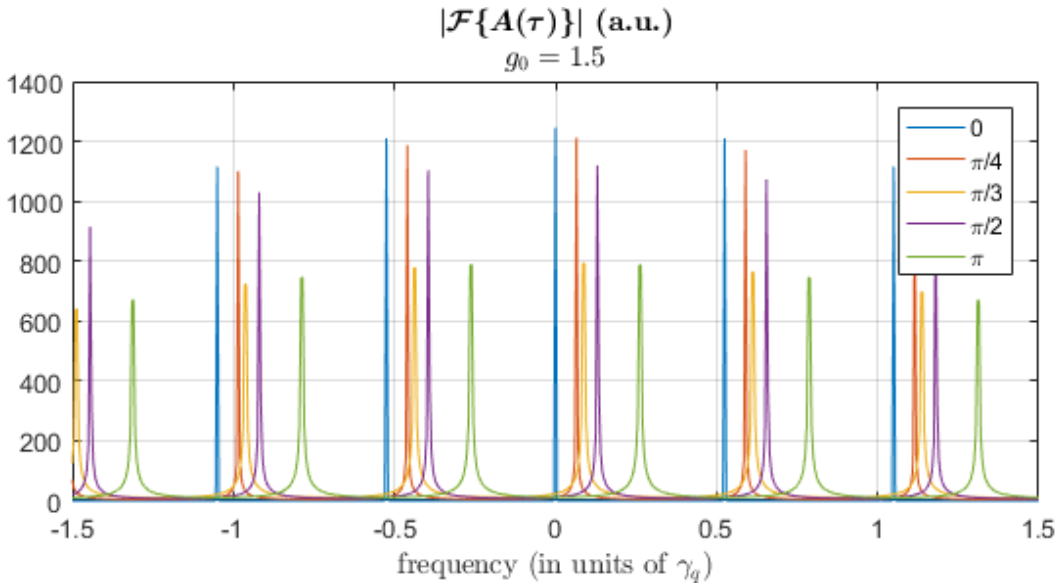

Figure 3.8: Frequency spectrum (in arbitrary units) for two coupled lasers at moderate pump levels for several values of the coupling parameter (denoted by the color code for the traces). The entire frequency comb is increasingly shifted as the coupling parameter value increases, and the magnitude of the shift is less than half of the cold-cavity free spectral range, which is $1/T = 1/1.875 \approx 0.53$. Table 3.2 lists the other parameter values, and here the numerical simulations are initialized with the in-phase initial history.

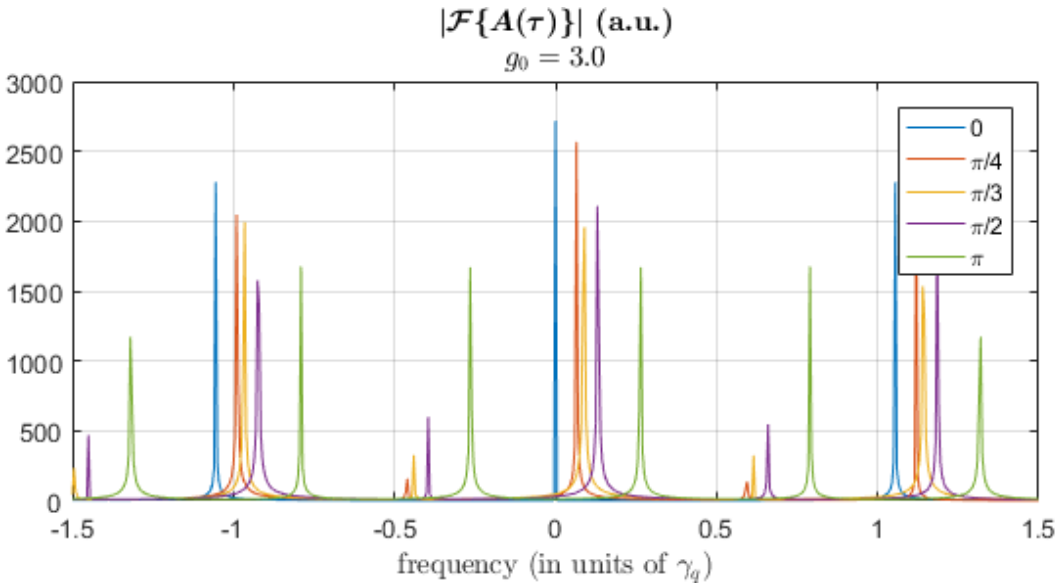

Figure 3.9: Same as Figure 3.8, except that the unsaturated gain is higher; here it corresponds to the 2nd harmonic mode-locked regime, in which the pulse repetition time is twice the roundtrip time, as evidenced by the fact that the comb lines are spaced twice as far apart as in Figure 3.8 (except for when $K'\ell = \pi$). Note again that the entire frequency comb is shifted by increasing amounts as the coupling parameter value increases. Table 3.2 lists the other parameter values, and here the numerical simulations are initialized with the in-phase initial history.

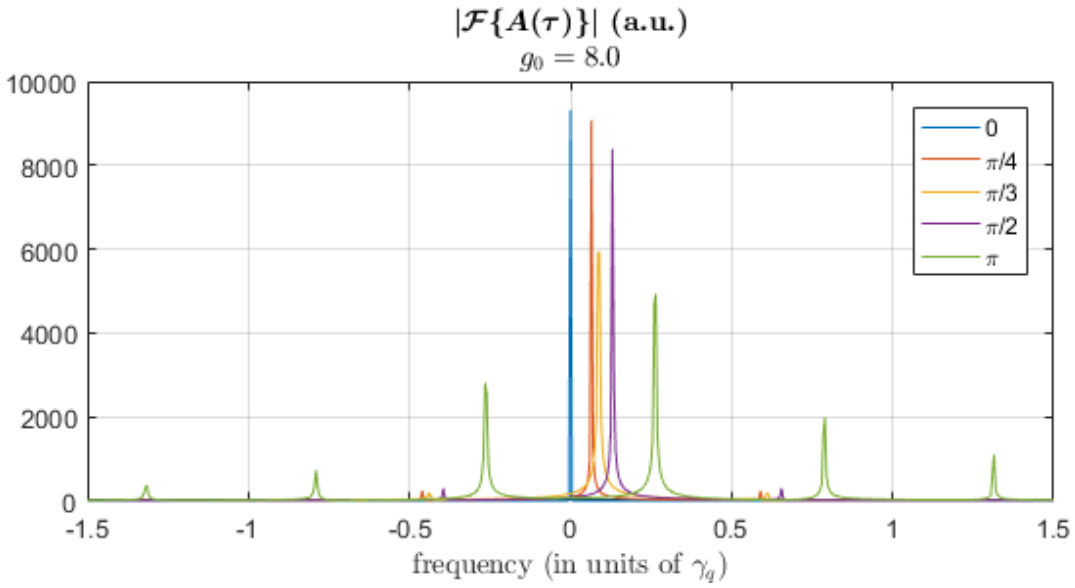

Figure 3.10: Same as Figure 3.8, except that now the two coupled lasers are at very high pump levels. Note that for most values of coupling, there is clearly a single dominant lasing mode, whose frequency is increasingly detuned from the center as coupling increases. For $\mathrm{K}'\ell = \pi$, the behavior is slightly different: several lasing modes are still excited. Table 3.2 lists the other parameter values, and here the in-phase initial history is used.

The same frequency shifts can be computed directly from the equations that arise when solving for the equilibria of the rotating-wave DDE model. For example, as derived in APPENDIX A.2.2, the occurrence of in-phase and frequency-locked CW solutions requires that the set of transcendental equations below are satisfied. Specifically, the second and third equations place constraints relating the parameters ω, γ, T, and $\mathrm{K}'\ell$, and they can be used to determine viable values for ω for a given parameter set. Recall that $\gamma\omega$ is the frequency of the CW solution (detuned from one of the cold-cavity modes of the solitary lasers).

$$1 + \omega^2 = \kappa e^{G^\circ - Q^\circ}$$

$$\cos(\gamma\omega T - \mathrm{K}'\ell) > 0$$

$$\omega + \tan(\gamma\omega T - \mathrm{K}'\ell) = 0$$

$$0 = g_0 - \Gamma G^\circ - e^{-Q^\circ}\left(e^{G^\circ} - 1\right)(A_r^\circ)^2$$

$$0 = q_0 - Q^\circ - s\left(1 - e^{-Q^\circ}\right)(A_r^\circ)^2$$

When coupling is off (i.e. $K'\ell = 0$), then $\omega = 0$ is the smallest frequency detuning to satisfy the equations, and it corresponds to a mode residing at the same location as the spectral filter's center frequency, i.e. at one of the cold-cavity modes (given that $\varphi = 0$). Although there are an infinite number of solutions for ω, the CW mode with minimal absolute detuning from the spectral filter, say ω_{min}, suffers the least loss and is the first (and only one) to bifurcate from the off-state once the threshold gain for lasing is reached [77]. However, as the coupling parameter is increased from 0 to π, this minimal solution ω_{min} increases. Accordingly, the frequency detuning occurs for the CW mode as well as for the centers of the frequency combs of the mode-locked and Q-switched mode-locked pulse waveforms, since the latter two waveforms emerge as periodic orbits that bifurcate from the CW solution.

3.4.2 Coupling-induced symmetry-breaking

With the initial histories of the lasers' state variables chosen to be fully identical (i.e. using the in-phase history), an interesting symmetry-breaking phenomenon is observed for small values of unsaturated gain when the two lasers are coupled. Here, the lasers' pulse trains undergo fluctuations in the peak heights, as shown in Figure 3.11, which contains plots of the steady-state temporal power for various values of coupling. Note that the solitary/uncoupled laser (the top subplot: $K'\ell = 0$) operates in the Q-switched mode-locked regime. For intermediate coupling values (the middle three subplots: $K'\ell = \pi/6$, $\pi/4$, and $\pi/3$), the fluctuations of the pulse amplitude heights/peaks differ between the two lasers. The fully cross-coupled system (the bottom subplot: $K'\ell = \pi/2$) presents an extreme case of broken symmetry, with perfectly anti-synchronous pulsing, for which the pulse spacing for each laser is double the roundtrip time (i.e. the repetition rate is a subharmonic of the fundamental mode-locked rate); this regime is

discussed in further detail in SECTION 3.4.3. Given that the two lasers are completely identical and also identically initialized, the observed symmetry-breaking and destabilization of the perfectly synchronized initial state can be attributed to the passive coupling. As the coupling parameter $K'\ell$ increases from 0 to $\pi/2$, the transition from the synchronized, Q-switched mode-locked state to the symmetry-broken behavior occurs more quickly (see Figure 3.12). An examination of the real/imaginary parts of the complex amplitudes indicates that the symmetry-broken state corresponds to the two lasers acquiring a 90° phase difference relative to each other (see Figure 3.13 and Figure 3.14). On the other hand, when the lasers are initialized 90° out-of-phase (instead of being initialized in-phase), the transition occurs immediately (see Figure 3.15).

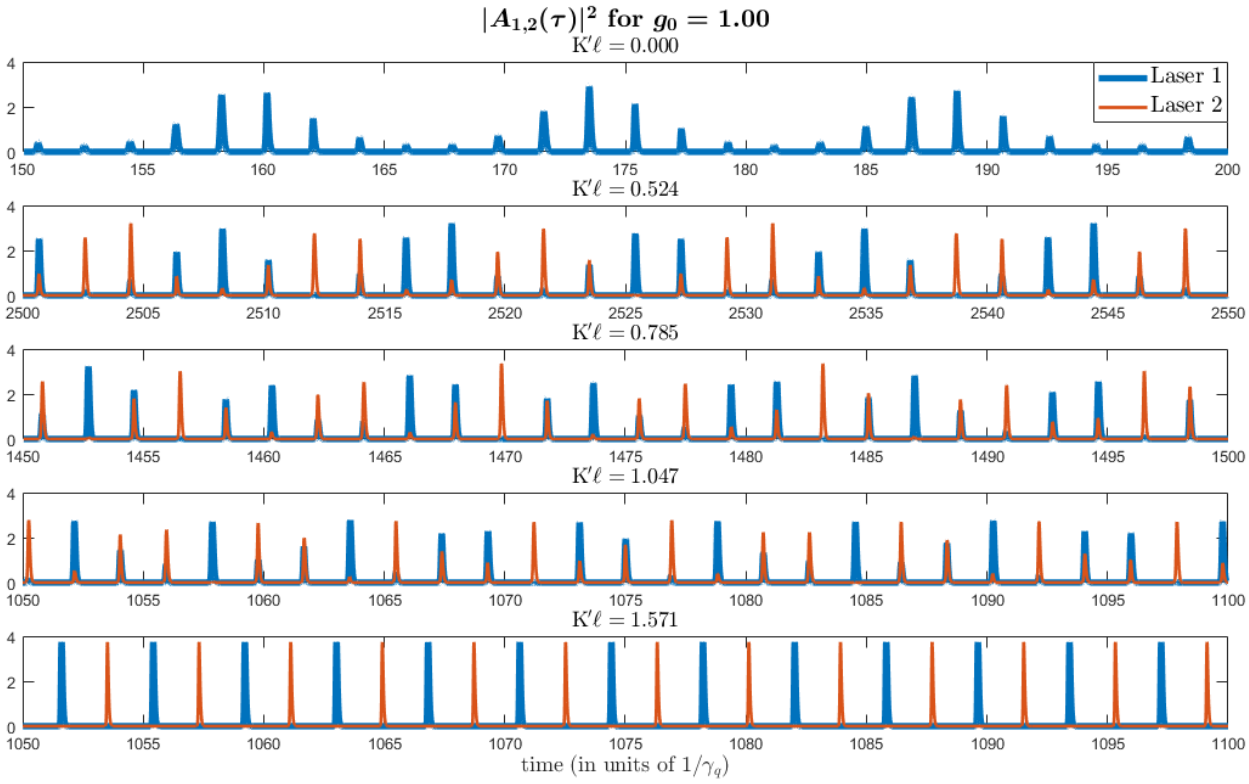

Figure 3.11: Output power temporal profile for two weakly-pumped lasers as coupling is varied. Note the symmetry-breaking in the presence of coupling: the fluctuations of the peak heights for Laser 1 differ from those of Laser 2. In an extreme case, fully cross-coupled lasers ($K'\ell = \pi/2 \approx 1.571$) exhibit perfectly anti-synchronous, mode-locked pulse trains. These behaviors are observed even in spite of the fact that this simulation is initialized with the in-phase history and that the lasers are completely identical in all other respects. Table 3.2 lists the other parameter values.

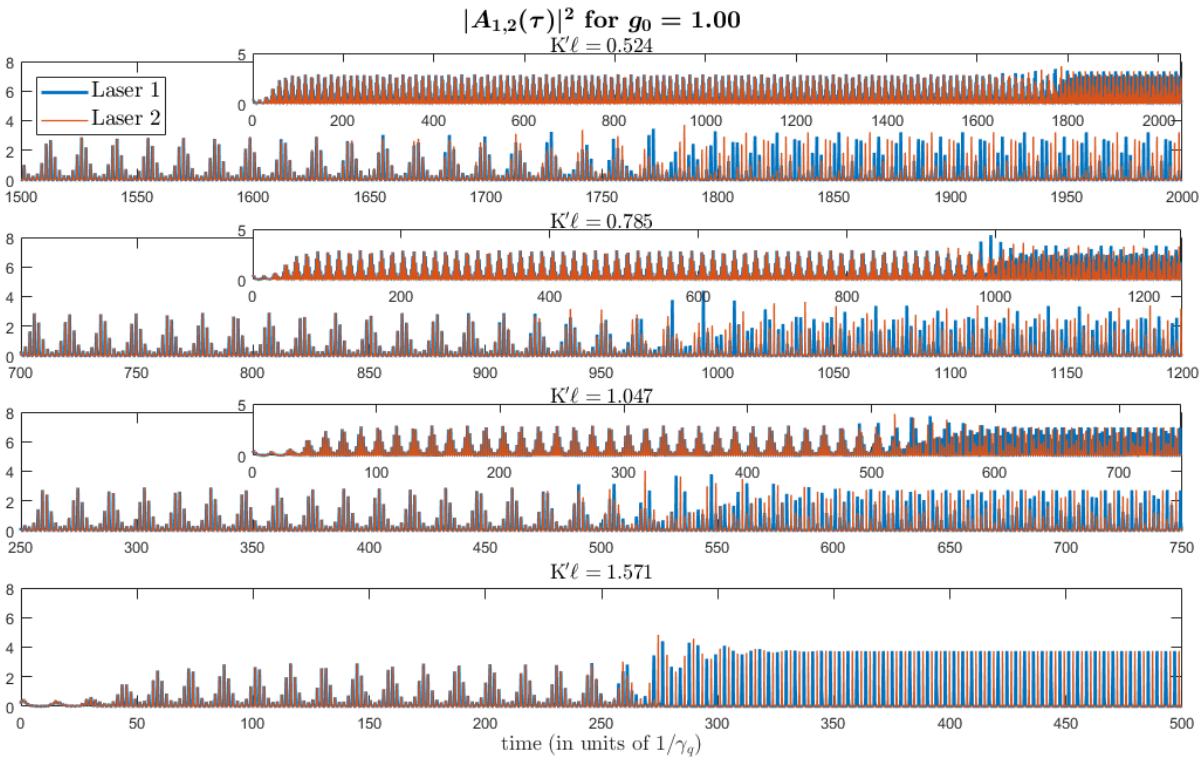

Figure 3.12: Output power for two weakly-pumped lasers as coupling is varied. The results are from the same simulations as in Figure 3.11. The transition to the symmetry-broken state occurs sooner with increased coupling. Note: the horizontal time scales of the subplots (and insets) are different.

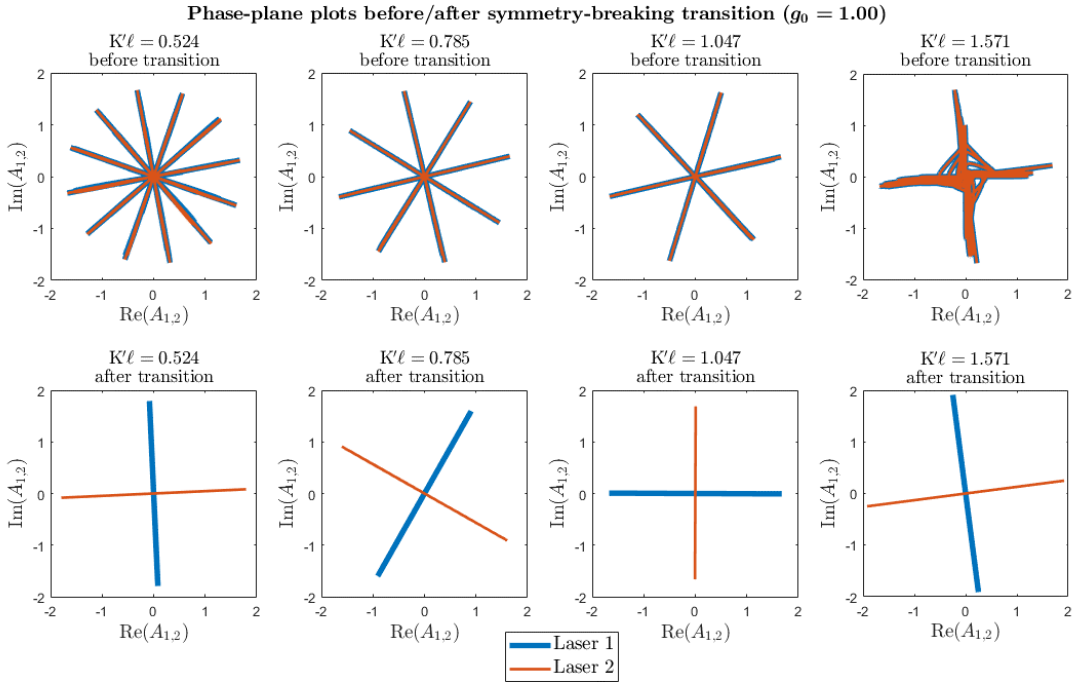

Figure 3.13: Phase-plane plots of complex amplitudes for the two lasers, showing that the lasers are in-phase before and 90° out-of-phase after the transition points observed in Figure 3.12.

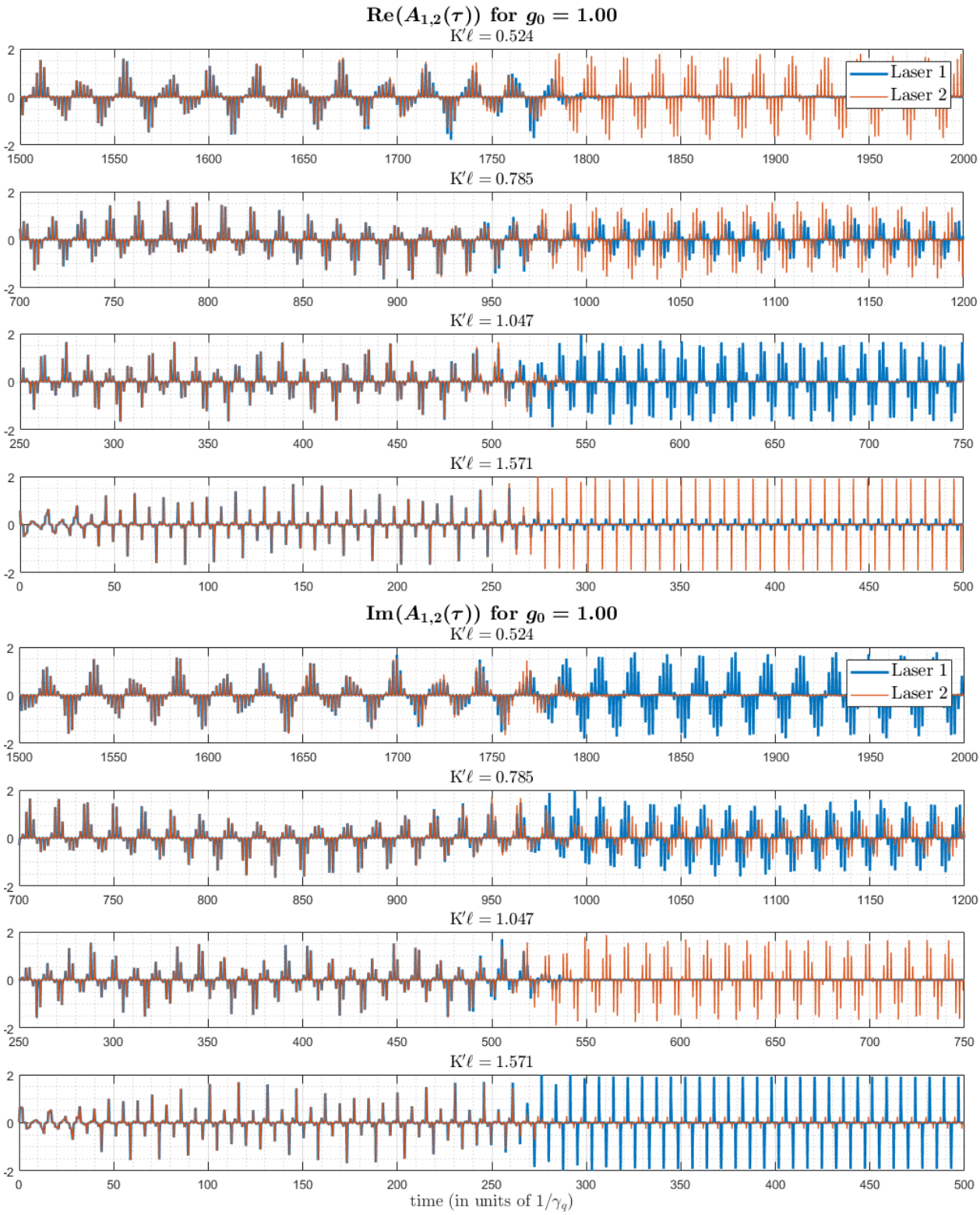

Figure 3.14: Temporal profiles of the real and imaginary parts of the lasers' complex amplitudes. The results are from the same simulations as in Figure 3.12. The transition points at which the two lasers' amplitudes switch from in-phase to 90° out-of-phase align with the transitions in Figure 3.12.

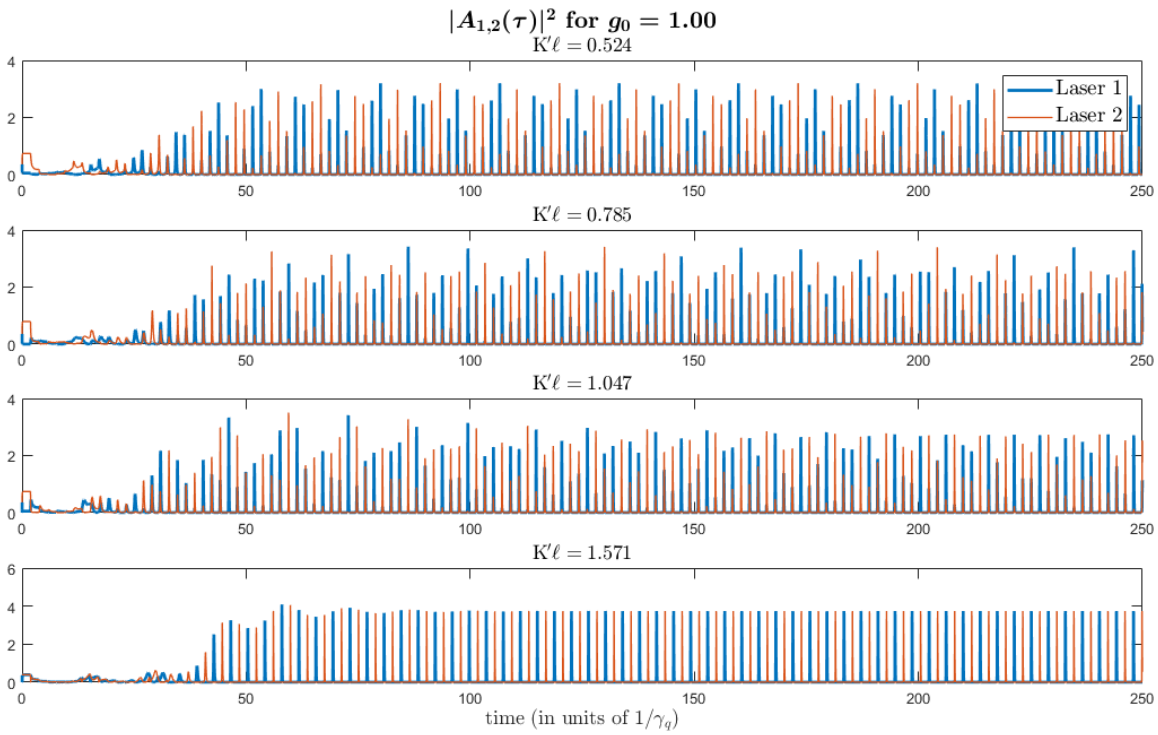

Figure 3.15: Same as Figure 3.12, except that the simulations are initialized with the 90° out-of-phase history. Here, the two lasers are immediately away from the in-phase, synchronized state. Examination of the real/imaginary parts of the complex amplitudes show that the two lasers' amplitudes maintain the 90° phase difference between each other (the results are not shown here).

A careful inspection of the symmetry-broken states, such as in Figure 3.12 and Figure 3.15, reveals that the two lasers' output power time series are in fact delay-synchronized by large multiples of the cavity roundtrip time. For example, Figure 3.16 shows that if one of the lasers' time series is shifted by roughly 7 times roundtrip delay, then it aligns nearly perfectly with the time series of the other laser (these time series considered here are from the same simulations as in Figure 3.12 for $\mathrm{K}'\ell = \pi/6 \approx 0.524$ and for $\mathrm{K}'\ell = \pi/3 \approx 1.047$). For each coupling value, this delay is numerically determined by identifying the delay time associated with the maximum peak in the cross-correlation profile of the two lasers' time series of complex-amplitudes. It is not entirely clear from a physical perspective why the "best" delay is 7 roundtrips in these two cases, but a more detailed investigation into this aspect is relegated for the future. Nevertheless, the delayed-synchronization behavior of this symmetry-broken state is interesting and important.

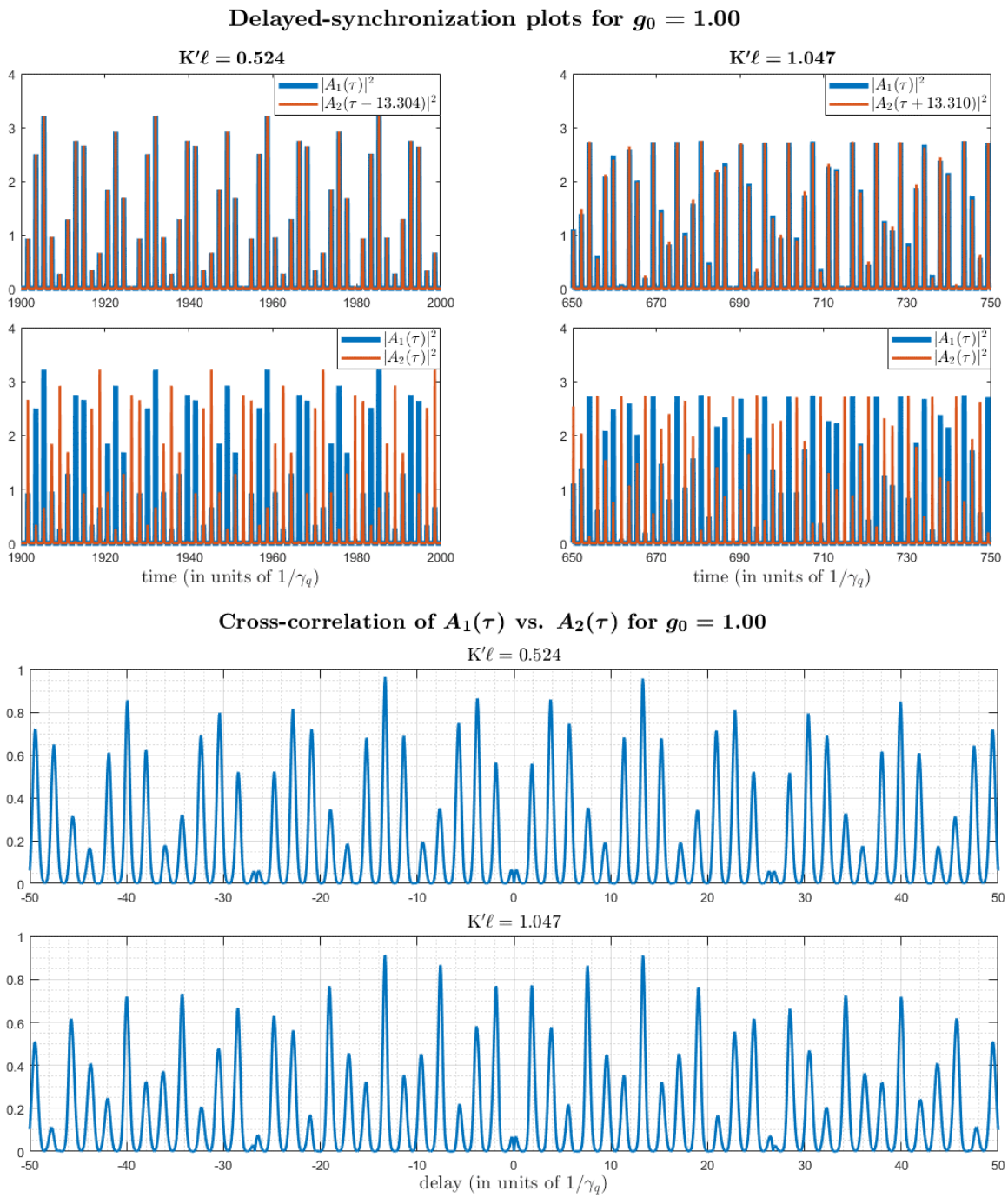

Figure 3.16: Plots showing delayed synchronization between the two lasers (for different coupling values) after the transition point where symmetry-breaking occurs. The results are from the same simulations as in Figure 3.12, and they indicate that, in the symmetry-broken state, the two lasers are delay-synchronized, in this case by roughly 7 times the cavity roundtrip delay. The middle two subplots are directly from Figure 3.12 (zoomed-in on the time axis), whereas in each of the top two subplots the time series of Laser 2 is shifted by the delay time at which the maximum peak in the corresponding cross-correlation profile occurs (shown in the bottom two subplots). The cross-correlation computations are performed on the lasers' complex-valued amplitudes. Also, note in those plots the nulls at zero delay, showing a clear absence of perfect, zero-delay synchronization

In contrast, for moderate/high pump levels (at which the solitary laser operates in the mode-locked/CW regimes), coupling-induced symmetry-breaking is absent when the initialization choice is the in-phase history, and a transition to in-phase synchronization can be seen even with non-identical initial histories (i.e. for which the lasers' amplitudes initially start with differences in magnitude and/or phase). This suggests that perfect synchronization can be achieved and/or preserved in the presence of coupling, under the right conditions. Specifically, there are initializations from which two coupled lasers can evolve to operate in an in-phase, synchronized manner, within the mode-locked/CW regimes similar to those of the solitary/uncoupled laser. At the same time, for other initial states, the coupled lasers can also behave in a 90°-out-of-phase, desynchronized manner coinciding with significant fluctuations in each laser's pulse heights.

To illustrate, consider an example case in which the coupling parameter value $\mathrm{K}'\ell = \pi/4$, corresponding to 50:50 coupling. Figure 3.17 and Figure 3.18 each compare the output temporal power from simulations using the in-phase vs. 90° out-of-phase histories, whereas Figure 3.19 presents examples of in-phase synchronization occurring even when the lasers are not initialized in-phase. In Figure 3.17 and Figure 3.19, the gain parameter $g_0 = 2$ (at which the solitary laser operates in the fundamental mode-locked regime). Note in Figure 3.17 the deteriorated pulse quality of each laser for the 90° out-of-phase initialization, along with the varying peak heights. In Figure 3.18, the unsaturated gain is $g_0 = 6$ (at which the solitary laser operates in the CW regime); interestingly here, coupling can induce large temporal power fluctuations in steady-state (e.g. see the results shown in the bottom-left subplot the figure, i.e. with the 90° out-of-phase initialization) for which the lasers appear to be delay-synchronized (compare the blue trace starting at time $\tau \approx 90$ to the red trace at $\tau \approx 94$ in the bottom-left subplot's inset).

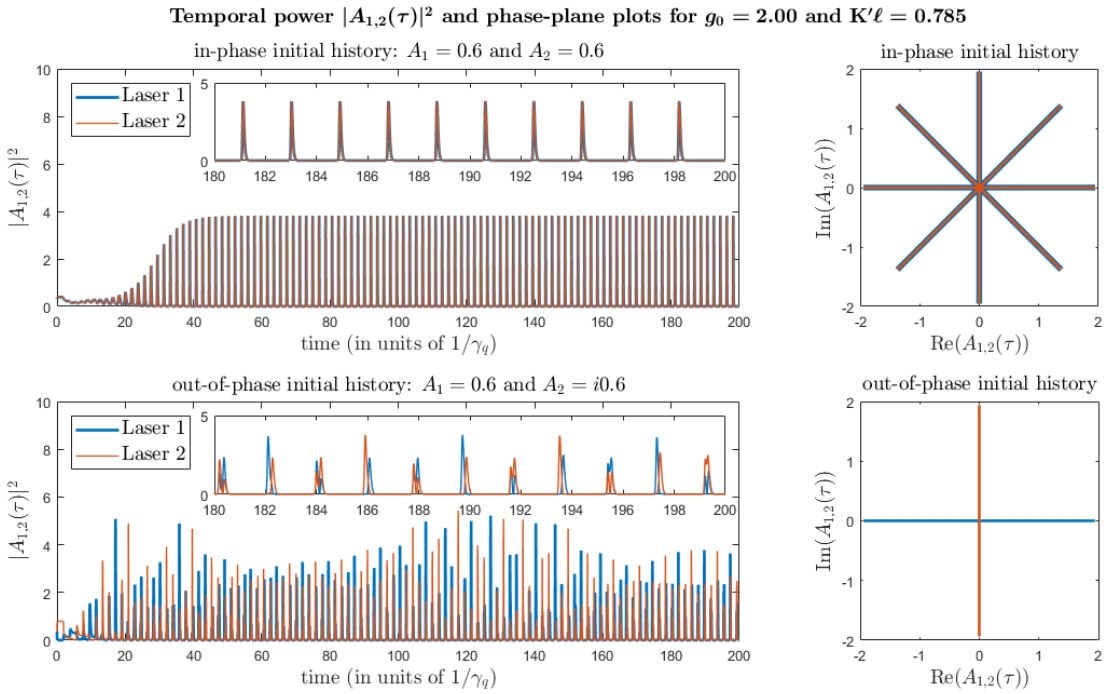

Figure 3.17: Output temporal power and phase-plane plots for two 50:50-coupled lasers with moderate pump value $g_0 = 2$ (at which the solitary laser is in the fundamental mode-locked regime). For the in-phase history, the two lasers are synchronized. For the 90° out-of-phase history, they are not, and in fact there is some deterioration of the pulse quality. Table 3.2 lists the other parameter values.

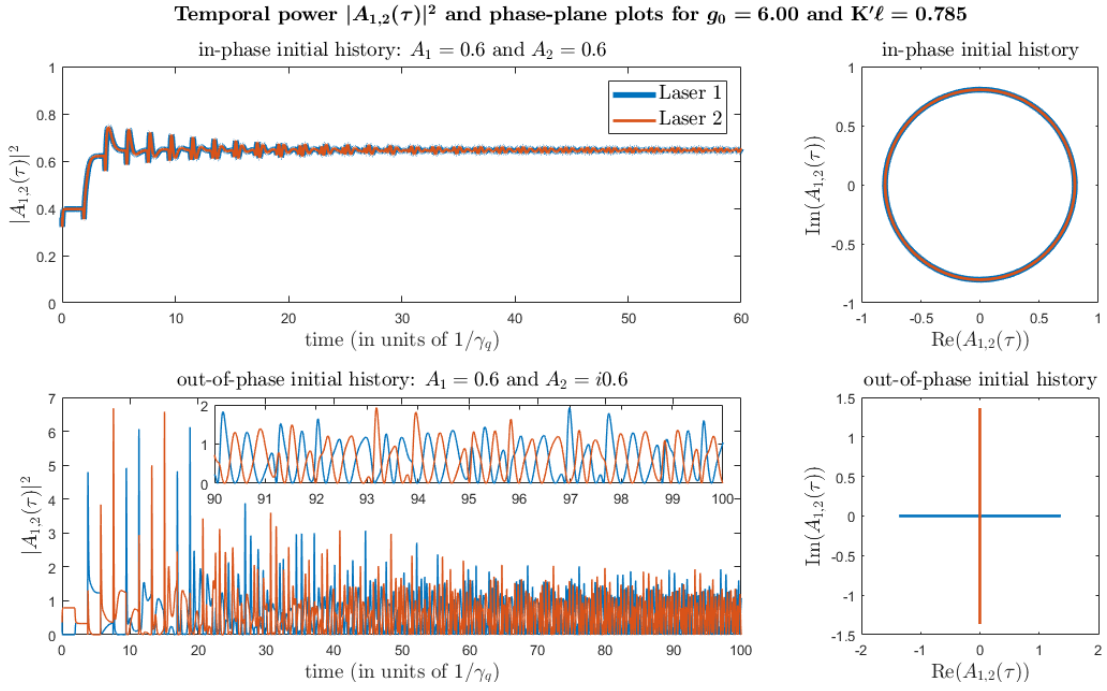

Figure 3.18: Same as Figure 3.17, except for high gain $g_0 = 6$ (at which the solitary laser is CW). Note the top-right subplot indicates a sinusoidal oscillation of the real/imaginary parts of the complex amplitude, consistent with the coupling-induced detuning of the CW mode shown in Figure 3.10.

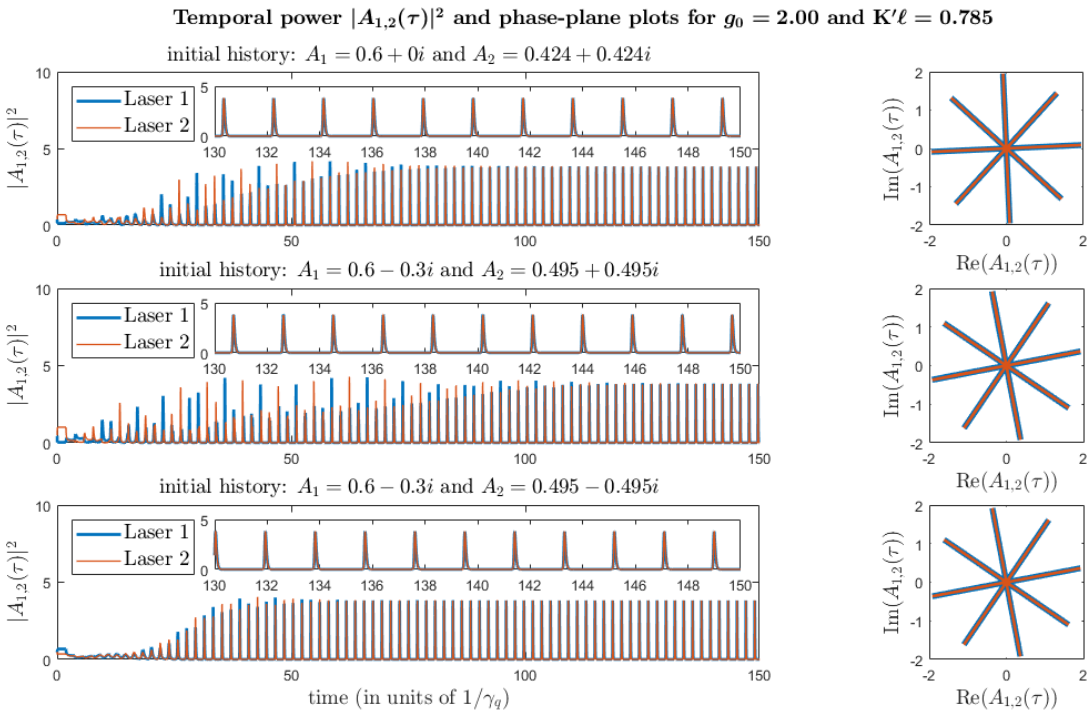

Figure 3.19: Similar to Figure 3.17, except for different initializations. The results evidence synchronization.

Further insight is gained from the bifurcation diagram with respect to the unsaturated gain g_0 (here considered as the sweep parameter) in Figure 3.20, showing branches of perfectly-synchronized, regular, mode-locked states (see the bottom subplot), as well as their bistability with regimes of complex modulations of the pulse heights (see the top subplot). This bifurcation diagram is generated by performing up- and down-sweeps of the gain parameter g_0. For each value of g_0 (i.e. each iteration), the numerical simulation is run with all other parameters fixed, and the local maxima/minima of the temporal power are extracted and then plotted. For the first iteration ($g_0 = 0.05$), the in-phase initial history is used, and the lasers are simulated to steady state. Each subsequent iteration runs a simulation, initialized/"seeded" by the previous iteration's solution / temporal profile, for a time span of ~ 100 roundtrips and finds the local extrema from the final ~ 50 roundtrips. This approach is somewhat analogous to an experiment

in which the pump current / unsaturated gain is incremented (decremented) slowly at regular time intervals in order to observe the different dynamical regimes.

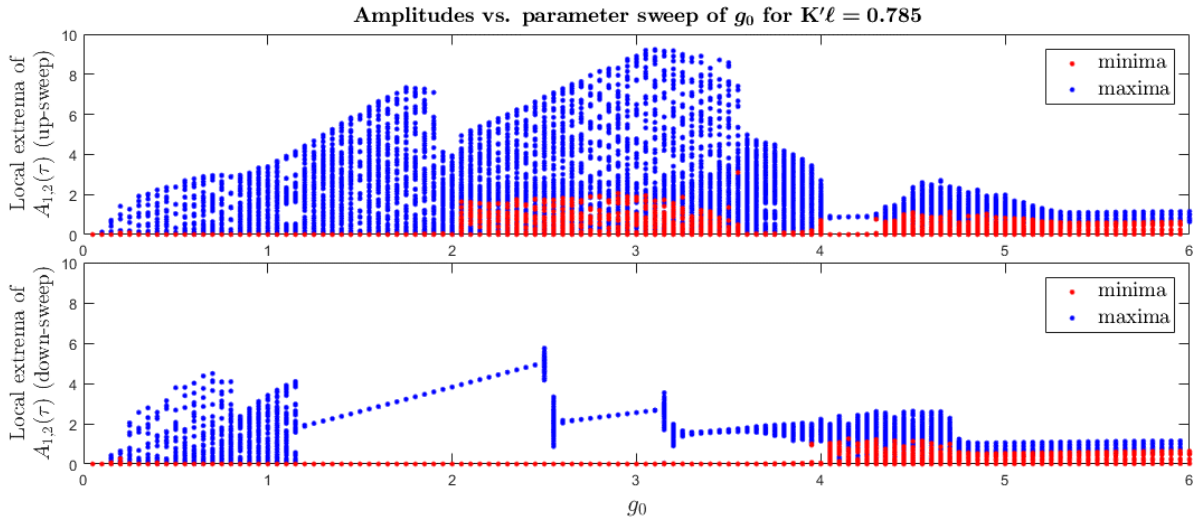

Figure 3.20: Bifurcation diagram with respect to the pump parameter g_0 for the case of 50:50-coupling. The plotted points are local maxima/minima extracted from the simulations for each value of g_0 (i.e. each iteration). Regular, "clean" mode-locked pulse train with no pulse height variations yield "straight-line" sections in the bifurcation plot. Fluctuations/modulations of the pulse heights yield a wide spread of the local extrema. Table 3.2 lists the other parameter values.

3.4.3 Subharmonic mode-locked regime with anti-synchronous pulsing

As described in the preceding section, the dynamical behavior and synchronization properties can be strongly affected by the presence of coupling. A particularly interesting scenario of symmetry-breaking occurs near $\mathrm{K}'\ell = \pi/2$, leading the lasers to perfect anti-synchrony for somewhat small pump levels. As the coupling nears $\mathrm{K}'\ell = \pi/2$, a "subharmonic mode-locked" regime emerges, as indicated by the bifurcation diagrams in Figure 3.21 and Figure 3.22. In this regime, the two lasers generate perfectly anti-synchronous pulse trains (without any modulation of the pulse amplitudes due to the Q-switching instabilities), each with a repetition rate of $1/(T_1 + T_2)$ (see Figure 3.23). For identical lasers ($T_1 = T_2$), this repetition rate is half of the fundamental mode-locked rate (i.e. it is a subharmonic), as previously presented in the bottom subplot of Figure 3.11 (time domain) and the fourth subplot of Figure 3.7 (frequency domain).

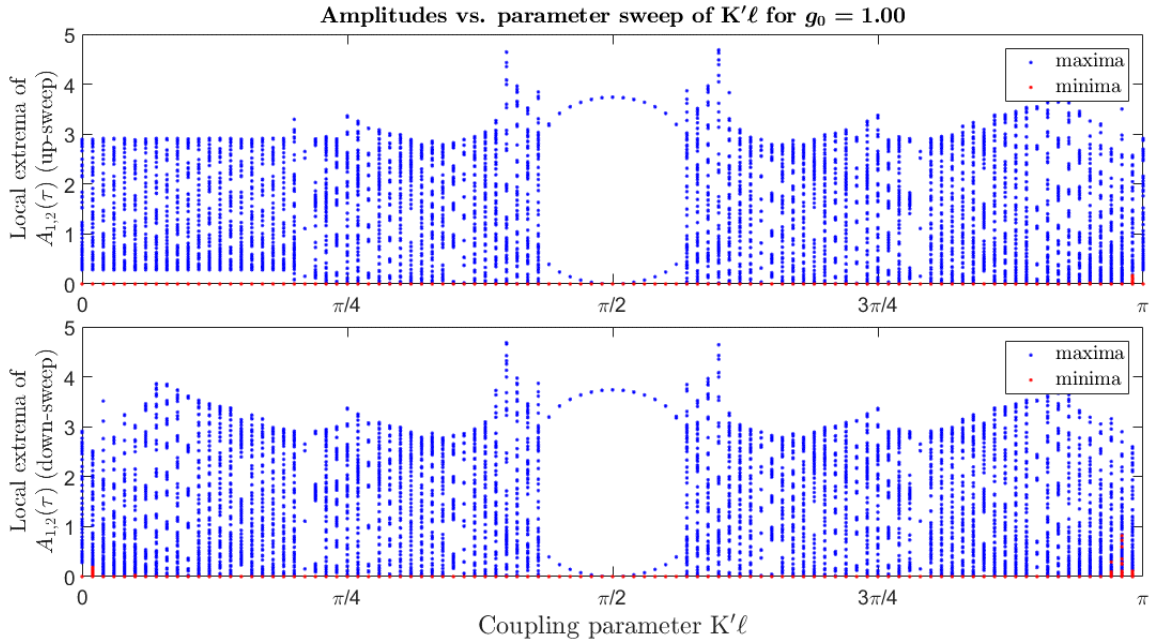

Figure 3.21: Bifurcation diagram, with respect to coupling K′ℓ as the sweep parameter, for two weakly-pumped lasers. Note the emergence of the 90° out-of-phase, anti-synchronous, subharmonic mode-locked regime for values of coupling near $\pi/2$. Outside of the interval, the two lasers undergo significant fluctuations in the pulse peak heights, similar to the behavior presented in SECTION 3.4.2. Table 3.2 lists the other parameter values.

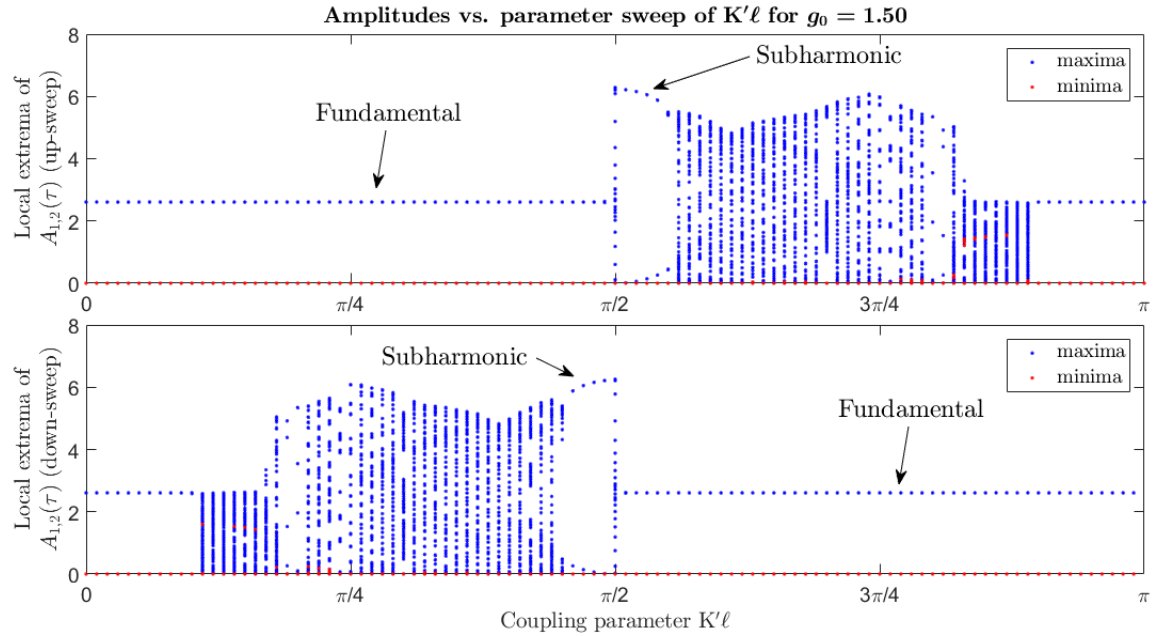

Figure 3.22: Same as Figure 3.21, except at slightly higher gain, $g_0 = 1.5$. Again, the subharmonic mode-locked regime appears for coupling values near $\pi/2$. However, at this pump level there is a bistability with the in-phase, synchronized, fundamental mode-locked regime, for both the region where the subharmonic exists and the region where the two lasers pulse trains irregularly fluctuate and are 90° out-of-phase (this corroborates the indications in SECTION 3.4.2).

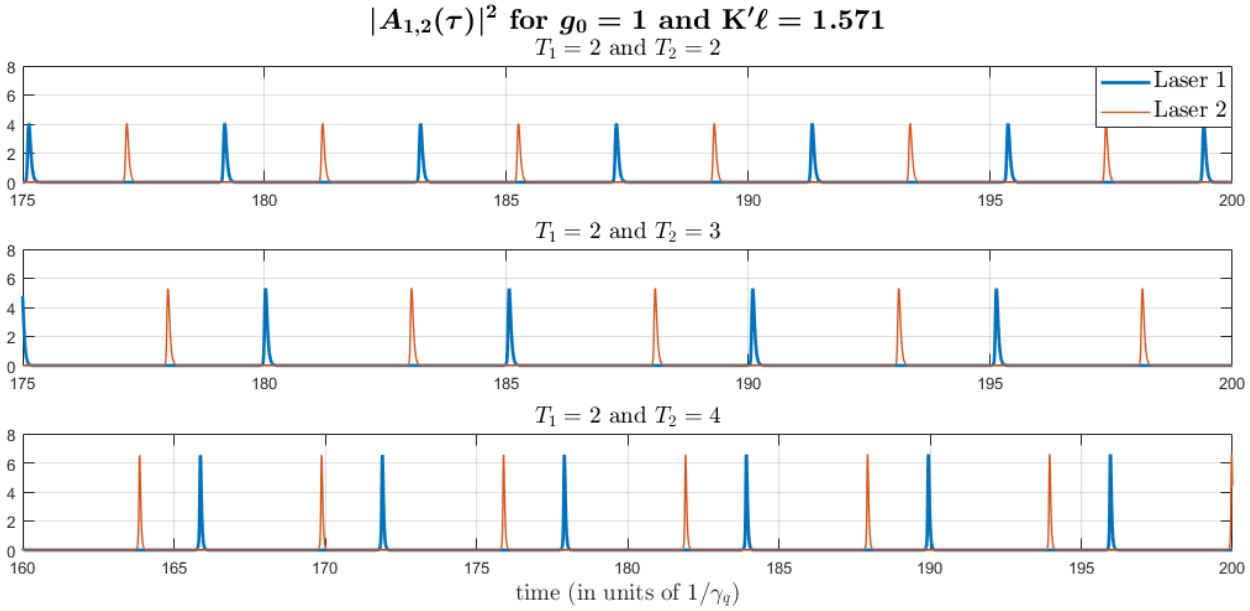

Figure 3.23: Temporal profile of output power of two fully cross-coupled, weakly-pumped lasers for varying roundtrip times. Note that the subharmonic repetition rate for each laser is $1/(T_1 + T_2)$ and that the lasers alternately generate pulses. The simulations are initialized with the 90° degree out-of-phase history. Table 3.2 lists the other parameter values.

The bifurcation diagram in Figure 3.24 assists in understanding the stability of the subharmonic mode-locking behavior, as well as the parameter space within which it occurs. A few important aspects of the phenomena and dynamics can be discerned. First, by comparing the top subplot to the bottom subplot, the transition away from Q-switched mode-locked operation is achieved at smaller pump levels for the two cross-coupled lasers (around $g_0 = 0.9$) as compared to the uncoupled lasers (around $g_0 = 1.2$). Thus, cross-coupling appears to mitigate the Q-switching instability to some degree. Second, the cross-coupled lasers allow a region of bistability between the subharmonic and fundamental mode-locking regimes. For the same values of unsaturated gain within this region, there are two possible output behaviors for the two lasers: in-phase, synchronized pulsations at the fundamental rate or 90° out-of-phase, anti-synchronized outputs with each laser pulsing at half the fundamental rate and with twice or more the peak pulse power. In addition, the bifurcation diagram reveals a few other mode-locked regimes of the cross-

coupled lasers that are not seen in the solitary lasers: 90° out-of-phase, anti-synchronous pulsations at 1.5 and 2.5 times that fundamental mode-locked repetition rate. Interestingly, in all of the observations of this thesis work, the integer harmonic mode-locked regimes (labeled as F, 2H, and 3H in the bottom subplot of Figure 3.24) all coincide with in-phase synchronization between the two lasers, while the "half harmonics" (labeled as SH, 1.5H, and 2.5H) all coincide with 90° out-of-phase anti-synchronous behavior.

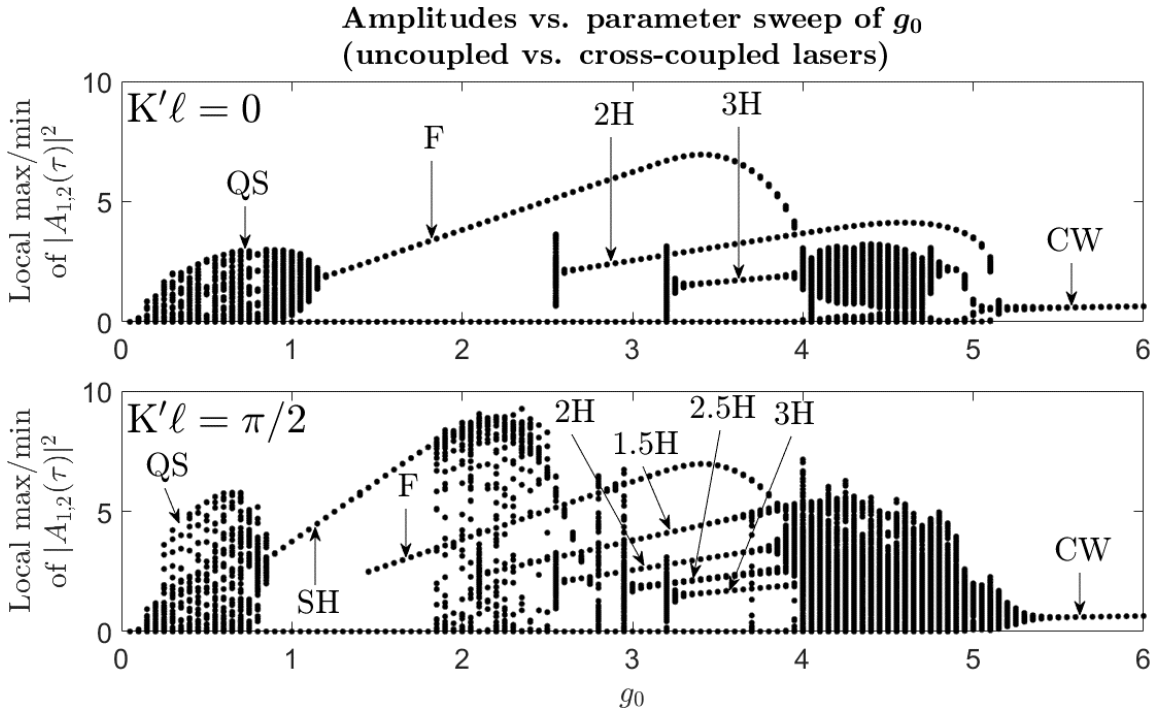

Figure 3.24: Bifurcation diagrams, as the unsaturated gain g_0 is swept back and forth (numerous times and each from a different set of initial histories) within the interval 0 to 6, for the solitary/uncoupled laser ($\mathrm{K}'\ell = 0$) and the fully cross-coupled lasers ($\mathrm{K}'\ell = \pi/2$). The different branches / dynamical regions labeled are as follows: subharmonic (SH), fundamental (F), and harmonic (1.5H, 2H, 2.5H, and 3H) mode-locked regimes (note the multistability); Q-switched mode-locking (QS); and continuous-wave operation (CW). Table 3.2 lists the other parameter values.

Time simulations (see Figure 3.25) indeed confirm this behavior and further indicate that the subharmonic mode-locked pulse has narrower pulsewidth and slightly less than twice the energy as compared to the fundamental. In Figure 3.25, for the subharmonic each pulse has an FWHM of ~0.062, a peak height/power of ~6.23, and a pulse energy of ~0.25, whereas for the

fundamental each pulse has an FWHM of ~0.085, a peak height/power of ~2.61, and a pulse energy of ~0.45, all in normalized units. It is also important to note the observation regarding the gain/absorption dynamics leading to the opening of a net gain window that facilitates mode-locked pulse generation. As seen in the bottom subplot of Figure 3.25, the net gain window for the fundamental is essentially contained within the time interval of the corresponding pulsewidth. On the other hand, the net gain window for the subharmonic opens before the corresponding subharmonic pulse's leading edge. The distinction between the two cases is just as discussed in SECTION 3.2.2, specifically the distinction drawn between the two cases of slow saturable absorber mode-locking in Figure 3.2 and Figure 3.3.

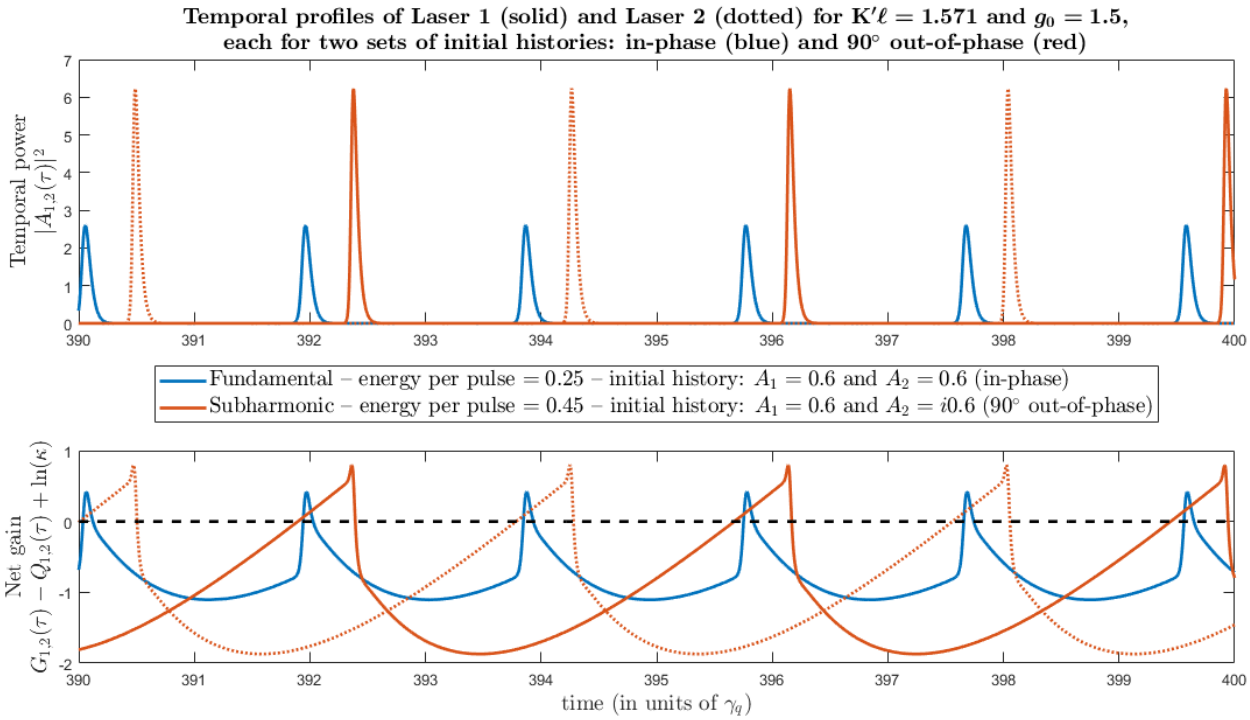

Figure 3.25: Temporal plots of the output power and the population dynamics of two fully cross-coupled lasers for two different initial histories: in-phase and 90° out-of-phase. Due to the bistability of the system at $g_0 = 1.5$, the former initial history leads to the lasers mode-lock at the fundamental repetition rate, while latter leads them to mode-lock at the subharmonic rate. Since the two lasers operating at the fundamental rate are synchronized, their outputs are identical, as shown by the blue trace. For the subharmonic, the lasers are anti-synchronous, as shown by the red trace (solid and dotted, for Laser 1 and Laser 2, respectively).

The results indicate that the underlying physics of the subharmonic mode-locked regime is as follows. For two fully cross-coupled lasers, i.e. $K'\ell = \pi/2$, each laser transfers 100% of its radiation to the other cavity. In a sense, the effective roundtrip time is then effectively the sum $T_1 + T_2$ of the two individual roundtrip times (for example, see Figure 3.23), because any circulating radiation or circulating pulse propagates through the figure-eight structure of both cavity before returning to the same point of origin. In the case of identical lasers ($T_1 = T_2 = T$), this means the roundtrip time is doubled, and so the pulse repetition rate is halved. Accordingly, the enhancement of the intensity in the case of subharmonic operation is consistent with the effective doubling of the round trip time and the slow recovery of the gain media (see Figure 3.25). For instance, the emission of an intense mode-locked pulse from Laser 1 depletes the gain in that laser cavity. Since the gain recovery time is much longer than the nominal round trip time T, a pulse that returns to Laser 1 after time $2T$ (after passing through both cavities) experiences a gain that has recovered more than a pulse that returns after a delay of T. As a result, the pulse with the longer delay extracts more energy from the gain medium.

The bifurcation diagrams presented so far are generated via direct time integration / numerical simulation of the DDE model over the parameter sweeping, thus yielding the stable mode dynamical phenomena that can occur for various combinations of parameter values and initial histories. In order to acquire even further insight, numerical continuation (via DDE-BIFTOOL) of equilibria of the rotating-wave DDE model provides a complementary approach to assist in quickly spanning the parameter space. Specifically, it allows numerical continuation of the Hopf bifurcations, which as described in SECTION 3.2.3 signify the presence of nearby limit cycles that bifurcate from the CW solution (noting that the CW solution is a fixed point of the rotating-

wave DDE model), such as mode-locked pulse trains that serve as periodic modulations of the CW amplitude. The dynamical structure of the branches of Hopf bifurcations in the (g_0, q_0) parameter space is useful to understand the emergence of this subharmonic mode-locked regime. In fact, for this thesis work, the numerical continuation (via DDE-BIFTOOL) approach was used first, to guide further exploration of the parameter space via direct time integration/simulation, in particular for the subharmonic mode-locked regime. Granted, the presentation of the content in the thesis does not exactly follow the chronology by which the research itself was conducted.

First, Figure 3.26 shows branches of Hopf bifurcations in the (g_0, q_0) parameter space for the single (or uncoupled) laser; the results are consistent with the findings in [77, 82]. The plots provide information on the whether the bifurcations are supercritical (blue trace) or subcritical (red trace), i.e. whether the limit cycles that bifurcate from the CW equilibrium at the Hopf point are stable or unstable, respectively. The plots also indicate whether the equilibrium itself is stable (thick linewidth) or unstable (thin linewidth) at each point on the Hopf branch; if the CW equilibrium is not stable, then neither would be the limit cycle that bifurcates from it in the vicinity of the Hopf point. The Hopf frequencies, $\nu = 2\pi n/T$, labeled in the figure correspond to the fundamental and harmonic mode-locked pulse repetition rates, where $n = 1, 2, 3, \ldots$ (positive integers), and T is the roundtrip time (here, $T = 1.875$). In addition, one of the Hopf branches is associated with the Q-switching frequency (for which $\nu \approx 0.2$) that amplitude-modulates the fundamental mode-locked pulse train for small unsaturated gain values g_0. Numerically, these frequencies are determined from the imaginary component of the complex-conjugate pair of eigenvalues that cross the imaginary axis at the Hopf bifurcation. When g_0 is

small, the branch associated with Q-switched mode-locking is initially supercritical and stable, and then it loses stability to the fundamental mode-locked state.

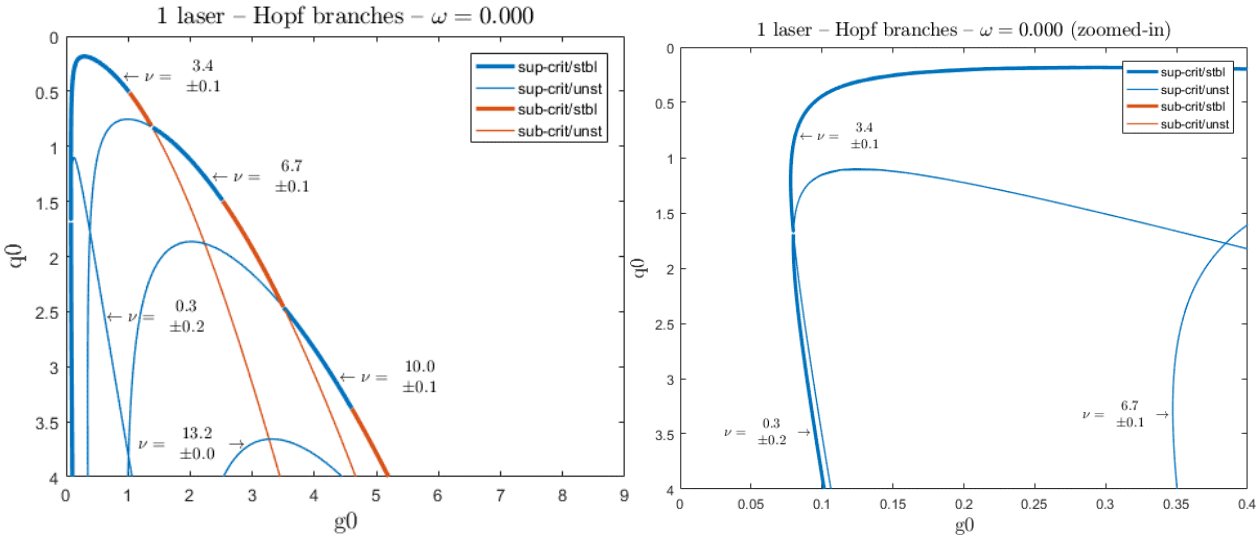

Figure 3.26: Branches of Hopf bifurcations in the (g_0, q_0) parameter space for a single/uncoupled laser. Each branch is labeled with the frequency ν associated with the periodic orbits that emerge (averaged over all of the branch points). The line color indicates whether the Hopf bifurcation at a particular point on a branch is super-critical (blue) or sub-critical (red), while the linewidth indicates whether the equilibrium point from which the periodic orbit bifurcates at the Hopf point is stable (thick) or unstable (thin). Table 3.2 lists the other parameter values used.

In contrast, the two-parameter bifurcation diagram shown in Figure 3.27 for $K'\ell = \pi/2$ has two very noticeable differences. First, there are roughly double the number of Hopf branches, at frequencies equal to $\nu = 2\pi n/T$, where now $n = 0.5, 1.0, 1.5, 2.0, ...$, and again $T = 1.875$. In addition, there is a Hopf branch with frequency $\nu \approx 0.2$, again identifying the Q-switched mode-locked regime. Second, as can be discerned from the zoomed-in plot in the figure, the branch labeled $\nu = 2\pi(1/2)/T \approx 1.8$ is supercritical and stable well before the $\nu \approx 0.2$ branch bifurcates from the CW equilibrium, unlike the single-laser case. This $\nu \approx 1.8$ branch identifies the subharmonic mode-locked pulse regime, as expected based on the discussion earlier in this section. In addition, all of the "half-harmonic" mode-locked regimes seen in Figure 3.24 (i.e. those labeled as SH, 1.5H, and 2.5H in the bottom subplot) are accounted for in Figure 3.27.

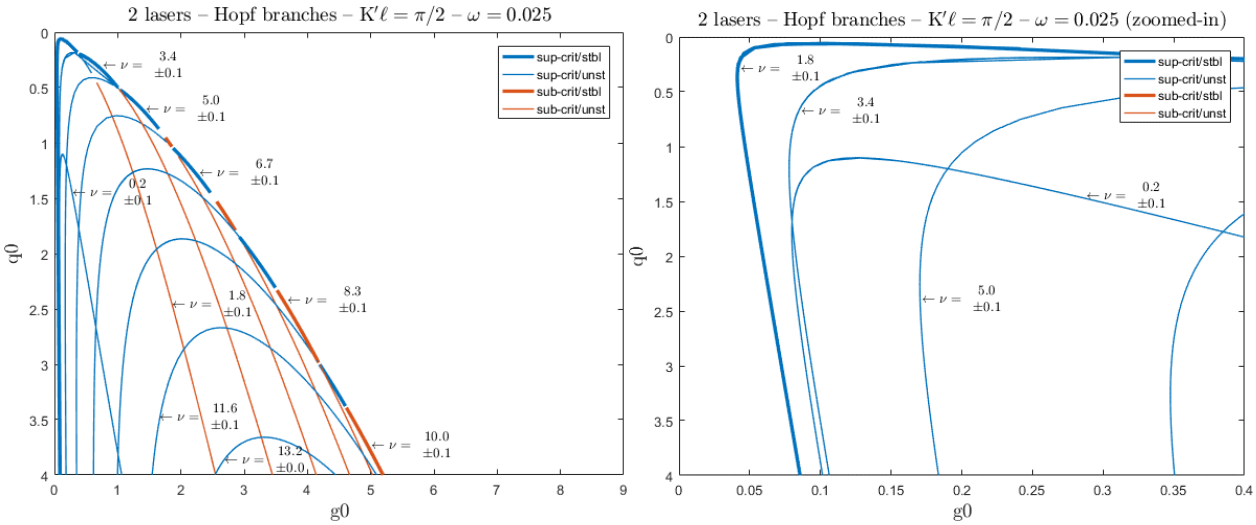

Figure 3.27: Branches of Hopf bifurcations in the (g_0, q_0) parameter space for 2 identical, fully cross-coupled lasers ($K'\ell = \pi/2$). Each branch is labeled with the frequency ν associated with the periodic orbits that emerge (averaged over all of the branch points). The line color indicates whether the Hopf bifurcation at a particular point on a branch is super-critical (blue) or sub-critical (red), while the linewidth indicates whether the equilibrium point from which the periodic orbit bifurcates at the Hopf point is stable (thick) or unstable (thin). Table 3.2 lists the other parameter values used.

3.5 Effect of the linewidth enhancement factors

The linewidth enhancement or α-factors, briefly mentioned in SECTION 3.4.1 for the solitary laser, describe carrier-density-dependent phase modulation effects. They play a key role in the destabilization of phase-locking of evanescently-coupled, continuous-wave semiconductor lasers [68] and the break-up of mode-locking for a single, mode-locked semiconductor laser [77]. Accordingly, the role of the α-factors is an essential consideration for the case of evanescently-coupled, mode-locked lasers. In this thesis, three important, representative cases are compared and contrasted: 1) zero α-factors, i.e. $\alpha_G = \alpha_Q = 0$; 2) unequal, non-zero α-factors, e.g. $\alpha_G = 3$ and $\alpha_Q = 1$; and 3) non-zero but equal α-factors, e.g. $\alpha_G = \alpha_Q = 3$. Furthermore, each of these cases is examined as coupling and pump current parameters are varied. To clarify, both lasers are set to have identical material parameters, including the values for α_G and α_Q (i.e. $\alpha_{G1} = \alpha_{G2}$ and $\alpha_{Q1} = \alpha_{Q2}$). The terms "unequal" or "equal" α-factors are used in the following discussions

instead to indicate whether $\alpha_G \neq \alpha_Q$ or $\alpha_G = \alpha_Q$ for each laser cavity, respectively (i.e. the linewidth enhancement factor of the gain section vs. that of the saturable absorption section).

3.5.1 Solitary/uncoupled lasers

The presence of the linewidth enhancement factors and the associated phase fluctuations disrupts the phase-locking of longitudinal modes necessary for mode-locking, and as a result, this leads to irregular pulse amplitude fluctuations and an overall decreased peak pulse power (see Figure 3.28). When the gain and absorber α-factors are set equal to each other, the linewidth enhancement effects of the gain and absorber sections compensate for each other in opposite directions [77], and a more regular mode-locked pulse train is observed for appropriate pump parameters (see Figure 3.29). On the other hand, sufficiently high pump parameter values nevertheless lead to CW operation with a minimally noticeable effect on the temporal power, perhaps because there is only one longitudinal mode significantly at play (see Figure 3.28). It is interesting to note that in one of the observed cases for weak pump levels, non-zero, unequal α-factors lead to a regular mode-locked pulse train (albeit with greatly decreased peak pulse power) while the zero-α-factor case results in Q-switched mode-locked operation (see Figure 3.30).

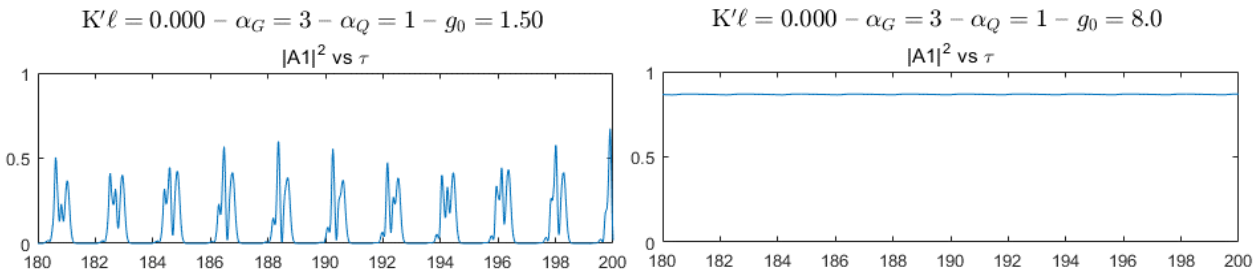

Figure 3.28: Output power temporal profile for a solitary/uncoupled laser with unequal, non-zero α-factors. For the left subplot, the pump parameter is moderate, and the temporal power has an appearance of deteriorated mode-locking. For the right subplot, the pump parameter is very high, and the uncoupled laser is in the CW regime. Table 3.2 lists the parameter values not specified here, and the initial history used is $[A, G, Q] = [0.6, 2.5, 0.1]$.

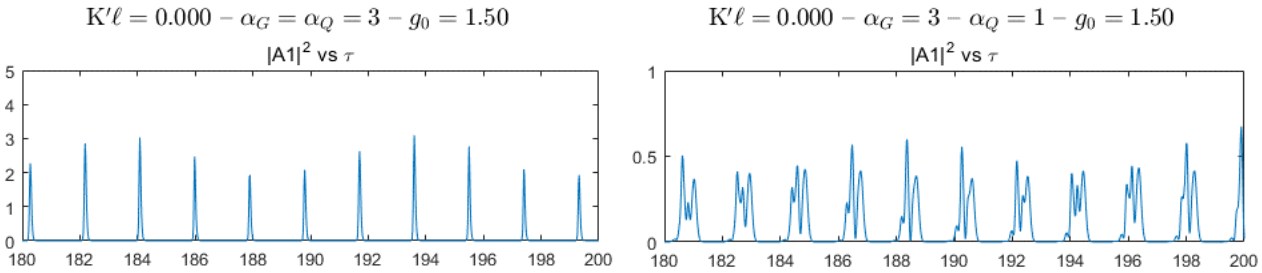

Figure 3.29: Output power temporal profile for a solitary/uncoupled laser with moderate pump currents and non-zero α-factors. For the left subplot, the gain and absorber α-factors are equal for each laser, and the pulses are regular in shape and repetition rate (but there is a slight variation in the pulse heights). For the right subplot, the α-factors are unequal, and mode-locking behavior and pulse shapes are deteriorated. Note that the vertical scales of the plots are different. Table 3.2 lists the parameter values not specified here, and the initial history used is $[A, G, Q] = [0.6, 2.5, 0.1]$.

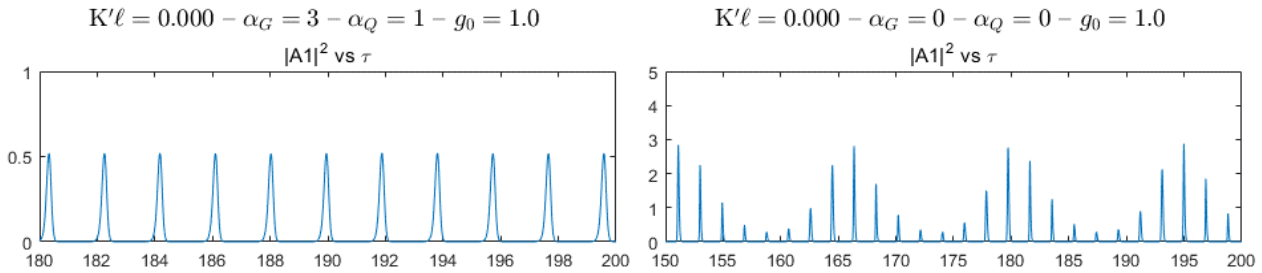

Figure 3.30: Output power temporal profile for a solitary-uncoupled laser at low pump parameters. For the left subplot, the α-factors are non-zero and unequal, and mode-locked operation is observed (although the peak pulse power is roughly an order of magnitude lower than in the case of zero α-factors), while in the right subplot the α-factors are zero for the gain/absorber sections, and Q-switched mode-locked operation is observed. Note: the vertical scales of the two plots are different. Table 3.2 lists the parameter values not specified here. The initial history is $[A, G, Q] = [0.6, 2.5, 0.1]$.

3.5.2 Two lasers with intermediate coupling strength

When the lasers are coupled, the synchronization properties become more complex in the presence of linewidth enhancement factors as compared to in their absence. Recall the two behaviors observed in the results of SECTION 3.4 for zero α-factors: in-phase synchronization vs. 90°-phase delayed-synchronization. In order to quickly reach the delayed-synchronization behavior and focus on how the behavior changes in the presence of the α-factors, the lasers are initialized to be 90° out-of-phase. With intermediate values of coupling (i.e. $0 \ll \mathrm{K}'\ell \ll \pi/2$) and non-zero α-factors, the delayed synchrony can still be partially present, but it is noticeably and often substantially degraded. To illustrate, consider an example case of 50:50 coupling (i.e.

$K'\ell = \pi/4$). Figure 3.31 and Figure 3.32 show the irregular power fluctuations (and the partial delayed-synchronization between the two lasers), along with auto- and cross-correlation plots of their complex-valued amplitudes, for moderate and strong pump parameters, respectively.

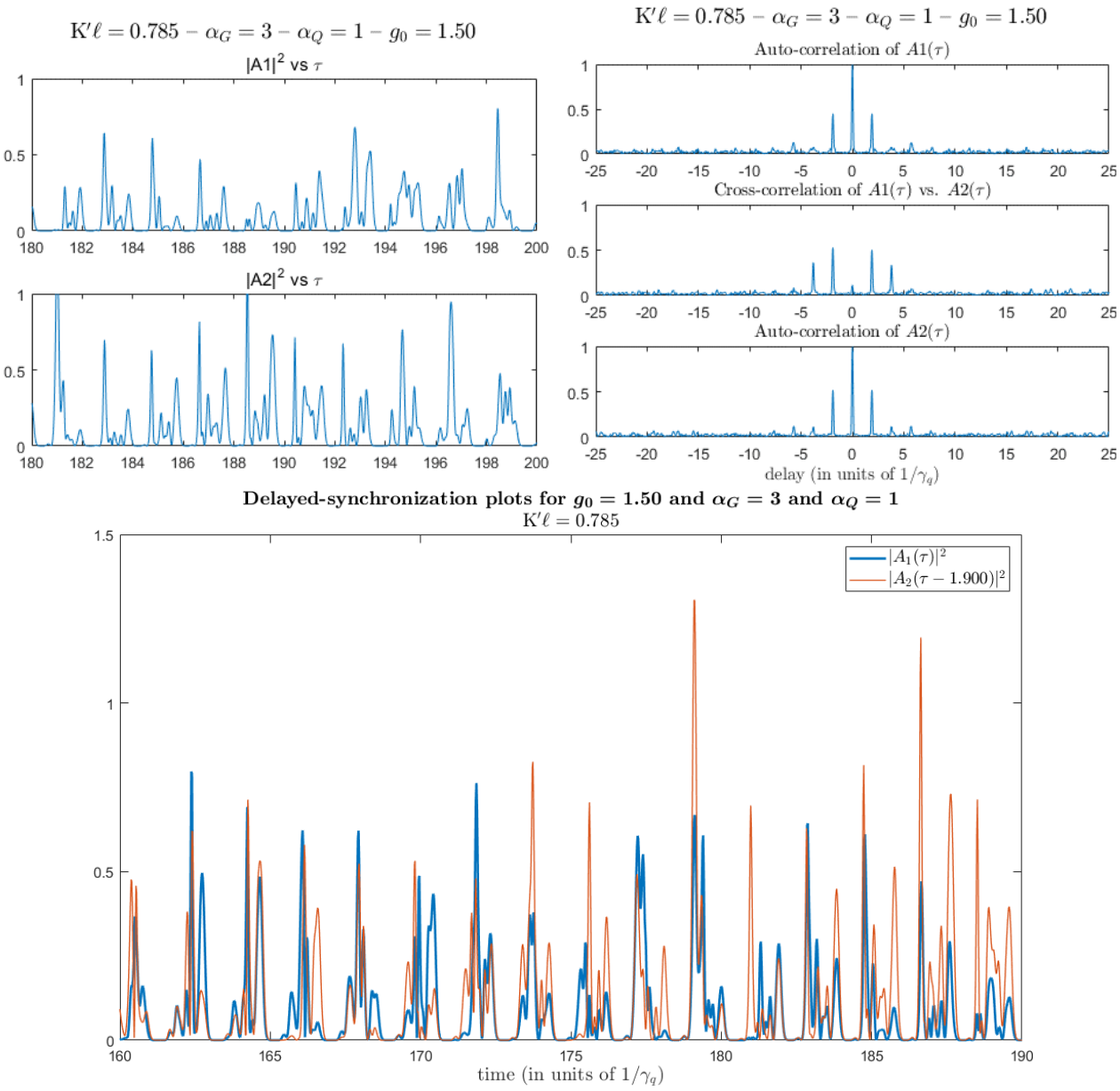

Figure 3.31: Results for two 50:50 coupled lasers at moderate pump levels and with non-zero, unequal α-factors. The top-left column of subplots show the temporal power for Laser 1 (top) and Laser 2 (bottom), while the top-right column of subplots show the auto- and cross-correlations of the complex-valued amplitudes of the two lasers. The bottom subplot shows the time series of Laser 2 shifted by the delay corresponding to the maximal peak in the cross-correlation. Table 3.2 lists the parameter values not specified here, and the 90° out-of-phase initial history is used.

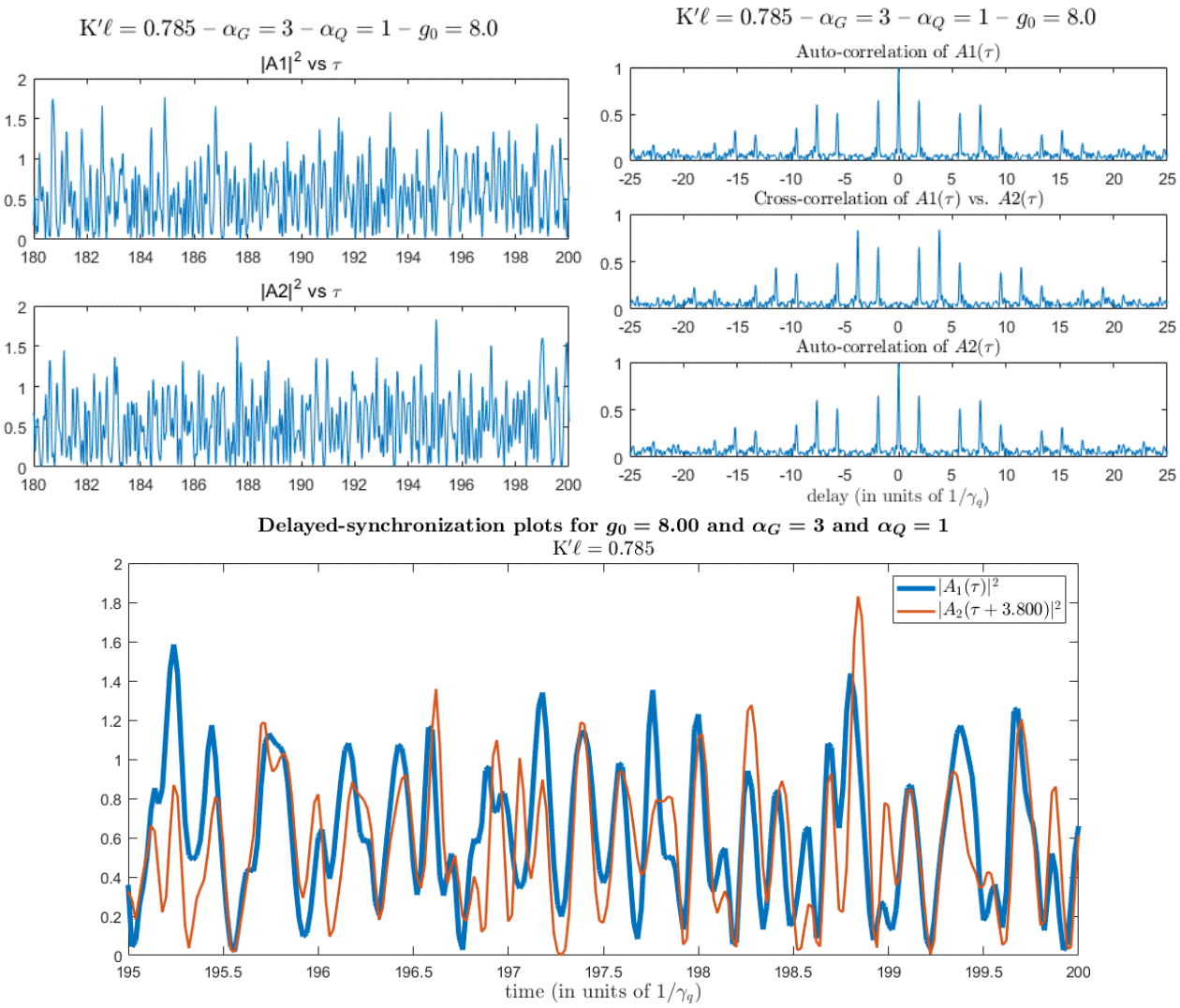

Figure 3.32: Similar to Figure 3.31, except for high pump parameter.

When the gain and absorber α-factors are set equal to each other, the regularity of each laser's mode-locked pulse train is much improved, and there is again some partial degree of delayed synchronization, as exemplified by the case of 50:50 coupling (i.e. $K'\ell = \pi/4$) in Figure 3.33 for a moderate pump parameter at which the laser generates mode-locked pulses. However, the equalization of the α-factors does not lead to any appreciable improvement of the (delayed) synchronization between the coupled lasers beyond that solely due to improving the pulse quality, pulse power, and regularity of each individual laser's temporal power profile (compare

Figure 3.33, for which $\alpha_G = \alpha_Q = 3$, to Figure 3.31, for which $\alpha_G = 3 \neq \alpha_Q = 1$). Instead, the results indicate that while equalizing the α-factors clearly improves each laser's correlation with itself, the presence of non-zero α-factors can continue to disrupt delayed synchronized behavior regardless of whether or not the gain and absorber sections' α-factors are set equal to each other. Likewise, in the case of the high pump parameter value, equalization of the α-factors does not appear to improve the delayed synchrony of the irregular fluctuations seen for unequal α-factors (compare Figure 3.34, for which $\alpha_G = \alpha_Q = 3$, to Figure 3.32, for which $\alpha_G = 3 \neq \alpha_Q = 1$).

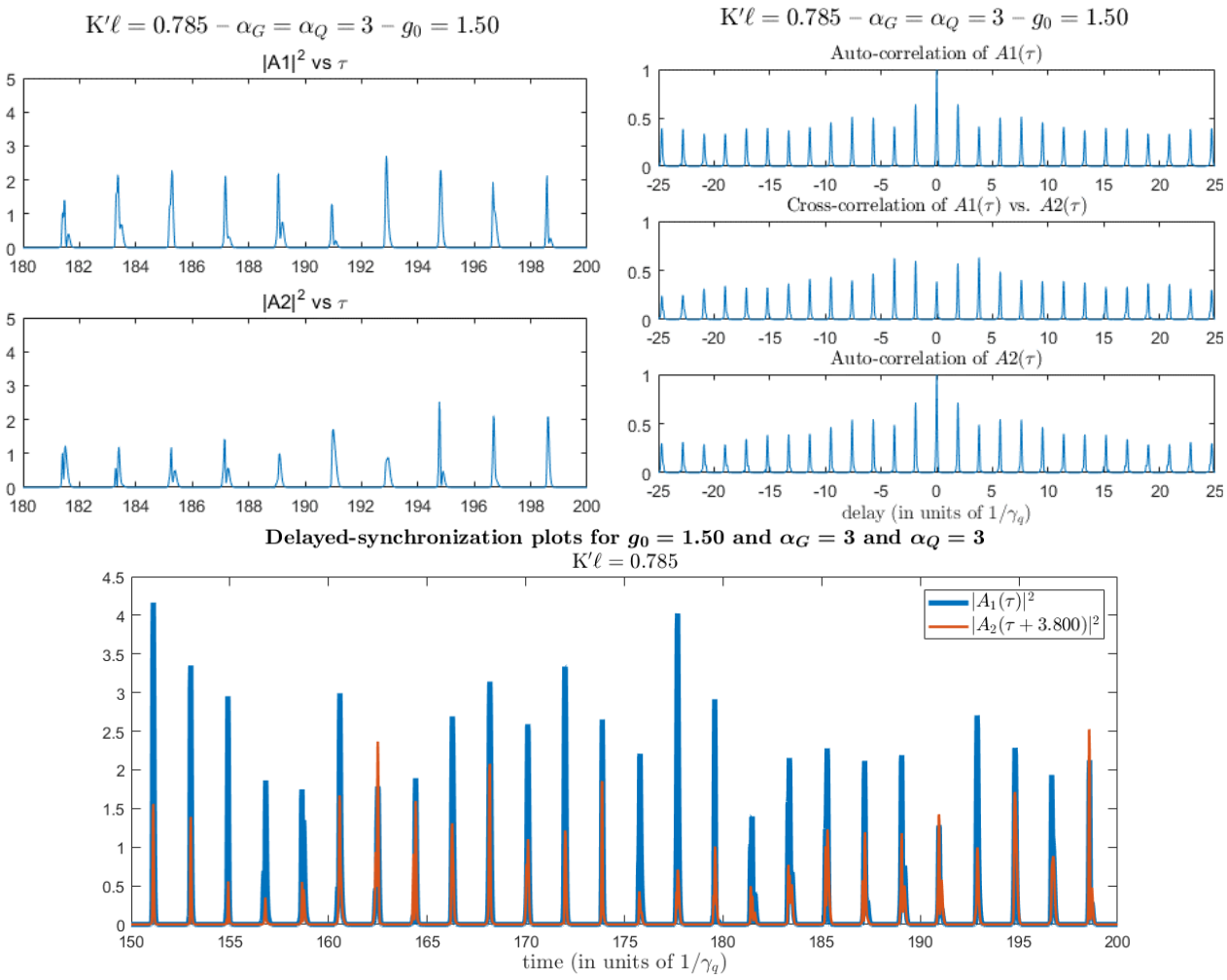

Figure 3.33: Same as Figure 3.31, except for equal, non-zero α-factors, i.e. $\alpha_G = \alpha_Q = 3$. The lasers are not delay-synchronized, even when the gain and absorber sections' α-factors are set equal to each other. Note: the axes limits/scales here are not the same as in Figure 3.31.

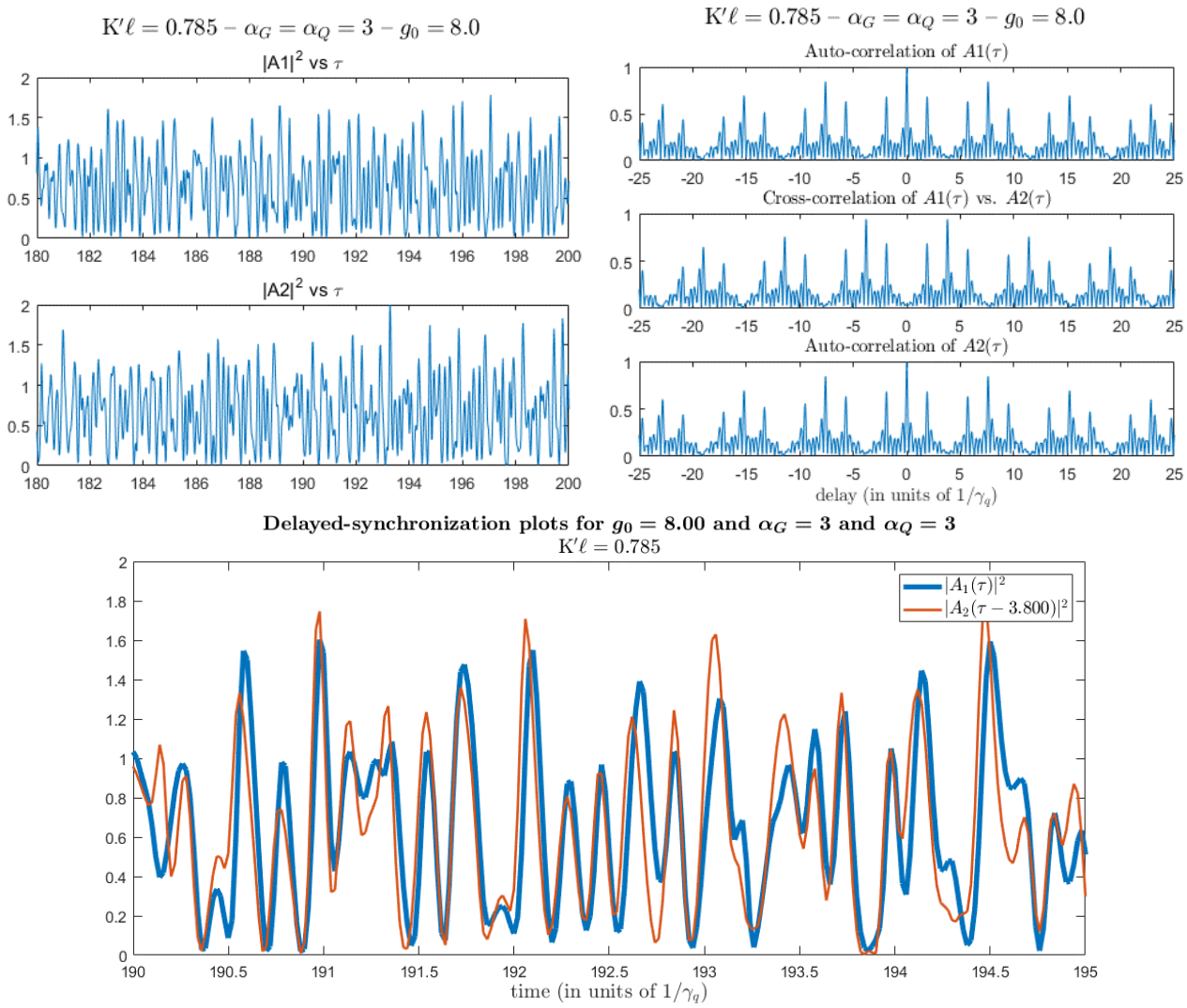

Figure 3.34: Same as Figure 3.32, but with equal, non-zero α-factors: $\alpha_G = \alpha_Q = 3$.

3.5.3 Fully cross-coupled lasers

For fully cross-coupled lasers, the results of SECTION 3.4.3 demonstrate the existence of anti-synchronous pulsing within the subharmonic mode-locked regime, and the bifurcation diagram in the bottom subplot of Figure 3.24 displays the many multistable dynamical regions in the g_0 parameter space. In contrast, here, the linewidth enhancement factors can disrupt the mode-locking process, including that of the subharmonic pulsing, by degrading the pulse quality and accordingly decreasing the pulse heights / peak powers. When the α-factors are non-zero and

unequal (see the bifurcation diagram in Figure 3.35), this degradation of the mode-locking processes is far more severe than when the α-factors are non-zero but equal (see the bifurcation diagram in Figure 3.36). Furthermore, in the latter case (i.e. $\alpha_G = \alpha_Q$) the cross-coupled lasers achieve clean CW operation at high pump levels.

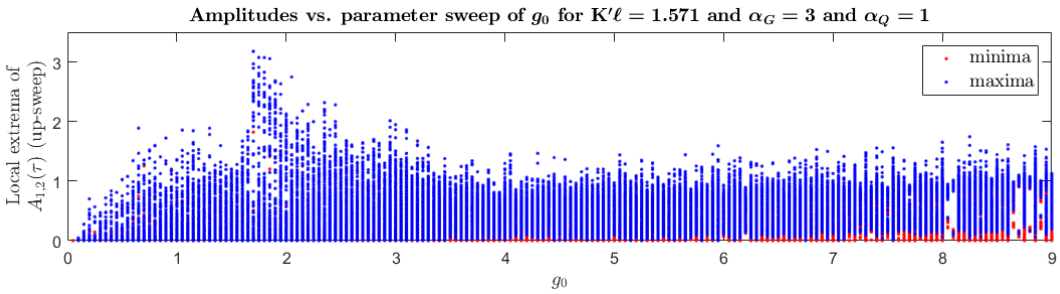

Figure 3.35: Bifurcation diagram, as the parameter g_0 is swept up from 0 to 9, for the case of non-zero and unequal α-factors. The down-sweep after the up-sweep follows more or less the same pattern; hence, only the up-sweep is shown here. Note the large variations in the local extrema, indicating the absence of clean mode-locked behavior. Table 3.2 lists the parameter values not specified here, and the in-phase initial history is used for the first iteration ($g_0 = 0.05$), after which the subsequent iterations are initialized with the solution structure from the previous iteration.

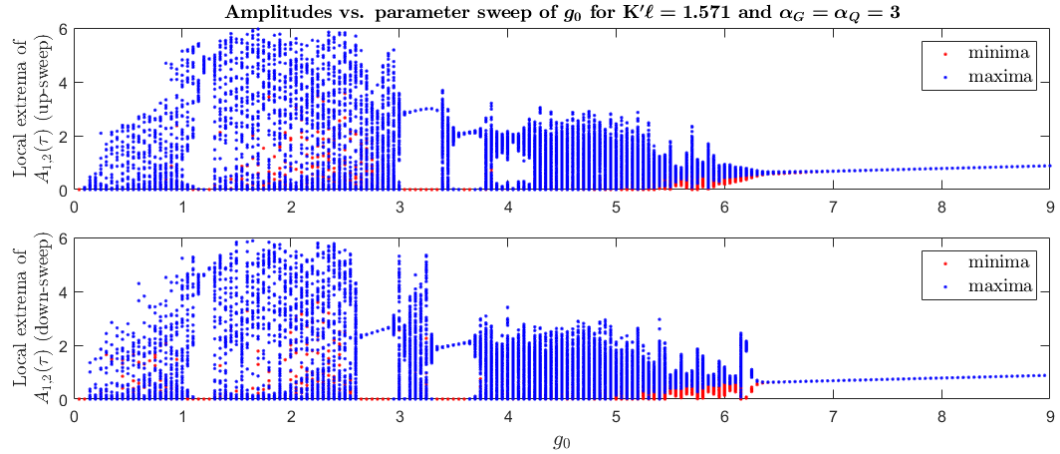

Figure 3.36: Same as Figure 3.35, except that here the α-factors are set equal to each other: $\alpha_G = \alpha_Q = 3$.

In addition, the anti-synchronous nature of the subharmonic mode-locked pulsations appears in both cases (see bottom two subplots of Figure 3.37). Moreover, the bistability (between the in-phase, synchronized pulsations at the fundamental mode-locked repetition rate and the 90° out-of-phase, anti-synchronous pulsations at the subharmonic rate) seen in the absence of α-factors is

also seen in their presence, as shown in Figure 3.37 for $\alpha_G \neq \alpha_Q$ (in the left column of subplots) and $\alpha_G = \alpha_Q$ (in the right column of subplots). Note that for unequal α-factors, the pulse quality is significantly deteriorated, but nevertheless the two qualitative behaviors of synchronization vs. anti-synchronization, depending on the initial history, is still evident.

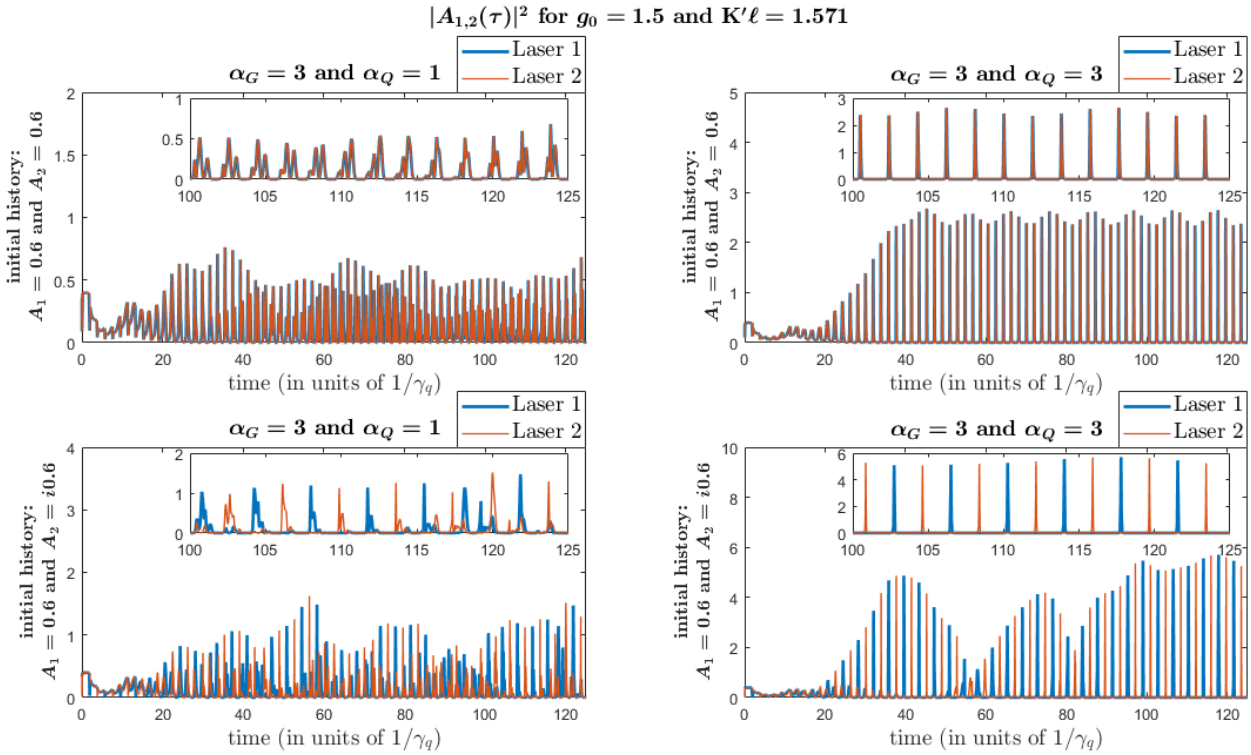

Figure 3.37: Temporal power for two cross-coupled lasers ($K'\ell = \pi/2$) with non-zero α-factors. The top two subplots are initialized with the in-phase history, while the bottom two subplots are initialized with the 90° out-of-phase history. The left two subplots are for unequal α-factors, while the right two subplots are for equal α-factors. Note that in both sets of α-factors, there is bistability between synchronized pulsing at the fundamental mode-locked rate and anti-synchronous pulsing at the subharmonic repetition rate, as shown by comparing the results initialized in-phase vs. 90° out-of-phase. Table 3.2 lists the parameter values not specified here.

3.6 Inclusion of a δ-correlated noise source term for each laser

The DDE model in the absence of noise (i.e. that is used to obtain the results in SECTION 3.4 and SECTION 3.5) serves as a good approach to studying the dynamics of the coupled lasers: it allows for quick numerical simulation via MATLAB's `dde23()` function and straightforward

bifurcation analysis via iterations of time simulations and via DDE-BIFTOOL. However, for numerical simulations performed by time integration of the model equations, the specification of the initial history vector does present somewhat of a limitation to the generality of the results. For example, the method commonly adopted in the literature sets the initial histories as non-zero, constant values for the entire time interval $-T_{\max} \leq -\tau \leq 0$ before the integration "begins" (where $T_{\max}$ is the largest time delay in the set of DDEs; in this thesis work, there is only one time delay $T = T_1 = T_2$). This choice is not entirely representative of practical situations, and it does not account for noise perturbations later applied to the system. Accordingly, it is unclear for the coupled lasers work presented in SECTION 3.4 and SECTION 3.5 whether the observed synchronization behaviors (or lack thereof) are completely intrinsic to the system or partially an artifact of any synchrony, phase relationship, and/or non-time-varying states all imposed at initialization. In addition, since the simulations with constant-valued initializations reveal regions of multistability, it is also useful to understand whether these dynamical regimes are accessible if the system is initialized to a zero-state and then allowed to evolve from noise.

The inclusion of noise into the DDE model facilitates a further generalized treatment of the system and the results from the numerical simulations, yielding insight into the stability of the dynamical regimes and robustness of the synchronization behaviors observed earlier, but now in the presence of noise perturbations. In this section, the implementation is phenomenological: a δ-correlated, complex-valued noise source term is simply added/appended to each of the amplitude DDEs (note that the two noise sources have no correlation with each other) in the DDE model from SECTION 3.3.2. These modified amplitude DDEs are given below in Equations (3.18) and (3.19), with all of the $R_{ij}(\tau)$ terms defined as per Equations (3.9) –

(3.12), and the DDEs for the saturable gain and absorption defined as per Equations (3.13) – (3.16). For the numerical simulation results that follow, each of the two complex-valued noise functions, $R_{\text{noise, (1, 2)}}(\tau)$, fluctuates randomly in both magnitude (within a uniform distribution between 0 and 0.1) and phase (within a uniform distribution between 0 and 2π). The initial history vector is set as zero-state, i.e. $\begin{bmatrix} A_{10}, & G_{10}, & Q_{10}, \\ A_{20}, & G_{20}, & Q_{20} \end{bmatrix} = \begin{bmatrix} 0, & 0, & 0, \\ 0, & 0, & 0 \end{bmatrix}$, such that the transient build-up from noise can be observed. For now, the scope of this section of the thesis is primarily to identify whether or not the behaviors observed in SECTION 3.4 and SECTION 3.5 can be observed in the presence of noise, with an additional focus on the dynamics of subharmonic pulse generation for full cross-coupling ($\mathrm{K}'\ell = \pi/2$). A more in-depth and extensive analysis of this stochastic version of the DDE model is reserved for the future.

In this section of the thesis, for the purpose of categorizing and cataloging the various phenomena, it is helpful to separate the discussion of moderately-pumped lasers (for which the solitary/uncoupled laser is mode-locked) into SECTION 3.6.1 and strongly-pumped lasers (for which the solitary/uncoupled laser operates in the CW regime) into SECTION 3.6.2. The cross-coupled lasers and the subharmonic regime are addressed separately in SECTION 3.6.3. Note that, as listed in Table 3.2, the simulation results in this section primarily use $T = 2$ as the parameter value for the (normalized) roundtrip time delay, in contrast to SECTION 3.4, which uses $T = 1.875$. The change is made simply for the convenience that $T = 2$ being an integer makes it easier to read the plots along the axis ticks.

$$\begin{aligned} \frac{\partial A_1(\tau)}{\partial \tau} = & -\gamma A_1(\tau) \\ & +\gamma e^{-i\varphi_1}\big(R_{11}(\tau - T_1)A_1(\tau - T_1) + R_{12}(\tau - T_1)A_2(\tau - T_1)\big) \\ & +R_{\text{noise, }1}(\tau) \end{aligned} \tag{3.18}$$

$$\frac{\partial A_2(\tau)}{\partial \tau} = -\gamma A_2(\tau) + \gamma e^{-i\varphi_2}\left(R_{21}(\tau - T_2)A_1(\tau - T_2) + R_{22}(\tau - T_2)A_2(\tau - T_2)\right) + R_{\text{noise, 2}}(\tau) \tag{3.19}$$

3.6.1 Moderate pump parameter values

First, the operation in the mode-locked regime is considered, using a moderate pump parameter value of $g_0 = 2$. As discussed in SECTION 3.4.2, the two coupled lasers are capable of synchronizing in-phase or achieving nearly perfect delayed synchronization, due to the bistability of the two behaviors, in the absence of linewidth enhancement factors. Both states are achievable in the presence of noise, even when the lasers are initialized to a zero state and allowed to evolve from low-amplitude noise. The left column of subplots in Figure 3.38 shows an example of in-phase synchronization for $\mathrm{K}'\ell = \pi/3$, while the right column of subplots in Figure 3.38 shows delayed synchronization for the same coupling value but with a different randomized noise function. Note that both simulations are run with the same exact set of parameter values and are initialized with the zero-state history, and so the difference in the two behaviors arises from the difference in the noise source term. This reaffirms the nature of the bistability. In addition, Figure 3.39 shows an example of 50:50 coupled lasers that evolve toward a state of synchronization of the temporal power but with a 180° phase difference between their complex amplitudes. The fact that there are bistable domains in the parameter space is not surprising, because even a single mode-locked laser has dynamical regions of multistability between the different mode-locked behaviors [84]. However, the interesting aspect here in the coupled mode-locked laser system is an additional manifestation of the multistability, namely that of synchrony vs. delay-synchrony, in which different initial states and/or different randomized noise perturbations can push the system into one domain or the other.

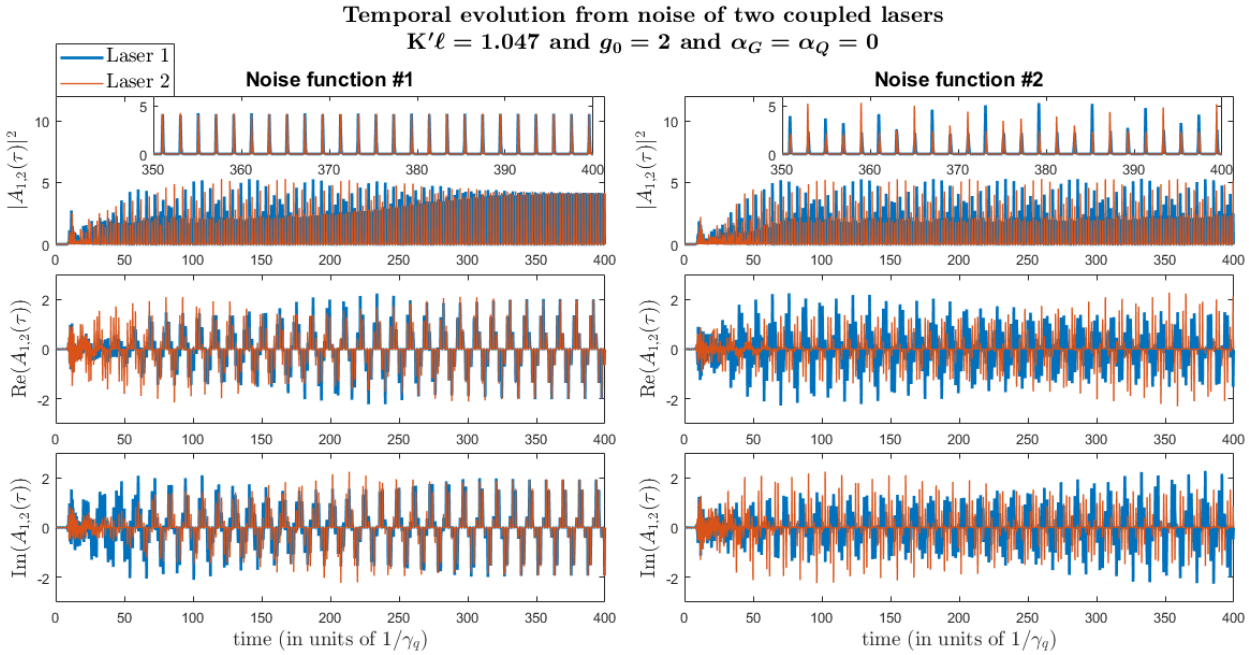

Figure 3.38: Temporal power for two coupled lasers with moderate pump level and zero α-factors. Here the coupled system exhibits a bistability between in-phase synchronization (the left column of subplots) and delay-synchrony (the right column of subplots). Both simulations use the same exact set of parameter values; the only difference between them is that they are started with different randomized noise terms. Table 3.2 lists the parameter values not specified here.

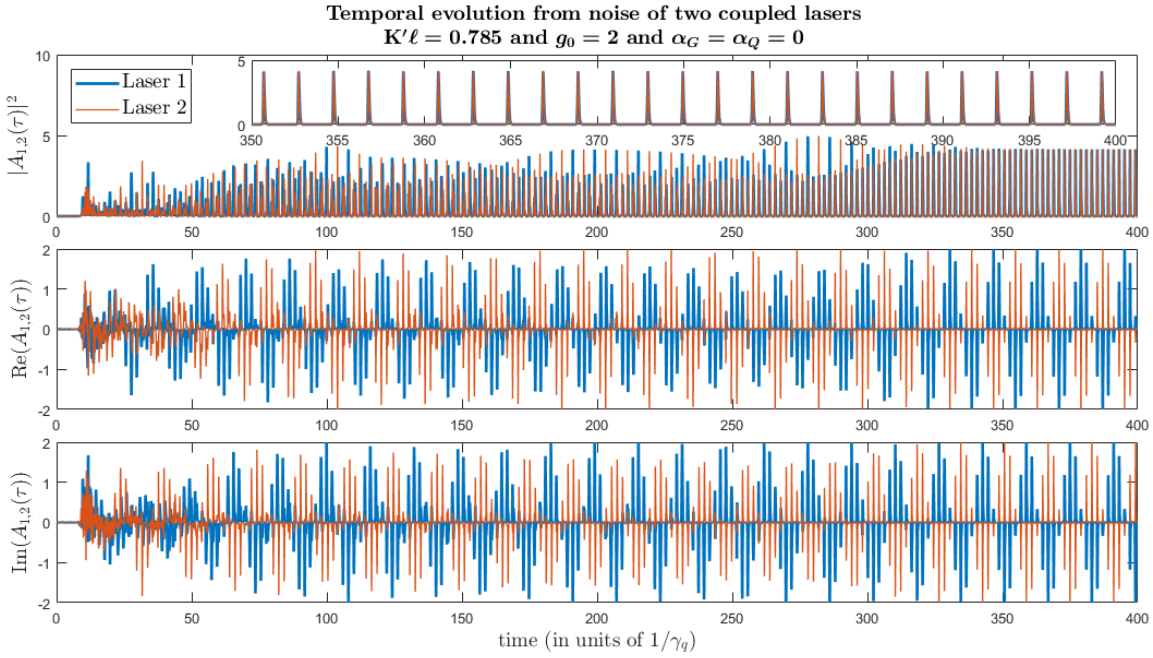

Figure 3.39: Temporal power for two 50:50 coupled lasers synchronizing with a 180° phase difference between their complex amplitudes. Table 3.2 lists the parameter values not specified here.

As seen in SECTION 3.5.2, the linewidth enhancement factors deteriorate mode-locking and disrupt synchronization, and the latter effect appears to be more severe in the simulations from noise. As an example, Figure 3.40 considers two 50:50 coupled lasers (i.e. $K'\ell = \pi/4$). When $\alpha_G = \alpha_Q = 0$, the two lasers evolve from uncorrelated noise to in-phase synchrony (top subplot of Figure 3.40). When $\alpha_G \neq \alpha_Q \neq 0$, the pulse quality is degraded (middle subplot of Figure 3.40), with what appear to be chaotic fluctuations (see auto-correlation plots in Figure 3.41), and there is no synchronization (see cross-correlation plot in Figure 3.41). When $\alpha_G = \alpha_Q \neq 0$, the pulse quality for each individual laser is significantly improved, and the pulse arrival times of Laser 1 align with those of the Laser 2 (bottom subplot of Figure 3.40). However, the modulations of the lasers' pulse amplitudes are not well-correlated with each other; accordingly, the cross-correlation in Figure 3.42 indicates no appreciable degree of delayed synchronization.

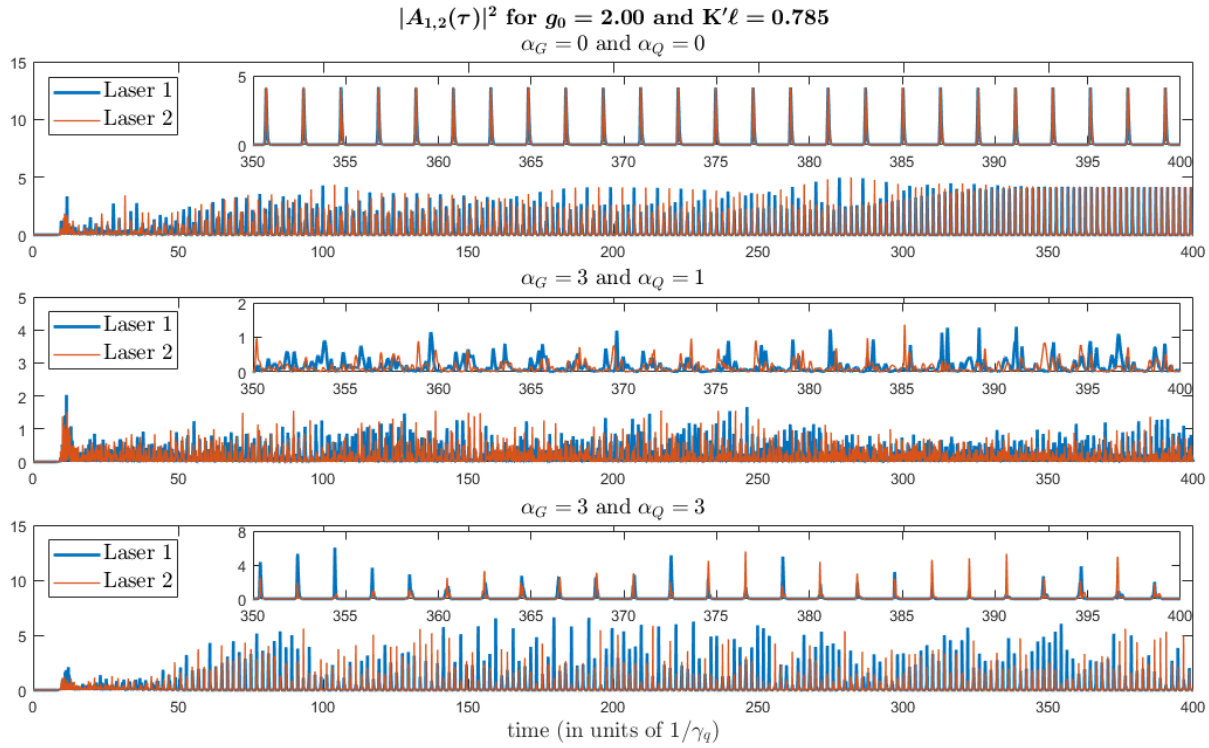

Figure 3.40: Temporal evolution of power from noise for two 50:50 coupled lasers with moderate pump level $g_0 = 2$ and varying α-factors. Table 3.2 lists the parameter values not specified here.

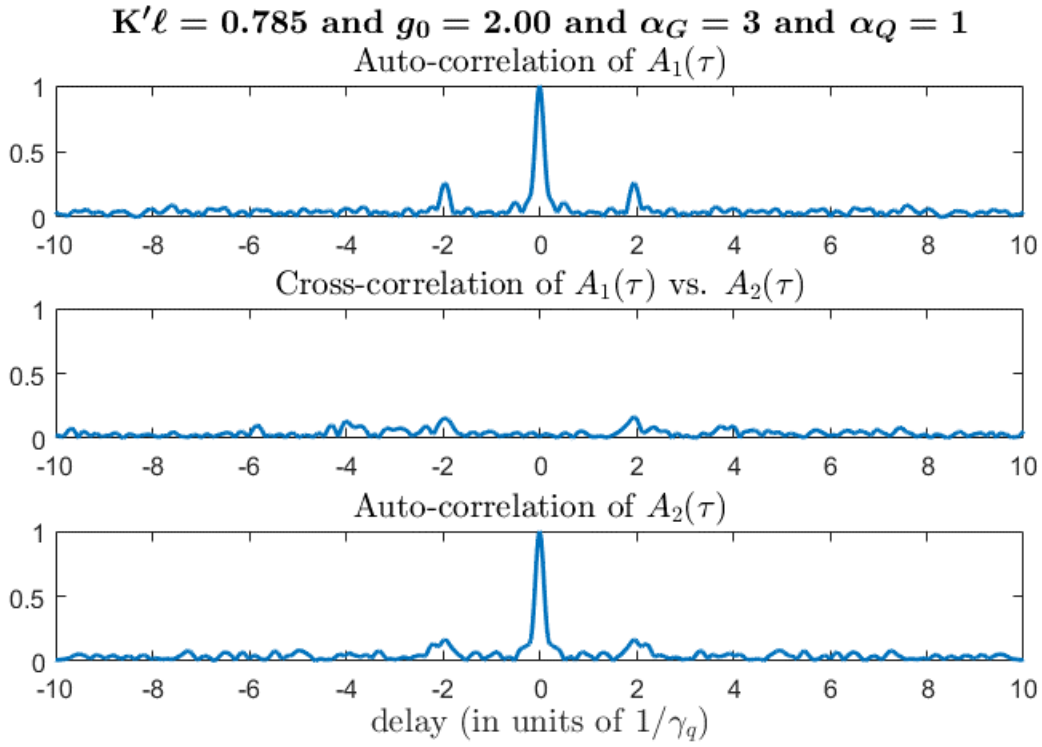

Figure 3.41: Auto- and cross-correlations of the complex-valued amplitudes of the two 50:50 coupled lasers for moderate pump level and non-zero, unequal α-factors. The results indicate that the amplitudes are somewhat irregular/chaotic, due to the presence of essentially only one strong peak (at zero delay) in the auto-correlation plots. The results also indicate that the two lasers have little to no synchronization between them, due to the absence of any significant peaks in the cross-correlation plot at any values of the delay. Table 3.2 lists the parameter values not specified here.

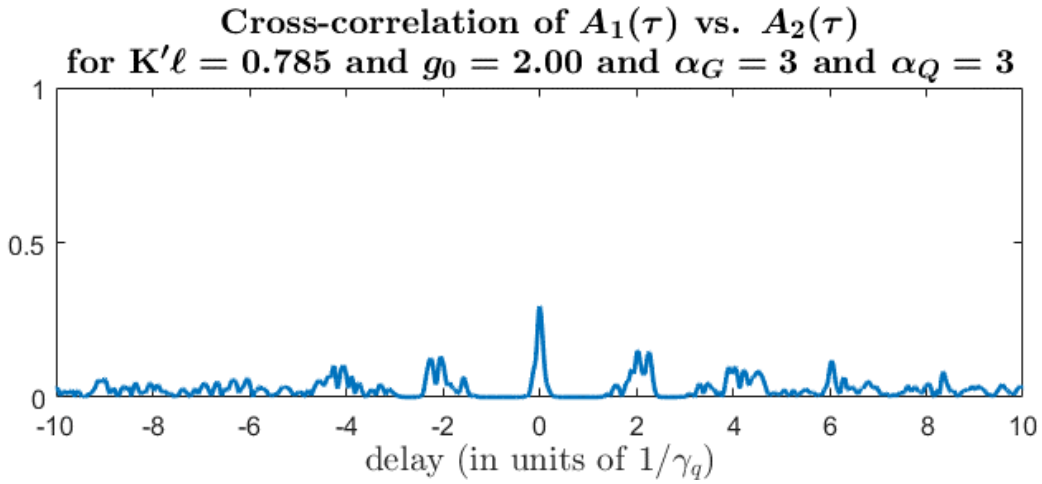

Figure 3.42: Cross-correlation profile of the complex-valued amplitudes of the two 50:50 coupled lasers for moderate pump level and non-zero, equal α-factors. The plots indicate that the modulations of the two lasers' pulse trains are not very well-correlated with each other. However, in the figure there are small peaks at delays that are integer multiples of the roundtrip time, consistent with the observation that the lasers' pulse arrival times align, although their peak heights and the modulation of such are not synchronized. Table 3.2 lists the parameter values not specified here.

3.6.2 Strong pump parameter values

Next, the coupled system is simulated (with noise) for a large pump parameter value of $g_0 = 6$. As expected, when the α-factors are zero, the solitary (uncoupled) lasers operate steadily in the CW regime (the top-most subplot of Figure 3.43). Interestingly, the noise simulation results in the middle subplots of Figure 3.43 show that, for intermediate values of coupling between the lasers ($0 \ll \mathrm{K}'\ell \ll \pi/2$), the two lasers can operate in a "burst-mode" regime, in which there are regularly occurring, delay-synchronized bursts of power fluctuations in the output temporal profiles. A particularly vivid display of this behavior is seen in the second subplot of Figure 3.43 for a coupling parameter value of $\mathrm{K}'\ell = \pi/6$. Also, looking at all of the subplots of Figure 3.43, the highest degree of fluctuations are found to occur for 50:50 coupling (the third subplot of Figure 3.43). This behavior is somewhat similar to the power fluctuations for the coupled laser system observed even when noise is absent, e.g. as in the bottom subplot of Figure 3.18 back in SECTION 3.4.2. Finally, note that the uncoupled lasers ($\mathrm{K}'\ell = 0$) and the fully cross-coupled lasers ($\mathrm{K}'\ell = \pi/2$) both show negligible power fluctuations. Indeed, the aforementioned behaviors are in the absence of amplitude-phase coupling provided via the linewidth enhancement factors. The inclusion of the α-factors induces appreciable temporal power fluctuations for the uncoupled lasers and large, complicated and irregular oscillations for the coupled lasers (see Figure 3.44). Furthermore, the delayed synchronization is heavily degraded, whether or not the non-zero gain and absorber α-factors are set equal to each other (i.e. whether or not $\alpha_G = \alpha_Q \neq 0$); this is evidenced in Figure 3.44 (temporal profile) and Figure 3.45 (profile of the cross-correlation of the lasers' complex-valued amplitudes with each other). The observed effects of the α-factors and their role in disrupting the synchronization are consistent with the previous observations from SECTION 3.5.

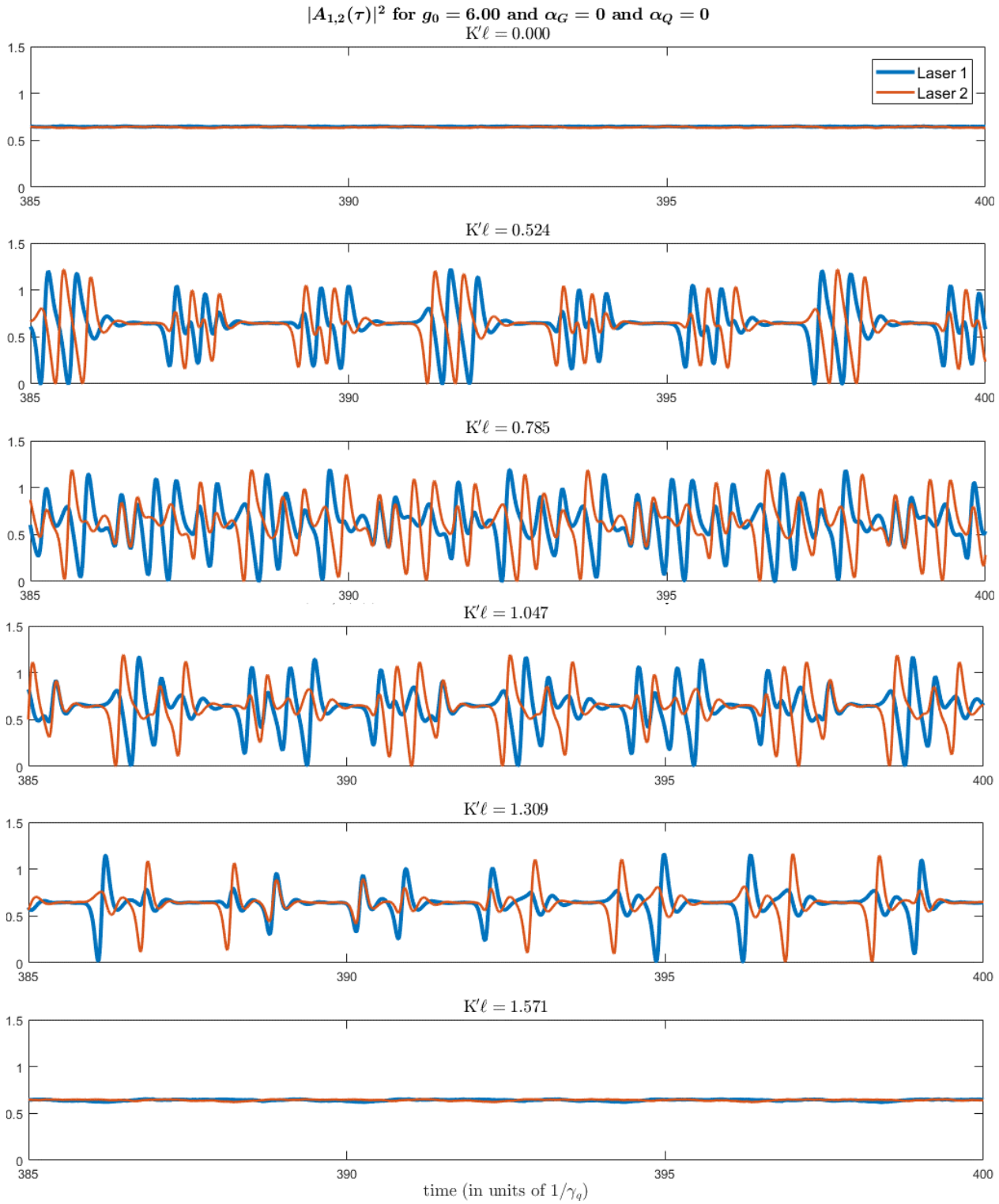

Figure 3.43: Temporal power for coupled lasers with high pump level and zero α-factors. Note the periodic bursts of power fluctuations, especially clear for $K'\ell = \pi/6 \approx 0.524$. Table 3.2 lists the parameter values not specified here.

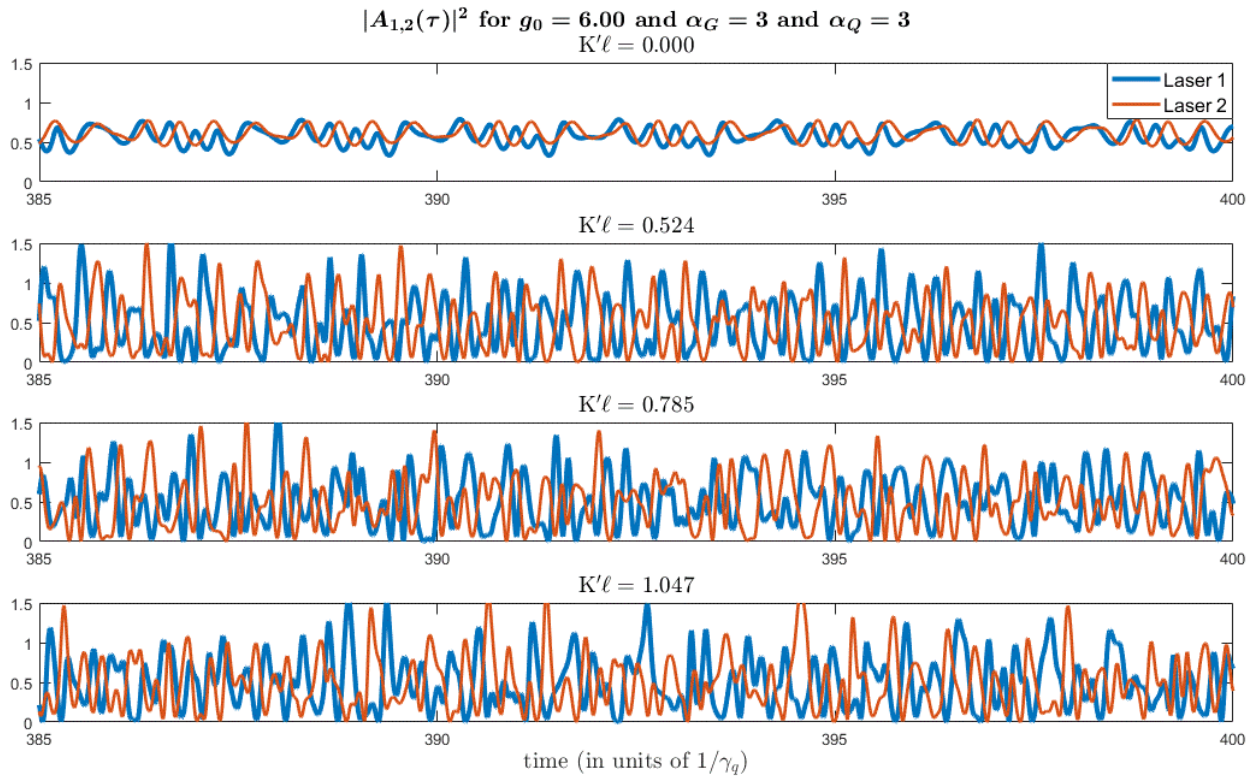

Figure 3.44: Same as a subset of the subplots in Figure 3.43, except for non-zero α-factors.

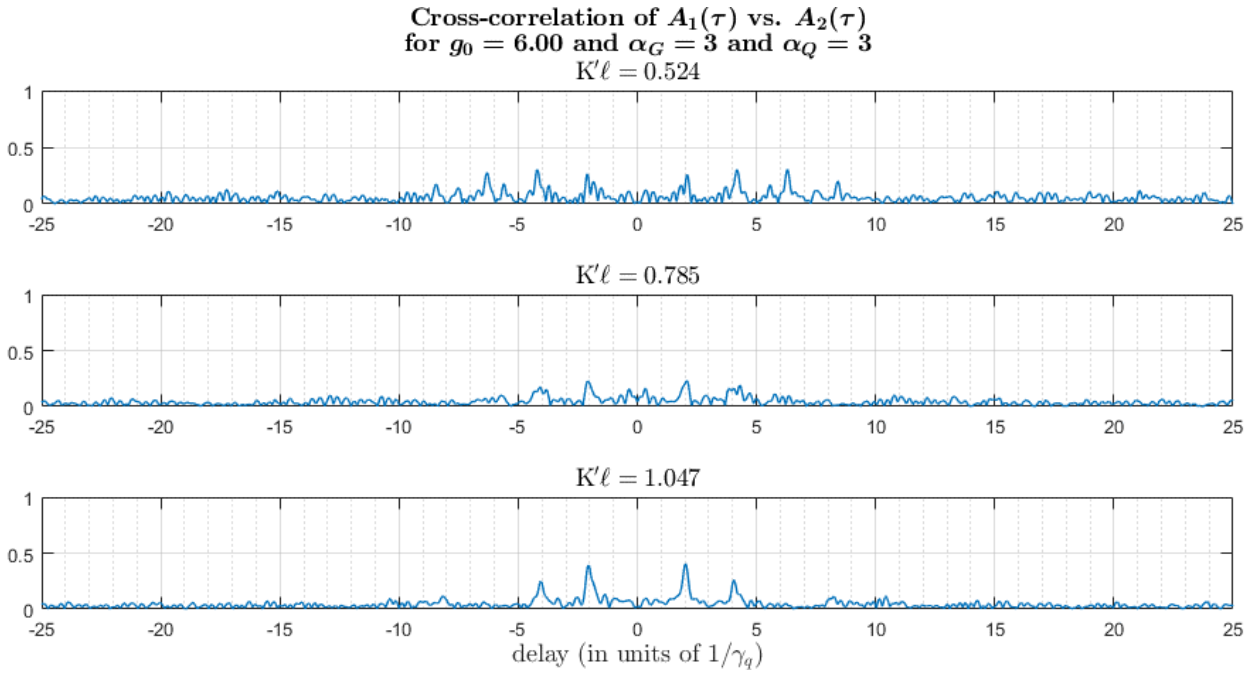

Figure 3.45: Cross-correlation plots of the two lasers' complex-valued amplitudes, corresponding to the same simulation results in Figure 3.44, for the respective coupling parameter values.

3.6.3 Fully cross-coupled lasers and robust subharmonic mode-locking

The results in Figure 3.46 provide evidence that the subharmonic mode-locked operation phenomenon (see SECTION 3.4.3) can occur in the presence of noise perturbations and non-zero linewidth enhancement factors, lending credence to its stability and robustness to some degree. In the figure, due to the amplitude-phase coupling due to the α-factors, there can be irregular modulations of the pulse peak amplitudes and possibly a noticeable worsening of the pulse quality. In any case, however, the pulses for each laser are separated by twice the roundtrip time, the two lasers alternately generate pulses in an anti-synchronous manner, and the lasers maintain a 90° phase difference (in complex amplitudes) between each other, all in the presence of noise and α-factors, as is consistent with the properties characteristic of the subharmonic regime.

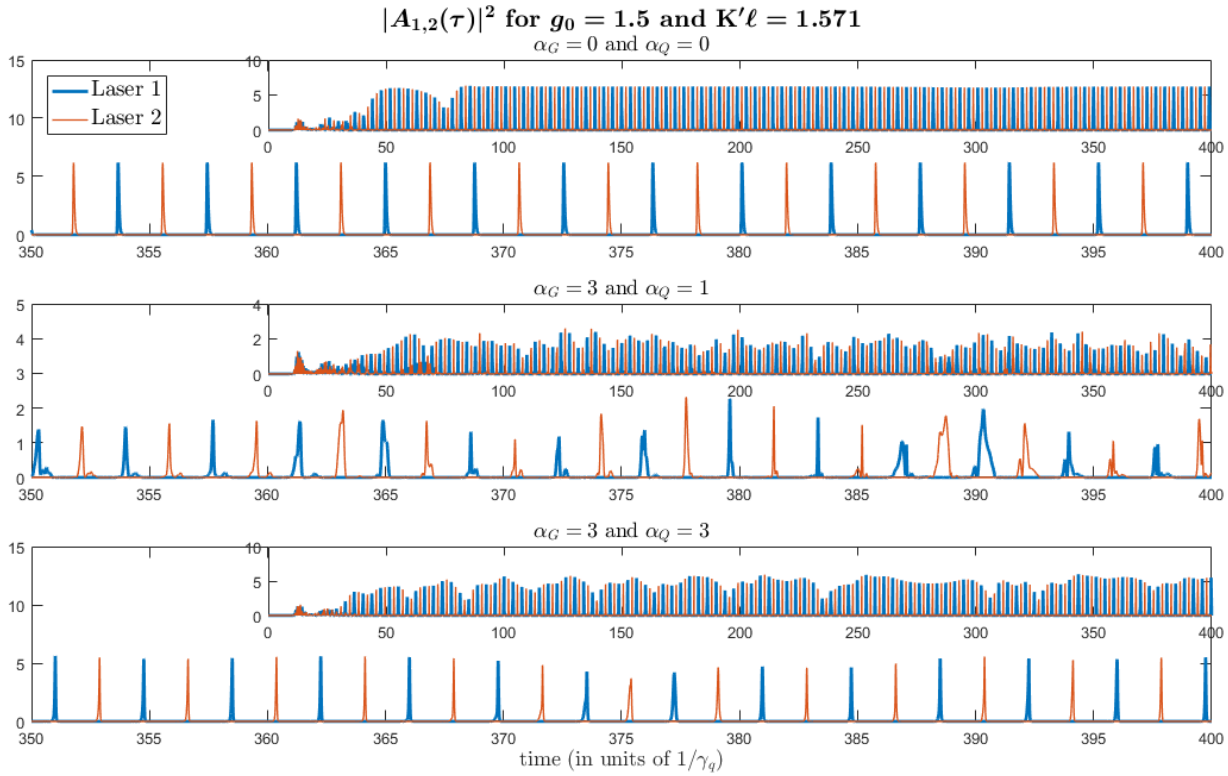

Figure 3.46: Temporal profile of fully cross-coupled lasers simulated from noise, operating in the subharmonic mode-locked regime, for varying α-factors. For these simulations, $T = 1.875$, in order to facilitate comparisons to the corresponding results in SECTION 3.4.3 and SECTION 3.5.3. Table 3.2 lists the parameter values not specified here.

Furthermore, anti-synchronous behavior can also occur in at higher values of unsaturated gain. As mentioned in SECTION 3.4.3, there are other "half-harmonic" mode-locked regimes for which the lasers are 90° out-of-phase and pulse anti-synchronously. Finally, Figure 3.47 and Figure 3.48 show an intriguing phenomenon obtained from the noise simulations of the lasers at high unsaturated gain g_0. Here, there is a nearly perfectly delay-synchronized temporal power profile of the cross-coupled lasers for each of three cases of linewidth enhancement factors, with the power fluctuations particularly noticeable for the non-zero α-factors. Interestingly, the temporal profile for each laser is somewhat periodic at the subharmonic rate, and the delay between time series for the two lasers is approximately one roundtrip for each set of α-factors.

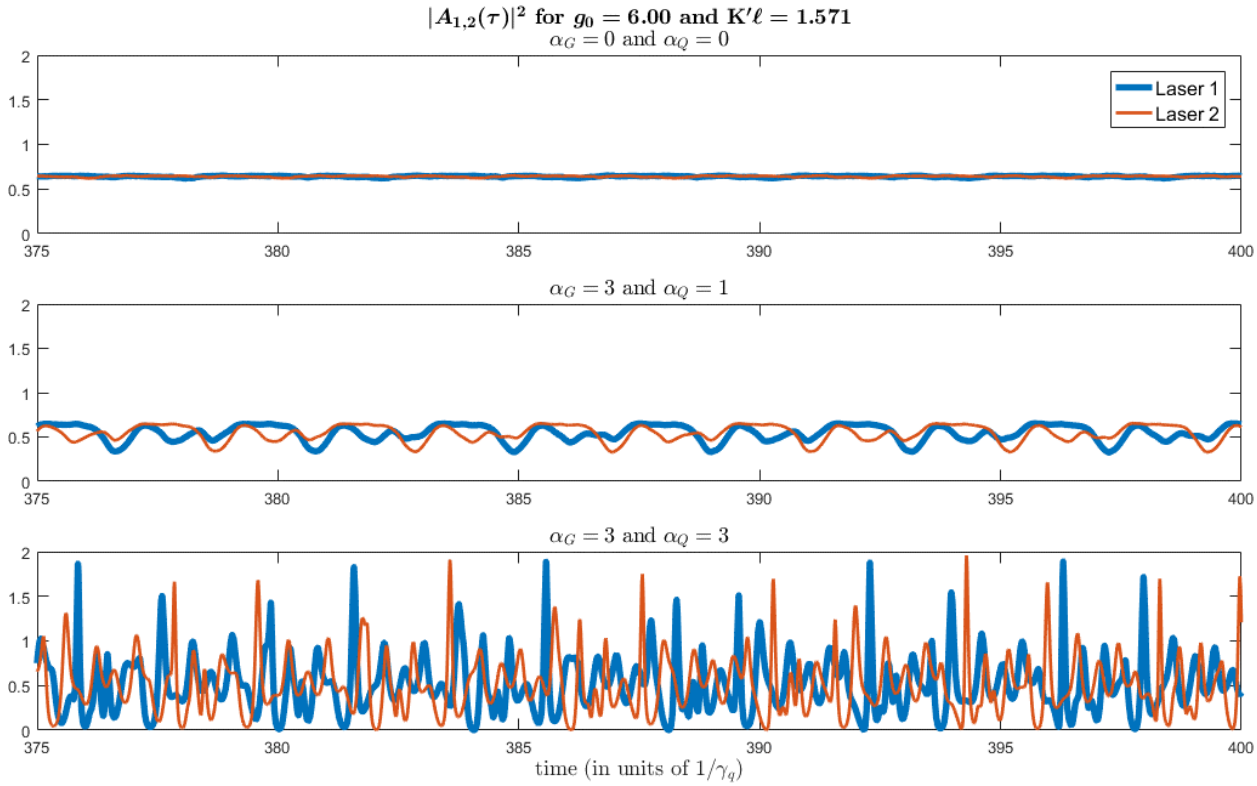

Figure 3.47: Temporal power for two fully cross-coupled lasers with large unsaturated gain values, as the α-factors are varied. Note that the top subplot here is the same as the bottom subplot of Figure 3.43. Recall that for other coupling values in that figure, the inclusion of the non-zero α-factors disturbed the delayed synchrony. On the other hand, for fully cross-coupled lasers, delayed synchrony is preserved even with non-zero α-factors, as is evidenced more clearly in Figure 3.48. Table 3.2 lists the parameter values not specified here.

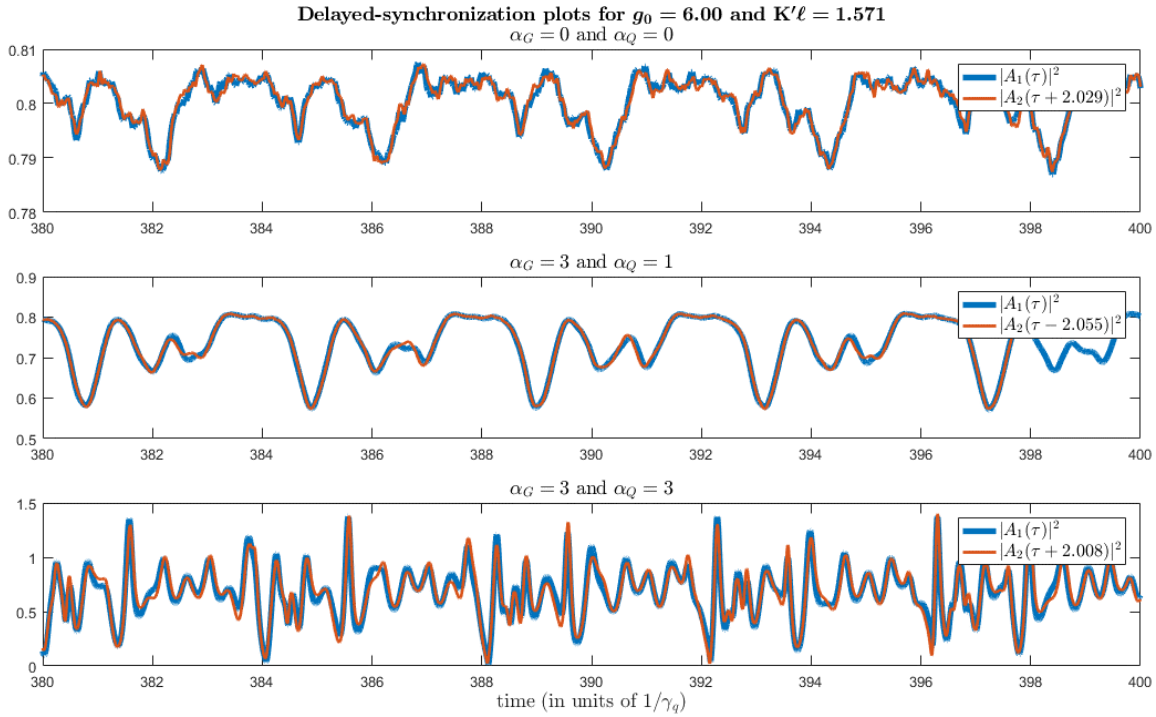

Figure 3.48: Same as a zoomed-in version of Figure 3.47, except that the time series for the second laser is shifted by the delay corresponding to the maximum peak in the cross-correlation profile of $A_1(\tau)$ vs. $A_2(\tau)$. Note that in all three subplots, this delay is approximately the roundtrip time $T = 2$. Also note that the vertical scales of the three subplots are different.

3.7 Conclusion

In conclusion, this chapter has investigated, explored, and uncovered a rich variety of passive coupling dynamics and synchronization phenomena of two identical, evanescently/directionally coupled, mode-locked, ring-cavity semiconductor lasers. The results show that passive coupling can 1) detune the lasers from their solitary lasing modes by up to half the cavity free spectral range, 2) induce symmetry-breaking effects that lead to strong modulations of and delayed synchronization between the two lasers' pulse trains, 3) provide a mechanism for the lasers to evolve from an initial unsynchronized state to nearly-perfect, in-phase synchronization, and 4) destabilize mode-locked and CW operation of the solitary lasers. The state of perfect synchrony of the lasers' temporal power / pulse trains is tied to the lasers acquiring a 0° (or also 180°) phase difference between their complex field amplitudes, whereas the delay-synchronized

behavior is tied to a 90° phase difference in the complex amplitudes. Two coupled lasers initialized with some other initial phase and/or amplitude differences can also evolve over time toward achieving one of the two aforementioned behaviors: in-phase, perfect synchronization or 90° out-of-phase, delayed synchronization. As a special case of the delayed synchrony, two fully cross-coupled lasers are capable of producing anti-synchronous mode-locked pulse trains, each at a subharmonic of the solitary laser's fundamental repetition rate, determined by the sum of the lasers' roundtrip times. For example, in the case of two identical lasers, the subharmonic repetition rate is one half of the fundamental rate, and the energy per pulse in the subharmonic regime can be close to twice that of each pulse in the fundamental mode-locked regime.

A third scenario is a degradation or even a complete lack of synchronization. In particular, non-zero linewidth enhancement factors introduce amplitude-phase coupling processes into the system that can disrupt the synchronization dynamics of the two lasers earlier described. Unequal α-factors (i.e. when $\alpha_G \neq \alpha_Q$) break up the mode-locked pulsing regime and the (delayed) synchrony. Equalizing the α-factors can aid the recovery of the mode-locked pulse quality and help realign the two lasers' pulse arrival times (at least for identical lasers), but the correlation between the two lasers' fluctuating pulse heights/amplitudes is seen to remain poor. Hence, the synchronization behavior is sensitive to the linewidth enhancement factors' effects.

In addition, the bifurcation analysis and simulations show that this coupled-laser system supports a fair degree of bistability or multistability between the different dynamical regimes. Finally, most of the above phenomena can be observed even in the presence of noise and/or non-zero α-factors; in particular, the subharmonic regime is relatively robust with regard to both aspects.

CHAPTER 4

Conclusion

4.1 Summary

This thesis has presented the results of theoretical and numerical investigations of two different passively coupled laser systems: 1) an array of fiber amplifiers in continuous-wave operation and coupled via a spatially-filtered ring geometry, and 2) two evanescently/directionally coupled, unidirectional-ring-cavity, mode-locked semiconductor lasers.

CHAPTER 2 used the results of numerical simulations to elucidate the phasing dynamics for the fiber laser array, including clear demonstrations of the time scale within which the passive phasing processes occur. Phase-locking was shown to occur on a much quicker time scale than the transient dynamics of power and gain, with the array reaching a locked state well before the onset of relaxation oscillations after the laser is turned on. In addition, it was found that the phase-locked state is quickly recovered after perturbation from steady-state, within merely a few cavity roundtrips, while the relaxation oscillation transients require many more roundtrips before recovery to steady-state. The results on passive phasing dynamics were found to be consistent and in agreement with previous theoretical (steady-state analysis) and experimental results. Next, the focus shifted to evaluating the role of Kerr nonlinearity in the combining architecture. Qualitative examination of the far-field output intensity profiles along with quantitative assessment of the combining efficiency for varying values of the nonlinear coefficient revealed

the nonlinearity's detrimental effect with regard to the system's ability to achieve in-phase coherent locking. The underlying physics was explained in the context of coincident mode theory, in that Kerr nonlinearity, through the mechanisms of spectral broadening and four-wave mixing, leads to the excitation of lossy axial modes at the expense of less lossy modes of the composite cavity, thus frustrating the system's self-organization processes.

CHAPTER 3 presented the results of numerical simulations and numerical bifurcation analysis that detailed the dynamics of synchronization and showcased the variety of interesting phenomena for a system of two identical, coupled mode-locked semiconductor lasers. The mathematical model was developed through the application of coupled-mode theory to the traveling wave equations and subsequent conversion of this partial differential equation system to a delay differential equation system. The DDE system was then theoretically investigated using methods of numerical simulations and bifurcation analysis. The results sections first discussed the coupling-induced frequency detuning (relative to the lasing modes of the solitary/uncoupled lasers) to which the lasers are subject, explained the physical mechanism by which coupling causes this detuning, and showed that the frequency shifts that arise from numerical simulation of the (multi-longitudinal-mode) DDE model match theoretical calculations using the DDE model. The numerical results and the theoretical approach both showed that the shift can range from zero to up to half the cavity free spectral range. Next, it was shown that the two lasers can achieve with respect to each other 1) perfect, in-phase synchronization, 2) 90° out-of-phase, delayed synchronization, or 3) lack of synchronization, as well as a number of other complex dynamics and behaviors. The chapter presented a special case of delayed synchronization in which the two lasers are fully cross-coupled, i.e. when the

action of the directional coupler leads each laser to transfers 100% of its circulating radiation to the other cavity. Here, the two lasers are capable of operating in perfect anti-synchrony in a well-defined and robust subharmonic mode-locked regime, in which each laser generates pulses at half of the fundamental mode-locked repetition rate. Also seen are other fractional (e.g. $3/2$ and $5/2$) harmonic mode-locked regimes. The chapter further investigated how the different synchronization properties and other behaviors/phenomena are affected by 1) the initial state, due to bistability/multistability between the dynamical regimes, 2) the coupling parameter, 3) the unsaturated gain / pump strength, 4) linewidth enhancement factors, and 5) noise.

4.2 Future work

The research work in passive coherent beam combining of fiber laser arrays has several interesting directions for future study:

- Include the resonant Kramers-Kronig nonlinearity (and perhaps other nonlinear effects, e.g. thermal variations), and compare its role in externally- vs. internally-coupled arrays
- Extend the model to consider mode-locked fiber laser arrays, as was done similarly in the past for internally-coupled arrays [107]
- Extend the model to account for transverse spatial considerations
- Identify or suggest possible robust and effective methods to overcome the limitations presented by external path differences in the coupling optics for the spatially-filtered ring geometry coupling architecture
- Apply the modeling approach to other externally-coupled array combining schemes that do not have the design limitations of this spatially-filtered ring geometry

The research work in passively coupled mode-locked semiconductor laser arrays also has a broad scope for further investigation, particularly with the following considerations:

- Reformulate the DDE model with the separation of the magnitude and phase of the lasers' complex amplitudes in order to facilitate (via direct numerical simulation) tracking of the evolution of the phase difference between the two lasers
- Understand the physics and factors that determine the amount of delay between the two lasers' output power temporal profiles when delay-synchronized, e.g. in Figure 3.16.
- Perform further bifurcation analysis of the effects of linewidth enhancement factors
- Examine the system's evolution from other initial histories, constant or time-varying
- As it relates to the stochastic version of the DDE model (i.e. with the inclusion of noise source terms), perform an analysis using a more rigorous probabilistic/statistical methodology and framework, include a treatment of various other types of noise, and/or adopt/implement an appropriate physical model for a spontaneous emission type of noise
- Extensively consider the effects of non-identical cavity lengths / roundtrip delay times $T_1 \neq T_2$, including their role in tuning the pulse repetition rate and frequency comb properties for different coupling strengths
- Investigate in depth the coupled system for non-identical pump currents $g_{01} \neq g_{02}$
- Explore of other sources of asymmetry in this system
- Apply a modulation or time-varying profile to the unsaturated gain / injection current
- Investigate cases of three or more adjacently-coupled, mode-locked semiconductor lasers
- Revise the mathematical model to be more closely and precisely tied to real experimental setups, and use it to develop practical applications

APPENDICES

APPENDIX A

Derivation of the coupled mode-locked semiconductor lasers model

Starting from the traveling-wave equation model given in SECTION 3.3.2, "the DDE model" is derived in APPENDIX A.1. This set of six DDEs is the one used for the numerical simulations (see APPENDIX B.2) that account for the bulk of the results presented in CHAPTER 3. Starting from this system of six DDEs, APPENDIX A.2.1 provides the subsequent derivation of "the rotating-wave DDE model" that consists of six DDEs and two algebraic "constraint" equations. In the process, the DDE system is reformulated into eight DDEs, specifically with the equations for the complex-valued amplitudes separated into magnitude and phase. This reformulation can enable numerical simulations that track the evolution of the phase time; however, this thesis work does not follow up on this aspect, and instead it is included in the list of work to be done in the future. Finally, APPENDIX A.2.2 shows the derivation of the formulae that can be used, given an initial set of parameter values, to solve for isolated equilibria (in this case, continuous-wave solutions) of the DDE system. These equilibria can be used as initial starting points for the bifurcation analysis / numerical continuation routines (see APPENDIX B.3).

A.1 Derivation of "the DDE model" (for numerical simulations)

Traveling-wave equation model
(note that the equations below do not include noise source terms as in SECTION 3.6)

Amplitude and carrier density equations for the absorber and gain sections…

$$\boxed{\frac{\partial E_{1,2}(t,z)}{\partial z} + \frac{1}{v}\frac{\partial E_{1,2}(t,z)}{\partial t} = \frac{g_r \Gamma_r}{2}(1 - i\alpha_r)\left(N_{(1,2),r}(t,z) - N_r^{tr}\right)E_{1,2}(t,z)}$$

$$\boxed{\frac{\partial N_{(1,2),r}(t,z)}{\partial t} = J_{(1,2),r} - \gamma_r N_{(1,2),r}(t,z) - v g_r \Gamma_r \left(N_{(1,2),r}(t,z) - N_r^{tr}\right)\left|E_{1,2}(t,z)\right|^2}$$

Amplitude equations for the passive section without coupling…

$$\boxed{\frac{\partial E_{1,2}(t,z)}{\partial z} + \frac{1}{v}\frac{\partial E_{1,2}(t,z)}{\partial t} = 0}$$

Amplitude equations for the passive section with coupling…

$$\boxed{\frac{\partial E_{1,2}(t,z)}{\partial z} + \frac{1}{v}\frac{\partial E_{1,2}(t,z)}{\partial t} = +i\mathrm{K}_{12,21}E_{2,1}(t,z)}$$

Equations describing the actions of the spectral filters

$\boxed{\hat{E}_{1,2}\left(w, z_1 + L_{1,2}\right) = \hat{f}(w)\hat{E}_{1,2}(w, z_5)}$, where the ^ indicates Fourier Transform

Ring cavity boundary conditions

$$\boxed{E_{1,2}\left(t, z + L_{1,2}\right) = E_{1,2}(t,z)}$$

Variables/parameters used in the above

$t \equiv$ time coordinate

$z \equiv$ spatial coordinate

- $z_1 < z < z_2$: Passive without coupling
- $z_2 < z < z_3$: Absorber
- $z_3 < z < z_4$: Gain
- $z_4 < z < z_5$: Passive with coupling
- $z_5 < z < z_1 + L_{1,2}$: Spectral filter

Subscripts 1,2 refer to the two individual lasers

Subscript $r = g, q$ refers to the gain, absorber sections

$E_{1,2}(t,z) \equiv$ E-field envelope

$L_{1,2} \equiv$ Cavity length

$N_{(1,2),(g,q)}(t,z) \equiv$ Carrier densities in gain, absorber sections

$N_{g,q}^{tr} \equiv$ Carrier densities at transparency threshold

$v \equiv$ Light group velocity

$\alpha_{g,q} \equiv$ Linewidth enhancement factors

$g_{g,q} \equiv$ Differential gains

$\Gamma_{g,q} \equiv$ Transverse modal fill factors

$\mathrm{K}_{12,21} \equiv$ Coupling coefficients; refers to coupling from 2→1, 1→2

$\gamma_{g,q} \equiv$ Carrier density relaxation rates

$J_{(1,2),(g,q)} \equiv$ Injection currents (note that $J_{(1,2),q} = 0$)

Coordinate change $(t,z) \rightarrow (\tau, \zeta)$ to a retarded time frame that moves along with the circulating waves/pulses in the laser cavities

$\tau = \gamma_q(t - z/v)$

$\zeta = z\gamma_q/v$

Derivation of the traveling-wave equation model after the coordinate change

$$\boxed{\frac{\partial A_{1,2}(\tau,\zeta)}{\partial\zeta}=\frac{1}{2}(1-i\alpha_r)n_{(1,2),r}(\tau,\zeta)A_{1,2}(\tau,\zeta)}\leftarrow \text{For the absorber and gain sections}$$

Start with $\frac{\partial E_{1,2}}{\partial z}+\frac{1}{v}\frac{\partial E_{1,2}}{\partial t}=\frac{g_r\Gamma_r}{2}(1-i\alpha_r)\left(N_{(1,2),r}-N_r^{tr}\right)E_{1,2}$

$\frac{\partial E_{1,2}}{\partial z}=\frac{\partial E_{1,2}}{\partial\zeta}\frac{\partial\zeta}{\partial z}+\frac{\partial E_{1,2}}{\partial\tau}\frac{\partial\tau}{\partial z}=\frac{\partial E_{1,2}}{\partial\zeta}\frac{\gamma_q}{v}-\frac{\partial E_{1,2}}{\partial\tau}\frac{\gamma_q}{v}$

$\frac{\partial E_{1,2}}{\partial t}=\frac{\partial E_{1,2}}{\partial\zeta}\frac{\partial\zeta}{\partial t}+\frac{\partial E_{1,2}}{\partial\tau}\frac{\partial\tau}{\partial t}=0+\frac{\partial E_{1,2}}{\partial\tau}\gamma_q$

$\rightarrow\frac{\partial E_{1,2}}{\partial z}+\frac{1}{v}\frac{\partial E_{1,2}}{\partial t}=\frac{\partial E_{1,2}}{\partial\zeta}\frac{\gamma_q}{v}-\frac{\partial E_{1,2}}{\partial\tau}\frac{\gamma_q}{v}+0+\frac{\partial E_{1,2}}{\partial\tau}\frac{\gamma_q}{v}=\frac{\partial E_{1,2}}{\partial\zeta}\frac{\gamma_q}{v}$

$\rightarrow\frac{\partial E_{1,2}}{\partial\zeta}\frac{\gamma_q}{v}=\frac{g_r\Gamma_r}{2}(1-i\alpha_r)\left(N_{(1,2),r}-N_r^{tr}\right)E_{1,2}$

$\rightarrow\frac{\partial E_{1,2}}{\partial\zeta}=\frac{v}{\gamma_q}\frac{g_r\Gamma_r}{2}(1-i\alpha_r)\left(N_{(1,2),r}-N_r^{tr}\right)E_{1,2}$

$\frac{\partial E_{1,2}}{\partial\zeta}=\frac{1}{2}(1-i\alpha_r)n_{(1,2),r}E_{1,2}$

where $n_{(1,2),r}\equiv\frac{vg_r\Gamma_r}{\gamma_q}\left(N_{(1,2),r}-N_r^{tr}\right)$

$\frac{\partial A_{1,2}}{\partial\zeta}=\frac{1}{2}(1-i\alpha_r)n_{(1,2),r}A_{1,2}$

where $A_{1,2}\equiv E_{1,2}\sqrt{\frac{vg_g\Gamma_g}{\gamma_q}}$

$$\boxed{\frac{\partial n_{(1,2),g}(\tau,\zeta)}{\partial\tau}=j_{(1,2),g}-\Gamma n_{(1,2),g}(\tau,\zeta)-n_{(1,2),g}(\tau,\zeta)\left|A_{1,2}(\tau,\zeta)\right|^2}\leftarrow \text{For the gain}$$

Start with $\frac{\partial N_{(1,2),g}}{\partial t}=\frac{\partial\left(N_{(1,2),g}-N_g^{tr}\right)}{\partial t}=J_{(1,2),g}-\gamma_gN_{(1,2),g}-vg_g\Gamma_g\left(N_{(1,2),g}-N_g^{tr}\right)\left|E_{1,2}\right|^2$

$\frac{\partial N_{(1,2),g}}{\partial t}=\frac{\partial N_{(1,2),g}}{\partial\tau}\frac{\partial\tau}{\partial t}+\frac{\partial N_{(1,2),g}}{\partial\zeta}\frac{\partial\zeta}{\partial t}=\frac{\partial N_{(1,2),g}}{\partial\tau}\gamma_q+0=\gamma_q\frac{\partial\left(N_{(1,2),g}-N_g^{tr}\right)}{\partial\tau}$

$\rightarrow\gamma_q\frac{\partial\left(N_{(1,2),g}-N_g^{tr}\right)}{\partial\tau}=J_{(1,2),g}-\gamma_gN_{(1,2),g}-vg_g\Gamma_g\left(N_{(1,2),g}-N_g^{tr}\right)\left|E_{1,2}\right|^2$

$n_{(1,2),g}=\frac{vg_g\Gamma_g}{\gamma_q}\left(N_{(1,2),g}-N_g^{tr}\right)\rightarrow\frac{\partial n_{(1,2),g}}{\partial\tau}=\frac{1}{\gamma_q}\frac{vg_g\Gamma_g}{\gamma_q}\gamma_q\frac{\partial\left(N_{(1,2),g}-N_g^{tr}\right)}{\partial\tau}$

$\rightarrow\frac{\partial n_{(1,2),g}}{\partial\tau}=\frac{vg_g\Gamma_g}{\gamma_q^2}\left(J_{(1,2),g}-\gamma_gN_{(1,2),g}\right)-\frac{vg_g\Gamma_g}{\gamma_q}\frac{vg_g\Gamma_g}{\gamma_q}\left(N_{(1,2),g}-N_g^{tr}\right)\left|E_{1,2}\right|^2$

$\rightarrow\frac{\partial n_{(1,2),g}}{\partial\tau}=\frac{vg_g\Gamma_g}{\gamma_q^2}\left(J_{(1,2),g}-\gamma_gN_g^{tr}\right)-\frac{1}{\gamma_q}\frac{vg_g\Gamma_g}{\gamma_q}\gamma_g\left(N_{(1,2),g}-N_g^{tr}\right)-\frac{vg_g\Gamma_g}{\gamma_q}n_{(1,2),g}\left(\frac{\gamma_q}{vg_g\Gamma_g}\left|A_{1,2}\right|^2\right)$

$\rightarrow\frac{\partial n_{(1,2),g}}{\partial\tau}=j_{(1,2),g}-\Gamma n_{(1,2),g}-n_{(1,2),g}\left|A_{1,2}\right|^2$

where $j_{(1,2),g}\equiv\frac{vg_g\Gamma_g}{\gamma_q^2}\left(J_{(1,2),g}-\gamma_gN_g^{tr}\right)$ and $\Gamma\equiv\gamma_g/\gamma_q$

$$\boxed{\frac{\partial n_{(1,2),q}(\tau,\zeta)}{\partial\tau}=-j_q-n_{(1,2),q}(\tau,\zeta)-sn_{(1,2),q}(\tau,\zeta)\left|A_{1,2}(\tau,\zeta)\right|^2}\leftarrow \text{For the absorber}$$

Start with $\frac{\partial N_{(1,2),q}}{\partial t}=\frac{\partial\left(N_{(1,2),q}-N_q^{tr}\right)}{\partial t}=J_{(1,2),q}-\gamma_qN_{(1,2),q}-vg_q\Gamma_q\left(N_{(1,2),q}-N_q^{tr}\right)\left|E_{1,2}\right|^2$

$\frac{\partial N_{(1,2),q}}{\partial t}=\frac{\partial N_{(1,2),q}}{\partial\tau}\frac{\partial\tau}{\partial t}+\frac{\partial N_{(1,2),q}}{\partial\zeta}\frac{\partial\zeta}{\partial t}=\frac{\partial N_{(1,2),q}}{\partial\tau}\gamma_q+0=\gamma_q\frac{\partial\left(N_{(1,2),q}-N_q^{tr}\right)}{\partial\tau}$

Also, recall that $J_{(1,2),q}=0\rightarrow\gamma_q\frac{\partial\left(N_{(1,2),q}-N_q^{tr}\right)}{\partial\tau}=0-\gamma_qN_{(1,2),q}-vg_q\Gamma_q\left(N_{(1,2),q}-N_q^{tr}\right)\left|E_{1,2}\right|^2$

$n_{(1,2),q}=\frac{vg_q\Gamma_q}{\gamma_q}\left(N_{(1,2),q}-N_q^{tr}\right)\rightarrow\frac{\partial n_{(1,2),q}}{\partial\tau}=\frac{1}{\gamma_q}\frac{vg_q\Gamma_q}{\gamma_q}\gamma_q\frac{\partial\left(N_{(1,2),q}-N_q^{tr}\right)}{\partial\tau}$

$$\rightarrow \frac{\partial n_{(1,2),q}}{\partial \tau} = -\frac{v g_q \Gamma_q}{\gamma_q^2}\gamma_q N_{(1,2),q} - \frac{v g_q \Gamma_q}{\gamma_q}\frac{v g_q \Gamma_q}{\gamma_q}\left(N_{(1,2),q} - N_q^{tr}\right)\left|E_{1,2}\right|^2$$

$$\rightarrow \frac{\partial n_{(1,2),q}}{\partial \tau} = -\frac{v g_q \Gamma_q}{\gamma_q^2}\gamma_q N_q^{tr} - \frac{1}{\gamma_q}\frac{v g_q \Gamma_q}{\gamma_q}\gamma_q\left(N_{(1,2),q} - N_q^{tr}\right) - \frac{v g_q \Gamma_q}{\gamma_q} n_{(1,2),q}\left(\frac{\gamma_q}{v g_g \Gamma_g}\left|A_{1,2}\right|^2\right)$$

$$\rightarrow \frac{\partial n_{(1,2),q}}{\partial \tau} = -j_q - n_{(1,2),q} - s n_{(1,2),q}\left|A_{1,2}\right|^2$$

where $j_q \equiv \frac{v g_q \Gamma_q}{\gamma_q} N_q^{tr}$ and $s \equiv \frac{g_q \Gamma_q}{g_g \Gamma_g}$

$\boxed{\frac{\partial A_{1,2}}{\partial \zeta} = 0}$ ← For the passive section without coupling

Start with $\frac{\partial E_{1,2}}{\partial z} + \frac{1}{v}\frac{\partial E_{1,2}}{\partial t} = 0$

$$\rightarrow \frac{\gamma_q}{v}\frac{\partial E_{1,2}}{\partial \zeta} = 0 \rightarrow \frac{\partial E_{1,2}}{\partial \zeta} = 0 \rightarrow \frac{\partial A_{1,2}}{\partial \zeta} = 0$$

$\boxed{\frac{\partial A_{1,2}}{\partial \zeta} = i\mathrm{K}'_{12,21} A_{2,1}}$ ← For the passive section with coupling

Start with $\frac{\partial E_{1,2}}{\partial z} + \frac{1}{v}\frac{\partial E_{1,2}}{\partial t} = i\mathrm{K}_{12,21} E_{2,1}$

$$\rightarrow \frac{\gamma_q}{v}\frac{\partial E_{1,2}}{\partial \zeta} = i\mathrm{K}_{12,21} E_{2,1} \rightarrow \frac{\partial E_{1,2}}{\partial \zeta} = i\mathrm{K}'_{12,21} E_{2,1} \rightarrow \frac{\partial A_{1,2}}{\partial \zeta} = i\mathrm{K}'_{12,21} A_{2,1}$$

where $\mathrm{K}'_{12,21} \equiv \frac{v}{\gamma_q}\mathrm{K}_{12,21}$

New variables/parameters introduced above

$\tau \equiv$ Normalized time coordinate $= \gamma_q(t - z/v)$

$\zeta \equiv$ Normalized spatial coordinate $= z\gamma_q/v$

$A_{1,2}(\tau, \zeta) \equiv$ Normalized amplitude $= E_{1,2}(t, z)\sqrt{v g_g \Gamma_g / \gamma_q}$

$n_{g,q}(\tau, \zeta) = v g_{g,q} \Gamma_{g,q}\left(N_{g,q}(t, z) - N_{g,q}^{tr}\right)/\gamma_q$

$j_{(1,2),g} = v g_g \Gamma_g \left(J_{(1,2),g} - \gamma_g N_g^{tr}\right)/\gamma_q^2$

$\Gamma = \gamma_g/\gamma_q$

$j_q = v g_q \Gamma_q N_q^{tr}/\gamma_q$

$s = \left(g_q \Gamma_q\right)/\left(g_g \Gamma_g\right)$

$\mathrm{K}'_{12,21} \equiv$ Normalized coupling coefficient $= \frac{v}{\gamma_q}\mathrm{K}_{12,21}$

Relations between the amplitudes in different sections for each laser cavity

$\boxed{A_{1,2}(\tau, \zeta_2) = A_{1,2}(\tau, \zeta_1)}$ ← Passive section without coupling

Start with $\frac{\partial A_{1,2}}{\partial \zeta} = 0$

$\rightarrow \partial A_{1,2} = 0 d\zeta$

$\rightarrow A_{1,2} =$ constant

$\rightarrow A_{1,2}(\tau, \zeta_2) = A_{1,2}(\tau, \zeta_1)$

$\boxed{A_{1,2}(\tau, \zeta_3) = e^{-(1 - i\alpha_q) Q_{1,2}(\tau)/2} A_{1,2}(\tau, \zeta_2)}$ ← Absorber section

Start with $\frac{\partial A_{1,2}}{\partial \zeta} = \frac{1}{2}\left(1 - i\alpha_q\right) n_{(1,2),q} A_{1,2} \rightarrow \frac{\partial A_{1,2}}{A_{1,2}} = \frac{1}{2}\left(1 - i\alpha_q\right) n_{(1,2),q} d\zeta$

$$\rightarrow \int_{\zeta_2}^{\zeta_3} \frac{\partial A_{1,2}}{A_{1,2}} = \frac{1}{2}\left(1 - i\alpha_q\right) \int_{\zeta_2}^{\zeta_3} n_{(1,2),q} d\zeta = -\frac{\left(1-i\alpha_q\right) Q_{1,2}(\tau)}{2}$$

where $Q_{1,2}(\tau) \equiv -\int_{\zeta_2}^{\zeta_3} n_{(1,2),q} d\zeta$

$$\rightarrow \ln\left(A_{1,2}(\tau,\zeta_3)\right) - \ln(A_{1,2}(\tau,\zeta_2) = \ln\left(\frac{A_{1,2}(\tau,\zeta_3)}{A_{1,2}(\tau,\zeta_2)}\right) = -\frac{\left(1-i\alpha_q\right) Q_{1,2}(\tau)}{2}$$

$$\rightarrow A_{1,2}(\tau,\zeta_3) = e^{-\left(1-i\alpha_q\right) Q_{1,2}(\tau)/2} A_{1,2}(\tau,\zeta_2)$$

$$\boxed{A_{1,2}(\tau,\zeta_4) = e^{\left(1-i\alpha_g\right) G_{1,2}(\tau)/2} A_{1,2}(\tau,\zeta_3)} \leftarrow \text{Gain section}$$

Start with $\frac{\partial A_{1,2}}{\partial \zeta} = \frac{1}{2}\left(1 - i\alpha_g\right) n_{(1,2),g} A_{1,2} \rightarrow \frac{\partial A_{1,2}}{A_{1,2}} = \frac{1}{2}\left(1 - i\alpha_g\right) n_{(1,2),g} d\zeta$

$$\rightarrow \int_{\zeta_3}^{\zeta_4} \frac{\partial A_{1,2}}{A_{1,2}} = \frac{1}{2}\left(1 - i\alpha_g\right) \int_{\zeta_3}^{\zeta_4} n_{(1,2),g} d\zeta = \frac{\left(1-i\alpha_g\right) G_{1,2}(\tau)}{2}$$

where $G_{1,2}(\tau) \equiv \int_{\zeta_3}^{\zeta_4} n_{(1,2),g} d\zeta$

$$\rightarrow \ln\left(A_{1,2}(\tau,\zeta_4)\right) - \ln\left(A_{1,2}(\tau,\zeta_3)\right) = \ln\left(\frac{A_{1,2}(\tau,\zeta_4)}{A_{1,2}(\tau,\zeta_3)}\right) = \frac{\left(1-i\alpha_g\right) G_{1,2}(\tau)}{2}$$

$$\rightarrow A_{1,2}(\tau,\zeta_4) = e^{\left(1-i\alpha_g\right) G_{1,2}(\tau)/2} A_{1,2}(\tau,\zeta_3)$$

$$\boxed{\begin{bmatrix} A_1(\tau,\zeta_5) \\ A_2(\tau,\zeta_5) \end{bmatrix} = \begin{bmatrix} \cos(\mathrm{K}'\ell) & \frac{i}{\mathrm{K}''}\sin(\mathrm{K}'\ell) \\ i\mathrm{K}''\sin(\mathrm{K}'\ell) & \cos(\mathrm{K}'\ell) \end{bmatrix} \begin{bmatrix} A_1(\tau,\zeta_4) \\ A_2(\tau,\zeta_4) \end{bmatrix}} \leftarrow \text{Passive section with coupling}$$

Start with system of equations $\begin{cases} \frac{\partial A_1}{\partial \zeta} = i\mathrm{K}'_{12} A_2 \\ \frac{\partial A_2}{\partial \zeta} = i\mathrm{K}'_{21} A_1 \end{cases}$

$$A_2 = -\frac{i}{K'_{12}} \frac{\partial A_1}{\partial \zeta} \rightarrow \frac{\partial A_2}{\partial \zeta} = -\frac{i}{K'_{12}} \frac{\partial^2 A_1}{(\partial \zeta)^2} = i\mathrm{K}'_{21} A_1$$

$$\rightarrow \frac{\partial^2 A_1}{(\partial \zeta)^2} + (\mathrm{K}'_{12}\mathrm{K}'_{21}) A_1 = \frac{\partial^2 A_1}{(\partial \zeta)^2} + (\mathrm{K}')^2 A_1 = 0, \text{ where } \mathrm{K}' \equiv \sqrt{\mathrm{K}'_{12}\mathrm{K}'_{21}}$$

$$\rightarrow \begin{cases} A_1(\tau,\zeta) = A_{0_1} \cos\left(\mathrm{K}'(\zeta - \zeta_4)\right) + A_{0_2} \sin\left(\mathrm{K}'(\zeta - \zeta_4)\right) \\ A_2(\tau,\zeta) = i\mathrm{K}'' A_{0_1} \sin\left(\mathrm{K}'(\zeta - \zeta_4)\right) - i\mathrm{K}'' A_{0_2} \cos\left(\mathrm{K}'(\zeta - \zeta_4)\right) \end{cases}$$

where A_{0_1} and A_{0_2} are constants (with respect to ζ), and $\mathrm{K}'' \equiv \sqrt{\frac{\mathrm{K}'_{21}}{\mathrm{K}'_{12}}}$

$$\rightarrow \begin{cases} A_{0_1} = A_1(\tau,\zeta_4) \\ A_{0_2} = \frac{i}{\mathrm{K}''} A_2(\tau,\zeta_4) \end{cases}$$

$$\rightarrow \begin{cases} A_1(\tau,\zeta_5) = \cos(\mathrm{K}'\ell)\, A_1(\tau,\zeta_4) + \frac{i}{\mathrm{K}''}\sin(\mathrm{K}'\ell)\, A_2(\tau,\zeta_4) \\ A_2(\tau,\zeta_5) = i\mathrm{K}''\sin(\mathrm{K}'\ell)\, A_1(\tau,\zeta_4) + \cos(\mathrm{K}'\ell)\, A_2(\tau,\zeta_4) \end{cases}$$

where $\ell \equiv \zeta_5 - \zeta_4$

New variables/parameters introduced above

$\mathrm{K}' \equiv \sqrt{\mathrm{K}'_{12}\mathrm{K}'_{21}}$

$\mathrm{K}'' \equiv \sqrt{\mathrm{K}'_{21}/\mathrm{K}'_{12}} = \mathrm{K}'_{21}/\mathrm{K}' = \mathrm{K}'/\mathrm{K}'_{12}$

$\ell \equiv$ Normalized length of passive section with coupling $= \zeta_5 - \zeta_4$

$Q_{1,2}(\tau) \equiv$ Saturable absorption $= -\int_{\zeta_2}^{\zeta_3} n_{(1,2),q} d\zeta$

$$G_{1,2}(\tau) \equiv \text{Saturable gain} = \int_{\zeta_3}^{\zeta_4} n_{(1,2),g} d\zeta$$

Combined transformation of the amplitudes by absorber, gain, and passive sections in each laser

$$\boxed{\begin{aligned} A_1(\tau,\zeta_5) = \quad & \cos(\mathrm{K}'\ell) e^{(1-i\alpha_g)G_1(\tau)/2-(1-i\alpha_q)Q_1(\tau)/2} A_1(\tau,\zeta_1) \\ & + \frac{i}{\mathrm{K}''} \sin(\mathrm{K}'\ell)\, e^{(1-i\alpha_g)G_2(\tau)/2-(1-i\alpha_q)Q_2(\tau)/2} A_2(\tau,\zeta_1) \end{aligned}}$$

$$\boxed{\begin{aligned} A_2(\tau,\zeta_5) = \quad & i\mathrm{K}'' \sin(\mathrm{K}'\ell)\, e^{(1-i\alpha_g)G_1(\tau)/2-(1-i\alpha_q)Q_1(\tau)/2} A_1(\tau,\zeta_1) \\ & + \cos(\mathrm{K}'\ell)\, e^{(1-i\alpha_g)G_2(\tau)/2-(1-i\alpha_q)Q_2(\tau)/2} A_2(\tau,\zeta_1) \end{aligned}}$$

Equations governing the saturable gain and saturable absorption

$$\boxed{\frac{\partial G_{1,2}(\tau)}{\partial \tau} = g_{0(1,2)} - \Gamma G_{1,2}(\tau) - \left|A_{1,2}(\tau,\zeta_4)\right|^2 + \left|A_{1,2}(\tau,\zeta_3)\right|^2} \leftarrow \text{Gain}$$

Start with $\frac{\partial n_{(1,2),g}}{\partial \tau} = j_{(1,2),g} - \Gamma n_{(1,2),g} - n_{(1,2),g}\left|A_{1,2}\right|^2$

$\rightarrow \int_{\zeta_3}^{\zeta_4} \frac{\partial n_{(1,2),g}}{\partial \tau} d\zeta = \int_{\zeta_3}^{\zeta_4} j_{(1,2),g} d\zeta - \Gamma \int_{\zeta_3}^{\zeta_4} n_{(1,2),g} d\zeta - \int_{\zeta_3}^{\zeta_4} n_{(1,2),g}\left|A_{1,2}\right|^2 d\zeta$

$\rightarrow \frac{\partial}{\partial \tau}\int_{\zeta_3}^{\zeta_4} n_{(1,2),g} d\zeta = \frac{\partial G_{1,2}(\tau)}{\partial \tau} = g_{0(1,2)} - \Gamma G_{1,2}(\tau) - \int_{\zeta_3}^{\zeta_4} n_{(1,2),g}\left|A_{1,2}\right|^2 d\zeta$

where $g_{0(1,2)} \equiv \int_{\zeta_3}^{\zeta_4} j_{(1,2),g} d\zeta$

Now consider $\frac{\partial A_{1,2}}{\partial \zeta} = \frac{1}{2}(1 - i\alpha_g) n_{(1,2),g} A_{1,2}$

$\rightarrow \frac{\partial A_{1,2}^*}{\partial \zeta} = \frac{1}{2}(1 + i\alpha_g) n_{(1,2),g} A_{1,2}^*$

$\rightarrow \begin{cases} A_{1,2}^* \frac{\partial A_{1,2}}{\partial \zeta} = \frac{1}{2}(1 - i\alpha_g) n_{(1,2),g}\left|A_{1,2}\right|^2 \\ A_{1,2} \frac{\partial A_{1,2}^*}{\partial \zeta} = \frac{1}{2}(1 + i\alpha_g) n_{(1,2),g}\left|A_{1,2}\right|^2 \end{cases}$

$\frac{\partial \left|A_{1,2}\right|^2}{\partial \zeta} = \frac{\partial\left(A_{1,2}A_{1,2}^*\right)}{\partial \zeta} = A_{1,2}\frac{\partial A_{1,2}^*}{\partial \zeta} + \frac{\partial A_{1,2}}{\partial \zeta} A_{1,2}^*$

$\rightarrow \frac{\partial \left|A_{1,2}\right|^2}{\partial \zeta} = \frac{1}{2}(1 + i\alpha_g) n_{(1,2),g}\left|A_{1,2}\right|^2 + \frac{1}{2}(1 - i\alpha_g) n_{(1,2),g}\left|A_{1,2}\right|^2$

$\rightarrow \frac{\partial \left|A_{1,2}\right|^2}{\partial \zeta} = n_{(1,2),g}\left|A_{1,2}\right|^2$

$\rightarrow \int_{\left|A_{1,2}(\tau,\zeta_3)\right|^2}^{\left|A_{1,2}(\tau,\zeta_4)\right|^2} \partial\left|A_{1,2}\right|^2 = \int_{\zeta_3}^{\zeta_4} n_{(1,2),g}\left|A_{1,2}\right|^2 d\zeta$

$\rightarrow \int_{\zeta_3}^{\zeta_4} n_{(1,2),g}\left|A_{1,2}\right|^2 d\zeta = \left|A_{1,2}(\tau,\zeta_4)\right|^2 - \left|A_{1,2}(\tau,\zeta_3)\right|^2$

Therefore $\frac{\partial G_{1,2}(\tau)}{\partial \tau} = g_{0(1,2)} - \Gamma G_{1,2}(\tau) - \left|A_{1,2}(\tau,\zeta_4)\right|^2 + \left|A_{1,2}(\tau,\zeta_3)\right|^2$

$$\boxed{\frac{\partial Q_{1,2}(\tau)}{\partial \tau} = q_0 - Q_{1,2}(\tau) + s\left|A_{1,2}(\tau,\zeta_3)\right|^2 - s\left|A_{1,2}(\tau,\zeta_2)\right|^2} \leftarrow \text{Absorber}$$

Start with $\frac{\partial n_{(1,2),q}}{\partial \tau} = -j_q - n_{(1,2),q} - s n_{(1,2),q}\left|A_{1,2}\right|^2$

$\rightarrow \int_{\zeta_2}^{\zeta_3} \frac{\partial n_{(1,2),q}}{\partial \tau} d\zeta = -\int_{\zeta_2}^{\zeta_3} j_q d\zeta - \int_{\zeta_2}^{\zeta_3} n_{(1,2),q} d\zeta - s\int_{\zeta_2}^{\zeta_3} n_{(1,2),q}\left|A_{1,2}\right|^2 d\zeta$

$\rightarrow -\frac{\partial}{\partial \tau}\int_{\zeta_2}^{\zeta_3} n_{(1,2),q} d\zeta = \frac{\partial Q_{1,2}(\tau)}{\partial \tau} = q_0 - Q_{1,2}(\tau) + s\int_{\zeta_2}^{\zeta_3} n_{(1,2),q}\left|A_{1,2}\right|^2 d\zeta$

where $q_0 \equiv \int_{\zeta_2}^{\zeta_3} j_q d\zeta$

Now consider $\frac{\partial A_{1,2}}{\partial \zeta} = \frac{1}{2}(1 - i\alpha_q) n_{(1,2),q} A_{1,2}$

$\rightarrow \frac{\partial A_{1,2}^*}{\partial \zeta} = \frac{1}{2}(1 + i\alpha_q) n_{(1,2),q} A_{1,2}^*$

$\rightarrow \begin{cases} A_{1,2}^* \frac{\partial A_{1,2}}{\partial \zeta} = \frac{1}{2}(1 - i\alpha_q) n_{(1,2),q} \left|A_{1,2}\right|^2 \\ A_{1,2} \frac{\partial A_{1,2}^*}{\partial \zeta} = \frac{1}{2}(1 + i\alpha_q) n_{(1,2),q} \left|A_{1,2}\right|^2 \end{cases}$

$\frac{\partial \left|A_{1,2}\right|^2}{\partial \zeta} = \frac{\partial \left(A_{1,2} A_{1,2}^*\right)}{\partial \zeta} = A_{1,2} \frac{\partial A_{1,2}^*}{\partial \zeta} + \frac{\partial A_{1,2}}{\partial \zeta} A_{1,2}^*$

$\rightarrow \frac{\partial \left|A_{1,2}\right|^2}{\partial \zeta} = \frac{1}{2}(1 + i\alpha_q) n_{(1,2),q} \left|A_{1,2}\right|^2 + \frac{1}{2}(1 - i\alpha_q) n_{(1,2),q} \left|A_{1,2}\right|^2$

$\rightarrow \frac{\partial \left|A_{1,2}\right|^2}{\partial \zeta} = n_{(1,2),q} \left|A_{1,2}\right|^2$

$\rightarrow \int_{\left|A_{1,2}(\tau,\zeta_2)\right|^2}^{\left|A_{1,2}(\tau,\zeta_3)\right|^2} \partial \left|A_{1,2}\right|^2 = \int_{\zeta_2}^{\zeta_3} n_{(1,2),q} \left|A_{1,2}\right|^2 d\zeta$

$\rightarrow \int_{\zeta_2}^{\zeta_3} n_{(1,2),q} \left|A_{1,2}\right|^2 d\zeta = \left|A_{1,2}(\tau,\zeta_3)\right|^2 - \left|A_{1,2}(\tau,\zeta_2)\right|^2$

Therefore $\frac{\partial Q_{1,2}(\tau)}{\partial \tau} = q_0 - Q_{1,2}(\tau) + s\left|A_{1,2}(\tau,\zeta_3)\right|^2 - s\left|A_{1,2}(\tau,\zeta_2)\right|^2$

New variables/parameters introduced above

$g_{0(1,2)} \equiv$ Unsaturated gain parameter $= \int_{\zeta_3}^{\zeta_4} j_{(1,2),g} d\zeta$

$q_0 \equiv$ Unsaturated absorption parameter $= \int_{\zeta_2}^{\zeta_3} j_q d\zeta$

$A_{1,2}(\tau) \equiv A_{1,2}(\tau, \zeta_1) \equiv$ Normalized amplitude at beginning of RT

$T_{1,2} \equiv$ Normalized cavity roundtrip time (same for τ and ζ) $= \gamma_q L_{1,2}/v$

$\kappa \equiv$ Attenuation factor, accounting for total nonresonant linear intensity loss per RT

Spectral filter (general)

$$A_1(\tau + T_1) = \int_{-\infty}^{\tau} f(\tau - \theta) R_{11}(\theta) A_1(\theta) d\theta + \int_{-\infty}^{\tau} f(\tau - \theta) R_{12}(\theta) A_2(\theta) d\theta$$
$$A_2(\tau + T_2) = \int_{-\infty}^{\tau} f(\tau - \theta) R_{21}(\theta) A_1(\theta) d\theta + \int_{-\infty}^{\tau} f(\tau - \theta) R_{22}(\theta) A_2(\theta) d\theta$$

where
$$\begin{cases} R_{11}(\tau) \equiv \cos(\mathrm{K}'\ell)\sqrt{\kappa} e^{\frac{(1-i\alpha_g)G_1(\tau)}{2} - \frac{(1-i\alpha_q)Q_1(\tau)}{2}} \\ R_{12}(\tau) \equiv \frac{i}{\mathrm{K}''}\sin(\mathrm{K}'\ell)\sqrt{\kappa} e^{\frac{(1-i\alpha_g)G_2(\tau)}{2} - \frac{(1-i\alpha_q)Q_2(\tau)}{2}} \\ R_{21}(\tau) \equiv i\mathrm{K}''\sin(\mathrm{K}'\ell)\sqrt{\kappa} e^{\frac{(1-i\alpha_g)G_1(\tau)}{2} - \frac{(1-i\alpha_q)Q_1(\tau)}{2}} \\ R_{22}(\tau) \equiv \cos(\mathrm{K}'\ell)\sqrt{\kappa} e^{\frac{(1-i\alpha_g)G_2(\tau)}{2} - \frac{(1-i\alpha_q)Q_2(\tau)}{2}} \end{cases}$$

First, use the periodic boundary condition: $E_{1,2}(t, z + L_{1,2}) = E_{1,2}(t, z)$

Recall that $\tau = \gamma_q\left(t - \frac{z}{v}\right)$, $\zeta = \frac{z\gamma_q}{v}$, and $A_{1,2}(\tau, \zeta) = E_{1,2}(t, z)\sqrt{\frac{v g_g \Gamma_g}{\gamma_q}}$

$\rightarrow E_{1,2}(t, z + L_{1,2}) = A_{1,2}\left(\gamma_q\left(t - \frac{z+L_{1,2}}{v}\right), \frac{(z+L_{1,2})\gamma_q}{v}\right) = A_{1,2}\left(\tau - \frac{\gamma_q L_{1,2}}{v}, \zeta + \frac{\gamma_q L_{1,2}}{v}\right)$

$E_{1,2}(t, z) = E_{1,2}(t, z + L_{1,2}) \rightarrow A_{1,2}(\tau, \zeta) = A_{1,2}\left(\tau - \frac{\gamma_q L_{1,2}}{v}, \zeta + \frac{\gamma_q L_{1,2}}{v}\right)$

$\rightarrow A_{1,2}\left(\tau+\frac{\gamma_q L_{1,2}}{v},\zeta\right)=A_{1,2}\left(\tau,\zeta+\frac{\gamma_q L_{1,2}}{v}\right)$

Therefore, $\boxed{A_{1,2}(\tau+T_{1,2},\zeta)=A_{1,2}(\tau,\zeta+T_{1,2})}$, where $T_{1,2}\equiv\gamma_q L_{1,2}/v$

Next, start with spectral filter $\hat{E}_{1,2}(\omega,z_1+L_{1,2})=\hat{f}(\omega)\hat{E}_{1,2}(\omega,z_5)$

$\rightarrow \hat{A}_{1,2}(\omega,\zeta_1+T_{1,2})=\hat{f}(\omega)\hat{A}_{1,2}(\omega,\zeta_5)$

$\rightarrow A_{1,2}(\tau,\zeta_1+T_{1,2})=\int_{-\infty}^{\tau}f(\tau-\theta)A_{1,2}(\theta,\zeta_5)d\theta$

$\rightarrow A_{1,2}(\tau+T_{1,2},\zeta_1)=\int_{-\infty}^{\tau}f(\tau-\theta)A_{1,2}(\theta,\zeta_5)d\theta$

Define $R_{11}(\tau)$, $R_{12}(\tau)$, $R_{21}(\tau)$, and $R_{22}(\tau)$

$R_{11}(\tau)\equiv\cos(\mathrm{K}'\ell)\sqrt{\kappa}e^{(1-i\alpha_g)G_1(\tau)/2-(1-i\alpha_q)Q_1(\tau)/2}$

$R_{12}(\tau)\equiv\frac{i}{\mathrm{K}''}\sin(\mathrm{K}'\ell)\sqrt{\kappa}e^{(1-i\alpha_g)G_2(\tau)/2-(1-i\alpha_q)Q_2(\tau)/2}$

$R_{21}(\tau)\equiv i\mathrm{K}''\sin(\mathrm{K}'\ell)\sqrt{\kappa}e^{(1-i\alpha_g)G_1(\tau)/2-(1-i\alpha_q)Q_1(\tau)/2}$

$R_{22}(\tau)\equiv\cos(\mathrm{K}'\ell)\sqrt{\kappa}e^{(1-i\alpha_g)G_2(\tau)/2-(1-i\alpha_q)Q_2(\tau)/2}$

The extra, appended term $\sqrt{\kappa}$ accounts for linear cavity loss

$\rightarrow\begin{cases}A_1(\tau,\zeta_5)=R_{11}(\tau)A_1(\tau,\zeta_1)+R_{12}(\tau)A_2(\tau,\zeta_1)\\A_2(\tau,\zeta_5)=R_{21}(\tau)A_1(\tau,\zeta_1)+R_{22}(\tau)A_2(\tau,\zeta_1)\end{cases}$

Define $A_{1,2}(\tau)\equiv A_{1,2}(\tau,\zeta_1)$

$\rightarrow\begin{cases}A_1(\tau+T_1)=\int_{-\infty}^{\tau}f(\tau-\theta)R_{11}(\theta)A_1(\theta)d\theta+\int_{-\infty}^{\tau}f(\tau-\theta)R_{12}(\theta)A_2(\theta)d\theta\\A_2(\tau+T_2)=\int_{-\infty}^{\tau}f(\tau-\theta)R_{21}(\theta)A_1(\theta)d\theta+\int_{-\infty}^{\tau}f(\tau-\theta)R_{22}(\theta)A_2(\theta)d\theta\end{cases}$

Lorentzian spectral filter response function

$\boxed{f(\tau)=\gamma e^{(-\gamma+i\Omega)\tau}u(\tau)}\rightarrow\boxed{\hat{f}(w)=\frac{\gamma}{\gamma+i(w-\Omega)}}$

$\gamma\equiv$ Bandwidth of spectral filter

$\Omega\equiv$ Detuning from spectral filter ($w-w_0$, where w_0 is the center frequency)

$u(\tau)\equiv$ Step function $=\begin{cases}0 & \tau<0\\1 & \tau\geq 0\end{cases}$

Delay differential equations

$$\boxed{\begin{aligned}&\frac{\partial\tilde{A}_1(\tau)}{\partial\tau}=-\gamma\tilde{A}_1(\tau)+\gamma e^{-i\varphi}\left(R_{11}(\tau-T)\tilde{A}_1(\tau-T)+R_{12}(\tau-T)\tilde{A}_2(\tau-T)\right)\\&\frac{\partial\tilde{A}_2(\tau)}{\partial\tau}=-\gamma\tilde{A}_2(\tau)+\gamma e^{-i\varphi}\left(R_{21}(\tau-T)\tilde{A}_1(\tau-T)+R_{22}(\tau-T)\tilde{A}_2(\tau-T)\right)\\&\text{where }\begin{cases}R_{11}(\tau)\equiv\cos(\mathrm{K}'\ell)\sqrt{\kappa}e^{(1-i\alpha_g)G_1(\tau)/2-(1-i\alpha_q)Q_1(\tau)/2}\\R_{12}(\tau)\equiv\frac{i}{\mathrm{K}''}\sin(\mathrm{K}'\ell)\sqrt{\kappa}e^{(1-i\alpha_g)G_2(\tau)/2-(1-i\alpha_q)Q_2(\tau)/2}\\R_{21}(\tau)\equiv i\mathrm{K}''\sin(\mathrm{K}'\ell)\sqrt{\kappa}e^{(1-i\alpha_g)G_1(\tau)/2-(1-i\alpha_q)Q_1(\tau)/2}\\R_{22}(\tau)\equiv\cos(\mathrm{K}'\ell)\sqrt{\kappa}e^{(1-i\alpha_g)G_2(\tau)/2-(1-i\alpha_q)Q_2(\tau)/2}\end{cases}\end{aligned}}\leftarrow\text{Amplitude DDEs}$$

Start with the following equations

$\begin{cases}A_1(\tau+T_1)=\int_{-\infty}^{\tau}f(\tau-\theta)R_{11}(\theta)A_1(\theta)d\theta+\int_{-\infty}^{\tau}f(\tau-\theta)R_{12}(\theta)A_2(\theta)d\theta\\A_2(\tau+T_2)=\int_{-\infty}^{\tau}f(\tau-\theta)R_{21}(\theta)A_1(\theta)d\theta+\int_{-\infty}^{\tau}f(\tau-\theta)R_{22}(\theta)A_2(\theta)d\theta\end{cases}$

$R_{11}(\tau)\equiv\cos(\mathrm{K}'\ell)\sqrt{\kappa}e^{(1-i\alpha_g)G_1(\tau)/2-(1-i\alpha_q)Q_1(\tau)/2}$

$R_{12}(\tau)\equiv\frac{i}{\mathrm{K}''}\sin(\mathrm{K}'\ell)\sqrt{\kappa}e^{(1-i\alpha_g)G_2(\tau)/2-(1-i\alpha_q)Q_2(\tau)/2}$

$$R_{21}(\tau) \equiv i\mathrm{K}'' \sin(\mathrm{K}'\ell)\sqrt{\kappa}e^{(1-i\alpha_g)G_1(\tau)/2-(1-i\alpha_q)Q_1(\tau)/2}$$
$$R_{22}(\tau) \equiv \cos(\mathrm{K}'\ell)\sqrt{\kappa}e^{(1-i\alpha_g)G_2(\tau)/2-(1-i\alpha_q)Q_2(\tau)/2}$$
$$f(\tau) = \gamma e^{(-\gamma+i\Omega)\tau}u(\tau)$$

Recall the Leibniz Integral Rule

$$\frac{d}{dt}\left(\int_{a(t)}^{b(t)} f(x,t)dx\right) = \int_{a(t)}^{b(t)} \frac{\partial f}{\partial t}dx + f(b(t),t)\cdot b'(t) - f(a(t),t)\cdot a'(t)$$

Proof: https://en.wikipedia.org/wiki/Leibniz_integral_rule

(see the proofs section for the "general form with variable limits")

$$\rightarrow \begin{cases} \frac{\partial A_1(\tau+T_1)}{\partial\tau} = & \int_{-\infty}^{\tau} f'(\tau-\theta)R_{11}(\theta)A_1(\theta)d\theta + f(0)R_{11}(\tau)A_1(\tau) - 0 \\ & + \int_{-\infty}^{\tau} f'(\tau-\theta)R_{12}(\theta)A_2(\theta)d\theta + f(0)R_{12}(\tau)A_2(\tau) - 0 \\ \frac{\partial A_2(\tau+T_2)}{\partial\tau} = & \int_{-\infty}^{\tau} f'(\tau-\theta)R_{21}(\theta)A_1(\theta)d\theta + f(0)R_{21}(\tau)A_1(\tau) - 0 \\ & + \int_{-\infty}^{\tau} f'(\tau-\theta)R_{22}(\theta)A_2(\theta)d\theta + f(0)R_{22}(\tau)A_2(\tau) - 0 \end{cases}$$

Note that $f(0) = \gamma$ and $f'(\tau) = (-\gamma + i\Omega)f(\tau)$ for $\tau > 0$

$$\rightarrow f'(\tau-\theta) = (-\gamma+i\Omega)f(\tau-\theta)$$

$$\rightarrow \begin{cases} \frac{\partial A_1(\tau+T_1)}{\partial\tau} = & (-\gamma+i\Omega)\int_{-\infty}^{\tau} f(\tau-\theta)R_{11}(\theta)A_1(\theta)d\theta + f(0)R_{11}(\tau)A_1(\tau) \\ & +(-\gamma+i\Omega)\int_{-\infty}^{\tau} f(\tau-\theta)R_{12}(\theta)A_2(\theta)d\theta + f(0)R_{12}(\tau)A_2(\tau) \\ \frac{\partial A_2(\tau+T_2)}{\partial\tau} = & (-\gamma+i\Omega)\int_{-\infty}^{\tau} f(\tau-\theta)R_{21}(\theta)A_1(\theta)d\theta + f(0)R_{21}(\tau)A_1(\tau) \\ & +(-\gamma+i\Omega)\int_{-\infty}^{\tau} f(\tau-\theta)R_{22}(\theta)A_2(\theta)d\theta + f(0)R_{22}(\tau)A_2(\tau) \end{cases}$$

$$\rightarrow \begin{cases} \frac{\partial A_1(\tau+T_1)}{\partial\tau} = (-\gamma+i\Omega)A_1(\tau+T_1) + \gamma R_{11}(\tau)A_1(\tau) + \gamma R_{12}(\tau)A_2(\tau) \\ \frac{\partial A_2(\tau+T_2)}{\partial\tau} = (-\gamma+i\Omega)A_2(\tau+T_2) + \gamma R_{21}(\tau)A_1(\tau) + \gamma R_{22}(\tau)A_2(\tau) \end{cases}$$

$$\rightarrow \begin{cases} \frac{\partial A_1(\tau)}{\partial\tau} + (\gamma-i\Omega)A_1(\tau) = \gamma R_{11}(\tau-T_1)A_1(\tau-T_1) + \gamma R_{12}(\tau-T_1)A_2(\tau-T_1) \\ \frac{\partial A_2(\tau)}{\partial\tau} + (\gamma-i\Omega)A_2(\tau) = \gamma R_{21}(\tau-T_2)A_1(\tau-T_2) + \gamma R_{22}(\tau-T_2)A_2(\tau-T_2) \end{cases}$$

Let $A_{1,2}(\tau) = \tilde{A}_{1,2}(\tau)e^{i\Omega\tau}$

$$\rightarrow \frac{\partial A_{1,2}(\tau)}{\partial\tau} = \frac{\partial\tilde{A}_{1,2}(\tau)}{\partial\tau}e^{i\Omega\tau} + i\Omega\tilde{A}_{1,2}(\tau)e^{i\Omega\tau}$$

$$\rightarrow \begin{cases} \left(\frac{\partial\tilde{A}_1(\tau)}{\partial\tau}e^{i\Omega\tau} + i\Omega\tilde{A}_1(\tau)e^{i\Omega\tau}\right) = & \gamma R_{11}(\tau-T_1)\tilde{A}_1(\tau-T_1)e^{i\Omega(\tau-T_1)} \\ \quad +(\gamma-i\Omega)\left(\tilde{A}_1(\tau)e^{i\Omega\tau}\right) & +\gamma R_{12}(\tau-T_1)\tilde{A}_2(\tau-T_1)e^{i\Omega(\tau-T_1)} \\ \left(\frac{\partial\tilde{A}_2(\tau)}{\partial\tau}e^{i\Omega\tau} + i\Omega\tilde{A}_2(\tau)e^{i\Omega\tau}\right) = & \gamma R_{21}(\tau-T_2)\tilde{A}_1(\tau-T_2)e^{i\Omega(\tau-T_2)} \\ \quad +(\gamma-i\Omega)\left(\tilde{A}_2(\tau)e^{i\Omega\tau}\right) & +\gamma R_{22}(\tau-T_2)\tilde{A}_2(\tau-T_2)e^{i\Omega(\tau-T_2)} \end{cases}$$

$$\rightarrow \begin{cases} \frac{\partial\tilde{A}_1(\tau)}{\partial\tau} = -\gamma\tilde{A}_1(\tau) + \gamma e^{-i\Omega T_1}\left(R_{11}(\tau-T_1)\tilde{A}_1(\tau-T_1) + R_{12}(\tau-T_1)\tilde{A}_2(\tau-T_1)\right) \\ \frac{\partial\tilde{A}_2(\tau)}{\partial\tau} = -\gamma\tilde{A}_2(\tau) + \gamma e^{-i\Omega T_2}\left(R_{21}(\tau-T_2)\tilde{A}_1(\tau-T_2) + R_{22}(\tau-T_2)\tilde{A}_2(\tau-T_2)\right) \end{cases}$$

Therefore $\begin{cases} \frac{\partial\tilde{A}_1(\tau)}{\partial\tau} = -\gamma\tilde{A}_1(\tau) + \gamma e^{-i\varphi_1}\left(R_{11}(\tau-T_1)\tilde{A}_1(\tau-T_1) + R_{12}(\tau-T_1)\tilde{A}_2(\tau-T_1)\right) \\ \frac{\partial\tilde{A}_2(\tau)}{\partial\tau} = -\gamma\tilde{A}_2(\tau) + \gamma e^{-i\varphi_2}\left(R_{21}(\tau-T_2)\tilde{A}_1(\tau-T_2) + R_{22}(\tau-T_2)\tilde{A}_2(\tau-T_2)\right) \end{cases}$

where $\varphi_{1,2} \equiv \Omega T_{1,2}$ and $\tilde{A}_{1,2}(\tau) \equiv A_{1,2}(\tau)e^{-i\Omega\tau}$

$$\boxed{\frac{\partial G_{1,2}(\tau)}{\partial \tau} = g_{0(1,2)} - \Gamma G_{1,2}(\tau) - e^{-Q_{1,2}(\tau)}\left(e^{G_{1,2}(\tau)} - 1\right)\left|\tilde{A}_{1,2}(\tau)\right|^2} \leftarrow \text{Gain DDEs}$$

Start with the following relations

$$\frac{\partial G_{1,2}(\tau)}{\partial \tau} = g_{0(1,2)} - \Gamma G_{1,2}(\tau) - \left|A_{1,2}(\tau,\zeta_4)\right|^2 + \left|A_{1,2}(\tau,\zeta_3)\right|^2$$

$$A_{1,2}(\tau,\zeta_2) = A_{1,2}(\tau,\zeta_1) = A_{1,2}(\tau)$$

$$\rightarrow \left|A_{1,2}(\tau,\zeta_2)\right|^2 = \left|A_{1,2}(\tau)\right|^2$$

$$A_{1,2}(\tau,\zeta_3) = e^{-(1-i\alpha_q)Q_{1,2}(\tau)/2}A_{1,2}(\tau,\zeta_2) = e^{-(1-i\alpha_q)Q_{1,2}(\tau)/2}A_{1,2}(\tau)$$

$$\rightarrow \left|A_{1,2}(\tau,\zeta_3)\right|^2 = e^{-Q_{1,2}(\tau)}\left|A_{1,2}(\tau)\right|^2$$

$$A_{1,2}(\tau,\zeta_4) = e^{(1-i\alpha_g)G_{1,2}(\tau)/2}A_{1,2}(\tau,\zeta_3)$$

$$\rightarrow \left|A_{1,2}(\tau,\zeta_4)\right|^2 = e^{G_{1,2}(\tau)}\left|A_{1,2}(\tau,\zeta_3)\right|^2 = e^{G_{1,2}(\tau)}e^{-Q_{1,2}(\tau)}\left|A_{1,2}(\tau)\right|^2$$

$$\rightarrow \frac{\partial G_{1,2}(\tau)}{\partial \tau} = g_{0(1,2)} - \Gamma G_{1,2}(\tau) - e^{G_{1,2}(\tau)}e^{-Q_{1,2}(\tau)}\left|A_{1,2}(\tau)\right|^2 + e^{-Q_{1,2}(\tau)}\left|A_{1,2}(\tau)\right|^2$$

Also note that $\left|A_{1,2}(\tau)\right|^2 = \left|\tilde{A}_{1,2}(\tau)\right|^2$

$$\boxed{\frac{\partial Q_{1,2}(\tau)}{\partial \tau} = q_0 - Q_{1,2}(\tau) - s\left(1 - e^{-Q_{1,2}(\tau)}\right)\left|\tilde{A}_{1,2}(\tau)\right|^2} \leftarrow \text{Absorber DDEs}$$

Start with the following relations

$$\frac{\partial Q_{1,2}(\tau)}{\partial \tau} = q_0 - Q_{1,2}(\tau) + s\left|A_{1,2}(\tau,\zeta_3)\right|^2 - s\left|A_{1,2}(\tau,\zeta_2)\right|^2$$

$$A_{1,2}(\tau,\zeta_2) = A_{1,2}(\tau,\zeta_1) = A_{1,2}(\tau)$$

$$\rightarrow \left|A_{1,2}(\tau,\zeta_2)\right|^2 = \left|A_{1,2}(\tau)\right|^2$$

$$A_{1,2}(\tau,\zeta_3) = e^{-(1-i\alpha_q)Q_{1,2}(\tau)/2}A_{1,2}(\tau,\zeta_2) = e^{-(1-i\alpha_q)Q_{1,2}(\tau)/2}A_{1,2}(\tau)$$

$$\rightarrow \left|A_{1,2}(\tau,\zeta_3)\right|^2 = e^{-Q_{1,2}(\tau)}\left|A_{1,2}(\tau)\right|^2$$

$$\rightarrow \frac{\partial Q_{1,2}(\tau)}{\partial \tau} = q_0 - Q_{1,2}(\tau) + se^{-Q_{1,2}(\tau)}\left|A_{1,2}(\tau)\right|^2 - s\left|A_{1,2}(\tau)\right|^2$$

Also note that $\left|A_{1,2}(\tau)\right|^2 = \left|\tilde{A}_{1,2}(\tau)\right|^2$

New variables/parameters introduced above

$\tilde{A}_{1,2}(\tau) \equiv$ Normalized, "detuned" amplitude at beginning of RT $= A_{1,2}(\tau)e^{-i\Omega\tau}$

$\varphi_{1,2} = \Omega T_{1,2}$

Finally, below is "the DDE model" that can be solved by time integration / numerical simulation (note: for convenience of notation, the ~ for $\tilde{A}_{1,2}(\tau)$ is dropped)

$$\boxed{\begin{aligned}
&\frac{\partial A_1(\tau)}{\partial \tau} = -\gamma A_1(\tau) + \gamma e^{-i\varphi_1}\left(R_{11}(\tau - T_1)A_1(\tau - T_1) + R_{12}(\tau - T_1)A_2(\tau - T_1)\right)\\
&\frac{\partial A_2(\tau)}{\partial \tau} = -\gamma A_2(\tau) + \gamma e^{-i\varphi_2}\left(R_{21}(\tau - T_2)A_1(\tau - T_2) + R_{22}(\tau - T_2)A_2(\tau - T_2)\right)\\
&\text{where } \begin{cases} R_{11}(\tau) \equiv \cos(\mathrm{K}'\ell)\sqrt{\kappa}e^{(1-i\alpha_g)G_1(\tau)/2 - (1-i\alpha_q)Q_1(\tau)/2} \\ R_{12}(\tau) \equiv \frac{i}{\mathrm{K}''}\sin(\mathrm{K}'\ell)\sqrt{\kappa}e^{(1-i\alpha_g)G_2(\tau)/2 - (1-i\alpha_q)Q_2(\tau)/2} \\ R_{21}(\tau) \equiv i\mathrm{K}''\sin(\mathrm{K}'\ell)\sqrt{\kappa}e^{(1-i\alpha_g)G_1(\tau)/2 - (1-i\alpha_q)Q_1(\tau)/2} \\ R_{22}(\tau) \equiv \cos(\mathrm{K}'\ell)\sqrt{\kappa}e^{(1-i\alpha_g)G_2(\tau)/2 - (1-i\alpha_q)Q_2(\tau)/2} \end{cases}
\end{aligned}} \leftarrow \text{Amplitude DDEs}$$

$$\boxed{\begin{matrix}\frac{\partial G_1(\tau)}{\partial \tau} = g_{01} - \Gamma G_1(\tau) - e^{-Q_1(\tau)}\left(e^{G_1(\tau)} - 1\right)|A_1(\tau)|^2 \\ \frac{\partial G_2(\tau)}{\partial \tau} = g_{02} - \Gamma G_2(\tau) - e^{-Q_2(\tau)}\left(e^{G_2(\tau)} - 1\right)|A_2(\tau)|^2\end{matrix}} \leftarrow \text{Gain DDEs}$$

$$\boxed{\begin{matrix}\frac{\partial Q_1(\tau)}{\partial \tau} = q_0 - Q_1(\tau) - s\left(1 - e^{-Q_1(\tau)}\right)|A_1(\tau)|^2 \\ \frac{\partial Q_2(\tau)}{\partial \tau} = q_0 - Q_2(\tau) - s\left(1 - e^{-Q_2(\tau)}\right)|A_2(\tau)|^2\end{matrix}} \leftarrow \text{Absorber DDEs}$$

A.2 Derivation of "the rotating-wave DDE model" (for bifurcation analysis)

A.2.1 The "rotating-wave DDE model"

Amplitude DDEs

$$\begin{cases}\frac{\partial A_1}{\partial \tau} = -\gamma A_1(\tau) + \gamma e^{-i\varphi_1}\left(R_{11}(\tau - T_1)A_1(\tau - T_1) + R_{12}(\tau - T_1)A_2(\tau - T_1)\right) \\ \frac{\partial A_2}{\partial \tau} = -\gamma A_2(\tau) + \gamma e^{-i\varphi_2}\left(R_{21}(\tau - T_2)A_1(\tau - T_2) + R_{22}(\tau - T_2)A_2(\tau - T_2)\right)\end{cases}$$

$$\text{where } \begin{cases}R_{11}(\tau) = \cos(\mathrm{K}'\ell)\sqrt{\kappa}e^{(1-i\alpha_g)G_1(\tau)/2 - (1-i\alpha_q)Q_1(\tau)/2} \\ R_{12}(\tau) = \frac{i}{\mathrm{K}''}\sin(\mathrm{K}'\ell)\sqrt{\kappa}e^{(1-i\alpha_g)G_2(\tau)/2 - (1-i\alpha_q)Q_2(\tau)/2} \\ R_{21}(\tau) = i\mathrm{K}''\sin(\mathrm{K}'\ell)\sqrt{\kappa}e^{(1-i\alpha_g)G_1(\tau)/2 - (1-i\alpha_q)Q_1(\tau)/2} \\ R_{22}(\tau) = \cos(\mathrm{K}'\ell)\sqrt{\kappa}e^{(1-i\alpha_g)G_2(\tau)/2 - (1-i\alpha_q)Q_2(\tau)/2}\end{cases}$$

In order to write these expressions in a more compact form, define
$\vartheta_{T\#L\#} \equiv \frac{G_{L\#}(\tau - T_{T\#}) - Q_{L\#}(\tau - T_{T\#})}{2}$ and $\theta_{T\#L\#} \equiv -\frac{\alpha_g G_{L\#}(\tau - T_{T\#})}{2} + \frac{\alpha_q Q_{L\#}(\tau - T_{T\#})}{2} - \varphi_{T\#}$
where $L\#$ can be 1 or 2, referring to either of the two lasers
and $T\#$ can be 1 or 2, referring to either delay/roundtrip time T_1 or T_2

Substitute these expressions above to get a more compact form of the amplitude DDEs

$$\rightarrow \begin{cases}\frac{\partial A_1}{\partial \tau} = -\gamma A_1(\tau) + \gamma\sqrt{\kappa}\left(\cos(\mathrm{K}'\ell)\, e^{\vartheta_{11} + i\theta_{11}}A_1(\tau - T_1) + \frac{i}{\mathrm{K}''}\sin(\mathrm{K}'\ell)\, e^{\vartheta_{12} + i\theta_{12}}A_2(\tau - T_1)\right) \\ \frac{\partial A_2}{\partial \tau} = -\gamma A_2(\tau) + \gamma\sqrt{\kappa}\left(i\mathrm{K}''\sin(\mathrm{K}'\ell)\, e^{\vartheta_{21} + i\theta_{21}}A_1(\tau - T_2) + \cos(\mathrm{K}'\ell)\, e^{\vartheta_{22} + i\theta_{22}}A_2(\tau - T_2)\right)\end{cases}$$

Gain DDEs

$$\begin{cases}\frac{\partial G_1(\tau)}{\partial \tau} = g_{01} - \Gamma G_1(\tau) - e^{-Q_1(\tau)}\left(e^{G_1(\tau)} - 1\right)|A_1(\tau)|^2 \\ \frac{\partial G_2(\tau)}{\partial \tau} = g_{02} - \Gamma G_2(\tau) - e^{-Q_2(\tau)}\left(e^{G_2(\tau)} - 1\right)|A_2(\tau)|^2\end{cases}$$

Absorber DDEs

$$\begin{cases}\frac{\partial Q_1(\tau)}{\partial \tau} = q_0 - Q_1(\tau) - s\left(1 - e^{-Q_1(\tau)}\right)|A_1(\tau)|^2 \\ \frac{\partial Q_2(\tau)}{\partial \tau} = q_0 - Q_2(\tau) - s\left(1 - e^{-Q_2(\tau)}\right)|A_2(\tau)|^2\end{cases}$$

Let $A_{1,2}(\tau) = A_{r(1,2)}(\tau)e^{iA_{\phi(1,2)}(\tau)}\ldots$

Then the left-hand-side of the amplitude DDEs (the derivative) is given by

$$\frac{\partial A_{1,2}}{\partial \tau} = \left(\frac{\partial A_{r(1,2)}}{\partial \tau} + iA_{r(1,2)}(\tau)\frac{\partial A_{\phi(1,2)}}{\partial \tau}\right)e^{iA_{\phi(1,2)}(\tau)}$$
$$= \left(\frac{\partial A_{r(1,2)}}{\partial \tau}\cos\left(A_{\phi(1,2)}(\tau)\right) - A_{r(1,2)}(\tau)\frac{\partial A_{\phi(1,2)}}{\partial \tau}\sin\left(A_{\phi(1,2)}(\tau)\right)\right)$$
$$+i\left(\frac{\partial A_{r(1,2)}}{\partial \tau}\sin\left(A_{\phi(1,2)}(\tau)\right) + A_{r(1,2)}(\tau)\frac{\partial A_{\phi(1,2)}}{\partial \tau}\cos\left(A_{\phi(1,2)}(\tau)\right)\right)$$

Substitute $A_{1,2}(t) = A_{r(1,2)}(\tau)e^{iA_{\phi(1,2)}(\tau)}$ into the right-hand-side of the amplitude DDEs

The amplitude DDEs (in compact form) are repeated below, for convenience

$$\begin{cases}\frac{\partial A_1}{\partial \tau} = -\gamma A_1(\tau) + \gamma\sqrt{\kappa}\left(\cos(\mathrm{K}'\ell)\,e^{\vartheta_{11}+i\theta_{11}}A_1(\tau-T_1) + \frac{i}{\mathrm{K}''}\sin(\mathrm{K}'\ell)\,e^{\vartheta_{12}+i\theta_{12}}A_2(\tau-T_1)\right)\\ \frac{\partial A_2}{\partial \tau} = -\gamma A_2(\tau) + \gamma\sqrt{\kappa}\left(i\mathrm{K}''\sin(\mathrm{K}'\ell)\,e^{\vartheta_{21}+i\theta_{21}}A_1(\tau-T_2) + \cos(\mathrm{K}'\ell)\,e^{\vartheta_{22}+i\theta_{22}}A_2(\tau-T_2)\right)\end{cases}$$

Substitution

$$\begin{cases}\frac{\partial A_1}{\partial \tau} = -\gamma A_{r1}(\tau)e^{iA_{\phi1}(\tau)} + \gamma\sqrt{\kappa}\begin{pmatrix}\cos(\mathrm{K}'\ell)\,e^{\vartheta_{11}}e^{i\theta_{11}}A_{r1}(\tau-T_1)e^{iA_{\phi1}(\tau-T_1)}\\ +\frac{i}{\mathrm{K}''}\sin(\mathrm{K}'\ell)\,e^{\vartheta_{12}}e^{i\theta_{12}}A_{r2}(\tau-T_1)e^{iA_{\phi2}(\tau-T_1)}\end{pmatrix}\\ \frac{\partial A_2}{\partial \tau} = -\gamma A_{r2}(\tau)e^{iA_{\phi2}(\tau)} + \gamma\sqrt{\kappa}\begin{pmatrix}i\mathrm{K}''\sin(\mathrm{K}'\ell)\,e^{\vartheta_{21}}e^{i\theta_{21}}A_{r1}(\tau-T_2)e^{iA_{\phi1}(\tau-T_2)}\\ +\cos(\mathrm{K}'\ell)\,e^{\vartheta_{22}}e^{i\theta_{22}}A_{r2}(\tau-T_2)e^{iA_{\phi2}(\tau-T_2)}\end{pmatrix}\end{cases}$$

Combine the complex exponential terms inside the parentheses

$$\begin{cases}\frac{\partial A_1}{\partial \tau} = -\gamma A_{r1}(\tau)e^{iA_{\phi1}(\tau)} + \gamma\sqrt{\kappa}\begin{pmatrix}\cos(\mathrm{K}'\ell)\,e^{\vartheta_{11}}A_{r1}(\tau-T_1)e^{i\left(\theta_{11}+A_{\phi1}(\tau-T_1)\right)}\\ +\frac{i}{\mathrm{K}''}\sin(\mathrm{K}'\ell)\,e^{\vartheta_{12}}A_{r2}(\tau-T_1)e^{i\left(\theta_{12}+A_{\phi2}(\tau-T_1)\right)}\end{pmatrix}\\ \frac{\partial A_2}{\partial \tau} = -\gamma A_{r2}(\tau)e^{iA_{\phi2}(\tau)} + \gamma\sqrt{\kappa}\begin{pmatrix}i\mathrm{K}''\sin(\mathrm{K}'\ell)\,e^{\vartheta_{21}}A_{r1}(\tau-T_2)e^{i\left(\theta_{21}+A_{\phi1}(\tau-T_2)\right)}\\ +\cos(\mathrm{K}'\ell)\,e^{\vartheta_{22}}A_{r2}(\tau-T_2)e^{i\left(\theta_{22}+A_{\phi2}(\tau-T_2)\right)}\end{pmatrix}\end{cases}$$

Separate the real and imaginary parts of each equation

$$\begin{cases}\mathrm{Re}\left\{\frac{\partial A_1}{\partial \tau}\right\} = -\gamma A_{r1}(\tau)\cos\left(A_{\phi1}(\tau)\right)\\ \qquad +\gamma\sqrt{\kappa}\cos(\mathrm{K}'\ell)\,e^{\vartheta_{11}}A_{r1}(\tau-T_1)\cos\left(\theta_{11}+A_{\phi1}(\tau-T_1)\right)\\ \qquad -\gamma\sqrt{\kappa}\frac{1}{\mathrm{K}''}\sin(\mathrm{K}'\ell)\,e^{\vartheta_{12}}A_{r2}(\tau-T_1)\sin\left(\theta_{12}+A_{\phi2}(\tau-T_1)\right)\\ \mathrm{Im}\left\{\frac{\partial A_1}{\partial \tau}\right\} = -\gamma A_{r1}(\tau)\sin\left(A_{\phi1}(\tau)\right)\\ \qquad +\gamma\sqrt{\kappa}\cos(\mathrm{K}'\ell)\,e^{\vartheta_{11}}A_{r1}(\tau-T_1)\sin\left(\theta_{11}+A_{\phi1}(\tau-T_1)\right)\\ \qquad +\gamma\sqrt{\kappa}\frac{1}{\mathrm{K}''}\sin(\mathrm{K}'\ell)\,e^{\vartheta_{12}}A_{r2}(\tau-T_1)\cos\left(\theta_{12}+A_{\phi2}(\tau-T_1)\right)\end{cases}$$

$$\begin{cases} \mathrm{Re}\left\{\frac{\partial A_2}{\partial \tau}\right\} = -\gamma A_{r2}(\tau)\cos\left(A_{\phi 2}(\tau)\right) \\ \qquad\qquad -\gamma\sqrt{\kappa}\mathrm{K}''\sin(\mathrm{K}'\ell)\, e^{\vartheta_{21}} A_{r1}(\tau - T_2)\sin\left(\theta_{21} + A_{\phi 1}(\tau - T_2)\right) \\ \qquad\qquad +\gamma\sqrt{\kappa}\cos(\mathrm{K}'\ell)\, e^{\vartheta_{22}} A_{r2}(\tau - T_2)\cos\left(\theta_{22} + A_{\phi 2}(\tau - T_2)\right) \\ \mathrm{Im}\left\{\frac{\partial A_2}{\partial \tau}\right\} = -\gamma A_{r2}(\tau)\sin\left(A_{\phi 2}(\tau)\right) \\ \qquad\qquad +\gamma\sqrt{\kappa}\mathrm{K}''\sin(\mathrm{K}'\ell)\, e^{\vartheta_{21}} A_{r1}(\tau - T_2)\cos\left(\theta_{21} + A_{\phi 1}(\tau - T_2)\right) \\ \qquad\qquad +\gamma\sqrt{\kappa}\cos(\mathrm{K}'\ell)\, e^{\vartheta_{22}} A_{r2}(\tau - T_2)\sin\left(\theta_{22} + A_{\phi 2}(\tau - T_2)\right) \end{cases}$$

Equations for $\mathrm{Re}\{\partial A_{1,2}/\partial\tau\}$

$$\begin{aligned} \frac{\partial A_{r1}}{\partial \tau}\cos\left(A_{\phi 1}(\tau)\right) &= -\gamma A_{r1}(\tau)\cos\left(A_{\phi 1}(\tau)\right) \\ -A_{r1}(\tau)\frac{\partial A_{\phi 1}}{\partial \tau}\sin\left(A_{\phi 1}(\tau)\right) &\quad +\gamma\sqrt{\kappa}\cos(\mathrm{K}'\ell)\, e^{\vartheta_{11}} A_{r1}(\tau - T_1)\cos\left(\theta_{11} + A_{\phi 1}(\tau - T_1)\right) \\ &\quad -\gamma\sqrt{\kappa}\frac{1}{\mathrm{K}''}\sin(\mathrm{K}'\ell)\, e^{\vartheta_{12}} A_{r2}(\tau - T_1)\sin\left(\theta_{12} + A_{\phi 2}(\tau - T_1)\right) \end{aligned}$$

$$\begin{aligned} \frac{\partial A_{r2}}{\partial \tau}\cos\left(A_{\phi 2}(\tau)\right) &= -\gamma A_{r2}(\tau)\cos\left(A_{\phi 2}(\tau)\right) \\ -A_{r2}(\tau)\frac{\partial A_{\phi 2}}{\partial \tau}\sin\left(A_{\phi 2}(\tau)\right) &\quad -\gamma\sqrt{\kappa}\mathrm{K}''\sin(\mathrm{K}'\ell)\, e^{\vartheta_{21}} A_{r1}(\tau - T_2)\sin\left(\theta_{21} + A_{\phi 1}(\tau - T_2)\right) \\ &\quad +\gamma\sqrt{\kappa}\cos(\mathrm{K}'\ell)\, e^{\vartheta_{22}} A_{r2}(\tau - T_2)\cos\left(\theta_{22} + A_{\phi 2}(\tau - T_2)\right) \end{aligned}$$

Equation for $\mathrm{Im}\{\partial A_{1,2}/\partial\tau\}$

$$\begin{aligned} \frac{\partial A_{r1}}{\partial \tau}\sin\left(A_{\phi 1}(\tau)\right) &= -\gamma A_{r1}(\tau)\sin\left(A_{\phi 1}(\tau)\right) \\ +A_{r1}(\tau)\frac{\partial A_{\phi 1}}{\partial \tau}\cos\left(A_{\phi 1}(\tau)\right) &\quad +\gamma\sqrt{\kappa}\cos(\mathrm{K}'\ell)\, e^{\vartheta_{11}} A_{r1}(\tau - T_1)\sin\left(\theta_{11} + A_{\phi 1}(\tau - T_1)\right) \\ &\quad +\gamma\sqrt{\kappa}\frac{1}{\mathrm{K}''}\sin(\mathrm{K}'\ell)\, e^{\vartheta_{12}} A_{r2}(\tau - T_1)\cos\left(\theta_{12} + A_{\phi 2}(\tau - T_1)\right) \end{aligned}$$

$$\begin{aligned} \frac{\partial A_{r2}}{\partial \tau}\sin\left(A_{\phi 2}(\tau)\right) &= -\gamma A_{r2}(\tau)\sin\left(A_{\phi 2}(\tau)\right) \\ +A_{r2}(\tau)\frac{\partial A_{\phi 2}}{\partial \tau}\cos\left(A_{\phi 2}(\tau)\right) &\quad +\gamma\sqrt{\kappa}\mathrm{K}''\sin(\mathrm{K}'\ell)\, e^{\vartheta_{21}} A_{r1}(\tau - T_2)\cos\left(\theta_{21} + A_{\phi 1}(\tau - T_2)\right) \\ &\quad +\gamma\sqrt{\kappa}\cos(\mathrm{K}'\ell)\, e^{\vartheta_{22}} A_{r2}(\tau - T_2)\sin\left(\theta_{22} + A_{\phi 2}(\tau - T_2)\right) \end{aligned}$$

For laser 1…

Add $\mathrm{Re}\{\partial A_1/\partial\tau\}\cdot\cos\left(A_{\phi 1}(\tau)\right)$ and $\mathrm{Im}\{\partial A_1/\partial\tau\}\cdot\sin\left(A_{\phi 1}(\tau)\right)$

$$\begin{aligned} \frac{\partial A_{r1}}{\partial \tau} &= -\gamma A_{r1}(\tau) \\ &\quad +\gamma\sqrt{\kappa}\cos(\mathrm{K}'\ell)\, e^{\vartheta_{11}} A_{r1}(\tau - T_1)\cos\left(\theta_{11} + A_{\phi 1}(\tau - T_1) - A_{\phi 1}(\tau)\right) \\ &\quad -\gamma\sqrt{\kappa}\frac{1}{\mathrm{K}''}\sin(\mathrm{K}'\ell)\, e^{\vartheta_{12}} A_{r2}(\tau - T_1)\sin\left(\theta_{12} + A_{\phi 2}(\tau - T_1) - A_{\phi 1}(\tau)\right) \end{aligned}$$

Add $-\mathrm{Re}\{\partial A_1/\partial\tau\}\cdot\sin\left(A_{\phi 1}(\tau)\right)$ and $\mathrm{Im}\{\partial A_1/\partial\tau\}\cdot\cos\left(A_{\phi 1}(\tau)\right)$

$$\frac{dA_{\phi 1}}{\partial\tau} = \frac{\gamma\sqrt{\kappa}}{A_{r1}(\tau)}\cos(\mathrm{K}'\ell)\, e^{\vartheta_{11}} A_{r1}(\tau - T_1)\sin\Big(\theta_{11} + A_{\phi 1}(\tau - T_1) - A_{\phi 1}(\tau)\Big)$$
$$+\frac{\gamma\sqrt{\kappa}}{A_{r1}(\tau)}\frac{1}{\mathrm{K}''}\sin(\mathrm{K}'\ell)\, e^{\vartheta_{12}} A_{r2}(\tau - T_1)\cos\Big(\theta_{12} + A_{\phi 2}(\tau - T_1) - A_{\phi 1}(\tau)\Big)$$

For laser 2…

Add $\mathrm{Re}\{\partial A_2/\partial\tau\}\cdot\cos\Big(A_{\phi 2}(\tau)\Big)$ and $\mathrm{Im}\{\partial A_2/\partial\tau\}\cdot\sin\Big(A_{\phi 2}(\tau)\Big)$

$$\frac{\partial A_{r2}}{\partial\tau} = -\gamma A_{r2}(\tau)$$
$$-\gamma\sqrt{\kappa}\mathrm{K}''\sin(\mathrm{K}'\ell)\, e^{\vartheta_{21}} A_{r1}(\tau - T_2)\sin\Big(\theta_{21} + A_{\phi 1}(\tau - T_2) - A_{\phi 2}(\tau)\Big)$$
$$+\gamma\sqrt{\kappa}\cos(\mathrm{K}'\ell)\, e^{\vartheta_{22}} A_{r2}(\tau - T_2)\cos\Big(\theta_{22} + A_{\phi 2}(\tau - T_2) - A_{\phi 2}(\tau)\Big)$$

Add $-\mathrm{Re}\{\partial A_2/\partial\tau\}\cdot\sin\Big(A_{\phi 2}(\tau)\Big)$ and $\mathrm{Im}\{\partial A_2/\partial\tau\}\cdot\cos\Big(A_{\phi 2}(\tau)\Big)$

$$\frac{\partial A_{\phi 2}(\tau)}{\partial\tau} = \frac{\gamma\sqrt{\kappa}}{A_{r2}(\tau)}\mathrm{K}''\sin(\mathrm{K}'\ell)\, e^{\vartheta_{21}} A_{r1}(\tau - T_2)\cos\Big(\theta_{21} + A_{\phi 1}(\tau - T_2) - A_{\phi 2}(\tau)\Big)$$
$$+\frac{\gamma\sqrt{\kappa}}{A_{r2}(\tau)}\cos(\mathrm{K}'\ell)\, e^{\vartheta_{22}} A_{r2}(\tau - T_2)\sin\Big(\theta_{22} + A_{\phi 2}(\tau - T_2) - A_{\phi 2}(\tau)\Big)$$

Rotating-wave / continuous-wave (CW) solutions

Consider the following case:

$A_1(\tau) = A_{r1}(\tau)e^{i\gamma\omega\tau} \rightarrow A_{\phi 1}(\tau) = \gamma\omega\tau \rightarrow A_{\phi 1}(\tau - T_{1,2}) = \gamma\omega\tau - \gamma\omega T_{1,2}$

$A_2(\tau) = A_{r2}(\tau)e^{i(\gamma\omega\tau+\sigma)} \rightarrow A_{\phi 2}(\tau) = \gamma\omega\tau + \sigma \rightarrow A_{\phi 2}(\tau - T_{1,2}) = \gamma\omega\tau - \gamma\omega T_{1,2} + \sigma$

where σ is a constant (time-independent) phase shift between the two amplitudes

$A_{\phi 1}(\tau)$, $A_{\phi 2}(\tau)$ linear → rotational symmetry of $A_1(\tau)$, $A_2(\tau)$ in complex plane

The boxed equations below serve as "the rotating-wave DDE model"

$$\boxed{\begin{aligned}\frac{\partial A_{r1}}{\partial\tau} &= -\gamma A_{r1}(\tau)\\ &+\gamma\sqrt{\kappa}\cos(\mathrm{K}'\ell)\, e^{\frac{G_1(\tau-T_1)-Q_1(\tau-T_1)}{2}}\cos\Big(-\frac{\alpha_g G_1(\tau-T_1)}{2}+\frac{\alpha_q Q_1(\tau-T_1)}{2}-\varphi_1-\gamma\omega T_1\Big)A_{r1}(\tau-T_1)\\ &-\gamma\sqrt{\kappa}\frac{1}{\mathrm{K}''}\sin(\mathrm{K}'\ell)\, e^{\frac{G_2(\tau-T_1)-Q_2(\tau-T_1)}{2}}\sin\Big(-\frac{\alpha_g G_2(\tau-T_1)}{2}+\frac{\alpha_q Q_2(\tau-T_1)}{2}-\varphi_1-\gamma\omega T_1+\sigma\Big)A_{r2}(\tau-T_1)\end{aligned}}$$

$$\boxed{\frac{\partial G_1(\tau)}{\partial\tau} = g_{01} - \Gamma G_1(\tau) - e^{-Q_1(\tau)}\big(e^{G_1(\tau)}-1\big)\big(A_{r1}(\tau)\big)^2}$$

$$\boxed{\frac{\partial Q_1(\tau)}{\partial\tau} = q_0 - Q_1(\tau) - s\big(1-e^{-Q_1(\tau)}\big)\big(A_{r1}(\tau)\big)^2}$$

$$\boxed{\begin{aligned}\frac{\partial A_{r2}}{\partial\tau} &= -\gamma A_{r2}(\tau)\\ &-\gamma\sqrt{\kappa}\mathrm{K}''\sin(\mathrm{K}'\ell)\, e^{\frac{G_1(\tau-T_2)-Q_1(\tau-T_2)}{2}}\sin\Big(-\frac{\alpha_g G_1(\tau-T_2)}{2}+\frac{\alpha_q Q_1(\tau-T_2)}{2}-\varphi_2-\gamma\omega T_2-\sigma\Big)A_{r1}(\tau-T_2)\\ &+\gamma\sqrt{\kappa}\cos(\mathrm{K}'\ell)\, e^{\frac{G_2(\tau-T_2)-Q_2(\tau-T_2)}{2}}\cos\Big(-\frac{\alpha_g G_2(\tau-T_2)}{2}+\frac{\alpha_q Q_2(\tau-T_2)}{2}-\varphi_2-\gamma\omega T_2\Big)A_{r2}(\tau-T_2)\end{aligned}}$$

$$\boxed{\frac{\partial G_2(\tau)}{\partial\tau} = g_{02} - \Gamma G_2(\tau) - e^{-Q_2(\tau)}\big(e^{G_2(\tau)}-1\big)\big(A_{r2}(\tau)\big)^2}$$

$$\boxed{\frac{\partial Q_2(\tau)}{\partial\tau} = q_0 - Q_2(\tau) - s\big(1-e^{-Q_2(\tau)}\big)\big(A_{r2}(\tau)\big)^2}$$

Additional conditions/constraints (note that ω and σ are treated as "free parameters")

For laser 1…

$$\frac{dA_{\phi 1}}{\partial \tau} = \gamma\omega = \frac{\gamma\sqrt{\kappa}}{A_{r1}(\tau)}\cos(\mathrm{K}'\ell)\, e^{\vartheta_{11}} A_{r1}(\tau - T_1)\sin\left(\theta_{11} + A_{\phi 1}(\tau - T_1) - A_{\phi 1}(\tau)\right) + \frac{\gamma\sqrt{\kappa}}{A_{r1}(\tau)}\frac{1}{\mathrm{K}''}\sin(\mathrm{K}'\ell)\, e^{\vartheta_{12}} A_{r2}(\tau - T_1)\cos\left(\theta_{12} + A_{\phi 2}(\tau - T_1) - A_{\phi 1}(\tau)\right)$$

$$\rightarrow \boxed{\begin{aligned} 0 = {} & -\omega A_{r1}(\tau) \\ & + \sqrt{\kappa}\cos(\mathrm{K}'\ell)\, e^{\frac{G_1(\tau - T_1) - Q_1(\tau - T_1)}{2}} \sin\left(-\frac{\alpha_g G_1(\tau - T_1)}{2} + \frac{\alpha_q Q_1(\tau - T_1)}{2} - \varphi_1 - \gamma\omega T_1\right) A_{r1}(\tau - T_1) \\ & + \sqrt{\kappa}\frac{1}{\mathrm{K}''}\sin(\mathrm{K}'\ell)\, e^{\frac{G_2(\tau - T_1) - Q_2(\tau - T_1)}{2}} \cos\left(-\frac{\alpha_g G_2(\tau - T_1)}{2} + \frac{\alpha_q Q_2(\tau - T_1)}{2} - \varphi_1 - \gamma\omega T_1 + \sigma\right) A_{r2}(\tau - T_1) \end{aligned}}$$

For laser 2…

$$\frac{\partial A_{\phi 2}(\tau)}{\partial \tau} = \gamma\omega = \frac{\gamma\sqrt{\kappa}}{A_{r2}(\tau)}\mathrm{K}''\sin(\mathrm{K}'\ell)\, e^{\vartheta_{21}} A_{r1}(\tau - T_2)\cos\left(\theta_{21} + A_{\phi 1}(\tau - T_2) - A_{\phi 2}(\tau)\right) + \frac{\gamma\sqrt{\kappa}}{A_{r2}(\tau)}\cos(\mathrm{K}'\ell)\, e^{\vartheta_{22}} A_{r2}(\tau - T_2)\sin\left(\theta_{22} + A_{\phi 2}(\tau - T_2) - A_{\phi 2}(\tau)\right)$$

$$\rightarrow \boxed{\begin{aligned} 0 = {} & -\omega A_{r2}(\tau) \\ & + \sqrt{\kappa}\mathrm{K}''\sin(\mathrm{K}'\ell)\, e^{\frac{G_1(\tau - T_2) - Q_1(\tau - T_2)}{2}} \cos\left(-\frac{\alpha_g G_1(\tau - T_2)}{2} + \frac{\alpha_q Q_1(\tau - T_2)}{2} - \varphi_2 - \gamma\omega T_2 - \sigma\right) A_{r1}(\tau - T_2) \\ & + \sqrt{\kappa}\cos(\mathrm{K}'\ell)\, e^{\frac{G_2(\tau - T_2) - Q_2(\tau - T_2)}{2}} \sin\left(-\frac{\alpha_g G_2(\tau - T_2)}{2} + \frac{\alpha_q Q_2(\tau - T_2)}{2} - \varphi_2 - \gamma\omega T_2\right) A_{r2}(\tau - T_2) \end{aligned}}$$

A.2.2 Equilibria

"Equal-amplitude" equilibria (denoted by superscript ∘) for rotating-wave DDE model

Assume the case where…

$\mathrm{K}'' = 1 \leftarrow$ coupling coefficients between the two lasers are equal

$T_1 = T_2 = T \leftarrow$ cavity roundtrip times (normalized) for the two lasers are equal

$g_{01} = g_{02} = g_0 \leftarrow$ gain parameters for the two lasers are equal

$\alpha_g = 0$ and $\alpha_q = 0 \leftarrow$ zero linewidth enhancement factors

$\varphi_{1,2} = 0 \leftarrow \Omega T = 0 \leftarrow \Omega = 0 \leftarrow$ zero detuning from spectral filter center

Substitute these simplifications into the DDEs (and constraint equations on $A_{\phi 1}$ and $A_{\phi 2}$)

From the amplitude equation for laser 1…

$$0 = -\gamma A_{r1}^{\circ} + \gamma\sqrt{\kappa}\cos(\mathrm{K}'\ell)\, e^{\frac{G_1^{\circ} - Q_1^{\circ}}{2}} \cos(\gamma\omega T)\, A_{r1}^{\circ} + \gamma\sqrt{\kappa}\sin(\mathrm{K}'\ell)\, e^{\frac{G_2^{\circ} - Q_2^{\circ}}{2}} \sin(\gamma\omega T - \sigma)\, A_{r2}^{\circ}$$

$$\rightarrow A_{r1}^{\circ} = \sqrt{\kappa} e^{\frac{G_1^{\circ} - Q_1^{\circ}}{2}} A_{r1}^{\circ}\cos(\mathrm{K}'\ell)\cos(\gamma\omega T) + \sqrt{\kappa} e^{\frac{G_2^{\circ} - Q_2^{\circ}}{2}} A_{r2}^{\circ}\sin(\mathrm{K}'\ell)\sin(\gamma\omega T - \sigma)$$

$$\rightarrow (A_{r1}^{\circ})^2 = \kappa e^{G_1^{\circ} - Q_1^{\circ}} (A_{r1}^{\circ})^2 \cos^2(\mathrm{K}'\ell)\cos^2(\gamma\omega T) + \kappa e^{G_2^{\circ} - Q_2^{\circ}} (A_{r2}^{\circ})^2 \sin^2(\mathrm{K}'\ell)\sin^2(\gamma\omega T - \sigma) + 2\kappa e^{\frac{G_1^{\circ} - Q_1^{\circ} + G_2^{\circ} - Q_2^{\circ}}{2}} A_{r1}^{\circ} A_{r2}^{\circ}\sin(\mathrm{K}'\ell)\cos(\mathrm{K}'\ell)\sin(\gamma\omega T - \sigma)\cos(\gamma\omega T)$$

From the constraint equation for laser 1…

$$0 = -\omega A_{r1}^{\circ} - \sqrt{\kappa}\cos(\mathrm{K}'\ell)\, e^{\frac{G_1^{\circ} - Q_1^{\circ}}{2}} \sin(\gamma\omega T)\, A_{r1}^{\circ} + \sqrt{\kappa}\sin(\mathrm{K}'\ell)\, e^{\frac{G_2^{\circ} - Q_2^{\circ}}{2}} \cos(\gamma\omega T - \sigma)\, A_{r2}^{\circ}$$

$$\rightarrow \omega A_{r1}^{\circ} = -\sqrt{\kappa} e^{\frac{G_1^{\circ} - Q_1^{\circ}}{2}} A_{r1}^{\circ}\cos(\mathrm{K}'\ell)\sin(\gamma\omega T) + \sqrt{\kappa} e^{\frac{G_2^{\circ} - Q_2^{\circ}}{2}} A_{r2}^{\circ}\sin(\mathrm{K}'\ell)\cos(\gamma\omega T - \sigma)$$

$$\rightarrow \omega^2 (A_{r1}^{\circ})^2 = \kappa e^{G_1^{\circ} - Q_1^{\circ}} (A_{r1}^{\circ})^2 \cos^2(\mathrm{K}'\ell)\sin^2(\gamma\omega T) + \kappa e^{G_2^{\circ} - Q_2^{\circ}} (A_{r2}^{\circ})^2 \sin^2(\mathrm{K}'\ell)\cos^2(\gamma\omega T - \sigma) - 2\kappa e^{\frac{G_1^{\circ} - Q_1^{\circ} + G_2^{\circ} - Q_2^{\circ}}{2}} A_{r1}^{\circ} A_{r2}^{\circ}\sin(\mathrm{K}'\ell)\cos(\mathrm{K}'\ell)\sin(\gamma\omega T)\cos(\gamma\omega T - \sigma)$$

Combine the above two results

$$(1+\omega^2)(A_{r1}^\circ)^2 = \kappa e^{G_1^\circ - Q_1^\circ}(A_{r1}^\circ)^2\cos^2(\mathrm{K}'\ell) + \kappa e^{G_2^\circ - Q_2^\circ}(A_{r2}^\circ)^2\sin^2(\mathrm{K}'\ell)$$
$$+2\kappa e^{\frac{G_1^\circ - Q_1^\circ + G_2^\circ - Q_2^\circ}{2}} A_{r1}^\circ A_{r2}^\circ \sin(\mathrm{K}'\ell)\cos(\mathrm{K}'\ell)\begin{pmatrix}\sin(\gamma\omega T)\cos\sigma\cos(\gamma\omega T)\\ -\sin\sigma\cos^2(\gamma\omega T)\\ -\sin(\gamma\omega T)\cos(\gamma\omega T)\cos\sigma\\ -\sin^2(\gamma\omega T)\sin\sigma\end{pmatrix}$$
$$\rightarrow (1+\omega^2)(A_{r1}^\circ)^2 = \kappa e^{G_1^\circ - Q_1^\circ}(A_{r1}^\circ)^2\cos^2(\mathrm{K}'\ell) + \kappa e^{G_2^\circ - Q_2^\circ}(A_{r2}^\circ)^2\sin^2(\mathrm{K}'\ell)$$
$$-2\kappa e^{\frac{G_1^\circ - Q_1^\circ + G_2^\circ - Q_2^\circ}{2}} A_{r1}^\circ A_{r2}^\circ \sin(\mathrm{K}'\ell)\cos(\mathrm{K}'\ell)\sin\sigma$$

From the amplitude equation for laser 2…

$$0 = -\gamma A_{r2}^\circ + \gamma\sqrt{\kappa}\sin(\mathrm{K}'\ell)\, e^{\frac{G_1^\circ - Q_1^\circ}{2}}\sin(\gamma\omega T+\sigma)\, A_{r1}^\circ + \gamma\sqrt{\kappa}\cos(\mathrm{K}'\ell)\, e^{\frac{G_2^\circ - Q_2^\circ}{2}}\cos(\gamma\omega T)\, A_{r2}^\circ$$
$$\rightarrow A_{r2}^\circ = \sqrt{\kappa} e^{\frac{G_1^\circ - Q_1^\circ}{2}} A_{r1}^\circ \sin(\mathrm{K}'\ell)\sin(\gamma\omega T+\sigma) + \sqrt{\kappa} e^{\frac{G_2^\circ - Q_2^\circ}{2}} A_{r2}^\circ \cos(\mathrm{K}'\ell)\cos(\gamma\omega T)$$
$$\rightarrow (A_{r2}^\circ)^2 = \kappa e^{G_1^\circ - Q_1^\circ}(A_{r1}^\circ)^2\sin^2(\mathrm{K}'\ell)\sin^2(\gamma\omega T+\sigma) + \kappa e^{G_2^\circ - Q_2^\circ}(A_{r2}^\circ)^2\cos^2(\mathrm{K}'\ell)\cos^2(\gamma\omega T)$$
$$+2\kappa e^{\frac{G_1^\circ - Q_1^\circ + G_2^\circ - Q_2^\circ}{2}} A_{r1}^\circ A_{r2}^\circ \sin(\mathrm{K}'\ell)\cos(\mathrm{K}'\ell)\sin(\gamma\omega T+\sigma)\cos(\gamma\omega T)$$

From the constraint equation for laser 2…

$$0 = -\omega A_{r2}^\circ + \sqrt{\kappa}\sin(\mathrm{K}'\ell)\, e^{\frac{G_1^\circ - Q_1^\circ}{2}}\cos(\gamma\omega T+\sigma)\, A_{r1}^\circ - \sqrt{\kappa}\cos(\mathrm{K}'\ell)\, e^{\frac{G_2^\circ - Q_2^\circ}{2}}\sin(\gamma\omega T)\, A_{r2}^\circ$$
$$\rightarrow \omega A_{r2}^\circ = \sqrt{\kappa} e^{\frac{G_1^\circ - Q_1^\circ}{2}} A_{r1}^\circ \sin(\mathrm{K}'\ell)\cos(\gamma\omega T+\sigma) - \sqrt{\kappa} e^{\frac{G_2^\circ - Q_2^\circ}{2}} A_{r2}^\circ \cos(\mathrm{K}'\ell)\sin(\gamma\omega T)$$
$$\rightarrow \omega^2(A_{r2}^\circ)^2 = \kappa e^{G_1^\circ - Q_1^\circ}(A_{r1}^\circ)^2\sin^2(\mathrm{K}'\ell)\cos^2(\gamma\omega T+\sigma) + \kappa e^{G_2^\circ - Q_2^\circ}(A_{r2}^\circ)^2\cos^2(\mathrm{K}'\ell)\sin^2(\gamma\omega T)$$
$$-2\kappa e^{\frac{G_1^\circ - Q_1^\circ + G_2^\circ - Q_2^\circ}{2}} A_{r1}^\circ A_{r2}^\circ \sin(\mathrm{K}'\ell)\cos(\mathrm{K}'\ell)\sin(\gamma\omega T)\cos(\gamma\omega T+\sigma)$$

Combine the above to results

$$(1+\omega^2)(A_{r2}^\circ)^2 = \kappa e^{G_1^\circ - Q_1^\circ}(A_{r1}^\circ)^2\sin^2(\mathrm{K}'\ell) + \kappa e^{G_2^\circ - Q_2^\circ}(A_{r2}^\circ)^2\cos^2(\mathrm{K}'\ell)$$
$$+2\kappa e^{\frac{G_1^\circ - Q_1^\circ + G_2^\circ - Q_2^\circ}{2}} A_{r1}^\circ A_{r2}^\circ \sin(\mathrm{K}'\ell)\cos(\mathrm{K}'\ell)\begin{pmatrix}\sin(\gamma\omega T)\cos\sigma\cos(\gamma\omega T)\\ +\sin\sigma\cos^2(\gamma\omega T)\\ -\sin(\gamma\omega T)\cos(\gamma\omega T)\cos\sigma\\ +\sin^2(\gamma\omega T)\sin\sigma\end{pmatrix}$$
$$\rightarrow (1+\omega^2)(A_{r2}^\circ)^2 = \kappa e^{G_1^\circ - Q_1^\circ}(A_{r1}^\circ)^2\sin^2(\mathrm{K}'\ell) + \kappa e^{G_2^\circ - Q_2^\circ}(A_{r2}^\circ)^2\cos^2(\mathrm{K}'\ell)$$
$$+2\kappa e^{\frac{G_1^\circ - Q_1^\circ + G_2^\circ - Q_2^\circ}{2}} A_{r1}^\circ A_{r2}^\circ \sin(\mathrm{K}'\ell)\cos(\mathrm{K}'\ell)\sin\sigma$$

From the gain/absorber equations for lasers 1 and 2

$$0 = g_0 - \Gamma G_1^\circ - e^{-Q_1^\circ}\left(e^{G_1^\circ} - 1\right)(A_{r1}^\circ)^2$$
$$0 = q_0 - Q_1^\circ - s\left(1 - e^{-Q_1^\circ}\right)(A_{r1}^\circ)^2$$
$$0 = g_0 - \Gamma G_2^\circ - e^{-Q_2^\circ}\left(e^{G_2^\circ} - 1\right)(A_{r2}^\circ)^2$$
$$0 = q_0 - Q_2^\circ - s\left(1 - e^{-Q_2^\circ}\right)(A_{r2}^\circ)^2$$

Solve the above equations for A_r°, ω, σ, G°, and Q°

Add together the expressions for $(1+\omega^2)(A_{r1}^\circ)^2$ and $(1+\omega^2)(A_{r2}^\circ)^2$

$$\boxed{(1+\omega^2)\left((A_{r1}^\circ)^2 + (A_{r2}^\circ)^2\right) = \kappa\left(e^{G_1^\circ - Q_1^\circ}(A_{r1}^\circ)^2 + e^{G_2^\circ - Q_2^\circ}(A_{r2}^\circ)^2\right)}$$

The general approach has not progressed beyond this step

For now, a simplifying assumption is made (the general approach is left for future work...); consider the case in which the two lasers have the same equilibria for $|A|$, G, and Q

Specifically, assume the following:
$A_{r1}^{\circ} = A_{r2}^{\circ} = A_r^{\circ}$
$G_1^{\circ} = G_2^{\circ} = G^{\circ}$
$Q_1^{\circ} = Q_2^{\circ} = Q^{\circ}$

Furthermore, consider three special cases:

1. $\sigma = 0 \leftarrow$ The two lasers' complex amplitudes are in-phase
2. $\sigma = \pi/2 \leftarrow$ The two lasers' complex amplitudes are 90° out-of-phase
3. $\sigma = \pi \leftarrow$ The two lasers' complex amplitudes are 180° out-of-phase

If $\sigma = 0$ (in-phase)…

The amplitude and constraint equations are as follows when $\sigma = 0$
(note that, for $\sigma = 0$, the two sets equations below are identical)

Laser 1: $\begin{Bmatrix} 1 = \sqrt{\kappa} e^{\frac{G^{\circ}-Q^{\circ}}{2}} (\sin(\mathrm{K}'\ell)\sin(\gamma\omega T - 0) + \cos(\mathrm{K}'\ell)\cos(\gamma\omega T)) \\ \omega = \sqrt{\kappa} e^{\frac{G^{\circ}-Q^{\circ}}{2}} (\sin(\mathrm{K}'\ell)\cos(\gamma\omega T - 0) - \cos(\mathrm{K}'\ell)\sin(\gamma\omega T)) \end{Bmatrix}$

Laser 2: $\begin{Bmatrix} 1 = \sqrt{\kappa} e^{\frac{G^{\circ}-Q^{\circ}}{2}} (\sin(\mathrm{K}'\ell)\sin(\gamma\omega T + 0) + \cos(\mathrm{K}'\ell)\cos(\gamma\omega T)) \\ \omega = \sqrt{\kappa} e^{\frac{G^{\circ}-Q^{\circ}}{2}} (\sin(\mathrm{K}'\ell)\cos(\gamma\omega T + 0) - \cos(\mathrm{K}'\ell)\sin(\gamma\omega T)) \end{Bmatrix}$

Note the following:
$1 = \sqrt{\kappa} e^{\frac{G^{\circ}-Q^{\circ}}{2}} (\sin(\mathrm{K}'\ell)\sin(\gamma\omega T) + \cos(\mathrm{K}'\ell)\cos(\gamma\omega T)) = \sqrt{\kappa} e^{\frac{G^{\circ}-Q^{\circ}}{2}} \cos(\mathrm{K}'\ell - \gamma\omega T)$
$\omega = \sqrt{\kappa} e^{\frac{G^{\circ}-Q^{\circ}}{2}} (\sin(\mathrm{K}'\ell)\cos(\gamma\omega T) - \cos(\mathrm{K}'\ell)\sin(\gamma\omega T)) = \sqrt{\kappa} e^{\frac{G^{\circ}-Q^{\circ}}{2}} \sin(\mathrm{K}'\ell - \gamma\omega T)$

Square both equations and then add them → $\boxed{1 + \omega^2 = \kappa e^{G^{\circ}-Q^{\circ}}}$

Note that $\left(\sqrt{\kappa} e^{\frac{G^{\circ}-Q^{\circ}}{2}}\right)^{-1} > 0 \rightarrow \boxed{\cos(\gamma\omega T - \mathrm{K}'\ell) > 0}$

Divide the two equations → $\boxed{\omega + \tan(\gamma\omega T - \mathrm{K}'\ell) = 0}$

From the gain and absorber DDEs (which are also identical due to the fact that $A_{r1}^{\circ} = A_{r2}^{\circ} = A_r^{\circ}$ and $G_1^{\circ} = G_2^{\circ} = G^{\circ}$ and $Q_1^{\circ} = Q_2^{\circ} = Q^{\circ}$)

$\boxed{0 = g_0 - \Gamma G^{\circ} - e^{-Q^{\circ}}\left(e^{G^{\circ}} - 1\right)(A_r^{\circ})^2}$

$\boxed{0 = q_0 - Q^{\circ} - s\left(1 - e^{-Q^{\circ}}\right)(A_r^{\circ})^2}$

Solve the following…

1. ω Solve $\boxed{\omega + \tan(\gamma\omega T - \mathrm{K}'\ell) = 0}$ and $\boxed{\cos(\gamma\omega T - \mathrm{K}'\ell) > 0}$
2. Q° Solve $\boxed{0 = g_0 - \Gamma\left(Q^{\circ} + \ln\left(\frac{1+\omega^2}{\kappa}\right)\right) + \left(e^{-Q^{\circ}} - \frac{1+\omega^2}{\kappa}\right)\frac{q_0 - Q^{\circ}}{s\left(1 - e^{-Q^{\circ}}\right)}}$
3. G° $\boxed{G^{\circ} = Q^{\circ} + \ln\left(\frac{1+\omega^2}{\kappa}\right)}$

4. A_r° $\boxed{A_r^\circ = \sqrt{\frac{q_0 - Q^\circ}{s\left(1 - e^{-Q^\circ}\right)}}}$

Derivation for 2, 3, and 4 above…

$$\kappa e^{G^\circ - Q^\circ} = 1 + \omega^2 \rightarrow G^\circ = Q^\circ + \ln\left(\frac{1+\omega^2}{\kappa}\right)$$

$$(A_r^\circ)^2 = \frac{q_0 - Q^\circ}{s\left(1 - e^{-Q^\circ}\right)}$$

$$\rightarrow 0 = g_0 - \Gamma\left(Q^\circ + \ln\left(\frac{1+\omega^2}{\kappa}\right)\right) - e^{-Q^\circ}\left(e^{Q^\circ}\frac{1+\omega^2}{\kappa} - 1\right)\left(\frac{q_0 - Q^\circ}{s\left(1 - e^{-Q^\circ}\right)}\right)$$

$$\rightarrow 0 = g_0 - \Gamma\left(Q^\circ + \ln\left(\frac{1+\omega^2}{\kappa}\right)\right) + \left(e^{-Q^\circ} - \frac{1+\omega^2}{\kappa}\right)\frac{q_0 - Q^\circ}{s\left(1 - e^{-Q^\circ}\right)}$$

If $\sigma = \pi$ (180° out-of-phase)…

Left for future work…

If $\sigma = \pi/2$ (90° out-of-phase)…

Left for future work…

For arbitrary σ (“intermediate” phase)…

Using DDE-BIFTOOL, start with equilibrium point for $\sigma = 0$, and then continue the branch as σ is varied; left for future work…

Note that for the trivial steady state (in which both lasers are “off”)…

$A_r^\circ = 0$

$G^\circ = g_0/\Gamma$

$Q^\circ = q_0$

Bifurcation from the trivial solution

Note that the CW solution bifurcates from the trivial, zero-amplitude solution at the intersection of the equations $G^\circ = g_0/\Gamma$, $Q^\circ = q_0$, and $\kappa e^{G^\circ - Q^\circ} - 1 - \omega^2 = 0$

This happens when the gain parameter g_0 crosses the following condition:

$\ln\kappa + G^\circ - Q^\circ = \ln(1 + \omega^2)$

$\rightarrow G^\circ = \frac{g_0}{\Gamma} = Q^\circ - \ln\kappa + \ln(1 + \omega^2) = q_0 - \ln\kappa + \ln(1 + \omega^2)$

$\rightarrow \boxed{g_0 = \Gamma(q_0 - \ln\kappa + \ln(1 + \omega^2))}$

APPENDIX B

List of MATLAB codes written and used for the thesis work

Due to formatting constraints, in particular a lack of adequate page-width for proper display of the MATLAB code, the following section does not include the entire codes used for the thesis. Instead, descriptions of the .m files written / developed for the thesis work are provided. To request a copy of the code, please send an email to the author at sivas@umich.edu and/or the author's research advisor (and dissertation committee chair) at arrays@umich.edu.

B.1 Simulation of coherent beam combining of fiber laser arrays

The dynamical evolution of the system from "turn-on" and as it recovers from a perturbation on its steady state are simulated by use of the numerical code in the following .m files:

- `coupledGlobal_M_fiber.m` implements the Split-Step Fourier Method for nonlinear wave propagation through the fiber laser array, the Euler Method for the gain dynamics, and the Fourier-Transform-based boundary condition imposed by the spatially-filtered ring geometry coupling mechanism).
- `test_fiber_array.m` is the main script file: it initializes the parameter sets and runs the simulations by calling `coupledGlobal_M_fiber`).

B.2 Simulation of coupled mode-locked semiconductor lasers

The following .m files run the numerical simulations via time integration of the DDE model:

- `mlsl_2.m` numerically solves the model equations for a given parameter set and initial history (which can be a constant vector, a function handle, or a previous simulation's solution structure). The code makes use of `dde23()`, a built-in MATLAB function.
- `mlsl_2_bif1p.m` generates the one-parameter bifurcation diagrams, for a given parameter set, a given set of values for the sweep parameter over which the iterations are performed, and a given initial history to use for the first iteration, in the manner described as follows. The first iteration uses the given initial history and then simulates the system to steady using the parameter set and the first value of the sweep parameter. Each subsequent iteration, after updating the sweep parameter to its next value, runs a simulation initialized/"seeded" by the previous iteration's solution structure. Every iteration extracts and plots the local minima/maxima.

B.3 Bifurcation analysis of coupled mode-locked semiconductor lasers

The following .m files used here make use of DDE-BIFTOOL (version 3.1, August 22, 2015, developed in the MATLAB language [105, 81]) and automate the bifurcation analysis:

- `mlslBIF2.m` automates the bifurcation routines for the rotating-wave DDE model and plots the branch of the equilibria / periodic orbits in one parameter as well as the continuation of Hopf branches in two parameters (and identifies their stability/criticality).
- `stdystsol2.m` solves for the equilibrium (and the rotating frequency ω) given an input parameter set, as per the method described in APPENDIX A.2.2, to provide an initial point for the branch of equilibria created by `mlslBIF2` for the parameter sweeps.

BIBLIOGRAPHY

[1] G. P. Agrawal, *Applications of Nonlinear Fiber Optics,* 2nd ed. Burlington, MA: Academic Press, 2008.

[2] B. E. A. Saleh and M. C. Teich, *Fundamentals of Photonics,* 2nd ed. Hoboken, NJ: Wiley, 2007.

[3] D. J. Richardson, J. Nilsson and W. A. Clarkson, "High power fiber lasers: current status and future perspectives [Invited]," *J. Opt. Soc. Am. B,* vol. 27, no. 11, pp. B63-B92, 2010.

[4] R. Paschotta, J. Nilsson, A. C. Tropper and D. C. Hanna, "Ytterbium-Doped Fiber Amplifiers," *IEEE Journal of Quantum Electronics,* vol. 33, no. 7, pp. 1049-1056, 1997.

[5] C. Jauregui, J. Limpert and A. Tünnermann, "High-power fibre lasers," *Nature Photonics,* vol. 7, no. 11, pp. 861-867, 2013.

[6] C. Jauregui et al., "Physical origin of mode instabilities in high-power fiber laser systems," *Optics Express,* vol. 20, no. 12, pp. 12912-12925, 2012.

[7] T. Y. Fan, "Laser Beam Combining for High-Power, High-Radiance Sources," *IEEE Journal of Selected Topics in Quantum Electronics,* vol. 11, no. 3, pp. 567-577, 2005.

[8] J. E. Rothenberg and G. D. Goodno, "Advances and Limitations in Beam Combination of Kilowatt Fiber Amplifiers," *Proc. of SPIE,* vol. 7686, pp. 1-8, 2010.

[9] S. J. Augst, J. K. Ranka, T. Y. Fan and A. Sanchez, "Beam combining of ytterbium fiber amplifiers (Invited)," *J. Opt. Soc. Am. B,* vol. 24, no. 8, pp. 1707-1715, 2007.

[10] E. J. Bochove and S. A. Shakir, "Analysis of a Spatial-Filtering Passive Fiber Laser Beam Combining System," *IEEE Journal of Selected Topics in Quantum Electronics,* vol. 15, no. 2, pp. 320-327, 2009.

[11] S. Sivaramakrishnan, W.-Z. Chang, A. Galvanauskas and H. G. Winful, "Dynamics of Passively Phased Ring Oscillator Fiber Laser Arrays," *IEEE Journal of Quantum Electronics,* vol. 51, no. 8, pp. 1-9, Aug. 2015.

[12] A. Shirakawa, T. Saitou, T. Sekiguchi and K.-i. Ueda, "Coherent addition of fiber lasers by use of a fiber coupler," *Optics Express,* vol. 10, no. 21, pp. 1167-1172, 2002.

[13] D. Sabourdy et al., "Power scaling of fibre lasers with all-fibre interferometric cavity," *Electronic Letters,* vol. 38, no. 14, pp. 692-693, 2002.

[14] E. J. Bochove, P. K. Cheo and G. G. King, "Self-organization in a multicore fiber laser array," *Optics Letters,* vol. 28, no. 14, pp. 1200-1202, 2003.

[15] C. J. Corcoran and P. A. Pasch, "Modal analysis of a self-Fourier laser cavity," *J. Opt. A: Pure Appl. Opt.,* vol. 7, no. 5, pp. L1-L7, 2005.

[16] C. J. Corcoran and F. Durville, "Experimental demonstration of a phase-locked laser array using a self-Fourier cavity," *Applied Physics Letters,* vol. 86, no. 20, pp. 1-3, 2005.

[17] C. J. Corcoran, F. Durville and K. A. Pasch, "Coherent Array of Nonlinear Regenerative Fiber Amplifiers," *IEEE Journal of Quantum Electronics,* vol. 44, no. 3, pp. 275-282, 2008.

[18] M. Wrage et al., "Phase locking in a multicore fiber laser by means of a Talbot resonator," *Optics Letters,* vol. 25, no. 19, pp. 1436-1438, 2000.

[19] L. Li et al., "Phase locking and in-phase supermode selection in monolithic multicore fiber lasers," *Optics Letters,* vol. 31, no. 17, pp. 2577-2579, 2006.

[20] S. M. Redmond et al., "Diffractive coherent combining of a 2.5 kW fiber laser array into a 1.9 kW Gaussian beam," *Optics Letters,* vol. 37, no. 14, pp. 2832-2834, 2012.

[21] E. C. Cheung et al., "Diffractive-optics-based beam combination of a phase-locked fiber laser array," *Optics Letters,* vol. 33, no. 4, pp. 354-356, 2008.

[22] E. J. Bochove et al., "Model of the Self-Q-Switching Instability of Passively Phased Fiber Laser Arrays," *IEEE Journal of Quantum Electronics,* vol. 47, no. 6, pp. 777-785, 2011.

[23] J. Lhermite, A. Desfarges-Berthelemot, V. Kermene and A. Barthelemy, "Passive phase locking of an array of four fiber amplifiers by an all-optical feedback loop," *Optics Letters,* vol. 32, no. 13, pp. 1842-1844, 2007.

[24] T. H. Loftus et al., "Four-channel, high power, passively phase locked fiber array," *Advanced Solid-State Photonics, OSA Technical Digest Series (CD),* pp. paper WA4, 1-3, 2008.

[25] J. Guillot, A. Desfarges-Berthelemot, V. Kermène and A. Barthélémy, "Experimental study of cophasing dynamics in passive coherent combining of fiber lasers," *Optics Letters,* vol. 36, no. 15, pp. 2907-2909, 2011.

[26] S. A. Shakir et al., "Power scaling of passively phased fiber amplifier arrays," *Proc. of SPIE,* vol. 7070, pp. 1-6, 2008.

[27] M. Fridman, M. Nixon, N. Davidson and A. A. Friesem, "Passive phase locking of 25 fiber lasers," *Optics Letters,* vol. 35, no. 9, pp. 1434-1436, 2010.

[28] H.-S. Chiang, J. R. Leger, J. Nilsson and J. Sahu, "Direct observation of Kramers-Kronig self-phasing in coherently combined fiber lasers," *Optics Letters,* vol. 38, no. 20, pp. 4104-4107, 2013.

[29] H.-S. Chiang, J. Nilsson, J. Sahu and J. R. Leger, "Experimental measurements of the origin of self-phasing in passively coupled fiber lasers," *Optics Letters,* vol. 40, no. 6, pp. 962-965, 2015.

[30] F. Jeux et al., "Passive coherent combining of lasers with phase-contrast filtering for enhanced efficiency," *Appl. Phys. B,* vol. 108, no. 1, pp. 81-87, 2012.

[31] F. Jeux, A. Desfarges-Berthelemot, V. Kermène and A. Barthelemy, "Experimental demonstration of passive coherent combining of fiber lasers by phase contrast filtering," *Optics Express,* vol. 20, no. 27, pp. 28941-28946, 2012.

[32] F. Jeux, A. Desfarges-Berthelemot, V. Kermène and A. Barthelemy, "Efficient passive phasing of an array of 20 ring fiber lasers," *Laser Phys. Lett.,* vol. 11, no. 9, pp. 1-4, 2014.

[33] J. L. Rogers, S. Peleš and K. Wiesenfeld, "Model for High-Gain Fiber Laser Arrays," *IEEE Journal of Quantum Electronics,* vol. 41, no. 6, pp. 767-773, 2005.

[34] W. Ray, J. L. Rogers and K. Wiesenfeld, "Coherence between two coupled lasers from a dynamics perspective," *Optics Express,* vol. 17, no. 11, pp. 9357-9368, 2009.

[35] V. Roy, M. Piché, F. Babin and G. W. Schinn, "Nonlinear wave mixing in a multilongitudinal-mode erbium-doped fiber laser," *Optics Express,* vol. 13, no. 18, pp. 6791-6797, 2005.

[36] T.-w. Wu, W.-z. Chang, A. Galvanauskas and H. G. Winful, "Model for passive coherent beam combining in fiber laser arrays," *Optics Express,* vol. 17, no. 22, pp. 19509-19518, 2009.

[37] T.-w. Wu, W.-z. Chang, A. Galvanauskas and H. G. Winful, "Dynamical, bidirectional model for coherent beam combining in passive fiber laser arrays," *Optics Express,* vol. 18, no. 25, pp. 25873-25886, 2010.

[38] W.-z. Chang, T.-w. Wu, H. G. Winful and A. Galvanauskas, "Array size scalability of passively coherently phased fiber laser arrays," *Optics Express,* vol. 18, no. 9, pp. 9634-9642, 2010.

[39] E. J. Bochove, M. R. Zunoubi and C. J. Corcoran, "Effect of Kerr and resonant nonlinearities on phase locking of a multistable fiber amplifier array," *Optics Letters,* vol. 38, no. 23, pp. 5016-5019, 2013.

[40] C. J. Corcoran and K. A. Pasch, "Output Phase Characteristics of a Nonlinear Regenerative Fiber Amplifier," *IEEE Journal of Quantum Electronics,* vol. 43, no. 6, pp. 437-439, 2007.

[41] C. J. Corcoran and F. Durville, "Passive Phasing in a Coherent Laser Array," *IEEE Journal of Selected Topics in Quantum Electronics,* vol. 15, no. 2, pp. 294-300, 2009.

[42] A. P. Napartovich, N. N. Elkin and D. V. Vysotsky, "Influence of non-linear index on coherent passive beam combining of fiber lasers," *Proc. of SPIE,* vol. 7914, pp. 1-10, 2011.

[43] G. P. Agrawal, *Nonlinear Fiber Optics,* 5th ed. Oxford, U.K.: Elsevier, 2013.

[44] C. X. Yu et al., "Coherent combining of a 4 kW, eight-element fiber amplifier array," *Optics Letters,* vol. 36, no. 14, pp. 2686-2688, 2011.

[45] D. Kouznetsov, J.-F. Bisson, A. Shirakawa and K.-i. Ueda, "Limits of Coherent Addition of Lasers: Simple Estimate," *Optical Review,* vol. 12, no. 6, pp. 445-447, 2005.

[46] R. Paschotta, *Field Guide to Lasers,* Bellingham, WA: SPIE Press, 2008.

[47] M. C. Soriano, J. García-Ojalvo, C. R. Mirasso and I. Fischer, "Complex photonics: Dynamics and applications of delay-coupled semiconductors lasers," *Rev. Mod. Phys.,* vol. 85, no. 1, pp. 421-470, 2013.

[48] W. W. Chow and S. W. Koch, *Semiconductor-Laser Fundamentals: Physics of the Gain Materials,* Berlin, Germany: Springer-Verlag, 1999.

[49] E. Tangdiongga et al., "Optical Flip-Flop Based on Two-Coupled Mode-Locked Ring Lasers," *IEEE Photonics Technology Letters,* vol. 17, no. 1, pp. 208-210, 2005.

[50] R. Lang and K. Kobayashi, "External Optical Feedback Effects on Semiconductor Injection Laser Properties," *IEEE Journal of Quantum Electronics,* vol. 16, no. 3, pp. 347-355, 1980.

[51] J. Mørk, B. Tromborg and J. Mark, "Chaos in Semiconductor Lasers with Optical Feedback: Theory and Experiment," *IEEE Journal of Quantum Electronics,* vol. 28, no. 1, pp. 93-108, 1992.

[52] J. Mørk, J. Mark and B. Tromborg, "Route to Chaos and Competition between Relaxation Oscillations for a Semiconductor Laser with Optical Feedback," *Physical Review Letters,* vol. 65, no. 16, pp. 1999-2002, 1990.

[53] D. Lenstra, B. H. Verbeek and A. J. Den Boef, "Coherence Collapse in Single-Mode Semiconductor Lasers Due to Optical Feedback," *IEEE Journal of Quantum Electronics,* vol. 21, no. 6, pp. 674-679, 1985.

[54] V. Rottschäfer and B. Krauskopf, "THE ECM-BACKBONE OF THE LANG-KOBAYASHI EQUATIONS: A GEOMETRIC PICTURE," *Int. J. Bifurcation Chaos,* vol. 17, no. 5, pp. 1575-1588, 2007.

[55] K. Green, "Stability near threshold in a semiconductor laser subject to optical feedback: A bifurcation analysis of the Lang-Kobayashi equations," *Physical Review E,* vol. 79, no. 3, pp. 1-12, 2009.

[56] E. A. Viktorov and P. Mandel, "Low Frequency Fluctuations in a Multimode Semiconductor Laser with Optical Feedback," *Physical Review Letters,* vol. 85, no. 15, pp. 3157-3160, 2000.

[57] H. Erzgräber, et al., "Mutually delay-coupled semiconductor lasers: Mode bifurcation scenarios," *Optics Communications,* vol. 255, no. 4-6, pp. 286-296, 2005.

[58] H. Erzgräber, D. Lenstra and B. Krauskopf, "Stability of locking in mutually delay-coupled semiconductor lasers," *Proc. of SPIE,* vol. 6184, pp. 1-9, 2006.

[59] H. Erzgräber, E. Wille, B. Krauskopf and I. Fischer, "Amplitude-phase dynamics near the locking region of two delay-coupled semiconductor lasers," *Nonlinearity,* vol. 22, no. 3, pp. 585-600, 2009.

[60] L. Junges and J. A. C. Gallas, "Stability diagrams for continuous wide-range control of two mutually delay-coupled semiconductor lasers," *New Journal of Physics,* vol. 17, pp. 1-11, 2015.

[61] L. Junges, A. Gavrielides and J. A. C. Gallas, "Synchronization properties of two mutually delay-coupled semiconductor lasers," *J. Opt. Soc. Am. B,* vol. 33, no. 7, pp. C65-C71, 2016.

[62] T. Heil et al., "Chaos Synchronization and Spontaneous Symmetry-Breaking in Symmetrically Delay-Coupled Semiconductor Lasers," *Physical Review Letters,* vol. 86, no. 5, pp. 795-798, 2001.

[63] J. Mulet, C. Mirasso, T. Heil and I. Fischer, "Synchronization scenario of two distant mutually coupled semiconductor lasers," *J. Opt. B: Quantum Semiclass. Opt.,* vol. 6, no. 1, pp. 97-105, 2004.

[64] J. A. Collera, "Symmetry-breaking bifurcations in two mutually delay-coupled lasers," *International Journal of Philippine Science and Technology,* vol. 8, no. 1, pp. 17-21, 2015.

[65] A. Hohl, A. Gavrielides, T. Erneux and V. Kovanis, "Localized Synchronization in Two Coupled Nonidentical Semiconductor Lasers," *Physical Review Letters,* vol. 78, no. 25, pp. 4745-4748, 1997.

[66] S. Yanchuk, K. R. Schneider and L. Recke, "Dynamics of two mutually coupled semiconductor lasers: Instantaneous coupling limit," *Physical Review E,* vol. 69, no. 5, pp. 1-12, 2004.

[67] S. S. Wang and H. G. Winful, "Dynamics of phase-locked semiconductor laser arrays," *Appl. Phys. Lett.,* vol. 52, no. 21, pp. 1774-1776, 1988.

[68] H. G. Winful and S. S. Wang, "Stability of phase locking in coupled semiconductor laser arrays," *Appl. Phys. Lett.,* vol. 53, no. 20, pp. 1894-1896, 1988.

[69] H. G. Winful and L. Rahman, "Synchronized Chaos and Spatiotemporal Chaos in Arrays of Coupled Lasers," *Physical Review Letters,* vol. 65, no. 13, pp. 1575-1578, 1990.

[70] D. T. Nichols and H. G. Winful, "The effect of nonlinear gain on the stability of evanescently coupled semiconductor laser arrays," *J. Appl. Phys.,* vol. 73, no. 1, pp. 459-461, 1993.

[71] H. A. Haus, "Mode-Locking of Lasers," *IEEE Journal of Selected Topics in Quantum Electronics,* vol. 6, no. 6, pp. 1173-1185, 2000.

[72] E. A. Avrutin and E. U. Rafailov, "Advances in Mode-Locked Semiconductor Lasers," *Semiconductors and Semimetals,* vol. 86, pp. 93-147, 2012.

[73] L. Jaurigue, *Passively Mode-Locked Semiconductor Lasers: Dynamics and Stochastic Properties in the Presence of Optical Feedback,* Cham, Switzerland: Springer, 2017.

[74] H. A. Haus, "Theory of mode locking with a fast saturable absorber," *Journal of Applied Physics,* vol. 46, no. 7, pp. 3049-3058, 1975.

[75] F. X. Kärtner, J. Aus der Au and U. Keller, "Mode-Locking with Slow and Fast Saturable Absorbers—What's the Difference?," *IEEE Journal of Selected Topics in Quantum Electronics,* vol. 4, no. 2, pp. 159-168, 1998.

[76] H. A. Haus, "Theory of mode locking with a slow saturable absorber," *IEEE Journal of Quantum Electronics,* vol. 11, no. 9, pp. 736-746, 1975.

[77] A. G. Vladimirov and D. Turaev, "Model for passive mode locking in semiconductor lasers," *Physical Review A,* vol. 72, no. 3, pp. 1-13, 2005.

[78] R. Paschotta and U. Keller, "Passive mode locking with slow saturable absorbers," *Appl. Phys. B,* vol. 73, no. 7, pp. 653-662, 2001.

[79] J. L. A. Dubbeldam, J. A. Leegwater and D. Lenstra, "Theory of mode-locked semiconductor lasers with finite absorber relaxation times," *Appl. Phys. Lett.,* vol. 70, no. 15, pp. 1938-1940, 1997.

[80] S. H. Strogatz, "Nonlinear Dynamics and Chaos: With Applications To Physics, Biology, Chemistry, and Engineering," Reading, MA: Perseus, 1994.

[81] J. Sieber, K. Engelborghs, T. Luzyanina, G. Samaey and D. Roose, "DDE-BIFTOOL v. 3.1 Manual — Bifurcation analysis of delay differential equations," 2015, http://arxiv.org/abs/1406.7144.

[82] A. G. Vladimirov, D. Turaev and G. Kozyreff, "Delay differential equations for mode-locked semiconductor lasers," *Optics Letters,* vol. 29, no. 11, pp. 1221-1223, 2004.

[83] A. G. Vladimirov and D. V. Turaev, "A new model for a mode-locked semiconductor laser," *Radiophys. Quantum Electron.,* vol. 47, no. 10-11, pp. 769-776, 2004.

[84] M. Nizette, D. Rachinskii, A. Vladimirov and M. Wolfrum, "Pulse interaction via gain and loss dynamics in passive mode locking," *Physica D,* vol. 218, no. 1, pp. 95-104, 2006.

[85] A. G. Vladimirov, A. S. Pimenov and D. Rachinskii, "Numerical Study of Dynamical Regimes in a Monolithic Passively Mode-Locked Semiconductor Laser," *IEEE Journal of Quantum Electronics,* vol. 45, no. 5, pp. 462-468, 2009.

[86] R. M. Arkhipov, A. Amann and A. G. Vladimirov, "Pulse repetition-frequency multiplication in a coupled cavity passively mode-locked semiconductor lasers," *Appl. Phys. B,* vol. 118, no. 4, pp. 539-548, 2015.

[87] C. Otto et al., "Delay-induced dynamics and jitter reduction of passively mode-locked semiconductor lasers subject to optical feedback," *New Journal of Physics,* vol. 14, pp. 1-29, 2012.

[88] L. Jaurigue et al., "Dynamics of a passively mode-locked semiconductor laser subject to dual-cavity optical feedback," *Physical Review E,* vol. 93, no. 2, pp. 1-12, 2016.

[89] L. Jaurigue, B. Lingnau and K. Lüdge, "Advanced Control Schemes for Passively Mode-Locked Lasers: Coupled Lasers and Dual-Feedback Approaches," *International Conference on Numerical Simulation of Optoelectronic Devices (NUSOD),* pp. 123-124, 2015.

[90] E. A. Viktorov, P. Mandel, A. G. Vladimirov and U. Bandelow, "Model for mode locking in quantum dot lasers," *Applied Physics Letters,* vol. 88, no. 20, pp. 1-3, 2006.

[91] A. G. Vladimirov et al., "Dynamical regimes in a monolithic passively mode-locked quantum dot laser," *J. Opt. Soc. Am. B,* vol. 27, no. 10, pp. 2102-2109, 2010.

[92] A. Yariv, "Coupled-Mode Theory for Guided-Wave Optics," *IEEE Journal of Quantum Electronics,* vol. 9, no. 9, pp. 919-933, 1973.

[93] W.-P. Huang, "Coupled-mode theory for optical waveguides: an overview," *J. Opt. Soc. Am. A,* vol. 11, no. 3, pp. 963-983, 1994.

[94] G. Orosz and G. Stépán, "Hopf Bifurcation Calculations in Delayed Systems with Translational Symmetry," *J. Nonlinear Sci.,* vol. 14, no. 6, pp. 505-528, 2004.

[95] B. Haegeman et al., "Stability and rupture of bifurcation bridges in semiconductor lasers subject to optical feedback," *Physical Review E,* vol. 66, no. 4, pp. 1-11, 2002.

[96] P. M. Słowiński, "Bifurcation analysis of a semiconductor laser with two filtered optical feedback loops," Ph.D. dissertation, Dept. Eng. Math., Univ. of Bristol, Bristol, U.K., 2011.

[97] N. Blackbeard, H. Erzgräber and S. Wieczorek, "Shear-Induced Bifurcations and Chaos in Models of Three Coupled Lasers," *SIAM J. Applied Dynamical Systems,* vol. 10, no. 2, pp. 469-509, 2011.

[98] B. Krauskopf, G. H. M. van Tartwijk and G. R. Gray, "Symmetry properties of lasers subject to optical feedback," *Optics Communications,* vol. 177, no. 1-6, pp. 347-353, 2000.

[99] S. M. Verduyn Lunel and B. Krauskopf, "The mathematics of delay equations with an application to the Lang-Kobayashi," *AIP Conference Proceedings,* vol. 548, pp. 66-86, 2000.

[100] G. P. Agrawal and N. A. Olsson, "Self-Phase Modulation and Spectral Broadening of Optical Pulses in Semiconductor Laser Amplifiers," *IEEE Journal of Quantum Electronics,* vol. 25, no. 11, pp. 2297-2306, 1989.

[101] B. Tromborg, H. E. Lassen and H. Olesen, "Traveling Wave Analysis of Semiconductor Lasers: Modulation Responses, Mode Stability and Quantum Mechanical Treatment of Noise Spectra," *IEEE Journal of Quantum Electronics,* vol. 30, no. 4, pp. 939-956, 1994.

[102] U. Bandelow, M. Radziunas, J. Sieber and M. Wolfrum, "Impact of Gain Dispersion on the Spatio-Temporal Dynamics of Multisection Lasers," *IEEE Journal of Quantum Electronics,* vol. 37, no. 2, pp. 183-188, 2001.

[103] L. F. Shampine, S. Thompson and J. Kierzenka, "Solving Delay Differential Equations with dde23," 2002.

[104] L. F. Shampine and S. Thompson, "Solving DDEs in MATLAB," *Applied Numerical Mathematics,* vol. 37, no. 4, pp. 441-458, 2001.

[105] K. Engelborghs, T. Luzyanina and D. Roose, "Numerical Bifurcation Analysis of Delay Differential Equations Using DDE-BIFTOOL," *ACM Transactions on Mathematical Software,* vol. 28, no. 1, pp. 1-21, 2002.

[106] C. H. Henry, "Theory of the Linewidth of Semiconductor Lasers," *IEEE Journal of Quantum Electronics,* vol. 18, no. 2, pp. 259-264, 1982.

[107] C. Zhang, W.-z. Chang, A. Galvanauskas and H. G. Winful, "Simultaneous passive coherent beam combining and mode locking of fiber laser arrays," *Optics Express,* vol. 20, no. 15, pp. 16245-16257, 2012.